Chair of Molecular Nanoscience
& Chemical Physics of Interfaces (E20)
Department of Physics
Technical University of Munich

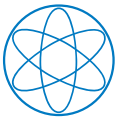

Technische Universität München

Compact and versatile electrospray - controlled ion beam deposition with adjustable frequency RF ion guides and extended mass range

Andreas Walz

PhD Thesis
Datum 09.2020

Lehrstuhl für Molekulare Nanowissenschaften
& Chemische Physik von Grenzflächen (E20)
Physik-Department
Technische Universität München

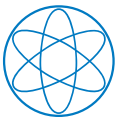

Technische Universität München

Compact and versatile electrospray - controlled ion beam deposition with adjustable frequency RF ion guides and extended mass range

Andreas Walz

Vollständiger Abdruck der von der Fakultät für Physik der Technischen Universität München zur Erlangung des akademischen Grades eines

Doktors der Naturwissenschaften (Dr. rer. nat.)

genehmigten Dissertation.

Vorsitzende/r:	Prof. Dr. Ulrich Gerland
Prüfende der Dissertation:	1. Prof. Dr. Johannes Barth
	2. Prof. Dr. Stephan Rauschenbach

Die Dissertation wurde am 02.10.2020 bei der Technischen Universität München eingereicht und durch die Fakultät für Physik am 08.12.2020 angenommen.

Abstract

Complex, functional organic or bio-molecules and nanoparticles gain increasing relevance and value as building blocks to design sophisticated nanoarchitectures in surface and nano science. Sophisticated analysis of such molecules on surfaces typically requires an ultra-high vacuum (UHV) environment. Classical deposition methods typically employ thermal sublimation of the compounds in UHV. However, a plethora of interesting and promising molecular species and nanoobjects in most cases cannot be sublimed due to their thermolability, investigation and modification with sophisticated analysis tools under UHV conditions is prevented. Preparation under ambient conditions however goes along with impurities and undefined mixtures of the objects, limiting significance. Thus, the aim of this thesis was the design of a UHV compliant deposition apparatus for solvable thermolabile molecules. Like a commercial mass spectrometer, the analyte molecules are charged by an electrospray ionization (ESI) source from solution under ambient conditions, transferred into UHV by a series of different ion guides and analysed and selected according to mass-to-charge ratio (m/z). In contrast to common analytical mass spectrometers, the ions are not discarded after m/z analysis but deposited on a target for further investigations. Consequently, the focus of this electrospray - controlled ion beam deposition (ES-CIBD) system made for preparative mass spectrometry (pMS) is on a high flux under controlled kinetic energy with precisely selected m/z. Moderate energies ensure soft-landing of intact molecules while reactive-landing with higher energies provides a new pathway for on-surface chemistry. Recently developed square-wave driven radio frequency (RF) ion guides (3 patents pending) and a digital quadrupole mass spectrometer (dQMS) provide virtually unlimited m/z range of possible analytes. The designs were probed by ion trajectory simulations with the software package SIMION. m/z resolved spectra with resolutions up to 700 allow for precise investigation and selection of the deponent, high m/z selected intensities (up to $2.2\,\mathrm{nA}$ and $10^{10}\,\mathrm{ions/s}$) and a deposition pressure in the UHV regime ($< 10^{-10}\,\mathrm{mbar}$) ensure fast and ultra-clean sample preparation. An outstanding system efficiency with more than $4\,\%$ recovery, referencing molecules in solution to deponents on the target, demonstrates the applicability of this technique even to smallest

analyte amounts and provides prospects to future use as a purification tool. The advanced pressure interfaces of the ion guides allow for low gas flow between adjacent vacuum chambers and transfer of ions from ambient to UHV after 4 differentially pumped chambers and a compact overall size of the ES-CIBD.

The biggest advantage of ES-CIBD - the vast scope of applicable chemical species and masses - was demonstrated with a mass spectrometric treatment of five examples. Depositied samples can be further analysed by means of a connected scanning tunnelling microscope (STM): An organic dye, Rhodamine B ($m = 443\,\mathrm{Da}$), and the reactive porphyrin derivate Cu-TCPP ($m = 854\,\mathrm{Da}$) used as a building-block for metal-organic networks, are representatives for relatively small species. Deposition of a synthetic n-doped graphene nanoribbon (GNR, $m = 2.3\,\mathrm{kDa}$) demonstrates usability for hydrophobic nanocarbon units used in nanoelectronics. The protein insulin ($m = 5.8\,\mathrm{kDa}$) and pioneering experiments with pUC19 DNA ($m = 1.7\,\mathrm{MDa}$) highlight the value of the technology for high masses and biologically relevant molecules with currently no limits in sight.

Zusammenfassung

Komplexe, funktionelle organische oder biologische Moleküle sowie Nanopartikel als Bausteine zum Design von anspruchsvollen Nanotech-Konstruktionen werden zunehmend relevant und wertvoll. Das kontrollierte Ablegen und Anordnen solcher Moleküle auf Oberflächen und deren Analyse erfordert Ultra-Hoch Vakuum (UHV). Klassische Depositionsmethoden basieren auf der thermischen Sublimation der Bausteinmoleküle in UHV. Diese hochinteressanten und vielversprechenden organischen Moleküle sind jedoch aufgrund ihrer niedrigen Zerfallstemperatur oft nicht sublimierbar. Deswegen ist die Untersuchung und Modifikation solcher Objekte mit anspruchsvollen Analysetechniken im Ultrahochvakuum (UHV) bisher nur bedingt möglich. Präparationen unter Normalbedingungen sind zwar möglich, gehen aber immer mit Kontaminationen und einem undefiniertem Komponentenmix einher, was die Aussagekraft deutlich reduziert. Der Aufbau einer UHV-basierten Depositionsanlage für lösliche thermolabile Moleküle ist deshalb Ziel dieser Arbeit. Ähnlich wie bei kommerziell erhältlichen Massenspektrometern werden die zur Analyse vorgesehen Moleküle mithilfe einer Elektrospray Ionisationsquelle (ESI) unter Normalbedingungen geladen, mit Hilfe von Ionenleitern ins UHV transportiert um dort anhand ihres Masse-zu-Ladung Verhältnisses (m/z) analysiert und selektiert zu werden. Der Hauptunterschied zu kommerziellen analytischen Systemen ist die anschließende Deposition der Ionen nach ihrer m/z Separation für weitere Untersuchungen, anstelle sie zu verwerfen.

Das Ziel einer solchen Elektrosprayquelle mit kontrollierter Ionenstrahldeposition (ES-CIBD), welche für präparative Massenspektrometrie (pMS) verwendet wird ist eine hohe Strahlintensität, bei kontrollierten kinetischen Energien und präzise selektiertem m/z. Niedrige Energien erlauben ein weiches Landen von intakten Molekülen. Hohe Aufprallenergien ermöglichen chemische Reaktionen, welche neue Optionen in der oberflächeninduzierten chemischen Synthese eröffnen. Neuentwickelte, mit Rechtecksignalen angesteuerte Radiofrequenz (RF) Ionenleiter (3 Patente angemeldet), sowie ein digitales Quadrupol Massenspektrometer (dQMS) erlauben die Deposition faktisch jeglicher Molekülmasse. Die Entwicklung wurde durch Simulationen der Ionenflugbahn mithilfe des

Programms SIMION unterstützt. Massenspektren mit Auflösungen bis zu 700 ermöglichen präzise Untersuchungen des Ionenstrahls. Hohe Strahlintensitäten (bis zu $2.2\,\mathrm{nA}$ und $10^{10}\,\mathrm{ions/s}$) und eine Deposition im UHV ($< 10^{-10}\,\mathrm{mbar}$) erzeugen schnelle und saubere Präparationen. Eine im Vergleich zu anderen Autoren außergewöhnlich hohe Rückgewinnungsquote von mehr als $4\,\%$ der aus der Lösung gesprühten Moleküle im Vergleich zu den auf dem Target gelandeten Molekülen belegt die Anwendbarkeit für kleinste Mengen und eine potentielle Nutzung zur Aufreinigung. Verbesserte Schnittstellen der Ionenleiter zwischen aufeinanderfolgenden Vakuumkammern machen eine Druckreduzierung von Raumdruck bis ins UHV und eine kompakte Bauweise mit nur 4 separat evakuierten Kammern möglich.
Der größte Vorteil einer ES-CIBD, nämlich das weite Spektrum an deponierbaren chemischen Spezies und Molekülmassen, wurde anhand von fünf Beispielen und mithilfe eines Rastertunnelmikroskops (STM) gezeigt. Repräsentanten für kleinere Moleküle sind der organische Farbstoff Rhodamin B ($m = 443\,\mathrm{Da}$) und ein reaktives Porphyrin Derivat (Cu-TCPP, ($m = 854\,\mathrm{Da}$)), welches als Baustein für metallorganische Netzwerke verwendet wird. Auch in der Nanoelektronik eingesetzte hydrophobe Nanocarbone sind zugänglich, wie an synthetischen n-dotierten Graphen Nanobändern (GNR, ($m = 2.3\,\mathrm{kDa}$)) demonstriert. Das Protein Insulin ($m = 5.8\,\mathrm{kDa}$) und richtungsweisende Experimente mir pUC19 DNA ($m = 1.7\,\mathrm{MDa}$) belegen die Anwendbarkeit auf hochmolekulare und biologische Moleküle, bisher ohne absehbare Größenbegrenzung.

Contents

1 Introduction

Surface and nano science employs the investigation and controlled manipulation of atoms and molecules with a spatial extend in the nanometer regime. Quantum mechanical effects, 2D-arrangements and periodicity dominate the properties of any object on this length scale and engender innovative macroscopic effects. Progress in ultra-high vacuum (UHV) technology, commercialization of single crystal production and an increasing number of techniques for investigation promoted the developments in these fields [1]. In its early days, surface science was dominated by spectroscopic and diffraction experiments, but the introduction of the scanning probe techniques like scanning tunnelling microscopy [2] and atomic force microscopy [3] gave access to real space information of surfaces with atomic precision.

One of the main driving forces of nanoscale science is the need of always smaller electronic devices. The famous Moore's law from the year 1965 recognized the transistor density of integrated circuits to double every two years [4]. For decades, history proofed him right, but during recent years the currently preferred top down fabrication methods seem to approach their fundamental limits in miniaturization [5, 6]. The impact of quantum mechanics and especially tunnelling effects prohibit feature sizes below few nanometers for robust electronic architectures or magnetic data storage elements.

Surface and nano science provide a promising alternative route for molecular-level miniaturization via utilizing interactions and quantum effects of single atoms and molecules to trigger their self-assembly. This bottom-up approach employs nanostructured materials as functional components to provide an alternative for the currently used top-down designs[5]. Exact control of size, shape and composition on an atomic level allows for ultimate downscaling and engineering of quantum mechanics for the desired purpose. Quite a few examples, i.e. organic light emitting diodes [7] or organic solar cells [8] already made their way into mass production, although most of the research currently still focusses on fundamentals in physics, chemistry and electronics by investigating model systems. Examples can be found in various fields: energy conversion [9–11], light emission [7, 12, 13] , molecular machines [14, 15], catalysis [16–21], chemical sensors [22, 23], molecular electronics [24, 25], quantum computing [26, 27], spintronics or information storage [28–30].

A clean and well defined underlying substrate like a single crystal surface is mandatory to conduct self assembly processes of extended nanostructures from small buidling blocks [5]. Another important requirement is the precisely controlled deposition of atoms and molecules in UHV to guarantee for few impurities and detrimental effects due to sample preparation and the surrounding atmosphere [31]. So far, commonly used techniques for

UHV depositions of organic molecules base on thermal evaporation via organic molecular beam epitaxy (OMBE). Chemical vapour deposition (CVD), physical vapour deposition (PVD), and molecular beam epitaxy (MBE) are more frequently used for semiconductor materials and will not be discussed in the following. Thermal evaporation of organic molecules in vacuum is limited to sublimable species. Thermolabile, reactive, and large species tend to undergo unwanted reactions or fragmentations before reaching a suitable evaporation temperature [31]. For such species pulse injection provides an alternative route. Here, a fast valve injects a small amount of dissolved molecules into the vacuum chamber, leading to a simultaneous deposition of both, solvent and desired analyte species. In some cases, the solvent might be desorbed from the surface by gentle annealing without affecting the molecules of interest [31]. Other non-UHV methods to deposit molecules from solution, such as spin coating, and inkjet printing hardly reach the requested low impurity densities [32], though providing high economic efficiency. However, applicability to surface science of all previously mentioned methods is often limited either by their range of applicable chemical species or a lack of purity.

A complementary way to expand the range of depositable molecular species under ultra-clean conditions originates from mass spectroscopy (MS). The basic components of a mass spectrometer are its ion source, its transfer ion guides, its mass-to-charge selective device and its detector [33]. Since the invention of MS in the early 20th century, many different ionization techniques for various purposes have been developed such as electron impact ionization, chemical ionization, field ionization, and fast atom bombardment [34]. Since the 1980s two further ionization techniques, matrix-assisted laser desorption ionization (MALDI), and electrospray ionization (ESI) conquer the chemical laboratories. Both allow for very soft ionization of comparably big and thermally sensitive analytes with high ionization and transfer efficiencies [35]. In 1989, the group of Fenn demonstrated the possibility to transfer large biomolecules into the gas phase [36]. John Fenn and Koichi Tanaka were awarded the Nobel Prize for the electrospray principle in 2002 [37]. Nowadays, ESI is the probably most widely used ionization techniques due to its nearly unrestricted range of analytes, its low chemical specificity and the tremendous mass range up to whole virus assemblies with $18\,\mathrm{MDa}$ in mass [35]. Alongside, several different types of mass spectrometers have emerged e.g. magnetic sector MS , linear quadrupole mass spectrometers (QMS), three dimensional quadrupoles, time-of-flight (TOF) instruments, and Fourier-transform techniques such as ion cyclotron resonance instruments and Orbitraps. Most commercial high-resolution MS systems nowadays employ TOFs or Fourier-transform mass spectrometers which require complex vacuum systems, precise machining,

complex electronics and a timed structure of the ion beam. Nevertheless, the less complex QMS is still mostly preferred when the need for high resolving power is not dominant. Its compact geometry, its ease in operation, the low kinetic energy of the emergent ions, its high transmission of continuous ion beams, and last but not least its comparably low price are major arguments for such a device. A more detailed comparison of properties, pros, and cons of different types of mass spectrometers may be found in the literature [34].

From this analytical MS approach a new technique, the so-called preparative mass spectrometry (pMS) arised [38, 39]. The major difference compared to standard MS devices is the detector, which is replaced by a further stage that extracts the ions from the mass spectrometer for subsequent deposition on a sample surface. This technique allows for deposition of a beam of priorly purified ions from a mass spectrometer in an UHV environment and the advantages are numerous. The mass spectrometer provides precise information about the analyte and its integrity prior to any subsequent investigation and the ionic nature of the deponents allows for precise control of the kinetic energy of ions during landing. So-called soft-landing [40] with low kinetic energies which preserves the integrity of the deponent becomes possible as well as on purpose increased landing energies, so-called reactive landing, in order to trigger unique structural and chemical modifications during deposition [41]. But most importantly, analytical MS and pMS proved that ionization techniques like ESI clearly outperform standard UHV deposition techniques such as thermal evaporation in a sense of the scope of applicable analytes, especially when it comes to reactive, fragile or larger chemical species. Intact saccharides [42], proteins [43, 44], DNA [32], nano clusters [44, 45], and more have been deposited.

However, just a few scientific groups currently operate home-build pMS devices due to their complexity and a lack of commercial availability. One of the main challenges of pMS is the need for high ion beam intensities when compared to analytical MS. For pMS, a sample surface needs to be decorated with about a monolayer of molecules in about an hour. For typically sizes, this requires about 10^{14} molecules, incompatible with intensities of state of the art analytical high resolution MS devices like the Orbitrap or Fourier-transform ion cyclotron resonance spectrometers with about $10^4 - 10^6\,1/\mathrm{s}$ [46, 47].

It was the scope of this thesis to finalize the design and construction of a compact and home-build electrospray-controlled ion beam deposition (ES-CIBD) system including its characterization and conducting of first depositions confirming proof of concept. The acronym ES-CIBD composes from the generation of charged molecules via a ESI source and their subsequent deposition as an ion beam with controlled kinetic energy and dose after purification via a mass spectrometer and differential pumping. The result of this

work is a fully operational ES-CIBD device with a comparably high intensity of up to $10^{10}\,\mathrm{molecules/s}$ and a potentially unlimited mass range. Low impurity densities are ensured via well resolved mass spectra and fast depositions while maintaining a pressures in the low UHV regime. After deposition, samples are investigated by an attached scanning tunnelling microscope (STM).

2 | Fundamentals and theory

The starting point for controlled ion beam deposition (CIBD) is, of course, the ion source. There are plenty of possibilities to generate ions from different media and chemical species via various types of ion sources. Subsequently, the ions have to be transferred to the mass spectrometer via ion guides. An ion guides objective is not only the transfer of ions in space, it also serves as a ”sieve” to separate neutrals from ions, i.e. the ions have to be guided between different pressure stages to remove the neutrals by pumping. Most ion sources require a certain environment to operate properly, which is often not compatible with the required vacuum conditions of mass spectrometers typically used. Compact and efficient differential pumping is an important benchmark for CIBD systems. All routinely used transfer ion guides employ electric fields to steer ions along a desired path and can roughly be classified by the time dependence of their electric fields. Static fields are employed by electrostatic lenses or a quadrupole bender, and oscillating fields are used for stacked ring ion guides and multipoles. Once reaching the mass spectrometer, the ions in the beam are selected according to their mass-to-charge ratio (m/z) and deposited on the target. The kinetic energy during deposition plays an important role in order to softly land intact ions or trigger chemical reactions by controlled higher landing energies.

2.1. Electrospray ionization (ESI)

Generation of gas-phase ions from non-volatile compounds has been of interest for more than 50 years, especially for mass spectrometry [48]. Over the years, several different techniques have been established, for example: electron impact ionization (EI), fast atom bombardment (FAB), laser desorption techniques like matrix-assisted laser desorption ionization (MALDI), and electrospray ionization (ESI) [48, 49]. Besides those, there are numerous other more or less related ambient pressure ionization techniques used in MS [50]. Here ESI was chosen due to its capability to ionize very fragile chemical species, especially organic and biological molecules, to provide ”wings for molecular elephants” [37]. It is the most universal ionization technique with low chemical specificity and fairly unlimited mass range [35, 36, 51]. Furthermore, it was already used for preparative mass spectrometry [38, 39].

A simple ESI source consists of only a few components (see Figure 2.1). The starting point is always some kind of vessel, typically a syringe, with a pump to supply a solution of dissolved analyte molecules to a so-called emitter. The emitter consists of a small capillary, typically made from fused silica or metal. A high voltage (HV) source supplies

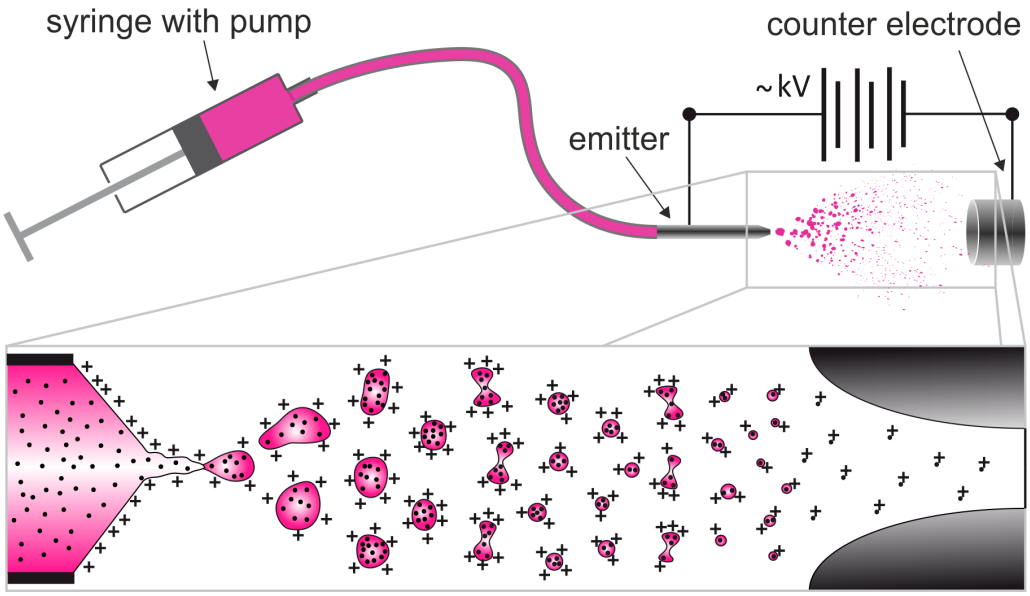

Figure 2.1.: Sketch of a simple ESI source, consisting of a syringe with a pump which supplies a dissolved analyte (purple) to an emitter. A strong electric field towards a counter electrode generates a spray of charged droplets at the tip of the emitter. Due to steady solvent evaporation and Coulomb fission, the charged droplets disintegrate down to bare analyte ions. The bore in the counter electrode acts as an atmospheric pressure interface and transfers the ions into vacuum. From [52] with modifications.

the analyte solution with a defined potential either via a partially conductive emitter or a separate electric contact. The tip of the emitter is positioned in front of a counter electrode to generate a strong electric field. Charge carriers accumulate on the liquid's surface and the electrostatic forces start to compete with the capillary forces. In 1964 Taylor demonstrated that a water droplet forms a cone towards an electrode, dependent on the pressure ratio inside versus outside the droplet. This so-called Taylor Cone ejects a spray of small charged droplets when a certain voltage is exceeded.[53].

2.1.1. Electrospray modes

Over the years, several different spray modes have been proposed and there is still ongoing work and discussions about the identification and physical understanding of different phenomena [54–59]. Pioneering experiments have already been reported about a century ago [60], but a lack of consistent terminology in literature makes the discussion even more complicated. Therefore, the terminology and most of the standpoints in the following originate from a very recent review by Rosell-Llompart [54].
As already mentioned above, there are four main forces acting on the liquid at the tip of an emitter. The momentum force, the electric force due to the applied potential, the gravitational force, and the capillary force. According to their relative strengths, different regimes and behaviours of the spray may be found. Due to the scope of this thesis, only spray modes in the electrohydrodynamic (EHD) regime will be described, as it is the only one used in practical applications. In this regime, the electric forces are of the same order or larger than the capillary forces. Surface tension, viscosity, vapour pressure and conductivity of the liquid are key parameters. Gravitational forces and momentum forces are negligible. Besides the physical properties of the liquid, the geometry and electric conductivity of the emitter, the surrounding gas, and applied potentials are important parameters.

Sorting from low to high applied potentials, the first EHD modes which occur are periodic ones. Here, the meniscus at the tip of the emitter, as well as the emitted current, change periodically. During so-called electro dripping (Figure 2.2a), one large main drop is detached one after another, resulting in a single current pulse per period. In spindle (Figure 2.2b) and intermittent cone-jet mode (Figure 2.2c), the meniscus already emits a fine spray of charged droplets. Each cycle is interrupted by the detachment of a larger fragment, or a periodic change of the meniscus shape, respectively.
The most desired spray modes for application are the so-called steady EHD modes at

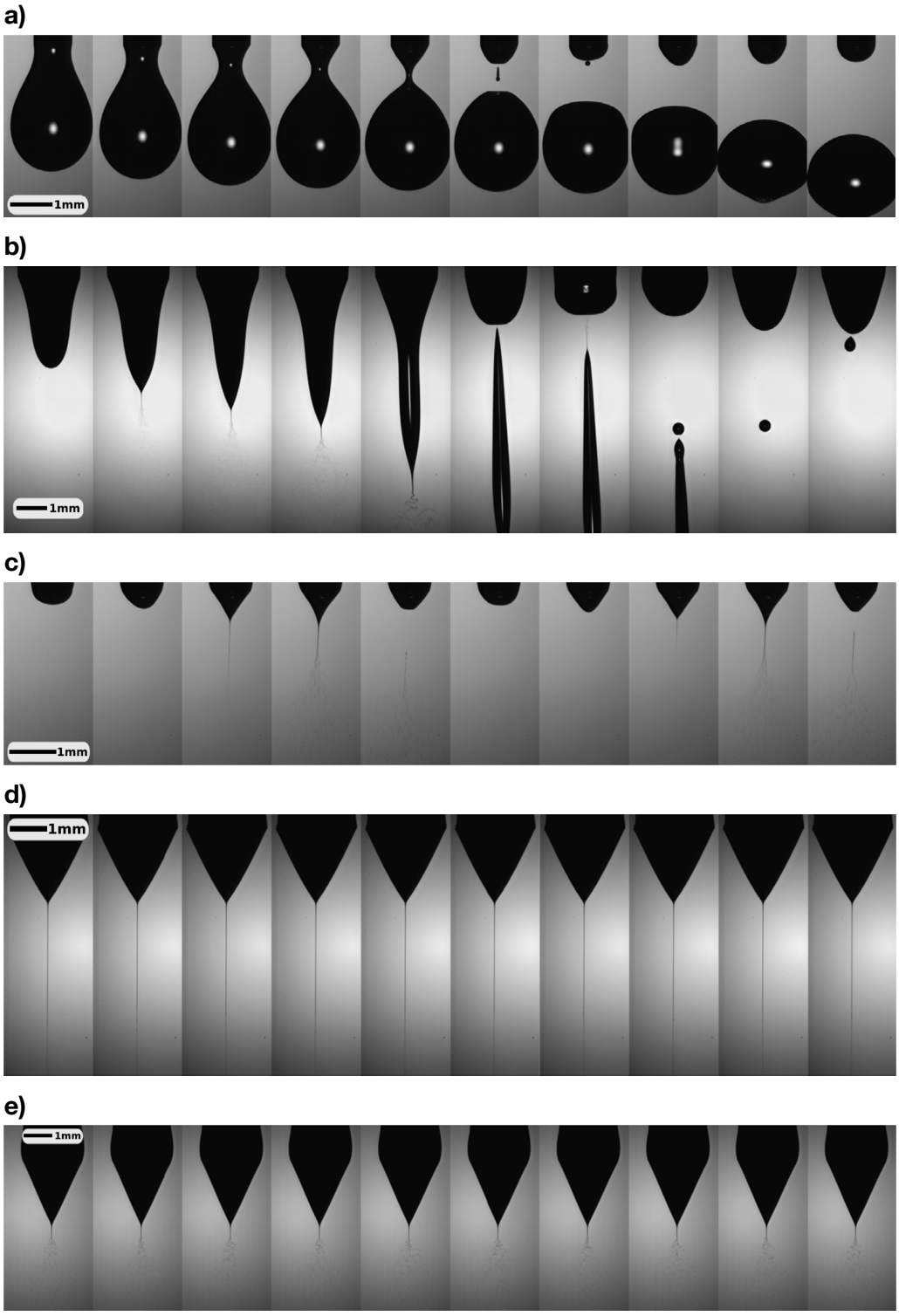

Figure 2.2.: Series of snapshots of the meniscus of an ESI emitter for different spray modes: a) electro dripping, b) spindle, c) intermittent cone-jet, d) cone-jet with varicose brake up, e) cone-jet with kink instabilities. From [59] with modifications.

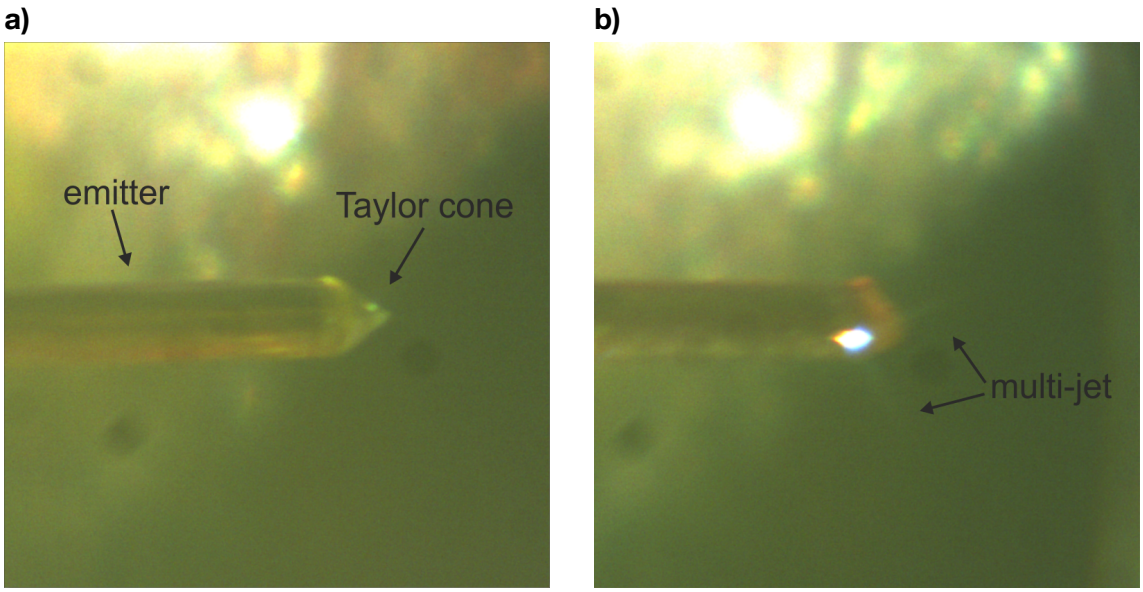

Figure 2.3.: Photographs of different spray modes from the current ES-CIBD system. a) shows a cone-jet mode with a stable Taylor cone. b) proposes a multi-jet mode.

medium potentials due to their high and continuous ion current. The most prominent is the cone-jet mode (Figures 2.2d, 2.2e). The shape of the meniscus is close to a perfect "Taylor cone" [53], but the exact profile and length of the cone depends on the flow rate, as well as on the analyte liquid's properties [61]. The second continuous, high current mode is the multi-jet (Figure 2.3b). In this case, the ions originate from multiple cones at the rim of the emitter [55, 56, 62].
Besides the shape of the menisci, the process of formation of the droplets when detaching is also influenced by various spray parameters (Figure 2.2d, 2.2e) [59, 63–68].

2.1.2. Coulomb fission

The resulting aerosol plume from the electrospray consists of highly charged droplets, that are accelerated towards a counter electrode. Due to the high surface to volume ratio of small spheres and the non-zero vapour pressure, the droplets rapidly shrink by evaporation of neutral solvent molecules. At the so-called Rayleigh limit [69], surface tension and Coulomb repulsion cancel out each other. The critical charge q_R for a spherical droplet is

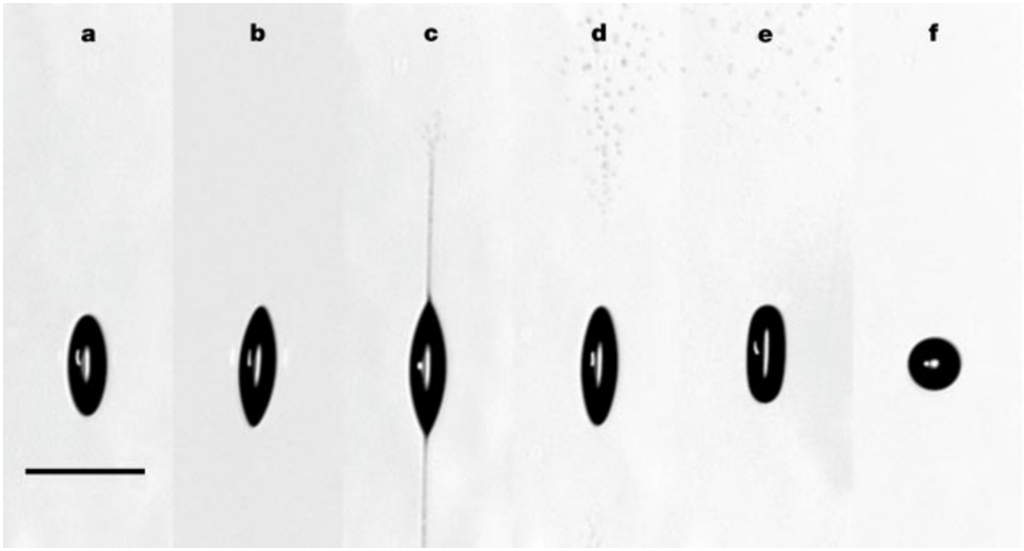

Figure 2.4.: Series of snapshots of a Rayleigh charged droplet undergoing Coulomb fission. a: elliptically deformed droplet, b: formation of tips, c: ejection of a Rayleigh jet from the tips, d-f: relaxation of the mother droplet and dispersion of daughter droplets. From [70].

given by

$$q_R = 8\pi\sqrt{\epsilon_o \gamma r^3} \tag{1}$$

with the vacuum permittivity ϵ_o, the liquid's surface tension γ, and the droplet's radius r. For $q \geq q_R$, the droplet becomes unstable for small perturbations and the so-called Coulomb fission occurs [70]. Here, the charged droplets split up and increase their surface above the Rayleigh limit.

The sequence of snapshots in Figure 2.4 was recorded by Duft [70] and shows a levitated droplet undergoing Coulomb fission. The droplet was previously charged, and neutral solvent molecules evaporated until the Rayleigh limit was undercut at a radius of about $24\,\mu\mathrm{m}$. Figure 2.4a depicts a droplet which is deformed into an ellipsoid due to a quadrupole-shaped oscillation. 2.4b shows the formation of two sharp tips right before the ejection of two Rayleigh jets of small droplets in 2.4c. 2.4d-f illustrate the relaxation of the mother droplet. During disintegration, about 100 small daughter droplets of approximately $1.5\,\mu\mathrm{m}$ diameter where emitted, which carry about $33\,\%$ of the charge and $0.3\,\%$ of the mass of the mother droplet [70].

The cycle of Coulomb fission and solvent evaporation repeats in a cascadic way and the droplet size decreases to few nm [71]. In the end, the bare analyte ion is formed. Note,

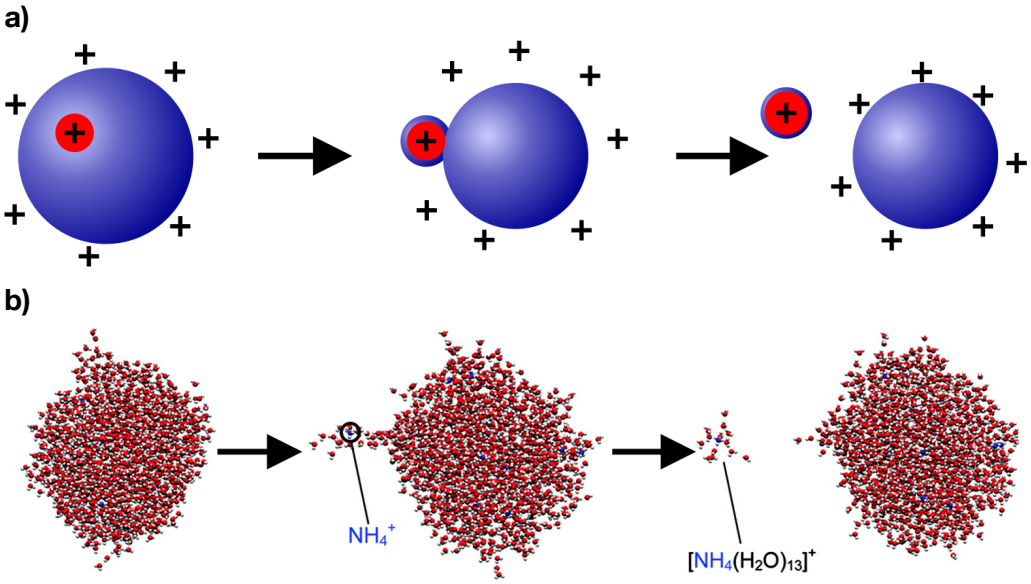

Figure 2.5.: Ion evaporation model (IEM): Already charged ions are ejected from the mother-droplet as the Coulomb limit is reached. a) Sketch of IEM with the ion being represented in red and the solvent in blue. The droplet shrinks due to solvent evaporation. Subsequently, the ion diffuses to the surface and forms a small protrusion to be ejected and thereby restoring stability of the mother droplet. Adapted from [71]. b) Snapshots of a respective molecular dynamics (MD) simulation. Colour code: white for hydrogen, red for oxygen, blue for nitrogen. From [73] with modifications.

that for this purpose a distinct relationship between analyte and solvent molecules is of great importance.

2.1.3. Ion generation

The exact process of gas-phase ion formation from a small charged droplet is still under debate [71, 72]. Nevertheless, there is a comprehensive publication by Konermann [71], which combines the three most common theoretical models with molecular dynamics simulations. Low molecular weight analytes may be described with the ion evaporation model (IEM), larger globular ones with the charge residue model (CRM) and long nonpolar ones with the chain ejection model (CEM). The basic concepts of all three models are sketched in Figures 2.5-2.7.

The ion evaporation model (IEM): This model describes the formation of gas-phase ions of low mass from solvated ions in a parent droplet (see Figure 2.5). The charge of the

ions either originates from the salt-like nature of the analyte or a charged atom or molecular group provided by the solvent is attached to an appropriate molecular group on the analyte molecule. In case of positive charging this amounts mostly to protonation. Both ways electric forces act on the ion in the droplet, whereas at the beginning with an excess of solvent, the charge of ions is typically screened to the surface of the droplet by solvent molecules, the ion itself is dissolved inside the droplet. When undercutting the Rayleigh limit, surface protrusions start to occur on the droplet's surface and a dissolved ion is ejected to restore stability of the mother droplet [73, 74]. IEM is very similar in nature to Coulomb fission and there might be no distinct discrimination between both processes for small droplets in the nano-meter regime [75].

During the process of IEM, a small daughter droplet with a charged molecule detaches from a larger mother droplet. Figure 2.5a shows a sketch of the process. The large blue circle indicates the charged mother droplet and the small red one is the charge that is emitted. For shrinking mother droplet diameters, the red charge starts to diffuse towards the surface. A protrusion of the mother droplet forms and the ion is ejected with a small shell of solvent molecules. Figure 2.5b depicts the corresponding molecular dynamics calculation by Ahadi et al. [73]. 11 ammonium ions are dissolved in 1500 water molecules to form a mother droplet. Taking a closer look at Figure 2.5b reveals that NH_4^+ ions are initially not located on the outermost surface of the droplet (leftmost picture). Gauss' Law predicts, that all charge carriers on an electrically isolated and conductive sphere to be equally distributed on the outermost shell. However, the NH_4^+ ions are dissolved in a polar medium, water. The charge of the ions is screened by surrounding polarized solvent molecules, a behavior, well known from the Debye Hückel theory. Thus as long as the shielded ion - solvent complex does not "touch" the droplets surface, i.e. the droplet is big enough, there is no Gaussian force on it and the charge remains on the surface, carried by the polarized solvent. In a previous paper, Ahadi et al. [76] performed MD simulations on the example of Na^+ ions dissolved in water and indeed found ions to prefer positions in the droplet, and that a screening of their charge to the surface of the droplet by the dipole moments of the water molecules is favourable. Similar argumentation might hold for the depicted example of NH_4^+ ions, too.

The snapshot in the middle depicts a mother droplet featuring a protrusion with a single NH_4^+ ion, encapsulated by water molecules. Directly after this snapshot, the protrusion detaches and forms a small daughter droplet consisting of one NH_4^+ ion, surrounded by 13 water molecules. The mother droplet relaxes to its initial spherical shape due to restored stability. Over time, the mother droplet will shrink again due to evaporation of neutral

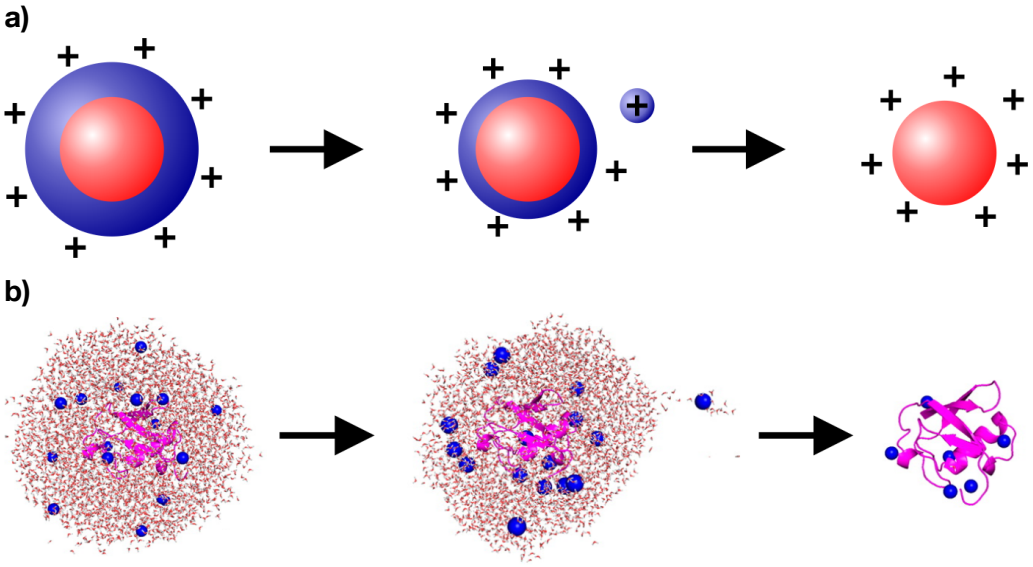

Figure 2.6.: Charge residue model (CRM): Generation of gas-phase ions of globular analytes from Rayleigh-charged droplets. The dissolved molecule stays close to the droplet's center and is charged with the last solvent molecules evaporating. a) Sketch of CRM with the molecule being represented by a red circle and the droplet by the blue surrounding. The droplet shrinks in size due to solvent evaporation and ejection of small charged daughter droplets (IEM). Finally, the charged analyte molecule is left. Adapted from [71]. b) Snapshots of a respective MD simulation. Colour code: small white for hydrogen, small red for oxygen, blue for Na^+ and magenta for the folded protein. From [72] with modifications.

water molecules, reaches a critical charge and repeats the process of IEM.

The charge residue model (CRM): The CRM is suitable for large and globular analytes like folded proteins. Figure 2.6 illustrates the different steps of the process. The sketch in 2.6a shows an analyte (red) remaining in the center of a Rayleigh charged droplet (blue), even though there is only a small solvation-shell left. The droplet is charged close to the Rayleigh limit during the whole process. Excess charge due to desolvation may be ejected by IEM. The charging of the analyte happens with the last solvent molecules evaporating [72, 77–80].

Figure 2.6b depicts a snapshot of corresponding MD simulation. The initial droplet consists of a folded ubiquitin molecule in a 3 nm water droplet, charged by 16 Na^+ ions. The droplet starts shrinking due to solvent evaporation and the ejection of small charged daughter droplets via an IEM-like process. Finally, the ubiquitin completely desolvates, charged by 6 residual Na^+ ions. As a result, the rather globular protein stays in a native-like conformation with a charge close to the Rayleigh limit of a solvent droplet of comparable

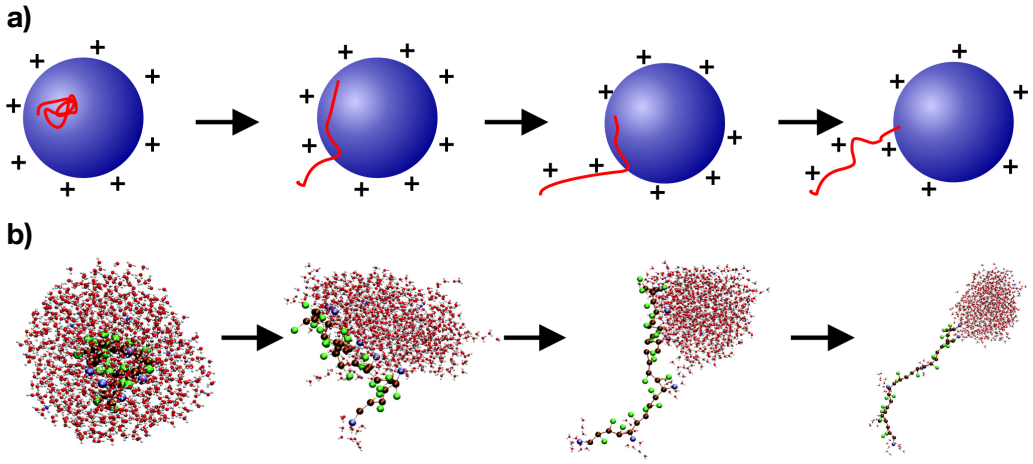

Figure 2.7.: Chain ejection model (CEM): A chain-like molecule, initially in globular conformation, in a Rayleigh charged droplet unfolds, migrates to the surface, and gets ejected as a charged molecular ion. a) Sketch of CEM with the molecule being represented by a red line and the droplet by a blue circle. Adapted from [71]. b) Snapshots of a respective MD simulation. The polymer is approximated by a chain of different beads in a coarse-grained model. Colour code: small white for hydrogen, small red for oxygen, small blue for nitrogen, large brown for neutral backbone of the chain, large blue for positive side chain, large green for neutral side chain, large orange for negative side chain. From [84] with modifications.

size [72]. The actual charge state of the resulting ion can be estimated from equation 1 and depends on the surface tension of the droplet. Furthermore, the charge scales with the square root of the volume of the sphere, which indicates that the m/z of the resulting ion increases with with the square root of mass assuming a constant density of the molecules. Experiments with proteins confirm such charge states [79, 81–83]. Note, that the charge carriers in the solution influence the chemistry and mass of the resulting ion. Care needs to be taken to not affect the native-like conformation of proteins by charging with inappropriate ions.

The chain ejection model (CEM): The behaviour of chain-like molecules that are disordered, poorly soluble, or bind excess charge can be described by the CEM. Examples for this class of analytes might be non-globular proteins, DNA or polymer chains. Proteins for example often show a globular conformation in neutral aqueous solutions with their hydrophilic groups exposed to the water and their hydrophobic parts in the center [85]. A change in pH for example might induce unfolding, which exposes their partly hydrophobic core to the solution. For the unfolded chains, it might be more favourable to diffuse

to the droplet's surface in order to desolvate hydrophobic sections. Following, the chain might be expelled stepwise from the droplet into gas-phase [84, 86].
An example of the CEM is depicted in Figure 2.7a. The chain-like molecule (red) is folded in a rather globular conformation. It starts to unfold in a Rayleigh charged droplet (blue) and migrates to its surface. Once one tail end touches the droplets surface, the electric forces of the external field act on the ion, extracting it from the droplet while being stepwise charged at the surface, further enhancing the external electric force. The snapshots in Figure 2.7b show a MD simulation of a polymer chain, approximated by a coarse-grained model and consisting of 27 backbone beads and 26 side chain beads. The different colours represent the backbone and the either positive, negative, or neutral side chains. The polymer is positioned close to the center of a water droplet with four additional ammonia ions. During ejection, small amounts of solvent molecules attach to hydrophilic side groups. Lastly, a strongly elongated chain detaches from the mother droplet [84]. For long and uniform chains, the molecules show a certain charge density per unit length. In contrast to CRM, the charge state scales linearly with the length of the chain and the m/z does not significantly change with the size of the molecule.
Summing up, all different spray modes and theoretical models aim to explain the formation of gas-phase ions from dissolved molecules. For the experimenter, it is important to understand these basic principles in order to "let the analytes fly" or find suitable solutions for trouble shooting. An unstable spray mode might be eliminated by simply changing the spray voltage or pumping speeds. When reaching a multi-jet, it is helpful to not further increase the potential drastically. Conformational information might already be figured out by the careful observation of m/z resolved spectra. Charge states close to the Rayleigh limit of their folded conformation might indicate a round, native-like conformation of proteins, while much higher charge states indicate a chain-like conformation [87–89]. The same argument for conformational forecasts based on the charge state might also be valid for other molecules.

2.1.4. The atmospheric pressure interface

In principle, a simple counter electrode close to the emitter is suitable to generate the required electric field for the spray process. The surface of this electrode would be sufficient to deposit an analyte. This type of electro-spray deposition is already used in industrial processes like painting, microencapsulation, electroemulsification, fine powder production, or micro- and nano-thin film deposition [90]. Unfortunately, one has no information

of the exact composition of the ion beam and the charge states. Furthermore, there are inevitable contaminations from the solvent and the surrounding atmosphere. However, it is possible to equip the counter electrode with a bore in order to form an interface to a vacuum chamber. Due to the ambient conditions of the emitter, ion trajectories are strongly influenced by the surrounding atmosphere's flow field as ions have a very short mean free path. Strong reduction of scattering events in a vacuum environment, however, allows trajectories to be easily controlled by application of suitable electric fields. MS for example takes advance of this fact in order to produce ions from an ESI source at ambient conditions and investigate them by means of their m/z in vacuum. Preparative MS further utilizes the m/z selected ions from the spectrometer for deposition. The advantages, of a deposition under UHV conditions are: a much higher degree of control due to the selected m/z of ions, a controllable deposition energy and essentially no impurities of the solvent molecules or the surrounding atmosphere.
Most ESI sources operate at ambient or close to ambient conditions to avoid discharges and enhance desolvation of droplets, but also reports on so-called subambient pressure ionization [91–93] and super-atmospheric pressure ion sources [94, 95] can be found in literature. Nevertheless, all devices have to overcome a gradient between the pressure of the electrospray and the high vacuum typically required for operating a mass spectrometer. Therefore, all ambient pressure sprays employ a so-called atmospheric pressure interface to transfer ions from the spray into vacuum. This interface ideally provides high ion transmission efficiency for high intensities, combined with low residual gas flow to reduce the required pumping speed in the first vacuum chamber. Since the early days of ESI, simple apertures and conical skimmers have been used for this purpose [77]. Even today, e.g. some commercial sources rely on the same principles [96]. Later designs employ elongated capillaries as pressure interfaces to reduce pumping speed [97, 98]. In the currently described ES-CIBD system, the design of the group around S. Rauschenbach with a funnel shaped inlet, followed by an elongated capillary, is used [99]. In most cases, the ESI interface employs some sort of heating in order to enhance the sprayed droplet's desolvation.

2.1.5. A short summary of different ESI sources

Besides the simple principles described above, many different designs and modifications of ESI sources have been investigated for different purposes. The following subsection provides a rough overview of previous work in literature without any claim to be com-

plete.
Starting with the emitter, there are several manufacturers and distributors offering emitter tubing material made from fused silica with inner diameters ranging from below $10\,\mu\mathrm{m}$ to few $100\,\mu\mathrm{m}$. Outer diameters are typically several hundred $\mu\mathrm{m}$. Probably the easiest way to manufacture an emitter is cutting this tubing into pieces of appropriate length and connecting it to the syringe. The drawbacks are comparably large inner and outer diameters of the tubing, as well as a potentially not very well defined surface at the freshly cut tip. Furthermore, the high voltage potential may not be contacted to the sample solution directly at the tip, but rather far away which requires a certain conductivity of the solution. In literature, it is shown that smaller emitter bores may by favourable due to a reduction of required solution flow rate combined with higher ionization efficiency. This leads to both, lower sample volumina, and improved mass spectra. [100, 101].
To come to smaller emitters, the so-called pulling of fused silica or glass tubes is a common technique. Here, a tension is applied along the axis of the fused silica tube while being heated in the middle. At some point the tubing's glass temperature is reached, it elongates due to the tension, and finally splits into two pieces. Cutting off the tubing at the pulled end at an appropriate position leads to a tip of small inner and outer diameter with very thin walls [102, 103]. Alternatively, the emitter may also be etched [103–105] or mechanically treated [106]. For direct electric contact, the tip of the emitter is often plated with a thin, electrically conductive film [103, 104, 106, 107]. With these techniques, emitter sizes in the low $\mu\mathrm{m}$ range are possible [101–103]. This type of electrospray is often referred to as nanoESI due to its typical analyte flow rates in the $\mathrm{nl/min}$ regime [102]. Several publications investigate the effects of flow rates on different ESI sources and the efficiency of the emitter [93, 108–110]. Further miniaturization of emitters was achieved by using lithography or focused ion beam etching to form nanofluidic capillary slots [111] or micro chip based emitter systems made from silicon [112–114].
Apart from the emitter's diameter, the tip's exact shape may also be important for the electrospray [115]. Duby et al. [116] compared a metal emitter with a polished, flat tip surface to an emitter with grooves at its tip. Especially at elevated voltages, multiple jets located at the grooves emerged due to the enhanced electric field at these positions. The generation of multiple jets in a single ESI-source has also been realized by arrays of fused silica emitters [117, 118] or multiple emitters on a single micro chip [113].
The electrospray's surrounding media may also influence its properties. Schneider et al. [108] showed that a small chamber around the emitter, which may be filled with a curtain gas of adjustable temperature, allows for a strong increase in ionization efficiency. Loscer-

tales et al. [119] demonstrated a coaxial emitter where a central liquid is surrounded by another one in order to generate small droplets consisting of two phases. Similar experiments with multiple gas and solvent channels have also been realized with a micro chip based emitter [114].
Another important part of the ESI source is its counter electrode, in most cases acting as the inlet into a vacuum chamber. Standard counter electrodes simply consist of an elongated metal tube with few cm length and bore diameters of about $1\,\mathrm{mm}$. The influence of length and diameter have been investigated in several publications [108, 109, 120, 121]. Also, different counter electrode materials have been investigated [120]. Additionally, the advantages of more sophisticated counter electrodes with multiple bores [110, 121] or funnel shaped inlets [99] have been demonstrated.
The group around R. D. Smith developed a subambient pressure source operating in the few 10 mbar regime [93, 110, 118]. The low pressure allows for elimination of the counter electrode and direct spraying into the first vacuum ion guide thus reducing the neutral gas load significantly. Possibly due to the deviating spray behaviour such an interface found no allies yet.
Several commercial ESI sources for MS systems have been compared by Stahnke et al [96]. Especially commercially available ESI sources aim for low contamination of the first vacuum ion guide with non-volatile analyte molecules in order to reduce maintenance and down-times. Therefore, most sources employ heated drying gas and skimmers to enhance desolvation of the droplets. Furthermore, the emitter is typically not axially aligned with respect to the counter electrode's bore. The angled arrangement is beneficial to prevent heavy, low charged droplets from reaching the vacuum. In some cases, another 90 degree bend of the ion beam is performed in the first vacuum chamber to further reduce contamination [96, 121].

2.2. Theory of RF ion guides and spectrometers

Since the first experiments with charged particles, the question for their control, containment and manipulation has been of great interest. Early attempts employed static electromagnetic fields like electrostatic lenses [122, 123]. Another milestone was the invention of the quadrupole mass spectrometer (QMS) in the 1950s by Paul and Steinwedel [124, 125]. Due to its low cost and simple handling, a broad field of mass spectrometry emerged in analytical chemistry, which was dominated by the QMS for decades [126, 127]. Besides,

particle accelerators and nuclear fusion research developed complementary technologies for ion confinement and manipulation [128, 129].
The current ES-CIBD system operates exclusively with RF driven ion guides. This section describes the theoretical background of these ion guides. A mathematical description of different concepts of ion guides and their respective properties will be provided. Other techniques based on electrostatic or magnetic confinement will not be discussed but can be found in literature [129–131].
A rather universal theoretical treatment of RF driven ion guides was published by D. Gerlich in 1992 [132]. A major part of the following discussion is based on this work.
Please note that the following theoretical treatment addresses a single particle movement in an idealized oscillating electric field, that is later approximated by a static and radial-symmetric pseudo potential. That means this theory is appropriate to describe ion guides and the quadrupole mass spectrometer with elongated electrodes, low ion density, and long residence time of the ions in the field. It does not concern any angular components or phase relation between particle motion and oscillating fields. The ES-CIBD described in this thesis exceeds these limits. In default of a universal theory, we concentrate on this widely used approximation and its description of basic properties.
We consider a particle of mass m and charge q in an external electromagnetic field $\mathbf{E}(\mathbf{r},t)$, $\mathbf{B}(\mathbf{r},t)$. For the non-relativistic case, the classical equation of motion is:

$$m\ddot{\mathbf{r}} = q\mathbf{E}(\mathbf{r},t) + q\dot{\mathbf{r}} \times \mathbf{B}(\mathbf{r},t). \tag{2}$$

For heavy particles in decent electric fields and rather low kinetic energies, the velocity $\dot{\mathbf{r}}$ is assumed to be small and the exclusion of strong quasi-stationary magnetic fields allows to neglect the last term of equation (2).
For further simplification, we assume a quasi-stationary electric field $\mathbf{E}(\mathbf{r},t)$ as a superposition of a static electric field $\mathbf{E}_s(\mathbf{r})$ and a time-dependent field $\mathbf{E}_0(\mathbf{r})\ cos(\Omega t + \delta)$. Here, $\mathbf{E}_0(\mathbf{r})$ represents the amplitude of the field, modulated with a constant angular frequency Ω. Now, equation 2 can be rewritten as:

$$m\ddot{\mathbf{r}} = q\mathbf{E}_s(\mathbf{r}) + q\mathbf{E}_0(\mathbf{r})\ cos(\Omega t) \tag{3}$$

Assuming a smooth electric field with and small oscillations of the ion trajectory, we may use a separation ansatz for the position $\mathbf{r}(t)$ with a smooth drift term $\mathbf{R}_0(t)$ and an oscillating

term $\mathbf{R}_1(t)$.

$$\mathbf{r}(t) = \mathbf{R}_0(t) + \mathbf{R}_1(t) \quad with \quad \mathbf{R}_1(t) = -\mathbf{a}(t)\ cos(\Omega t) \tag{4}$$

with $\mathbf{a}(t)$ as the amplitude of particle movement due to the oscillating field. The spatial coordinate's second derivative with respect to time can now be calculated as:

$$\ddot{\mathbf{r}}(t) = \ddot{\mathbf{R}}_0 + \ddot{\mathbf{a}}\ cos(\Omega t) - 2\Omega\dot{\mathbf{a}}\ sin(\Omega t) - \Omega^2\mathbf{a}\ cos(\Omega t). \tag{5}$$

Assuming a high angular frequency Ω and a slow change of $\mathbf{a}(t)$ with time leads to:

$$\ddot{\mathbf{r}}(t) = \ddot{\mathbf{R}}_0 - \Omega^2\mathbf{a}\ cos(\Omega t). \tag{6}$$

Approximation of the electric field by the first two terms of its Taylor expansion leads to:

$$T_1\ \mathbf{E}_0(\mathbf{R}_0; \mathbf{R}_0 - \mathbf{a}\ cos(\Omega t)) = \mathbf{E}_0(\mathbf{R}_0) - (\mathbf{a}\cdot\nabla)\mathbf{E}_0(\mathbf{R}_0)\ cos(\Omega t) \tag{7}$$

Insertion of equations (6) and (7) into the equation of motion (3) gives the rather complicated expression:

$$m\ddot{\mathbf{R}}_0 - m\Omega^2\mathbf{a}(t)\ cos(\Omega t) = q\mathbf{E}_s(\mathbf{r}) + q\mathbf{E}_0(\mathbf{R}_0)\ cos(\Omega t) - q(\mathbf{a}\cdot\nabla)\mathbf{E}_0(\mathbf{R}_0)\ cos^2(\Omega t) \tag{8}$$

Again, we assume a smooth electric field and a fast angular frequency Ω to keep the amplitude of the oscillations $\mathbf{a}(t)$ small. This leads to insignificant changes in the electric field in a single oscillation $\mathbf{E}_0(\mathbf{R}_0 \pm \mathbf{a}) \approx \mathbf{E}_0(\mathbf{R}_0)$. For slow drift velocities, the amplitude varies slowly with time and we can approximate the time-dependent amplitude by a position-dependent oscillation in a homogeneous field.

$$\mathbf{a}(t) = \mathbf{a}(\mathbf{R}_0) = \frac{q\mathbf{E}_0(\mathbf{R}_0)}{m\Omega^2} \tag{9}$$

Insertion of equation (9) into (8) allows for conversion of the last term by using the properties of a quasi-electrostatic field $\nabla \times \mathbf{E} = 0$:

$$(\mathbf{E}_0\cdot\nabla)\mathbf{E}_0 = \frac{1}{2}\nabla\mathbf{E}_0^2 - \mathbf{E}_0 \times (\nabla \times \mathbf{E}_0) = \frac{1}{2}\nabla\mathbf{E}_0^2 \tag{10}$$

Finally, the smooth drift motion $\mathbf{R}_0$ can be separated by calculating the time average, thus eliminating the cosine terms and replacing the cosine-square by $1/2$.

$$m\ddot{\mathbf{R}}_0 = q\mathbf{E}_s(\mathbf{r}) - \frac{q^2}{4m\Omega^2}\nabla\mathbf{E}_0^2 \tag{11}$$

The last term represents the so-called ponderomotive or field-gradient force [132–134]. This effect is the primal driving force of all RF ion guides. In brief words, a charged particle in an inhomogeneous oscillating electric field experiences a force pointing away from regions of high field-gradients. Note, that the force is independent of the sign of the charge. For simplification, a so-called pseudo potential V^* was introduced by replacing the static electric field by the gradient of a static potential $\mathbf{E}_s = -\nabla\Phi_s$:

$$m\ddot{\mathbf{R}}_0 = -q\nabla V^*(\mathbf{R}_0) \;\text{ with }\; V^*(\mathbf{R}_0) = \frac{q}{4m\Omega^2}\mathbf{E}_0^2 + \Phi_s \tag{12}$$

Integration of equation (12) leads to a constant total energy E_m of the ion in the field.

$$\frac{1}{2}m\dot{\mathbf{R}}_0^2 + \frac{q^2}{4m\Omega^2}\mathbf{E}_0^2 + q\Phi_s = E_m \tag{13}$$

Therefore, the energy of the smooth motion of the ion in the field can be transferred into effective potential energy and electrostatic potential energy. Note, there is no energy transfer between electric field and charged particle. Such a system is called adiabatic. This property is crucial for most RF driven ion guides as there is typically no damping of the ion motion via friction or scattering. A non-adiabatic system would constantly transfer energy to the charged particles until their kinetic energy exceeds the depth of the effective trapping potential of the ion guide, thus leaving the trapping volume and being lost.
The second term of equation (13) can be identified with the time-averaged kinetic energy of the fast oscillatory motion:

$$< \frac{1}{2}m\dot{\mathbf{R}}_1^2 >= \frac{q^2}{4m\Omega^2}\mathbf{E}_0^2 \tag{14}$$

This result indicates that the energy attributed to the effective potential is actually stored in the fast oscillatory motion of the charged particle. In general, energy transfer between a dynamic inhomogeneous electric field and a charged particle is possible and the total energy of the ion is not constant. Therefore, it is necessary to find a parameter that ensures the validity of the effective potential approximation and adiabaticity of the motion. A very

basic requirement to allow for the separation of the spatial coordinate in equation (4) and the termination of the taylor expansion in equation (7) is the smooth variation of the electric field in the peak to peak amplitude of a single oscillation $2\mathbf{a}$.

$$|2(\mathbf{a}\nabla)\mathbf{E}_0| < |\mathbf{E}_0| \tag{15}$$

To ensure the validity of this effective potential approach, the dimensionless adiabaticity parameter η was defined.

$$\eta = \frac{|2(\mathbf{a}\nabla)\mathbf{E}_0|}{|\mathbf{E}_0|} = \frac{2q|\nabla\mathbf{E}_0|}{m\Omega^2} \tag{16}$$

For small η, energy transfer between ion and electric field is inhibited and the effective potential approximation is valid. Larger values indicate unstable trajectories due to a gain of kinetic energy of the electric field over time leading to increasing amplitudes of the oscillations and finally to violations of boundary conditions like the size of the ion guide or depth of the effective potential.
Another important parameter is the charge capacity and the distribution of the ions in an ion guide. For low kinetic energies of the ions, the field-balance condition between the effective focusing field $\mathbf{E}^*$ and the space charge field $\mathbf{E}_{sc}$ needs to be fulfilled. Inserting Poisson's equations gives an expression for the charge distribution ρ:

$$-\nabla V^* = \mathbf{E}^* = -\mathbf{E}_{sc} \quad \text{and} \quad -\nabla\mathbf{E}_{sc} = \frac{\rho}{\epsilon_0} \tag{17}$$

In the following, the effective potential approach is apllied to the different types of ion guides of the ES-CIBD system. The first subsection describes the multipole ion guide in general, followed by a description of the special cases of a QMS and finally the ion funnel.

2.2.1. Linear multipole ion guides

The general idea behind linear multipole ion guides is to create a 2D trapping potential around a central axis in order to guide ions onto a desired path. This type of ion guide typically consists of an even number of electrodes starting by four, a quadrupole. The electrodes are arranged equidistantly on a circle around a central axis. To produce an ideal multipole field, these electrodes should have a hyperbolic shape. Since the manufacturing of such electrodes is very difficult and expensive, multipoles frequently employ cylindrical electrodes to approximate an ideal multipole field. In the following this sim-

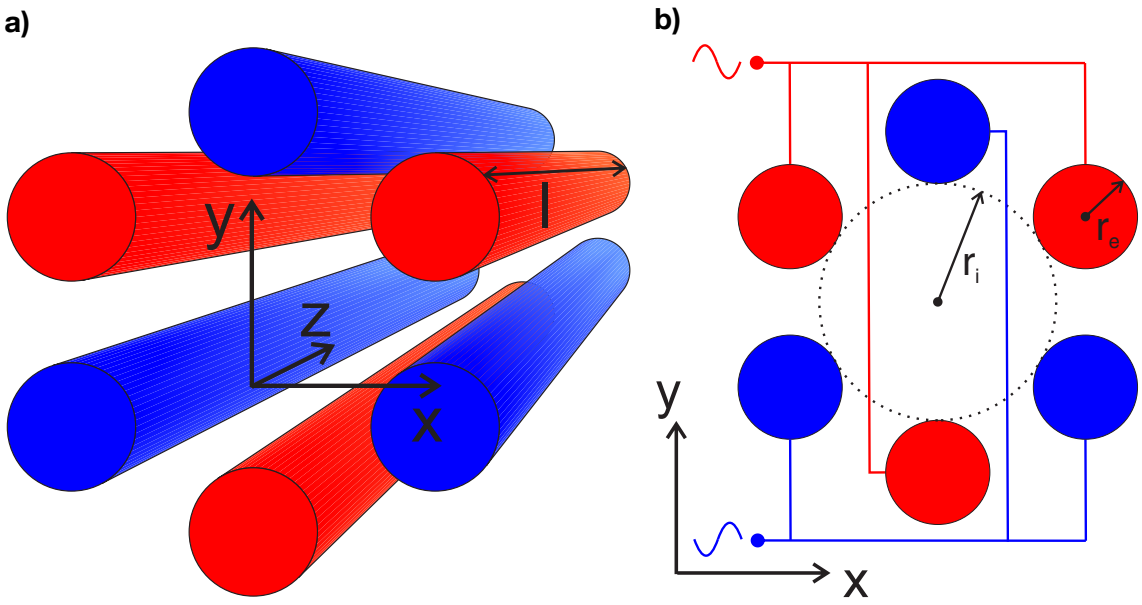

Figure 2.8.: Schematic drawings of a multipole ion guide with cylindrical electrodes arranged equidistantly around a central axis. The colour code in blue and red indicates the supply with two RF signals, phase-shifted by 180°. a) shows a hexapole made from six electrodes of length L. b) depicts a cross section perpendicular to the symmetry axis. The inscribed radius and the electrode radius are indicated by r_i and r_e, respectively. Adapted from [52, 135].

plification will be applied. A typical geometry of a multipole employing six electrodes, a so-called hexapole, is depicted in Figure 2.8. All electrodes have a length of L and a radius of r_e. The so-called inscribed radius r_i is defined as the radius of the largest circle inside the ion guide which does not touch the electrodes. r_i determines the volume of stable particle trajectories. Charged particles that exit this radius are considered lost e.g. by impinging on an electrode surface.

To generate an oscillating field neighbouring electrodes are supplied with sine-shaped RF potentials phase-shifted by 180° (indicated by blue and red). In general, it is possible to operate multipoles with different electric signal shapes like square waves or triangular waves. For simplicity, only the most common case of a sine-shaped RF signal of a resonant oscillating circuit will be discussed. Furthermore, we consider a long ion guide ($l \gg r_i$) with neglectable fringing fields at its ends. The cylindrical symmetry allows for elimination of the potential's z-component. The electric field's absolute amplitude of an

ideal multipole is given by [132, 136]:

$$E_{RF}(r) = \left(\frac{NU_{RF}}{r_i}\right) \hat{r}^{\,N-1} \tag{18}$$

Here, $2N$ represents the number of electrodes of the multipole, U_{RF} is the amplitude of the applied RF signal, and the reduced radius $\hat{r} = r/r_i$. A more detailed theoretical derivation and discussion of multipole fields can be found in literature [137, 138]. Now, the effective potential V^* of a multipole can be calculated from equation (12):

$$V^*(r) = \frac{q}{m} \left(\frac{NU_{RF}}{2r_i\Omega}\right)^2 \hat{r}^{\,2(N-1)} \tag{19}$$

From this formula, it is obvious that the shape of the potential is only dependent on the number of electrodes. A quadrupole, for example, produces a parabolic potential. Higher order multipoles ($N > 2$) have a higher exponent, which causes a flat potential in the center with a steep increase close to the electrodes. The respective adiabaticity parameter η from equation (16) is:

$$\eta = \frac{2N(N-1)qU_{RF}}{m\Omega^2 r_i^2} \hat{r}^{\,N-2} \tag{20}$$

Gerlich [132, 139] suggests adiabatic motion for $\eta_{max} < 0.3$ from the example of an octopole ion guide. Tolmachev [136] suggested higher values of $\eta_{max} < 1$. Note, that the radial component $\hat{r}^{\,N-2}$ equals unity in the special case of a quadrupole with $N = 2$. Thus, an RF amplitude exceeding the critical voltage $U_{RF,max}$ (where $\eta = \eta_{max}$) leads to merely unstable trajectories for a given charged particle and a frequency Ω. This behaviour is commonly known as low mass cut-off in the RF-only mode and will be discussed in section 2.2.3. Therefore, the following calculations exclude the case of a QMS and exclusively address higher order multipoles with $N > 2$. Rewriting equation (20) gives a maximum allowed radius for adiabatic trajectories:

$$r_{adiabatic} = r_i \left(\frac{\eta_{max} m\Omega^2 r_i^2}{2N(N-1)qU_{RF}}\right)^{\frac{1}{N-2}} \tag{21}$$

Following the restrictions of the adiabatic parameter η, Gerlich states a maximum allowed radius of $r_{max} = 0.8\, r_i$ for an octopole in order to provide some space for oscillations in the RF field without impinging of particles on an electrode surface.

The trapping and confinement of charged particles in a multipole is of atmost importance. Thus we look for the maximum kinetic energy of a particle which can be trapped by a multipole. The turning radius describes the maximum reachable radius of an ion's smooth motion in the effective potential. It can be calculated by the effective potential's depth and the ion's kinetic energy in the xy plane. In other words, a charged particle inside a given multipole is considered trapped, when its turning radius in the effective potential is smaller than a maximum allowed radius for ion trapping r_{trap}, which is limited by the smaller values of either maximum allowed radius or radius of adiabatic motion $r_{trap} = min\,(r_{max}, r_{adiabatic})$. Therefore, an ion which is injected into a multipole ion guide is considered trapped, when its initial radial kinetic energy is smaller than the effective potential energy at the trapping radius.

$$E_r < qV^*(r_{trap}) \quad \text{with} \quad r_{trap} = \min\,(r_{max}, r_{adiabatic}) \tag{22}$$

Inserting the radial restrictions into the multipole's effective potential in equation (19) leads to a trapping potential for both limitations of the form:

$$V^* = \begin{cases} \frac{q}{m}\left(\frac{r_{max}}{r_i}\right)^{2(N-1)}\left(\frac{NU_{RF}}{2r_i\Omega}\right)^2 & \text{for } r_{max} < r_{adiabatic} \\ \frac{N^2}{4}\left(\frac{m\Omega^2 r_i^2}{q}\right)^{\frac{N}{N-2}}\left(\frac{\eta_{max}}{2N(N-1)}\right)^{\frac{2N-2}{N-2}} U_{RF}^{-\frac{2}{N-2}} & \text{for } r_{max} > r_{adiabatic} \end{cases} \tag{23}$$

As mentioned in the very beginning of this section, a commonly used multipole ion guide employs a set of electrodes which are supplied by a LC circuit. Therefore, the frequency of the oscillation Ω of the field is typically determined by the resonance frequency. Only the applied potential may be adjusted. It is obvious that $r_{adiabatic}$ decreases with U_{RF} for a given ion guide and RF frequency. Following that, the effective potential is limited by r_{max} for low amplitudes and increases with the RF-amplitude's square. Note, this increase is independent of the order of the multipole. At a certain amplitude, $r_{max} = r_{adiabatic}$ is reached. For further increasing amplitudes, the effective potential is limited by $r_{adiabatic}$, which leads to a decrease in effective potential (see figure 2.9b). Following, there is a maximum effective potential V^*_{max} when $r_{max} = r_{adiabatic}$. The respective amplitude can be calculated as:

$$U_{RF,max} = \frac{\eta_{max} m\Omega^2 r_i^2}{2N(N-1)q}\left(\frac{r_i}{r_{max}}\right)^{N-2} \tag{24}$$

Inserting this amplitude into the effective potential gives an expression for the maximum potential depth of a multipole for a given particle and RF frequency:

$$V^*_{max} = \frac{\eta^2_{max} m \Omega^2 r^2_{max}}{16(N-1)^2 q} \tag{25}$$

This formula gives an upper limit for the maximum allowed kinetic energy of an injected charged particle to be stored in the ion guide. The height of this potential may be influenced by the geometry of the electrodes (r_i and N), or by a simultaneous increase of the RF frequency and amplitude. Note, that the ideal amplitude $U_{RF,max}$ scales with Ω^2.
Besides the potentials, the charge density and their distribution in the multipole are also important. The symmetry of the multipole field allows for cylindrical coordinates and a radial charge distribution $\rho(r)$. Equation (17) can be rewritten as:

$$\rho(r) = -\epsilon_0 \frac{1}{r} \frac{1}{\delta r}(r E^*) \tag{26}$$

We assume a high enough effective potential to trap the charged particles in the ion guide $\rho(r) = 0 \ \forall \ r > r_{trap}$. Furthermore, a finite amount of charge per unit length Q_l gives a maximum radius of the ion beam r_{ion} with $Q_l = \int_0^{r_{ion}} \rho(r) dr$ and:

$$\rho(r) = \begin{cases} \epsilon_0 (N-1)^2 \ \frac{q}{m} \ (\frac{N U_{RF}}{\Omega r_i^2})^2 \ \hat{r}^{2(N-2)} & \text{for } \ r \leq r_{ion} \\ 0 & \text{for } \ r > r_{ion} \end{cases} \tag{27}$$

For illustration purposes, some important properties of the multipole fields are depicted in Figure 2.9. The plot in 2.9a shows the typical shape of an effective multipole potential (grey) and the respective charge distribution for low energy particles (red). In this case, the ion distribution follows equation (27). The field balance in the middle of the ion cloud gives rise to a flat overall potential in the cloud. The overall potential (black dotted line) is flat for all $r \leq r_{ion}$ and follows the effective potential elsewhere. Therefore, the filled red area indicates the charge density's integral and can be interpreted as the finite amount of charge per unit length Q_l with its termination condition at $r = r_{ion}$. Note, that the charge distribution follows an exponent of $2(N-2)$. For higher order multipoles ($N > 2$), the exponent gives rise to a low ion density in the middle with a steep increase close to the electrodes.
The plot 2.9b compares the potentials of three different multipole orders. The parameters where chosen such that all curves share the same amplitude $U_{RF,max}$ for their maximum

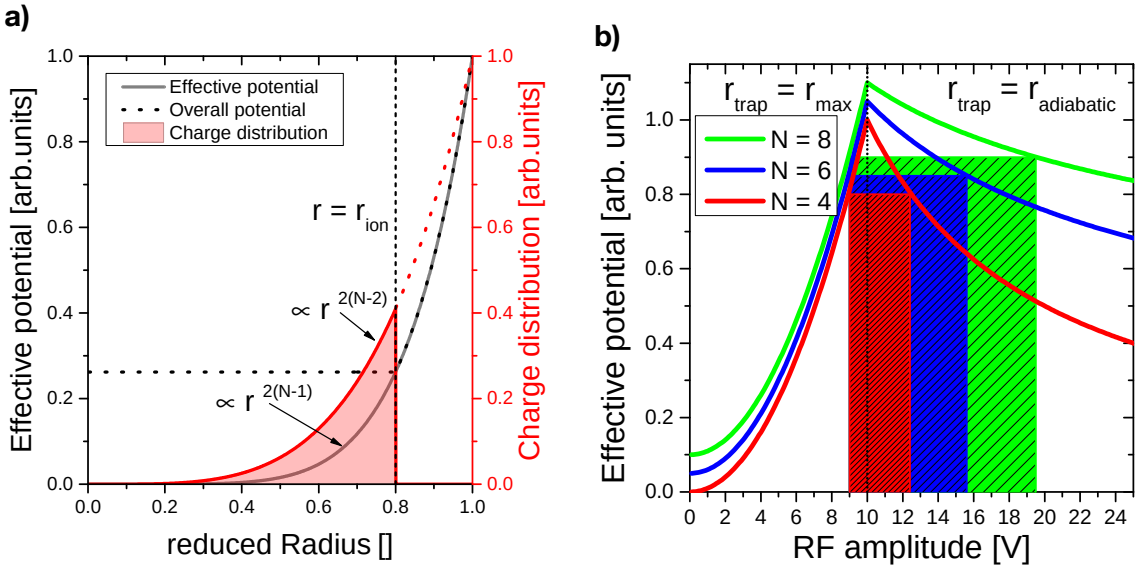

Figure 2.9.: Plots of different features of multipole fields. a) depicts a typical effective multipole potential (grey), filled with a certain amount of charge (red). Due to Coulomb repulsion, the electric fields need to be balanced in the ion distribution leading to a flattened center of the overall potential (black dots). b) shows trapping potentials of different multipoles for a range of RF amplitudes. All potentials share the same ideal amplitude $U_{RF,max}$. The filled areas represent the amplitudes capable of trapping an ion with a radial kinetic energy of $0.8\ qV^*_{max}$. Graphs with increasing order are shifted upwards for illustrative reasons by 0.05.

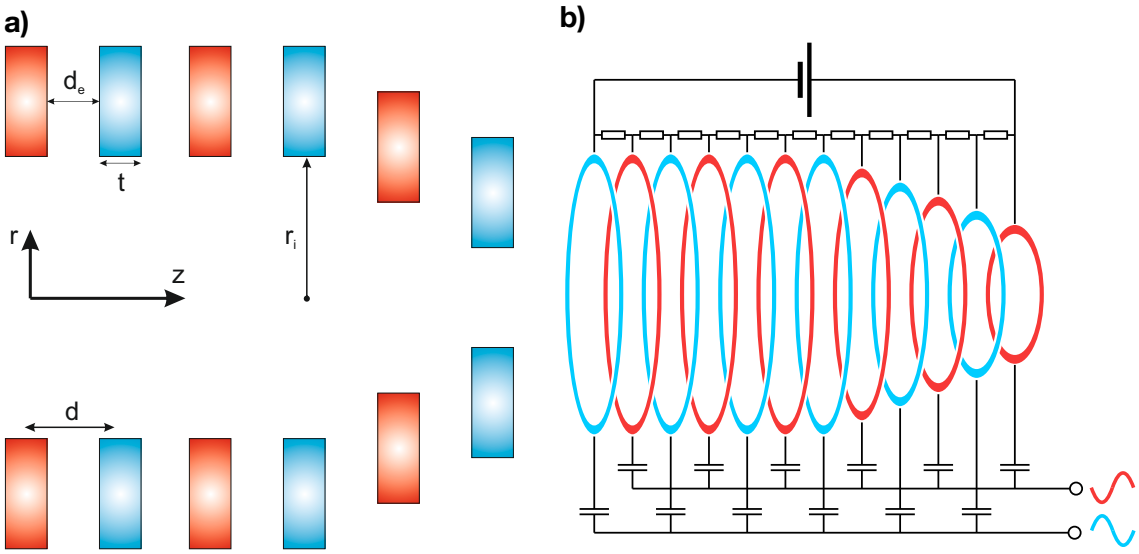

Figure 2.10.: Schematics of the electrode array of an ion funnel. a) depicts a cross section along the symmetry axis of the funnel. The electrode geometry is defined by inscribed radius r_i, the distance between electrodes d_e, their thickness t and the resulting electrode pitch $d = d_e + t$. From [135] with modifications. Figure b) shows a typical electrical supply scheme for an ion funnel. Neighbouring electrodes are supplied with $180°$ phase-shifted RF signals, indicated in blue and red. The RF signal is coupled to the electrodes via capacitors and an additional array of resistors superimposes a DC potential. From [52] with modifications.

trapping potential V^*_{max}. Furthermore, the curves have been normalized to unity. For visualization, the graphs were shifted upwards for increasing electrode numbers by 0.05. All rising edges have the same shape, independent of the electrode number (see equation (23) for $r_{trap} = r_{max}$). In contrast, the falling edge is limited by $r_{trap} = r_{adiabatic}$ and decreases more rapidly for low multipole orders. The dashed lines indicate the amplitude range in which an ion with $0.8\ qV^*_{max}$ kinetic energy in radial direction may be trapped. Note, that higher order multipoles show a slower decrease in effective potential for $U_{RF} > U_{RF,max}$ and, therefore tend to show broader amplitude windows for efficient charged particle trapping.

2.2.2. Stacked ring ion guides

Besides the multipoles mentioned above, there is a second type of RF ion guides predominantly used in regions of high background pressure: the stacked ring ion guide or ion funnel (see Figure 2.10). The path of the ions is defined by the axis of the stack of ring

electrodes. Neighbouring electrodes are supplied with RF signals with of 180° phase shift. In addition to the RF signal, a DC gradient may be applied along the axis of the ion guide [140].
in the ES-CIBD system, the ion funnel is used to collect and focus the ions from the outlet of the ESI source's atmospheric pressure interface in the first vacuum chamber. A typical funnel design employs a simple resistor network, acting as a voltage divider, and a stack of ring electrodes with shrinking inscribed radius towards the exit. The conical shape allows for focusing of the ion beam. One of the major advantages of an ion funnel compared to a multipole is its capability to operate in higher pressure regions. One of the reasons is the tunable DC potential along the z-axis. In regions of poor vacuum, scattering of ions with residual gas atoms needs to be considered and ions tend to follow the flow of the gas towards the vacuum pump. Thus, to keep ions on track, it is necessary to trap the ions in two dimensions in the funnel via the RF field and additionally generate a driving force towards the exit of the funnel via the potential gradient.
In the following theoretical description, we consider the simplest case of an elongated stacked ring ion guide with constant inscribed diameter. Furthermore, we assume a sine-shaped RF signal without a superimposed DC gradient. The effective potential can be written as [132, 140, 141]:

$$V^*(r,z) = V_{trap}\left[I_1^2(r/\delta)\cos^2(z/\delta) + I_0^2(r/\delta)\sin^2(z/\delta)\right] \tag{28}$$

with

$$V_{trap} = \frac{V_{max}}{I_0^2(r_i/\delta)} \quad \text{and} \quad V_{max} = \frac{qU_{RF}^2}{4m\Omega^2\delta} \tag{29}$$

Here, δ is related to the pitch distance of the electrodes $\pi\delta = d$ (see Figure 2.10a). I_0 and I_1 represent the zeroth and first order modified Bessel functions, respectively. Note, that V_{trap} is the potential's amplitude of oscillation in the center of the ion guide along the symmetry axis (see below). For $x \gg 1$ the Bessel functions can be approximated by $I_{1,2}(x) \approx e^x/\sqrt{2\pi x}$. Rewriting equation (28) thus leads to:

$$V^*(r) \approx V_{max}\frac{r_i}{r}\exp\left(\frac{r-r_i}{\delta/2}\right) \quad \text{for} \quad r \gg \delta \tag{30}$$

The criterion for the radius r implies that the inscribed radius of the electrodes must be large compared to the pitch distance $r_i \gg d$ [136, 141].

For small radii $r \approx 0$, the Bessel functions of equation (28) can be approximated by $I_0(0) = 1$ and $I_1(0) = 0$. The effective potential close to the central axis can therefore be approximated by [141]

$$V^*(z) = V_{trap}\, sin^2(z/\delta) \quad \text{for} \quad r \approx 0 \tag{31}$$

The potential V_{trap} of this formula can be attributed to the amplitude of the potential that traps ions between two electrodes. In Figure 2.11, the oscillation of the potential along the central axis can be nicely observed [142]. Note, that the straight funnel in 2.11a employs a large inscribed radius compared to the pitch repetition ($r \gg \delta$), which gives rise to small oscillations and trapping potentials in the center. Figure 2.11b depicts a potential landscape of a conical funnel, where the aforementioned condition is successively violated. The trapping potential and its oscillations increase for decreasing inscribed radii. For the design of an ion funnel it is therefore very important to keep V_{trap} small enough in order not to trap, accumulate, and subsequently lose ions at small inscribed radii. The trapping potential should be much smaller than the effective potential $V_{trap} \ll V_{max}$ and the inscribed radius in turn should be much larger than the pitch of the electrodes $r_i \ll d$. This problem can be tackled by applying a suitable DC gradient along the ion funnel. One can estimate that ions effectively overcome the potential barriers in the center, when their kinetic energy in the direction of the symmetry axis is larger than qV_{trap}. In most cases the movement of ions is influenced by the flow of the background gas. Flow-speed along the z-axis is small, as the gas is pumped perpendicular to the electrodes. Thus the DC potential between adjacent electrodes has to be larger than the trapping potential to generate enough kinetic energy of the ions. Note, that the confining properties of an ion funnel may also suffer when ions are moving too fast along the central axis. This might be the case when an ion's z-velocity v_z becomes fast enough to pass an electrode pair in a single RF cycle $v_z \approx \frac{\Omega}{2\pi} d$. In this case, there is no repulsive force due to the oscillating field any more. [136, 140, 141].
Finally, the adiabaticity parameter from equation (15) can be calculated as:

$$\eta = \frac{2qU_{RF}}{m\Omega^2\delta^2} \sqrt{\frac{r_i}{r}}\, \exp\left(\frac{r - r_i}{\delta}\right) \quad \text{for} \quad r \gg \delta \tag{32}$$

Again, we can limit the maximum allowed turning radius of a charged particle that is considered trapped r_{trap} in a funnel by a maximum radius r_{max} before impinging on electrodes and a maximum radius for adiabatic motion $r_{adiabatic}$. Unfortunately, rewriting equation

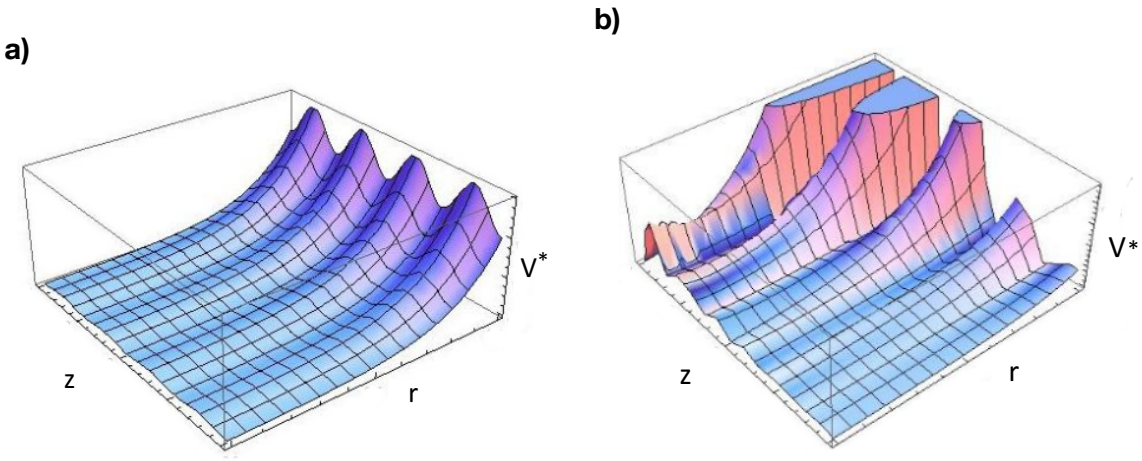

Figure 2.11.: Radial effective potential of an ion funnel. a) shows a linear ion funnel with constant inscribed radius and $r_i \gg \delta$. b) depicts the effective potential of a conical array with shrinking inscribed diameter. From [142] with modifications.

(32) for the radius r gives a rather complicated expression and the movement of the ions is strongly affected by the poor vacuum such a funnel is typically operated. Thus these aspects will not be further investigated. The take-home message here is analogous to the multipole discussion above. There is an ideal RF amplitude $U_{RF,max}$ for a maximum effective potential V^*_{max} of a given ion funnel, driven with a fixed RF frequency Ω, filled with a certain species of charged particles, exactly when $r_{max} = r_{adiabatic}$. Below $U_{RF,max}$ the trapping potential increases with U^2_{RF} (see equation (30)). Above this limit the potential decreases. This behaviour is similar to that of a higher order multipole.
Another similarity is the rather flat effective potential in the center with a steep increase close to the electrodes, thus leading to a comparably large ion distribution with respect to r_i. The major difference are the separated electrodes along the z-axis which allow for focusing and a potential gradient, but come at the expense of a much larger number of electrodes for elongated devices and a lower limit for the inscribed radius of the electrodes at a given electrode distance.

2.2.3. The linear Quadrupole Mass Spectrometer (QMS)

The quadrupole, the most widely used multipole, can be operated in another mode besides its application as an ion guide: Paul and Steinwedel used it in the 1950s to separate ions by their m/z [124, 143]. The linear Quadrupole Mass Spectrometer (QMS) became a

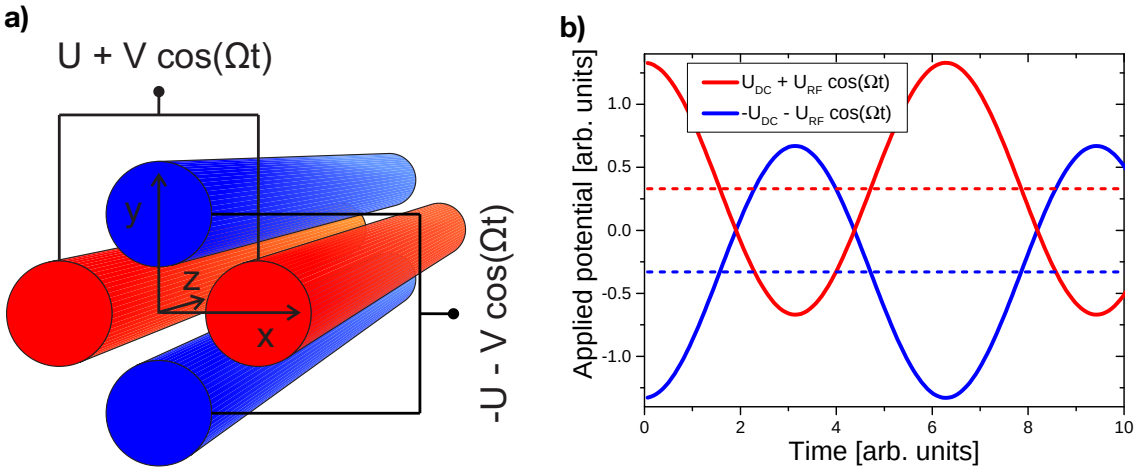

Figure 2.12.: Sketch of a typical QMS. a) shows four rod electrodes, arranged on a circle whereas neighbouring electrodes are supplied with RF signals of opposite sign. The applied sine-shaped signals with superimposed DC potentials are depicted in b).

prominent tool in physics and chemistry and Wolfgang Paul was awarded the Nobel Prize in physics in 1989 [144]. The small and simple construction, as well as its easy and fast operation for a comparably low price makes it one of the most frequently used ion guides and mass spectrometers to this day [34].

Starting from the linear QMS several variations have been developed, like quadrupole ion traps and the 3D quadrupole [34, 127]. Due to its pioneering role, the term ”linear” is often ignored in literature and it is referred to as QMS only.

Starting from the first QMS in 1955, the ideal hyperbolic electrodes have been replaced by cheaper circular rods in most applications [143, 145]. To approximate the ideal quadrupole field as precise as possible, a ratio between electrode rod radius and inscribed radius is the range between $r_e/r_i \approx 1.14 - 1.16$ was proposed [125, 145, 146]. Since this approximation seems not to influence the properties significantly, it will not be discussed in the following.

A sketch of a typical QMS including its electric supply is depicted in Figure 2.12. The electrode rod pairs in x-direction (red) and y-direction (blue) share two supply signals. The signal typically consists of a sine-shaped RF signal with amplitude U_{RF} and frequency Ω with a superimposed DC potential U_{DC}, the later is often called resolving DC. The sum of DC and RF potential is defined as the difference between both rod pairs. Note, its reference to ground is defined as a further DC voltage mostly denoted as field axis potential.

For the following theoretical calculations, the finite length of the rods is neglected in order to ignore the z-component. The equation of motion 2 can now be separated in x- and y-

direction by [34]:

$$\begin{aligned} \frac{d^2x}{dt^2} + \frac{q}{mr_i^2}(U_{DC} + U_{RF}\ cos\Omega t)\ x = 0 \\ \frac{d^2y}{dt^2} - \frac{q}{mr_i^2}(U_{DC} + U_{RF}\ cos\Omega t)\ y = 0 \end{aligned} \tag{33}$$

Rewriting these equations in dimensionless form leads to:

$$\begin{aligned} \frac{d^2x}{d\tau^2} + (a_x + 2q_y\ cos2\tau)\ x = 0 \\ \frac{d^2y}{d\tau^2} + (a_y + 2q_x\ cos2\tau)\ y = 0 \end{aligned} \tag{34}$$

$$\text{with}\ \ a_x = -a_y = \frac{4qU_{DC}}{mr_i^2\Omega^2}\ \ ,\ \ q_x = -q_y = \frac{2qU_{RF}}{mr_i^2\Omega^2}\ \ ,\ \ \tau = \frac{\Omega t}{2} \tag{35}$$

These equations of motion have the form of Mathieu equations. Stable ion trajectories with a radial extent smaller than the inscribed radius $r \leq r_i$ and the symmetry conditions $a_x = -a_y$, $q_x = -q_y$ can be plotted in a so-called stability diagram (see a-q space in Figure 2.13)[127]. The differently shaded areas indicate the a and q values for stable trajectories in x- and y-direction, respectively. There are several regions, labelled by Roman numerals, in which stability is given for motion in both x and y. These regions are typically called stability regions. Choosing the a and q parameters in the boundaries of a stability region allows for stable trajectories in the quadrupole field.
While operation in higher stability regions is possible [147–151], standard QMS systems typically employ the first stability region in order to discriminate between different m/z due to the decent a and q values (see 2.14). Note, that a is porportional to the applied DC potenital U_{DC} and q to the applied RF amplitude U_{RF}. The typical operation of such a QMS is depicted in Figure 2.14. The apices of the first stability region of all possible m/z (e.g. shaded blue and red) align on a line (solid black) in the U_{DC} vs U_{RF} diagramm. In order to perform a m/z resolving scan, the RF and DC amplitudes are ramped up simultaneously along a predefined curve, typically a straight line with smaller slope (dotted and dashed black lines) compared to the enveloping line of apices.
During a typical scan, the QMS is continuously supplied with ions at its inlet while a detector records the amount of transmitted ions at the exit. For each set of potentials on the scan line, only a m/z within a small range allows for stable trajectories in the QMS and

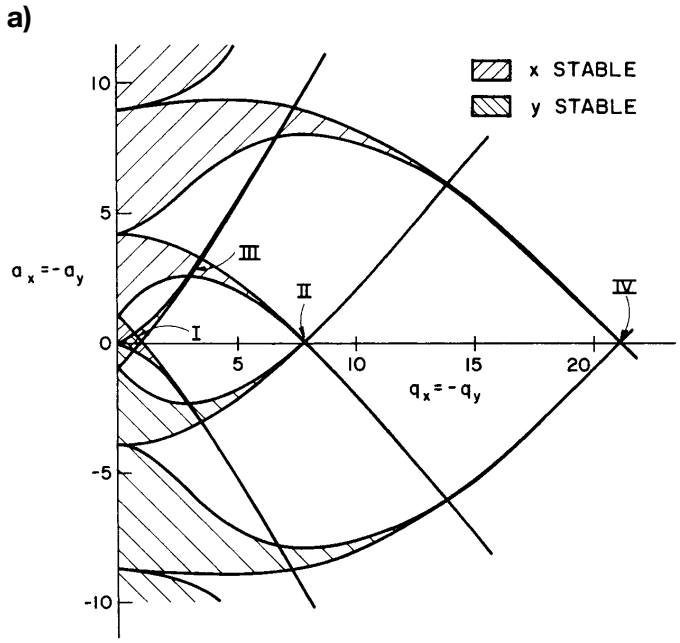

Figure 2.13.: Stability diagram of a QMS in a-q space. The differently hatched areas represent stable trajectories in x- and y-direction, respectively. In their intersections, the so-called stability regions, overall stable trajectories may be found. From [127].

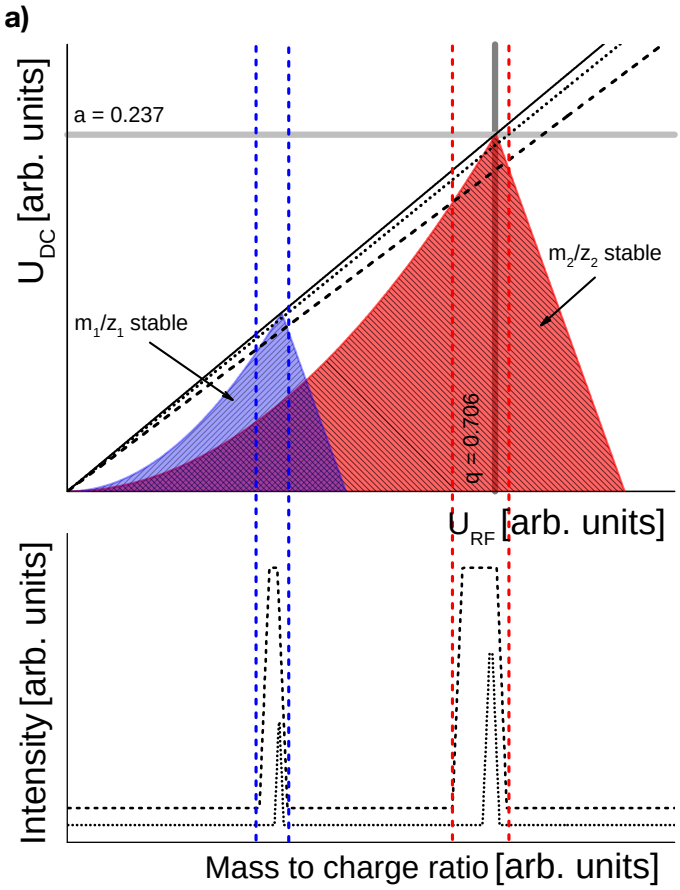

Figure 2.14.: Typical m/z resolved scan lines of a QMS operating in the first stability region. Stability regions of two different charged particle species are represented by the blue and red areas. Scan lines of two different resolving DC component and the resulting spectra are indicated by the dotted and dashed black lines, respectively.

might therefore be transmitted. All other species may impinge on the electrode rods or scatter out of the QMS between the rods. The exact scan parameters must be well chosen, due to the competition between transmission efficiency and resolution. A scan line close to the apices of the stability regions allows for sharp discrimination between different m/z, but might lead to low transmission. Decreasing the DC ratio will increase the transmission efficiency, but at the same time make it impossible to distinguish between two m/z in close proximity.
For analysis, each set of RF and DC potentials can be attributed to a certain m/z and the intensity spectrum can be assigned to different charged particle species with their respective m/z . For the exact interpretation, it is crucial to know that the resluting peaks are typically not symmetric due to the asymmetry of the first stability region and the slope of the scan line. For lower resolutions, there might be an apparent shift to lower m/z of the center of the peak.
Another less common way of scanning an ion beam with a QMS is the so-called RF-only scan. Here, no DC potential is superimposed and the scan line follows the U_{RF} axis in Figure 2.14. The stability diagram of each m/z shows an intersection with the U_{RF} axis, meaning that each m/z has a critical RF amplitude $U_{RF,crit}$ with no stable trajectories above that in the first stability region. For low RF amplitudes, the signal is composed of the sum of all intensities of all m/z with an $U_{RF,crit}$ exceeding said amplitude. While ramping the amplitude up, the intensity shows a significant drop each time when crossing $U_{RF,crit}$ of a charged particle species present in the incident ion beam.

2.3. Deposition of charged particles

The last step towards the deposition of molecules on a sample in vacuum is their successful landing. There are plenty of publications in literature examining the processes and interactions of charged particles landing on solid surfaces from gas-phase. A very instructive summary may be found in the review articles by Grill et al. [41] and Johnson et al. [152]. The different processes can be roughly divided into four groups by the kinetic energy of the charged particles during the landing process: The thermal range with energies below $1\,\mathrm{eV}$, the hyperthermal with $1-100\,\mathrm{eV}$, the low energy range from $100\,\mathrm{eV}-100\,\mathrm{keV}$, and finally the high energy range above $100\,\mathrm{keV}$ [41].
In the scope of this thesis, only the thermal and hyperthermal regions are of interest. In particular, the focus lies on processes where charged particles are actually adsorbed on

surfaces without chemical decomposition. So-called soft-landing is defined as the deposition of charged particles on surfaces without altering their structural or chemical integrity [40]. A rather rough criterion might be that for energies below about $10\,\mathrm{eV}/z$ per charge, the landing of intact ions is possible. Above that, the kinetic energy is comparable or greater than typical bond energies, which enables cleavage of single bonds without complete disruption of the whole molecule. This allows for conformational changes, as well as breaking and reformation of bonds, which is physically and chemically of strong interest. Energies above $100\,\mathrm{eV}$ are typically used for sputtering, and ion implantation [41].
Besides the kinetic energy durring landing, also the charged particle's nature and the surface itself play an important role in collision processes. Both strongly influence physics and chemistry during landing. Especially energy transfer via electronic and vibrational excitation, charge transfer, and possible reaction channels play an important role [41, 152]. Hard surfaces promote dissociative processes already at low kinetic energies [153, 154], while larger charged particles allow for higher energies due to their higher degrees of freedom [43, 152, 153, 155]. For the case of depositing ions from an ESI-source, larger ions tend to have more charges (see section 2.1). As discussed in section 2.1.3, the charge state of an ion increases for increasing molecule size. Thus, in our case, a maximum landing energy per charge of an ion seems to give a much more convenient criterion for larger species than an absolute energy value.
The ion's landing energy is determined by the electric potential of the target surface. Note, that a surface employed for such landing experiments needs to be electrically conductive or at least semi-conductive in order to allow the experimenter to apply a defined potential and to drain the charge. Non-conductive surfaces accumulate the charge of landed particles, leading to hardly controllable changes in potential and undefined landing energies. Landing particles of equal polarity, build up a repelling potential and finally cause blocking of deposition for further ions. Additionally, the electric current cannot be measured on insulating surfaces, even though it is an important indicator for the intensity of the ion beam, and the amount of deposited particles. On conductive surfaces, the charge of the landed particles is either directly neutralized or a mirror charge is induced. Both effects lead to a current on the sample, proportional to the ion beam intensity. Undesired charge transfer between surface and deposited particles may be inhibited by thin insulating layers [153, 156–160].
Some promising applications of soft-landing have been demonstrated by the group around S. Rauschenbach, S. Abb, and K. Kern by e.g. soft-landing of intact proteins, oligomers, peptides and carbohydrates [42, 44, 87, 161, 162]. Experiments with different landing en-

ergies confirmed soft-landing at kinetic energies $< 10\,\mathrm{eV}/z$ and reactive landing at some $10 - 100\,\mathrm{eV}/z$ [163–165]. Another example is the group around J. Laskin, which applied soft- and reactive-landing to peptides [155, 157, 166–168] and organometallic complexes with catalytic properties [169, 170].

2.4. Differentially pumped vacuum systems

A rather striking problem competing with the transfer of ions is an efficient differentially pumped vacuum system. As already mentioned above, the generation of ions via ESI requires a pressure close to ambient conditions to avoid discharges, and enhance desolvation of droplets. In contrast, the low deposition pressure for said ions in the ES-CIBD is inevitable to guarantee low impurity densities originating from neutral residual gas particles during long term depositions. Therefore, the ES-CIBD system demands a pressure gradient of round about 13 orders of magnitude between the electrospray and the deposition stage. As vacuum pumps require acquisition expenses, maintenance, and power consumption, it is worth discussing basic physics and the residual gas flow in all relevant pressure regimes. The basic layout of the pumps and the number of differentially pumped chambers was already outlined in the precedent thesis of T. Kaposi [52]. Nevertheless, basic concepts will be described again and progress during the current thesis as well as conclusions for future systems will be outlined. A more detailed discussion of vacuum physics may be found in literature [171, 172]. A comparison between theory and experiment for the ES-CIBD case may be found in 3.7.
The gas flow through a specific geometry like a orifice or a tube can be separated in two regimes: The continuum flow and the molecular flow. The Knudsen flow describes the regime in between, characterized by a complex mixture of both flows. The Knudsen number Kn is a measure to separate these regimes.

$$Kn = \lambda/d \tag{36}$$

d represents the characteristic length of the geometry investigated, typically it is the shortest distance one can choose like the diameter of a tube. λ is the mean free path of the residual gas defined by the pressure and temperature. In our case it ranges from about $10^{-7}\,\mathrm{m}$ at ambient conditions and $10^{6}\,\mathrm{m}$ in UHV. Knudsen numbers below $Kn < 10^{-2}$ indicate continuum flow, above $Kn > 1$ molecular flow prevails.
When ignoring undefined leaks and the boil-off rates, the chamber pressure is defined by

the flow through a leak q_{leak} and the flow through the pump q_{pump} of the vacuum chamber. Conservation of particles leads to $q_{leak} = q_{pump}$ with:

$$q_{leak} = p_{leak} \cdot C_{leak} \quad \text{and} \quad q_{pump} = p_{pump} \cdot S_{pump} \tag{37}$$

where p_{leak} is the pressure at the inlet of the leak with a corresponding conductivity C_{leak}, p_{pump} is the adjacent vacuum chamber pressure, and S_{pump} is the pumping speed. Note, that C_{leak} depends on the geometry of the orifice as well as on the type of flow correlated to the pressure. Furthermore, the pumping speed S_{pump} is typically not independent from pressure and depends on the type of vacuum pump used. Diagrams that correlate $S(p_{pump})$ with p_{pump} may be provided by the specific vacuum pump's manufacturer.
Calculation of the conductivity C or the flow q is determined by the flow regime and the geometry of the orifice. A precise estimation for non-standard geometries is complicated, but all commonly used pressure interfaces employ a more or less tubular shape or a round orifice. Due to the entanglement of properties of leaks and pumps with their respective operation pressure, calculating an exact forecast of the chamber pressures is rather difficult.
For realistic calculations at elevated pressures and a flow in the continuum regime, it is mandatory to calculate the Reynolds number Re. It indicates the flip from the laminar to the turbulent flow regime. As an example the properties of a tubulae pressure interface will be discussed in the following and the corresponding Reynolds number can be calculated by:

$$Re = \frac{\rho}{\eta} v d \tag{38}$$

with density ρ, the viscosity η, the flow speed v, and the diameter of the tube d . For tubes, Reynolds numbers of $Re \approx 2300$ may indicate turbulent flow and lower values may hint to laminar flow. The continuum flow through an elongated tubular pressure interface is calculated as [172]:

$$q_{tube,turbulent} = 1.015 \cdot d^{19/7} \left(\frac{\bar{c}^6}{\eta} \right)^{1/7} \cdot \left(\frac{p_1^2 - p_2^2}{l} \right)^{4/7} \tag{39}$$

$$q_{tube,laminar} = \frac{\pi \cdot d^4}{256 \cdot \eta \cdot l} (p_1^2 - p_2^2) \tag{40}$$

for the laminar and turbulent case. Here, d and l are the diameter and length of the interface, respectively. The mean thermal particle speed of dry air at $T = 20\ °\mathrm{C}$ is given by $\bar{c} = 463\,\mathrm{m/s}$, and the viscosity is $\eta = 18.2 \times 10^{-6}\,\mathrm{Pa\,s}$. p_1 is the pressure at the inlet and p_2 is the pressure at the exit of the tube. Furthermore, choked flow needs to be considered in the continuum regime as the pressure at the exit p_2 drops below a critical value p^*. The gas is accelerated to sonic speed and a further increase in velocity is impossible. Further expansion of the gas happens downstream the exit of the tubular pressure interface, inside the subsequent vacuum chamber. Thus, the flow of equations (39) and (40) are limited by replacing p_2 with the respective critical pressures for chocked flow [172]:

$$p^*_{tube,turbulent} = 1.92\frac{1}{a \cdot d}\left(\frac{\bar{c}^6}{\eta}\right)^{1/7}\left(\frac{d^3 \cdot p_1^2}{2l}\right)^{4/7} \tag{41}$$

$$p^*_{tube,laminar} = \frac{d^2 \cdot p_1^2}{64 \cdot \eta \cdot l \cdot c} \tag{42}$$

with c being the speed of sound. On the other end of the pressure scale, in high vacuum regions, large mean free paths of the residual gas molecules lead to Knudsen numbers above unity. The conductivity and flow of a tubular interface in the molecular regime is calculated by [172]:

$$C_{tube,molecular} = \frac{\bar{c} \cdot \pi \cdot d^3}{12 \cdot l} \quad \text{and} \quad q_{tube,molecular} = (p_1 - p_2)C_{tube,molecular} \tag{43}$$

A detailed discussion of the differentially pumped vacuum system of the ES-CIDB with a comparison of the theoretically calculated and the experimental values may be found in section 3.7.

2.5. Basics of scanning tunnelling microscopy (STM)

The scanning tunnelling microscope (STM) was invented by Binnig and Rohrer in 1981 [2]. The STM offers real space information of the electronic density of states of a sample down to the atomic scale. Due to its tremendous impact in surface-science, Binnig and Rohrer were awarded the Nobel Price in 1987 together with the inventor of the electron

microscope, Ernst Ruska [173]. Until today, STM is extensively used in surface-science and all kinds of related techniques have been developed. Due to the limited scope of this thesis, only the basics of STM will be briefly introduced. Most of the following standpoints originate from the book by Chen [174], where a more detailed introduction can be found.

The STM uses the quantum mechanical tunnelling effect, which was initially proposed to explain the α-decay of atomic nuclei in 1928 [175]. It is schematically depicted in Figure 2.15a and describes the probability of a wave-like particle to pass a potential barrier of finite height and width. The boundary conditions in quantum mechanics do not allow the probability density of a travelling wave to drop to zero immediately when reaching a potential barrier of finite height. More precisely, the probability density penetrates the potential barrier with exponentially decreasing amplitude. For a finite barrier width, the travelling wave continues behind the potential barrier with decreased amplitude.

An STM uses a microscopic probe, a so-called tip, in combination with the quantum mechanical tunnelling effect to investigate a surface (see Figure 2.15b). The tip is an electrically conductive needle with an atomically sharp apex. It is positioned closely to a electrically conductive sample surface and a bias potential of some volts is applied between tip and sample. For distances of the order of a single atom, a significant amount of electrons start to tunnel through the potential barrier of the gap between tip and sample. The tunnelling current is exponentially dependent on the width of the barrier. For tips with only a single atom at the apex, the dominant contribution to the electric current originates from this outermost atom, which confines the interaction to the atomic level. By moving the tip along a line over a sample surface, and keeping the tunnelling current constant by approaching and retracting the tip, an STM is capable of recording a topographic map of the tip-sample interactions with atomic resolution.

Figure 2.15 shows two schematic sketches of the operation of an STM with a metallic tip in close proximity to a metallic sample. For Figure 2.15a, the STM is considered to operate in vacuum and both work functions of the metals are indicated by Φ. A bias potential U_b between tip and sample gives rise to a shift in Fermi energies E_F. The incident wave penetrates the potential barrier and continues afterwards with reduced amplitude Ψ. For a rectangular barrier of hight Φ and width z the decay in amplitude of the wave function of an incident electron with energy E can be calculated as [174]:

$$\Psi(z) = \Psi(0) \cdot e^{-\frac{\sqrt{2m(\Phi-E)}}{\hbar} z} \tag{44}$$

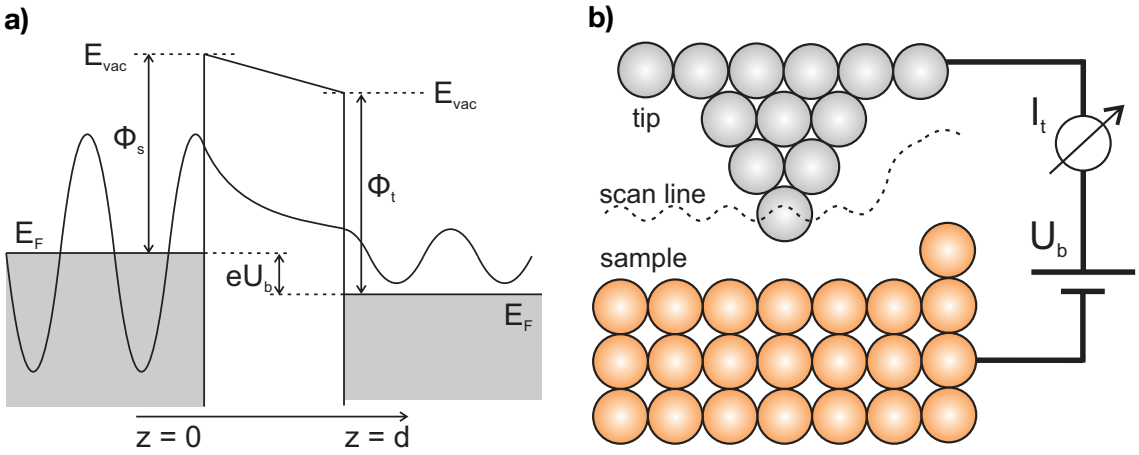

Figure 2.15.: Schematic sketch of the operation of a STM. a) depicts the tunnelling of a travelling wave through a vacuum gap between two metals. The probability density of the incident wave function penetrates the potential barrier with exponentially decreasing amplitude. A bias potential causes a shift in Fermi energies, enabling a classically forbidden tunnelling current. Adapted from [174]. b) shows the operation principle of a STM in constant current mode. The atoms of tip and sample are indicated by grey and orange circles. The tip moves along a scan line while the distance is continuously adjusted to keep the tunnelling current I_t constant.

with the mass m and Planck's constant $\hbar$. Figure 2.15b depicts a sketch of a corresponding STM geometry. The grey and orange spheres indicate the atoms of the tip and sample, respectively. The applied potential U_b induces a current I_t of electrons tunnelling from the sample to the tip. The current's intensity depends on the potential U_b, the width of the gap d, and the height of the potential barrier, in this case the vacuum level E_{vac}, and the density of states of the tip and the sample. The dotted line represents a typical scan profile in the commonly used constant current mode. Here, the tip is moved via piezo-electric motors while the height of the tip is adjusted for every point along the scan line in order to keep the tunnelling current I_t constant. The recorded height profiles can be transferred to a topographic map of the sample with atomic resolution.

The STM allows an experimenter to probe a sample surface in real space with atomic resolution. in the scope of this thesis, it is used to identify and investigate samples from the ES-CIBD device. The topographic maps show size, orientation, assemblies, and electronic information of the deposited species.

3 | Electrospray - controlled ion beam deposition (ES-CIBD)

The electrospray - controlled ion beam deposition (ES-CIBD) device presented aims the gentle deposition of predominantly big and reactive molecules on a plain surface to make them accessible for further scientific investigations. The acronym ES-CIBD consists of the ionization method - here ES for electrospray - and the subsequent deposition method - m/z selected, with controlled landing energy at UHV conditions, with low impurity densities. For charged particles from the ion source, this is possible by a mass spectrometric investigation of the ion beam prior to deposition in order to verify the presence of the desired analyte species. All kinds of other ions such as impurities, fragments or adducts can be identified and investigated, too. For deposition, the mass spectrometer acts as a filter that exclusively transmits the desired ions in a selected m/z window. All other ionic impurities are removed from the beam. A digital quadrupole mass spectrometer (dQMS) (see section 3.5) operated via square wave radio frequency (RF) signals from home-build electronics provides well resolved spectra with unlimited m/z range at high transmission efficiencies. The resulting continuous and uniform ion beam can be extracted by a conical multipole, the so-called Blade ion guide (patent pending [176], see section 3.6) which focuses the ions towards a sample surface.

Exclusion of uncharged impurities is ensured via a compact and efficient differentially pumped vacuum system. The ESI source operates at ambient (1000 mbar) conditions whereas the deposition takes place in UHV (10^{-10} mbar). Sophisticated transfer ion optics such as a combined ion funnel and tunnel, the so-called Twin (patent pending [177], see section 3.3) and miniaturized high order multipoles, the so-called small wire ion guide (SWIG) (patent pending [178], see section 3.4) allow for high ion beam intensities and low residual gas transmission. After just four differentially pumped stages, the partial pressure originating from the ESI source is reduced to a level below the detection limit of standard UHV pressure gauges ($\ll 10^{-10}\,\mathrm{mbar}$).

Another important control parameter for deposition is the landing energy of the analyte. The charge of the deponents and the application of suitable potentials to the surface to be decorated allows for investigations on the kinetic energy distribution of the ion beam and its landing with controlled energy. Low kinetic energy durring landing ensures intact deposition of the analyte (soft-landing) while higher energies may introduce unique on surface dissociations and chemistry (reactive-landing). One more important control parameter is the dose. The current of the landing ions can be monitored and its integral over time provides information about the amount of deposited molecules and the coverage of the sample surface. The combination of all aforementioned information already provides precise knowledge of the deposited layers prior to its investigation, which is a

unique feature of CIBD when compared to other deposition techniques. Furthermore, its combination with ion sources different to ESI is quite easy and provides a even larger range of possible analytes.

One of the main challenges of such a preparative mass spectrometry (pMS) approach is the need for high ion beam intensities compared to commercially available analytical MS systems. For pMS, a surface of typically $100\,\mathrm{mm}^2$ in size needs to be decorated with about a monolayer of molecules. For practical reasons, a decoration with small molecules with typical sizes in the $1\,\mathrm{nm}^2$ regime should not take much more than $1\,\mathrm{h}$. The required 10^{14} ions demand deposition rates of 10^{10} molecules per second, corresponding to about $1\,\mathrm{nA}$ of ion current assuming singly charged ions. Thus, high beam intensities landing on the sample surface subsequent to the selection by a mass spectrometer is a key factor for usability in pMS. Additionally, the ion beam properties at the end of the mass spectrometric treatment, notably spacial extension and kinetic energies play an important role for later deposition. State of the art analytical high resolution MS devices like the Orbitrap or Fourier-transform ion cyclotron resonance spectrometers are limited via Coulomb repulsion between ions. The interaction start to affect m/z resolved spectra at about $10^4 - 10^6$ elementary charges per spectrum [46, 47] leading to mean ion currents in the fA regime when considering a typical acquisition time to record a spectrum of about $1\,\mathrm{s}$. TOF instruments provide higher repetition rates and flux but extraction of ions is complicated due to the high accelerating voltages, the typically enlarged beam size and the complex time structure of the ejected ions [34].

Compared to other standard deposition techniques, pMS requires comparably complicated instrumentation. In simple terms, organic molecular beam epitaxy (OMBE) only requires a heated crucible inside a vacuum chamber, which was previously filled with molecules. For drop-casting the molecules are deposited with a pipette filled with dissolved molecules. There is no possibility for ”clean” depositions.

ES-CIBD on the other hand comes along with a sophisticated differentially pumped vacuum system, complex ion guides, advanced electronics and a tremendous parameter space, starting from the large number of solvents and additives, over different spray modes, emitters, solution flow rates, spray voltages and capillary heating over the settings of all employed ion guides including the mass spectrometer and finally the landing energy. All in all, there are currently around 30 electronic parameters to choose correctly. In fact, these problems are not that serious for a skilled user if the designer puts an eye on usability of the machine during construction. Most of the ion guide settings might be previously estimated from the m/z of the desired ion. The elaborated software allows for a comfortable

handling. Parameters from prior depositions of similar deponents may be applied or used as an educated guess for the next try. A multitude of interlocks, operation- and software-routines improve the user-friendliness significantly. The currently most time consuming step towards a deposition is the exploration of a suitable solvent-deponent system for the electrospray process. Once the desired ions are produced by the ESI source, it's only a few ten minutes upon deposition. Nevertheless, the generation of a sample via ES-CIBD is at least comparable in complexity and expense to its subsequent investigation with state of the art methods like scanning-probe, spectroscopy or desorption techniques.
ES-CIBD provides a dramatically extended range of accessible deponents when it comes to more challenging molecules. Furthermore, it provides a complementary deposition technique with a high degree of control and low impurity densities in case the experimenter is not quite sure about the integrity of the deponent, or the purity of the sample.
The following sections will describe all components of the ES-CIBD set-up in detail. Focus will be put on the challenging aspects of the construction, the different types of ion guides, and the electronic control unit.

3.1. Overview over the complete setup

The whole system of a variable temperature STM with an attached ES-CIDB is depicted in Figure 3.1. Starting from the left-hand side, the overview depicts a previously stand-alone STM chamber in green with the corresponding preparation chamber in blue. Both chambers are separated by a gate-valve to avoid contamination of the STM during preparations via an OMBE and a metal evaporator, or during sputtering and annealing cycles in the preparation chamber. The transfer manipulators (cyan) allow for sample transport. The STM system is described more detailed elsewhere [179, 180].
The ES-CIBD on the right-hand side is attached to said STM via another gate-valve. Following the flow of ions in the ES-CIBD machine, the starting point is the ESI source (green) on the very right. Here, the ions are generated and transported to the low vacuum section (purple) consisting of three differentially pumped vacuum chambers. The three vacuum regimes are located in a aluminium box and may be separated by modular walls. This part of the ES-CIBD may routinely be vented to atmospheric pressure for modifications and maintenance. The UHV section, which requires continuous pumping and a bake-out to reach a suitable base pressure may be separated via an in-beam gate-valve from the lower vacuum. The first UHV chamber (yellow) operates as a fourth differen-

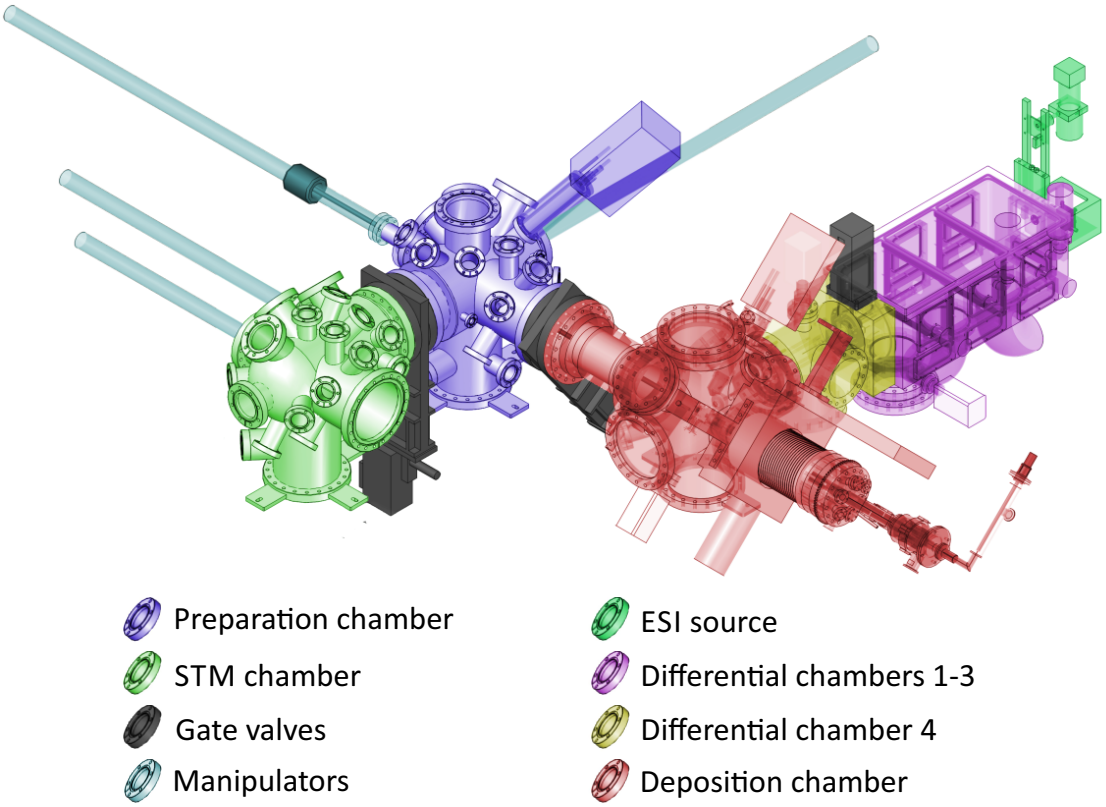

Figure 3.1.: Overview of the entity of ES-CIBD attached to a VT-STM. For illustrative reasons, exclusively the vacuum chambers without attachments are depicted. From [52] with modifications.

tially pumped chamber and is followed by the deposition chamber (red). The last ion optic of the ES-CIBD ends just a few centimetres behind the connecting flange between chamber 4 and deposition chamber. The actual ES-CIBD system is not much larger than the green, purple, and yellow chambers together. The deposition chamber is not exclusively used for ES-CIDB but also houses a sputter gun, a metal evaporator, leak valves, and a residual gas spectrometer for temperature programmed desorption (TPD). The manipulator allows for moving the sample and provides a controlled temperature by electron bombardment heating or liquid nitrogen or liquid helium cooling.

A more detailed sketch with most of the relevant components of the ES-CIBD machine and their performance is depicted in Figure 3.2. The current design consists of an ESI source (a, b, c), which was adapted from [99], 4 differentially pumped vacuum chambers (d, f, h, j), and a deposition chamber (l). The ESI-source operates at ambient conditions and provides an ion current of typically $I_{Ion} \approx 10\,\mathrm{nA}$. The first differentially pumped chamber (d) houses a combined ion funnel and ion tunnel, a so-called TWIN (see section 3.3) to confine and focus the ejected ions from the ESI source. In the second differentially pumped chamber (f), the first small wire ion guide (SWIG) (g) is used to conduct ions downstream. This high order multipole consists of 16 wire electrodes for ion confinement and a tubular pressure interface to reduce leak rates. The second SWIG (i) in the third vacuum chamber (h) transfers the ions through the in beam gate-valve (q) into the UHV section of the ES-CIBD. The third and last SWIG (k) in the fourth chamber (j) employs two tubular pressure interfaces towards the previous and the subsequent chamber. in the deposition chamber (l), a digital QMS (dQMS) (m) is used for investigation and purification of the ion beam. Subsequently, a conical high order multipole made from metal sheet electrodes, a so-called Blade ion guide (n), collects the ions from the dQMS and focuses them towards the sample (o).

To our best knowledge, the ES-CIBD is the first square-wave operated deposition system and designed without electrostatic lenses. All RF signals are generated by switching transistors and the resulting square wave can be controlled in frequency and voltage continuously. In addition, each ion guide has a defined DC offset with respect to ground to provide control of the kinetic energy of the ions. A high voltage supply for the emitter is mandatory for the ESI process as well as a suitable DC gradient from the atmospheric pressure interface all the way down to the exit of the ion funnel. The field in this region is of special importance due to frequent ion - neutral collisions in the first vacuum chamber. The DC offset of SWIG 1 roughly gives a reference for the kinetic energy in flow direction of the ions. The mean free path in subsequent pressure regimes is much larger than

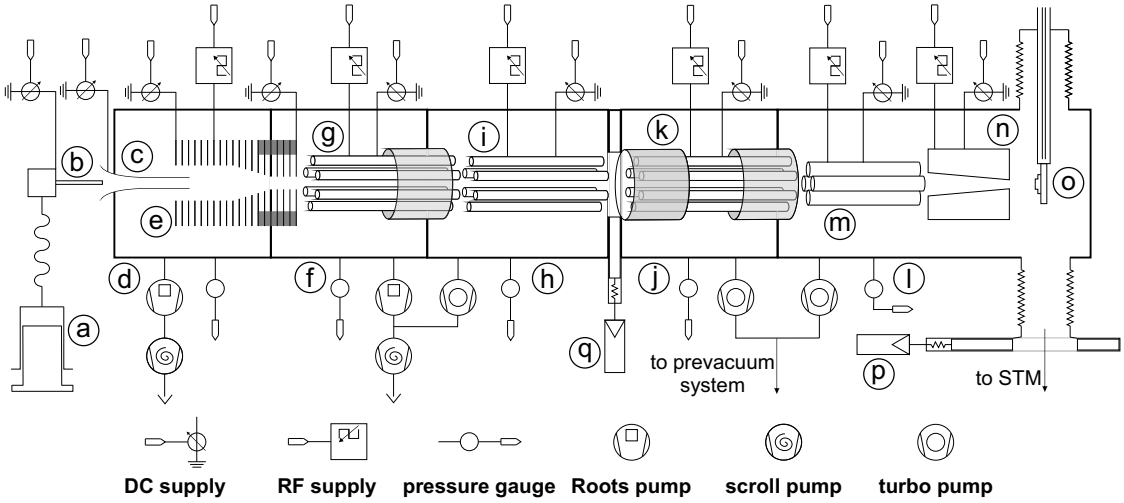

Performance	ESI-source (a-c)	TWIN (e)	SWIG 1 (g)	SWIG 2 (i)	SWIG 3 (k)	dQMS (m)	Blade (n)
Pressure [mbar]	1000	2	10^{-2}	10^{-7}	10^{-10}	$< 10^{-10}$	$< 10^{-10}$
Ion current [nA]	10	8	6.5	5	4	2.5	2.2
Inscribed diameter [mm]	1.1	30 to 1.5	1.6	2	2.5	16.6	7 to 4

Figure 3.2.: Schematic of the ES-CIBD system, its key components and their performance: (a) syringe with a pump to provide a solution of analyte molecules. (b) electrospray emitter connected to a high voltage supply. (c) counter electrode and atmospheric pressure interface with funnel shaped inlet (adapted from [99]). (d, f, h, j, l) differentially pumped vacuum system (e) so-called Twin, an optimized stacked ring ion guide for high pressure. (g, i, k) high order multipoles, so-called small wire ion guides (SWIGs). (m) digital quadrupole mass spectrometer (dQMS) to characterize and purify the ion beam. (n) conical multipole from metal sheet electrodes, a so-called Blade ion guide to focus the beam. (o) target surface to land the ions with controlled energy. (p, q) gate-valves. The ion currents in the table are measured for the test molecule Rhodamine B (see section 5.1)

the typical length of ion trajectories. Thus, the kinetic energy in z-direction in subsequent sections is defined by the difference in potentials $q \cdot (U_{DC} - U_{DC,\,SWIG\,1})$. For this reason, soft-landing conditions may be typically found few volts around $U_{DC,\,SWIG\,1}$ and the ion beam can be switched on and off at several locations by generating a potential barrier in z-direction via the ion guide's DC offset voltages. In consequence, inappropriate DC offsets and especially their sign are frequent candidates for maloperation.
The table on the bottom of Figure 3.2 lists the pressures, ion currents and inscribed radii of the ion guides downstream the ES-CIBD. A precise description of the evolution of pressures can be found in section 3.7. The ejected ion current decreases downstream the ES-CIBD system with typical transmission efficiencies of $\approx 80\,\%$ per ion guide. The ion losses most probably are not dominated by the length of the ion guides, but by their interfaces. Axial miss alignment as well as fringing fields are very probable candidates to cause inefficient transmission. Besides that, imperfections of the electrode geometry might also decrease efficiencies. While each SWIG employs parallel electrodes, their inscribed diameter increases one after another. In principle, it would be possible to achieve a comparable performance with constant inscribed diameters of all SWIGs, but larger diameters are more easy to handle in construction and mechanical alignment. Due to the spare capacities in differential pumping (see section 3.7), the enhanced leak rates from larger interface diameters do not reduce performance.
Figure 3.3a depicts a photograph of the current ES-CIBD device. The colour-code for the different components was adapted from Figure 3.1. Besides the aforementioned components, the syringe pump on the very bottom right, as well as all kinds of electronics are depicted. The major part of the electronic supplies is currently mounted directly above the ES-CIBD allowing for fast and easy rewiring. In future CIBD systems the electronic components are supposed to be binned to a rack, they are designed 19" compatible for this purpose. Another part of the electronics are the small boxes in the purple and yellow polygons, which house the RF-generators (see section 3.8.2). These boxes are intentionally located as close as possible to the vacuum feedthroughs as the waveform and the required supply power strongly benefit from short leads (see section 3.8.2).
Figure 3.3b is a photograph from the top of the purple chambers 1-3 with removed cover plate. The aluminium box, which houses all three pressure regimes is designed for fast access and maintenance. Therefore, the top cover consists of an easily removable aluminium plate with rubber gaskets, that is fixed due to the forces caused by the ambient pressure when operating under vacuum. The aluminium box divides into three pressure regimes by removable and adaptive walls. The exit of the ESI source (see section 3.2) ejects ions

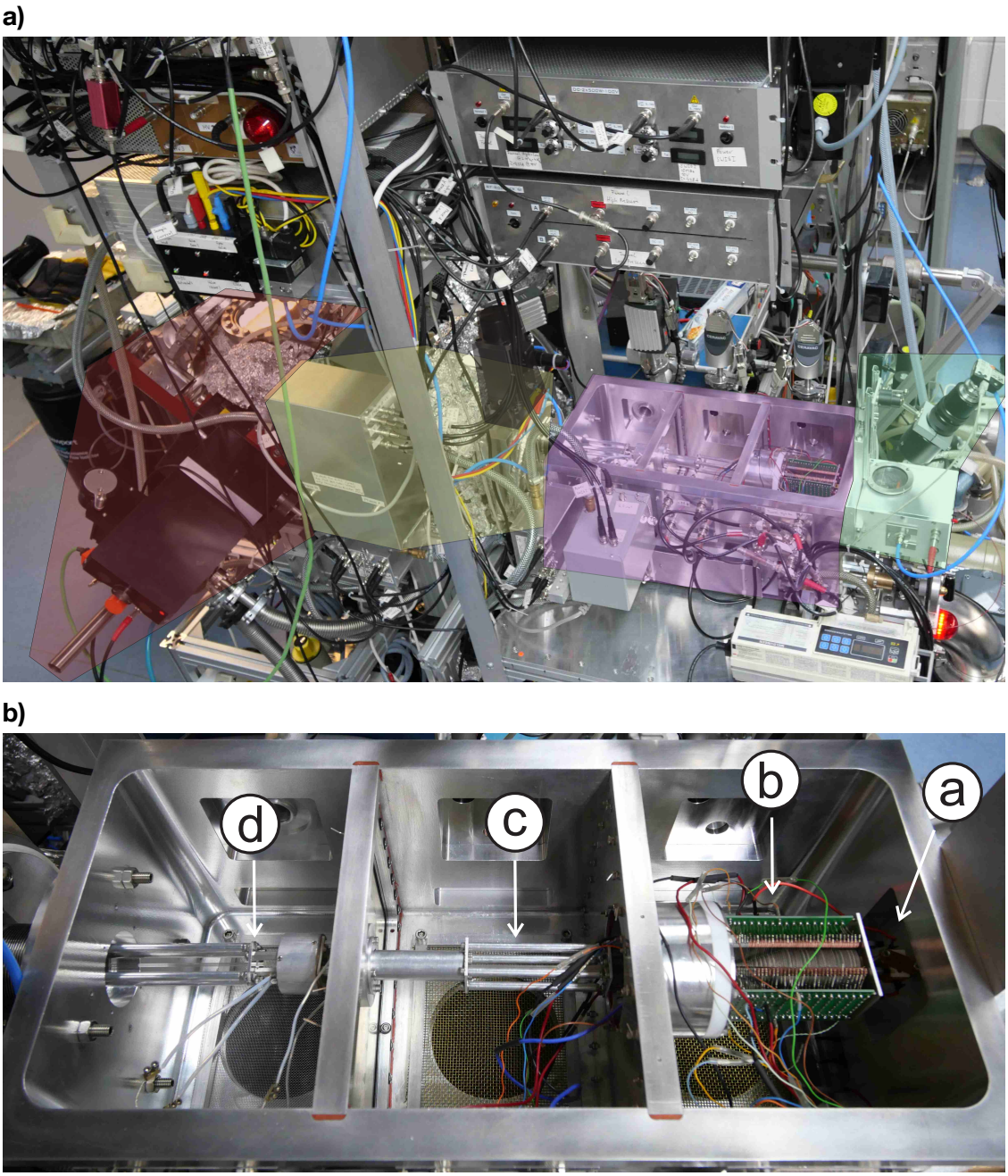

Figure 3.3.: Photograph of the current ES-CIBD device. a) depicts the ESI source in green, chambers 1-3 marked in purple, chamber 4 in yellow and the deposition chamber in red. b) is a photograph of the inner components of chambers 1-3 with the exit of the atmospheric pressure interface (a), the Twin (b), SWIG 1 (c), SWIG 2 (d).

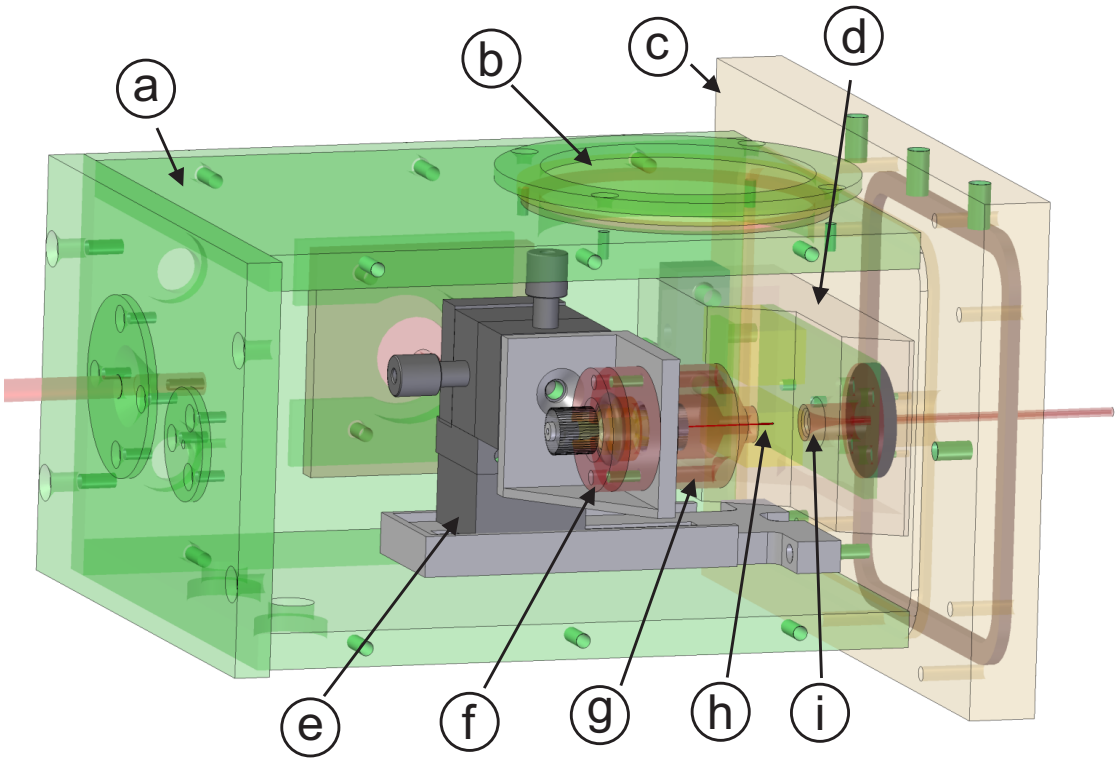

Figure 3.4.: 3D drawing of the home-build ESI source consisting of: (a) gas-tight housing, (b) window for camera, (c) vacuum flange, (d) atmospheric heating, (e) XYZ motion, (f) high voltage contact and adapter to connect a hose, (g) dry-gas supply, (h) emitter, (i) atmospheric pressure interface adapted from [99].

into the Twin ion guide (b) (see section 3.3), which confines and focusses them to a beam. Downstream, two SWIGs (c,d) transmit the ions further to UHV (see section 3.4).

3.2. The ESI source

The ion beam is generated by a home-made ESI source. The solution of molecules is stored in syringes of $10 - 500\ \mu$l volume, mounted in a syringe pump with adjustable pumping speed (IVAC 711). A hose made from PEEK or fused silica connects the syringe to the ESI source. All parts are connected tightly by fittings made by IDEX Health & Science 'MicroTight'.

Figure 3.4 depicts a 3D-drawing of the ESI source. The green box (a) is a small chamber around the ion source which allows for operation at reduced pressures or in a defined atmosphere. On the left end, the chamber is equipped with bores for gas-tight electric

feed-throughs, as well as two mechanical feed-throughs for operation of the z-motion and the supply hose of the analyte solution. The operation of the ESI source is monitored through the sealed window (b) via a camera (depicted in Figure 3.3a). The whole assembly is mounted via a separated vacuum flange (c) to the aluminium box of chambers 1-3 (see Figure 3.3a). Micrometer drives (e) in all three spatial directions allow for precise positioning of the emitter (h) in front of the counter electrode and atmospheric pressure interface (i). An metallic adapter (f), connecting the supply hose to the emitter allows for electric contact between analyte solution and high voltage supply. A further housing around the emitter (g) is used to generate a coaxial flow of dry-gas and a defined atmosphere. The atmospheric pressure interface (i) consists of a funnel shaped inlet, followed by an elongated brass tube of $60\,\mathrm{mm}$ length and $1.1\,\mathrm{mm}$ inner diameter. Based on the pioneering work of to the group around K. Kern and S. Rauschenbach [99, 181, 182] the design was implemented by T. Buberl, D. Reinisch, A. Walz, and T. Kaposi [52, 135, 183, 184]. The interface employs two separate heating systems, one on the atmospheric side (d) and one in the first vacuum chamber (not depicted) to allow for a uniform and controllable temperature distribution up to $200\,^{\circ}\mathrm{C}$ over the length of the atmospheric pressure interface.

3.3. The Twin ion guide

The Twin ion guide [177] is located in the first vacuum chamber and confines the ions, ejected from the ESI source. The capillary of the atmospheric pressure interface ends at the first ring electrode at the entrance of the Twin. The exact electrode geometry and stacking of the Twin is already described elsewhere [135]. In short, the Twin bases on the idea of a stacked ring ion guide (see section 2.2.2 and Figure 3.5). It composes of two sections, the funnel section (Figure 3.5a) and the tunnel section (Figure 3.5b) with antithetical residual gas flow properties. The funnel section at the inlet of the Twin follows a classical stacked ring ion guide or ion funnel. A stack of electrically insulated ring electrodes of constant or shrinking diameter defines an ion path along the symmetry axis. The gaps between the electrodes allow for pumping of residual gas, while the electric field from the applied potentials to the electrodes confines charged particles inside the ion guide volume. The shrinking diameters provide a focusing of the ion beam and a DC potential gradient along symmetry axis allows for an additional driving force for the flow of ions. At the end of the funnel section, the ion tunnel is attached. Contrary to the funnel, gaskets are employed

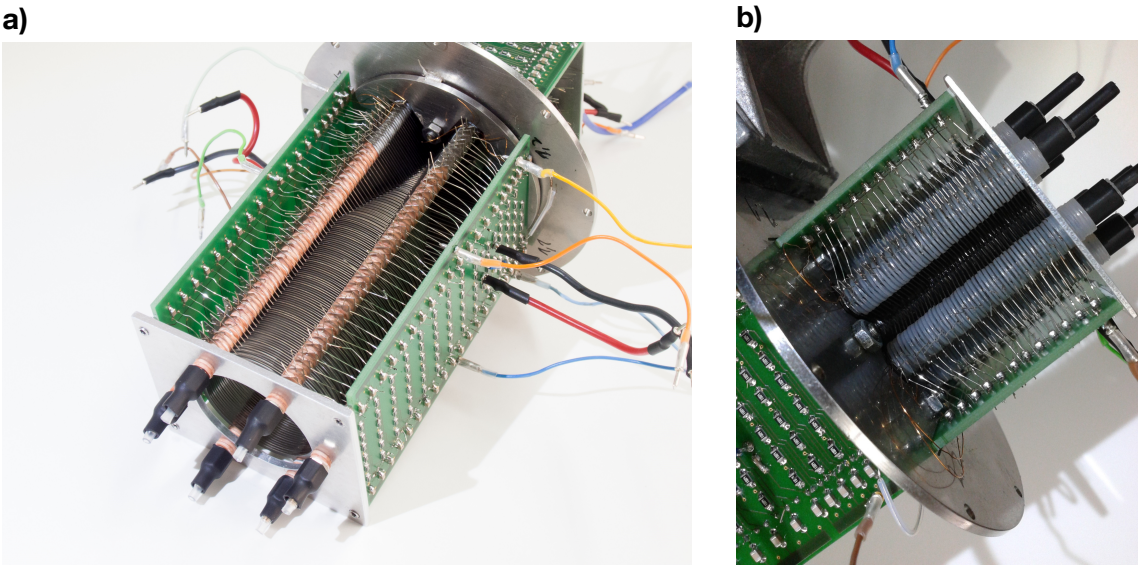

Figure 3.5.: Photographs of the Twin ion guide. a) depicts the focusing funnel section and b) the gas-tight tunnel section. From [135]

.

as spacers between electrodes to prevent residual gas atoms from exiting the ion guide volume. Thus, an elongated tubular pressure interface between adjacent vacuum regimes is formed and leak rates may be reduced significantly compared to an orifice of a single electrode (see section 3.7).
The current design of the Twin focuses the ion beam from an inscribed diameter of $30\,\mathrm{mm}$ at the inlet of the funnel down to $1.5\,\mathrm{mm}$ in the tunnel. The whole assembly consists of 272 ring electrodes, which are laser cut from a stainless steel sheet of 0.2 *mm* thickness and a spacing between neighbouring electrodes of $0.2\,\mathrm{mm}$ and $0.4\,\mathrm{mm}$.

3.4. The Small Wire Ion Guide

Commonly used multipoles employ 4, 6 or 8 electrodes. There are few examples of higher order multipoles, like 22-poles [185–188]. All these ion guides employ intrinsically solid electrodes, typically made from metallic rods that are mounted to some kind of frame. Therefore, electrodes require a certain physical size to withstand all kinds of forces, most importantly gravitation, without deformation. Especially for higher order multipoles, miniaturization of the ion guide is limited by the diameter of the electrodes. The recently developed Small Wire ion guide (SWIG) [178] overcomes these restrictions by employing thin wire electrodes instead of solid rods. The difference between wires and

rods is that wires are not intrinsically stable and require some sort of tensioning or fixation to keep shape. The most important advantages of a SWIG are small inscribed radii with high spatial acceptance and very low leak rates of background gas between adjacent vacuum chambers for efficient differential pumping.
SWIG 1 currently employs the smallest inscribed diameter of $1.64\,\mathrm{mm}$ by using round electrode wires of $0.18\,\mathrm{mm}$ diameter in a 16-pole. The inscribed diameter was chosen slightly larger than the inscribed diameter at the exit of the ion funnel of about $1.5\,\mathrm{mm}$ in order to efficiently transfer ions downstream. In principle even smaller inscribed diameters should be possible and also the order (even number) of the multipole may be chosen rather freely. Currently, solely 16-poles are in use due to their symmetry and the moderate complexity in manufacturing. Higher orders are of course possible, but come with an increased effort due to more complex mounting and positioning of the electrodes. As already discussed in theory (see section 2.2.1), the walls of the trapping potential become more steep and confined closer to the electrodes when increasing the number of electrodes. Therefore, the relative size of the field free center, in which ions may be injected smoothly slightly increases.
The probably biggest advantage of a SWIG is its reduced gas conductivity for the differentially pumped system due to its small electrode size compared to the size of the ion beam, that is exclusively possible for high orders of multipoles ($N \gg 2$). In most systems, each pressure regime employs its own multipole and adjacent ion guides are separated by metal sheets with apertures or electrostatic lenses. Therefore, the confining field of the multipole must be interrupted for the transfer of ions from one pressure regime to another. Additionally, apertures often limit the transmission efficiencies and have large diameters compared to their length, which is unfavourable for low leak rates. With the much smaller electrodes of a SWIG, it is possible to manufacture an elongated tubular pressure interface around the multipole electrodes with a size not much larger than the ion beam. Such types of pressure interface reduce leak rates significantly (see section 3.7) and provide transfer of ions between several pressure regimes without interruption of the confining multipole field from the electrodes. The pressure interface of SWIG 1, for example, consists of a tube of $2.5\,\mathrm{mm}$ inner diameter and a length of $80\,\mathrm{mm}$ surrounding the 16-pole's electrodes
.
Another important parameter is the diameter of the electrodes. The simulations of section 4.4 predict, that very small electrodes with large gaps in between show poor transmission properties when operated with equal RF signals. On the other hand, large electrodes increase the overall size of the SWIG impairing its pressure interface. The small gaps in

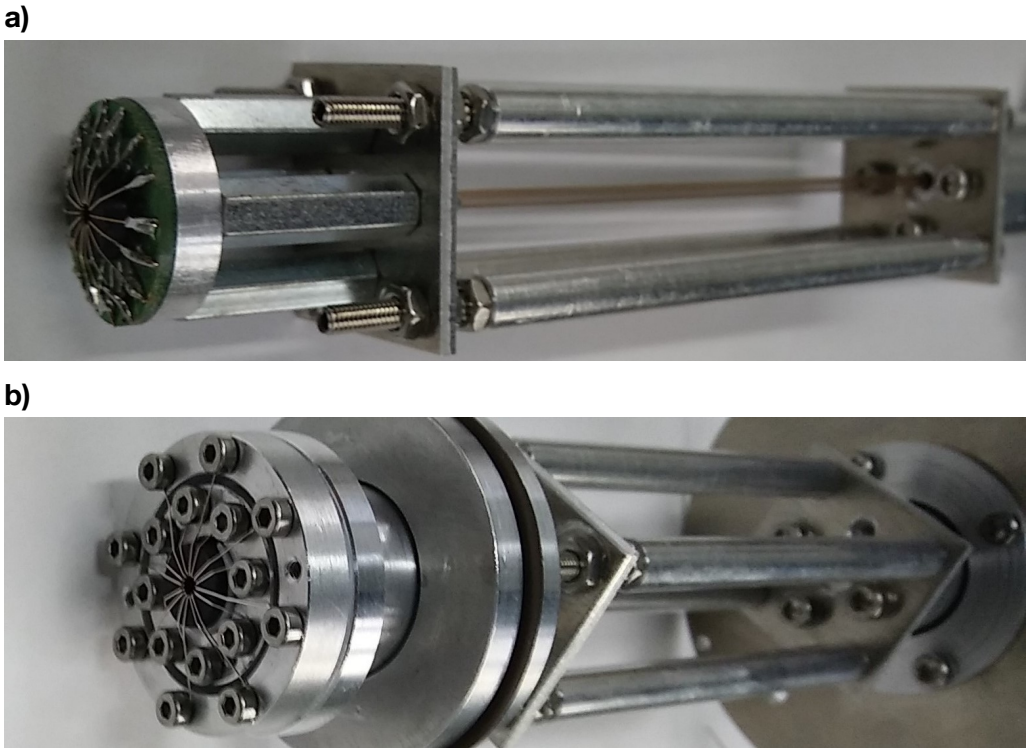

Figure 3.6.: Photographs of the inlet of SWIG 1 and SWIG 3. For fixation, the electrode wires are either soldered to a PCB or mounted via screws.

between make the system more vulnerable to an electrical short due to mechanical misaligned or slightly deformed electrodes. Furthermore, small gaps impede the pumping of residual gas from the beam. A reasonable compromise is a electrode gap ratio around unity.

SWIG 2 does not employ a pressure interface and is exclusively used to transfer ions through chamber 3 and the 'in-beam' gate valve (see Figure 3.2). The inscribed diameter was chosen slightly larger to about $2\,\mathrm{mm}$ with wire electrodes of about $0.25\,\mathrm{mm}$ diameter. The subsequent SWIG 3 employs an inscribed diameter of $2.5\,\mathrm{mm}$ with electrodes of about $0.25\,\mathrm{mm}$ diameter. It has two pressure interfaces of $3.5\,\mathrm{mm}$ inner diameter and $30\,\mathrm{mm}$ length to transfer ions from chamber 3 down to the preparation chamber. In principle, it would be possible to use equal electrode geometries for all SWIGs in the ES-CIBD. Due to excess capacities in the differentially pumped vacuum system (see section 3.7) and for the sake of easier construction and alignment, a slightly increasing inscribed diameter was chosen for each SWIG downstream. Figure 3.6 depicts the inlet of two of the currently used SWIG designs. 3.6a shows SWIG 1 with the wires being soldered to a PCB for

fixation at the inlet. In the center of the PCB, at an elevated position, a black ceramic ring with a bore is located and the wire electrodes guided over said ring and bent around the edge of the bore in order to form the inlet of the multipole. The ceramic ring is made from material with an intermediate electric conductivity. At the end of any ion guide fringing fields affect the beam. The limited transmission manifests here in stray ions, often decorating any non conductive object near to the beam. This charge may generate a potential barrier high enough to suppress the beam itself in case charge is not drained. Thus any material in close proximity of the beam has to be either fully conductive in the sense of a metal or it has to be partially conductive to drain the charge and at the same time sufficient isolating to avoid Joule heating when connecting electrodes of different polarity.
The whole system of electrodes, their fixation and the ceramic ring are mounted electrically insulated on an aluminium frame. It is equipped with screws for exact adjustment of the length and the position of the multipole. The frame consists of two different sections, comparable to the Twin ion guide. The first section employs a rather open frame, where tension rods are used as spacers to define the length of the SWIG. Here, the residual gas may be pumped from the ion guide volume through the gaps between the electrodes. On the very right hand side of Figure 3.6a the electrode wires are guided into a small hole, just slightly larger then the outer diameter of the electrodes. The corresponding tube is mounted in a gas-tight way to the separating wall between adjacent vacuum regimes and forms a elongated pressure interface with low leak rate.
Figure 3.6b shows a photograph of SWIG 3. It is located in the UHV regime and no PCBs may be used anymore for fixation of electrodes to avoid outgassing. Therefore, two separate metallic rings with screws are used to fix electrode wires of equal RF phase. Another feature of SWIG 3 are the two pressure interfaces. One directly after the mounting of electrodes on the left of Figure 3.6b and is tightened via an O-ring seal to the vacuum chamber. The second sits after a differentially pumped section in the middle of SWIG 3 on the very right of Figure 3.6b. This interface is mounted in a gas-tight way to a larger base plate.
Summing up, SWIGs combine high transmission with low leak rates of background gas and small beam diameters. They have a large spatial acceptance and are easy to implement and operate with just three adjustable parameters, RF frequency, RF amplitude and DC offset. Furthermore, it is principally possible to span all pressure regimes from the exit of the Twin down to UHV with one single ion guide, which would reduce the parameter-space and complexity compared to all current designs significantly. For historical and constructive reasons, this was not possible with the current set-up, yet.

3.5. The digital Quadrupole Mass Spectrometer

The operation of a standard QMS, with a sine-shaped RF signal was already described in section 2.2.3. The major drawback of such a system is the fixed RF frequency of the resonant LC-circuit leading to a limited m/z range. A solution for this problem was already suggested in 1973 by first experiments with rectangular wave forms [189]. It was found, that both ways of operation are very similar in nature when the sine-shaped signal is simply replaced by its square wave counter part. The main difference is a compression of the stability diagram in q direction, such that the apex of the first stability region (see Figure 2.14 and 3.7b) shifts to lower RF amplitudes whilst the DC offset is approximately the same ($q \approx 0.55$ and $a \approx 0.23$) [189–191]. The exact values for a and q are dependent on the wave-form and may change slightly due to imperfect signal shapes, such as slow rise and fall times of the transistors.

Besides that, the digital operation of a QMS opens a whole new playground of possible wave-forms. The first extension of the parameter space would be to introduce a so-called duty cycle or pulse width, where the residence time of the square wave on the upper and lower amplitude level are not equal. Figure 3.7 depicts an example of such a wave form and the corresponding stability diagrams. Here, the wave form may be characterized by its dimensionless amplitude q, the DC offset between both RF phases a and three additional timing parameters t_1, t_2 and t_3. The period of the square wave is given by $T = t_1 + t_2 + t_3$. t_1 and t_3 represent the regimes, where the two phases of the RF signal are on opposite amplitude levels and t_2 represents the time of equal amplitude level. The three examples in 3.7b depict the stability diagram of a square wave with different ratios of high and low times of the two RF-phases. The numbers separated by the slashes above the diagrams represent the corresponding values for t_1, t_2 and t_3. The two regions in lighter gray in a-q space indicate regions of stable motion in x-, or y- direction, respectively. The dark grey intersection indicates the parameter space of overall stable motion in the first stability region.

The diagram on the very left of Figure 3.7b depicts the example of equal high and low times of both RF-phases. The duty-cycle is 1:1 or $50\,\%$. This is the corresponding counterpart to the sine-shaped stability diagram of section 2.2.3. As already mentioned above, the shapes resemble one another with slight compression in q-direction in the digital case. The stability diagram in the middle originates from a signal of asymmetric duty cycle. The region of stable motion it tilted downwards to lower a values, such that a m/z resolved scan can be conducted by ramping up the RF amplitude without any resolving DC offset. The

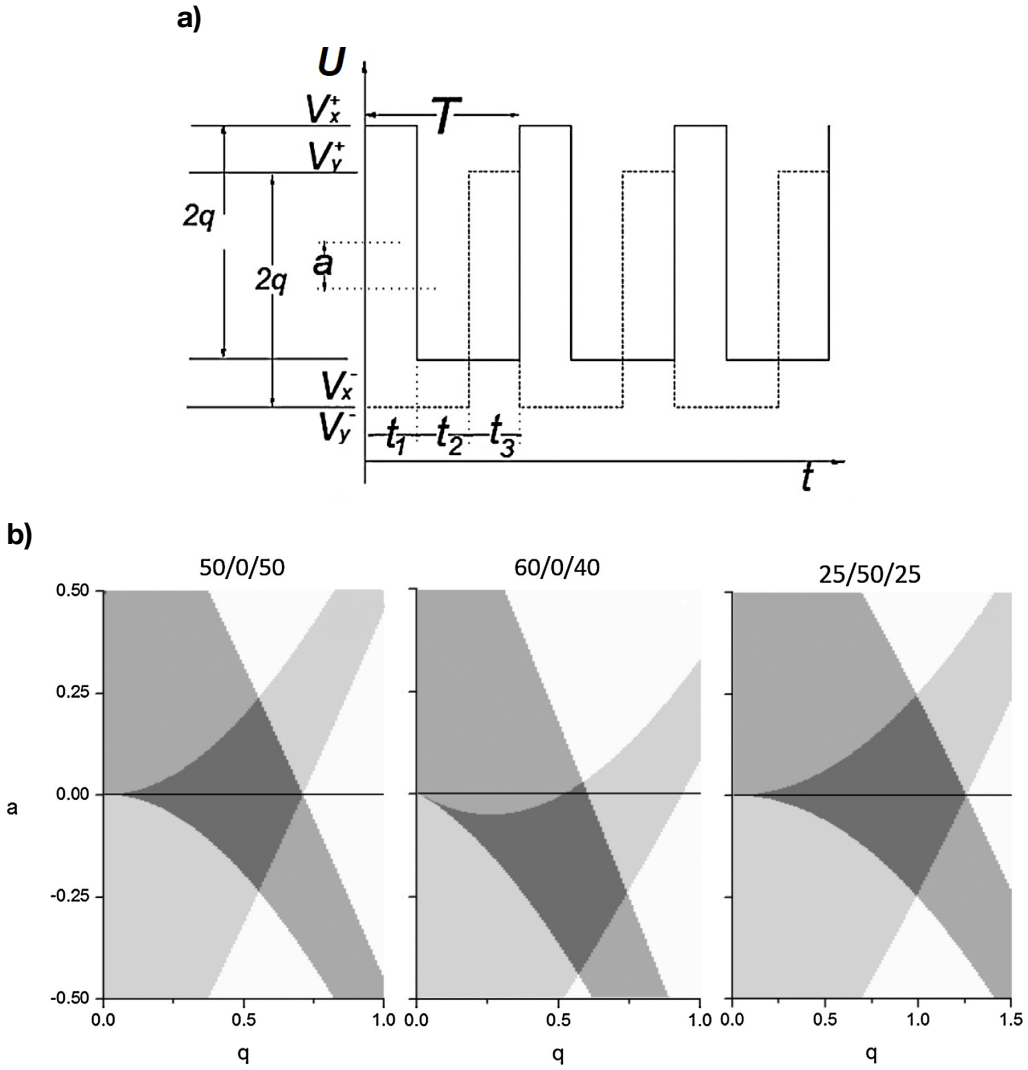

Figure 3.7.: Influence of the RF wave-form on the stability diagram of a QMS. a) duty cycle modulated square wave signal, defined by the three time intervals t_1, t_2 and t_3. The solid line is the potential attributed to one pair of the electrodes, the dotted line to the other. b) impact of the different wave-forms on the first stability region. From [191] with modifications.

rightmost diagram corresponds to a RF-signal, where both signals are on the lower level for half of the period. The shape stability region is the same as on the leftmost graph, but it is stretched along the q-axis to higher RF amplitudes.
Further improvement of resolution and transmission properties of quadrupoles have been reported for so-called auxiliary quadrupole excitation voltages [192–195] or EC signals [196, 197]. In both cases, a second periodic voltage is added to the RF-signal in order to modify the stability diagram. The resulting stability islands have been proven experimentally to show significantly improved transmission and resolution properties when compared to the standard operation at the apex of the first stability region. Another promising approach may be the use of electrode rod pairs of different size, which add a multipole component to the quadrupolar field and also may significantly improve performance [194, 198–201]. So far, we did not investigate the above mentioned improvements, but corresponding ion trajectory simulations and first experiments are planned.
The 19 mm quadrupole rod system with pre and post rods stems from Extrel. The rod electrodes have been gold plated by galvanization and the housing, as well as the stabilizing rods have been removed (see Figure 3.8a). The electrodes are precisely mounted by two ceramic holders (a), where the main rods (b), as well as the pre- and post-filter (c) are fixed with screws. Pole pairs on equal potential are connected with a wire. The electrode of the pre and postfilter are located in close proximity to the main electrodes (f), to form an implicit capacity, thus coupling to the RF component of the main rod signal. A separate resistor (e) applies a DC offset (see 3.8b). Each pole-pair of pre- and post-filter is coupled via a capacitance of about $10\,\mathrm{pF}$ to the main rod system in order to generate an RF signal of equal frequency and phase. The RF amplitude is lower compared to the main rods, as stray capacities are inevitable. A resistor with high impedance adds a DC offset voltage with a time-constant, much larger than typical RF cycle times $RC \gg 1/f$ and therefore without altering the RF signal significantly. Note, that this DC offset is not part of the resolving DC, but a field axis potential in order to control the kinetic energy of ions along the z-direction. In many cases, pre- and post-filters simply share the field axis of the main rods. Figure 3.8c depicts an in axis photograph through the QMS rod system at its actual location at the exit of SWIG 3. Both are axially aligned and separated just by a few mm in z-direction.
For electric supply we currently use a home-build digital RF supply. It provides a amplitude up to $1\,\mathrm{kV}$ and has a maximum possible thermal dissipation power of about $1\,\mathrm{kW}$. The rising and falling edges are about $30\,\mathrm{ns}$ wide corresponding to $6\,\%$ of the pulse width for the maximum tested frequency of $2\,\mathrm{MHz}$. The driving circuit of the supply currently

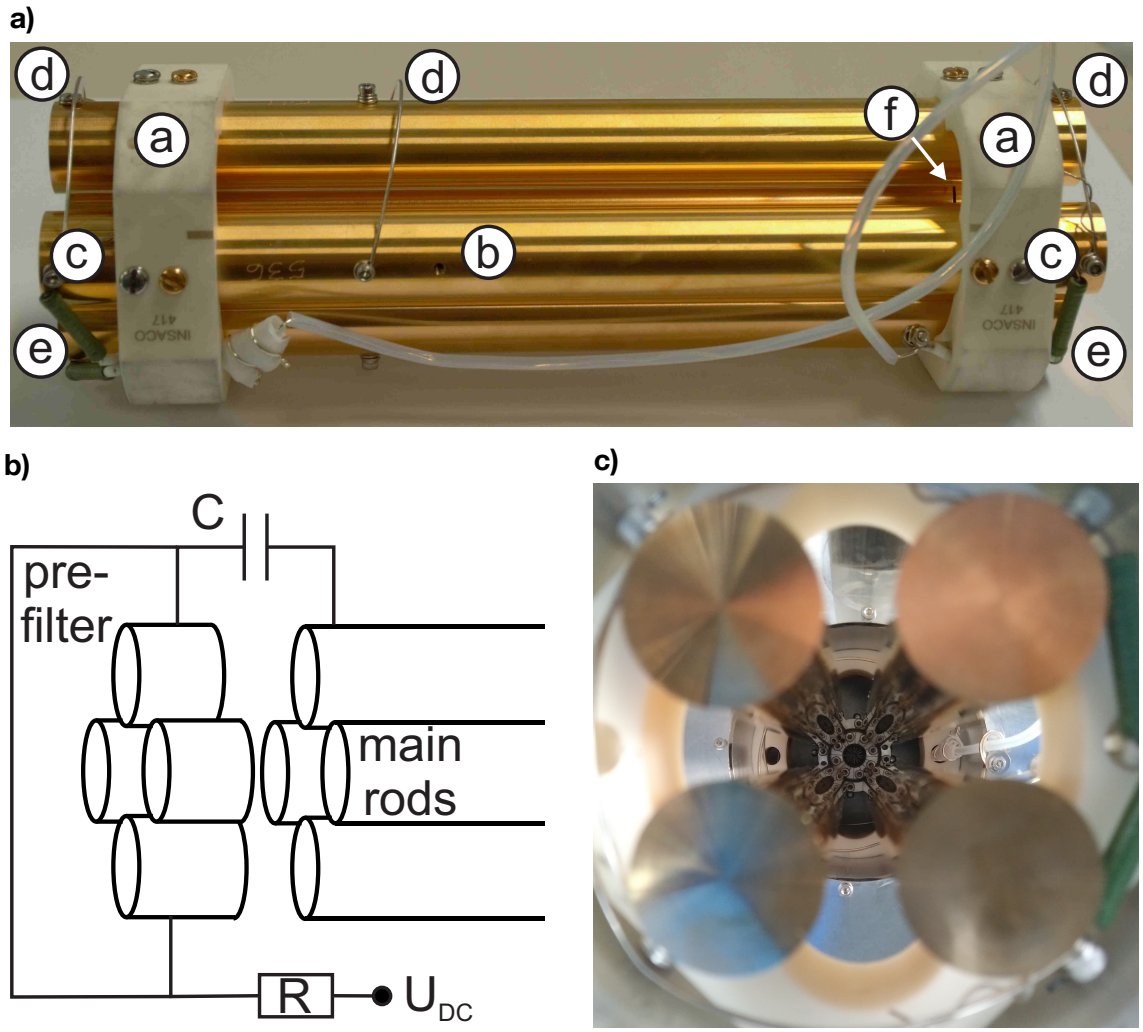

Figure 3.8.: Quadrupole electrodes. a) photograph of the components: (a) supporting ceramics, (b) main rods, (c) pre and post rods, (d) electric concretion between pole pairs, (e) DC coupling resistors and (f) capacitive RF coupling via a small gap of pre- and post-rods.

consists of a simple digital wave-form synthesizer which produces a square wave signal of $5\,\mathrm{V}$ peak to peak amplitude with a duty cycle of $50\,\%$ and adjustable frequency. Therefore, the currently used prototype operates comparable to a sine-shaped QMS by simultaneously ramping up a the RF amplitude and resolving DC. The only difference is the adjustable RF frequency for an unlimited m/z range. The aforementioned more arbitrary digital wave forms can in general be easily implemented by the current RF supply, just by using a more sophisticated driving circuit.

Besides the aforementioned advantages of a digital operation of a QMS, there is one major drawback, which is the power dissipation in the driving electronics. In a classical resonant LC-circuit, the current for the generation of the oscillating field is caused by the imaginary part of the power. The required energy is stored alternatingly in the magnetic field of the inductance in the power supply or in the capacitance of the rod system. Therefore, the driving electronics, that keep the oscillation running has to compensate for damping e.g. by Ohmic losses in the leads only. For properly designed systems, this is typically just a few percent of the absolute value of the power. In the digital case, the capacity of the quadrupole rods and its leads need to be continuously charged and discharged by the RF supply and the energy can not be stored. The required energy comes from the DC power supplies that define the upper and lower potential level. Two high voltage transistors pull the QMS rods to one and another potential. The power is dissipated durring the switching process, predominantly in the high voltage transistors due to their elevated resistance. The required power increases with the capacity of the system, the RF amplitude and frequency. A more detailed discussion of the layout of the electronics will be provided in section 3.8.2.

For preparative purposes, the dQMS fulfills two functions. Firstly, it is mandatory for investigating the ion beam prior to deposition. The existence and intensities of the desired ion species can be monitored, as well as impurities, fragments, adducts or conglomerates can be found. High resolution scans allow to exclude impurities with a m/z close to the ones of desired species. Comparing multiple m/z spectra after tuning all kinds of parameters, like solvent-molecule systems, spray parameters, and the parameters of up-stream ion optics allows for maximization of the desired signals.

Subsequently, the experimenter must choose a suitable point in the stability diagram to transmit as much desired ions as possible while still removing all ions of undesired m/z. For ion beams with no undesired intensities above the m/z of the desired species, the RF-only mode might be a good choice. For an analyte m/z in the vicinity of impurities, the resolution may be adjusted in such a way that the analyte intensity is maximized, but the

contribution originating from neighbouring peaks is still negligible.

3.6. The Blade ion guide

The Blade ion guide [176] is used downstream to the dQMS in order to refocus the ion beam towards the sample. The additional refinement of the ion beam before deposition is crucial as the QMS tends to increase the size and the kinetic energy of the ion beam drastically (see Section 4.5.2). On the other hand, a small ion beam with decent kinetic energy is required for soft-landing fragile molecules on small samples. Most other deposition devices employ electrostatic lenses to extract the ions from their QMS [32, 202–204]. The main problem with electrostatic lenses is that Liouville's theorem states a constant size of ion beams in phase space for electrostatic lens systems [194, 205], meaning that a spatially large ion beam can be focused to a small spot for the expense of elevated kinetics and vice versa, but not both at the same time. Another possibility is a conical RF driven ion guide with a multipole electrode array of shrinking inscribed diameter over its length. There have already been few conical multipoles, e.g. by using an array of rods of shrinking electrode and inscribed diameter [206, 207], or the cyclone ion guide in the UltivoTriple quadrupole LC/MS from Agilent Inc [208].
The fundamental problem of multipoles with non-constant inscribed diameter is that the electrode geometry changes over the length of the ion guide, meaning that the ideal operation parameters of RF frequency and amplitude may also change over the length. This problem can be tackled by sophisticated shape and mounting of the electrodes. In literature a conical multipoles have been realized via cone shaped electrode rods [206, 207]. Our currently pending patent [176] suggest an array of electrodes made from metal sheets with a wedge like profile. The advantage is a constant ratio of gap and electrode size. Furthermore, the effective potential loses its symmetry in z-direction which might cause problems especially for tight focusing e.g. by generation of a potential well due to field penetration towards the center of the ion guide. Fortunately, it is possible to find some sort of compromise between the aforementioned pitfalls and it is very well possible to design and construct a conical multipole with efficient transmission and focusing.
In the case of the ES-CIBD, we use a conical 16-pole as it has some advantages compared to lower orders, such as the small field penetration towards the center and a wide window of RF signals with high transmission. The above mentioned other conical multipoles employ round or conical electrode rods, which might be unfavourable for higher multipole

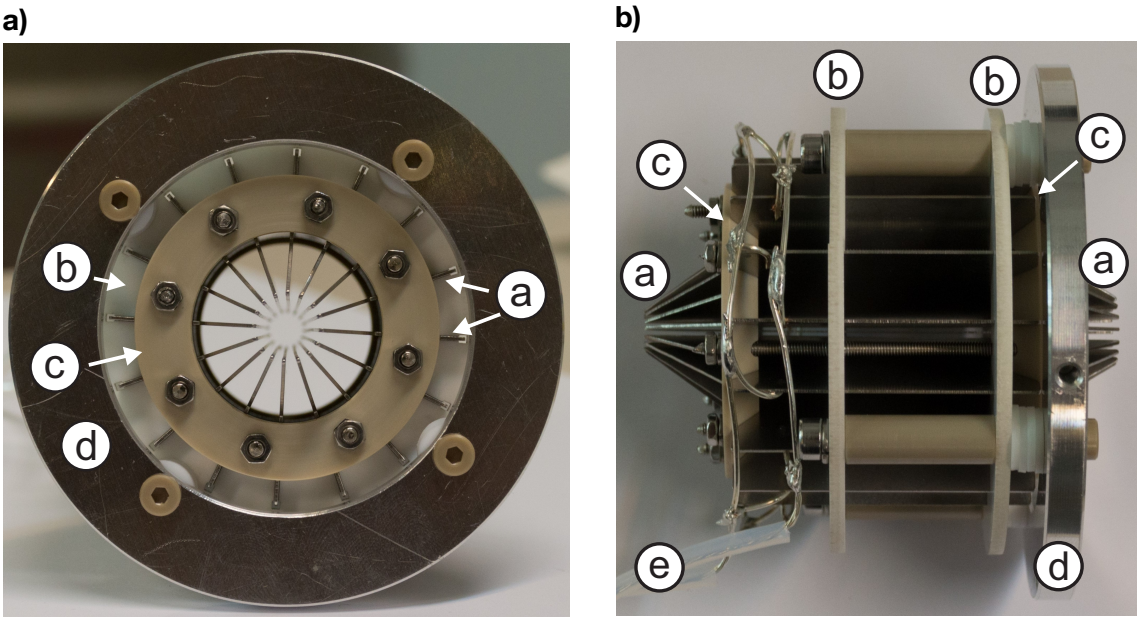

Figure 3.9.: Photographs of the Blade from an axial (a) and a side (b) perspective. (a) indicated the metal-sheet electordes, (b) and (c) are ceramic supports and peek rings for positioning, (d) is the base-plate and (e) are the leads for electric connection.

orders due to mechanical instability for the required small size. A simple solution for this problem was found by using metal-sheet electrodes, that are arranged in radial direction around the ion guide volume. Photographs of the currently used Blade are depicted in Figure 3.9. The main components are metal-sheet electrodes (a), that are positioned by two ceramic holders (b) and two peek rings (c). The whole structure is mounted on a base plate (d) and electrically connected by soldered and spot-welded leads (e). The current design uses 16 laser-cut stainless-steel metal-sheet electrodes of $0.5\,\mathrm{mm}$ thickness and $65\,\mathrm{mm}$ length. The inscribed radius at the entrance is $7\,\mathrm{mm}$, which continuously shrinks towards the exit to about $4\,\mathrm{mm}$.

3.7. The differentially pumped vacuum system

The first ES-CIBD design consists of five differentially pumped vacuum chambers as well as a deposition chamber [209]. Omitting the double bending of the ion beam leads to the actual design of 4 differentially pumped stages and the deposition chamber [52, 135]. A further a reduction to 3 differentially pumped stages besides the deposition chamber was

Pressure interface d [mm] / l [mm]	p_{exp} [mbar]	S [l/s]	q_{exp} [mbar l/s]	q_{theo} [mbar l/s]
ESI source – / –	1000	-	-	-
Chamber 1, capillary 1.1 / 60	2	140	280	160
Chamber 2, Twin 1.5 / 40	8×10^{-3}	55	0.22	0.03
Chamber 3, SWIG 1 2.5 / 80	2.6×10^{-7}	400	1×10^{-4}	1.9×10^{-4}
Chamber 4, SWIG 3 3.5 / 30	9×10^{-11}	400	3.6×10^{-8}	4.5×10^{-8}
Deposition, SWIG 3 3.5 / 30	$\approx 10^{-10}$	400	-	1.5×10^{-11}

Table 3.1.: Summary of the parameters of the differentially pumped system with the pressure interface diameter d and length l, the pressure p, the pumping speed S, the theoretically derived gas flow into the vacuum chamber q_{theo} and the corresponding experimentally derived value q_{exp}.

opened up due to optimizing the leak-rate of the ion guides compared to previous designs [52, 135]. A summary of all important parameters can be found in Table 3.1.
Starting with the ESI-source at ambient pressure, a funnel shaped counter electrode combined with a capillary of $l = 60\,\mathrm{mm}$ length and $d = 1.1\,\mathrm{mm}$ diameter forms an atmospheric pressure interface. The density of air at ambient conditions and a temperature of $T = 20\ ^\circ\mathrm{C}$ is given by $\rho = 1.2\,\mathrm{kg/m^3}$, the viscosity is $\eta = 18.2 \times 10^{-6}\,\mathrm{Pa\,s}$, and the speed of sound is $c = 343\,\mathrm{m/s}$. A Knudsen numbers of $Kn \approx 10^{-4}$ (see equation (36)) and Reynolds number of $Re \approx 2.5 \times 10^4$ (see equation (38)) for gas velocities in the sonic regime indicate turbulent flow. The application of a vacuum pump with high pumping speed at the exit causes chocked flow (see section 2.4). Thus, the critical exit pressure at the end of the capillary and the flow can be calculated via equations (41) and (39) as $p^*_{source} \approx 690\,\mathrm{mbar}$ and $q_{theo,\,source} \approx 160\,\mathrm{mbar\,l/s}$ with the mean thermal velocity of dry air at $T = 20\ ^\circ\mathrm{C}$ of $\bar{c} = 463\,\mathrm{m/s}$, and the ambient pressure of $p_1 \approx 1000\,\mathrm{mbar}$. The first vacuum chamber is evacuated via a Pfeiffer WKP500 Roots pump in combination with a Edwards XDS35i scroll forepump. This system reaches a pumping speed of $S_{chamber\ 1} \approx 140\,\mathrm{l/s}$. The pressure is measured to be $p_{chamber\ 1} \approx 2\,\mathrm{mbar}$ via a Leybold CERAVAC membrane pressure gauge. Therefore, the experimentally derived flow through the atmospheric pressure interface is about $q_{exp,\,source} \approx 280\,\mathrm{mbar\,l/s}$ (see equation (37).

The pressure interface between first and second chamber is formed by the tunnel section of the Twin ion guide (see section 3.3). It can be approximated by a $l = 40\,\mathrm{mm}$ long tube with a diameter of $d = 1.5\,\mathrm{mm}$. From the pressure in the first vacuum chamber, we can estimate the mean free path to be about $\lambda = 0.03\,\mathrm{mm}$ [172] and end up with a Knudsen number of $Kn \approx 2 \times 10^{-2}$. This Knudsen number is closely to the border between Knudsen and continuum regime. For simplicity we assume continuum flow in the following. High pumping speeds in chamber 2 and a Reynolds number of $Re < 100$ indicate chocked laminar flow and equations (42) and (40) lead to $p^*_{Twin} \approx 5.6 \times 10^{-2}\,\mathrm{mbar}$ and $q_{theo,\,Twin} \approx 0.034\,\mathrm{mbar\,l/s}$. In comparison, a thin aperture with equal diameter would lead to a flow rate of about $q_{theo,\,aperture} \approx 0.6\,\mathrm{mbar\,l/s}$ [172], thus reducing the gas load for the subsequent vacuum chamber by a factor of about 20 with the ion tunnel.
The pumping system of chamber 2 consists of a Pfeiffer WKP250 Roots pump which is backed by a Edwards XDS35i scroll pump. The pumps reach a pressure of $p_{chamber\,2} \approx 8 \times 10^{-3}\,\mathrm{mbar}$ which is measured, again, via a Leybold CERAVAC membrane pressure gauge. The data-sheet of of the Roots pump reveals, that the pumping speed already decreases from about $70\,\mathrm{l/s}$ to $S_{chamber\,2} \approx 55\,\mathrm{l/s}$ for such low pressures. From this data, we can calculate the leak rate of the Twin as $q_{exp,\,Twin} \approx 0.22\,\mathrm{mbar\,l/s}$. The higher experimental value most probably comes from incomplete expansion of the residual gas and elevated pressures at the inlet of the ion tunnel. It locates axially aligned and about $9\,\mathrm{cm}$ downstream of the atmospheric pressure interface's exit.
The third differentially pumped chamber connects via the pressure interface of SWIG 1 to the previous vacuum regime. It employs a tubular pressure interface of $d = 2.5\,\mathrm{mm}$ diameter and a length of $l = 80\,\mathrm{mm}$ (see section 3.4). A Knudsen number of $Kn \approx 3$ indicates molecular flow conditions and the conductivity of the interface can be calculated via equation (43) to $C_{theo,\,SWIG\,1} \approx 2.4 \times 10^{-2}\,\mathrm{l/s}$. Assuming a negligibly low pressure at the exit of the pressure interface $p_{chamber\,3} \ll p_{chamber\,2}$ allows for calculation of the flow $q_{theo,\,SWIG\,1} \approx 1.9 \times 10^{-4}\,\mathrm{mbar\,l/s}$. Comparison with a thin aperture of the size of the inscribed radius ($d_i = 1.64\,\mathrm{mm}$) leads to a conductivity of $C_{theo,\,aperture} \approx 2.6 \times 10^{-1}\,\mathrm{l/s}$ [172]. Although the diameter of the pressure interface of SWIG 1 is larger due to the feed-through of electrodes, the gas conductance can be reduced by a factor of about 10 by the elongated design with respect to an aperture. Despite that, the confining RF field is not interrupted by a pressure interface thus having benefits in ion transmission efficiency, too.
Chamber 3 is pumped by a Leybold TURBOVAC MAG W 600 iP turbo-molecular drag pump which shares its forepump with the Roots pump of the previous chamber. The turbo

pump connects to the chamber via a $100\,\mathrm{mm}$ long hose of $100\,\mathrm{mm}$ diameter which reduces the effective pumping speed from about $600\,\mathrm{l/s}$ to $S_{chamber\ 3} \approx 400\,\mathrm{l/s}$. The chamber pressure of about $p_{chamber\ 3} \approx 2.6 \times 10^{-7}\,\mathrm{mbar}$ is measured via a combined hot-cathode and Pirani gauge (Leybold IONIVAC ITR 90). The resulting flow from the previous chamber can be calculated as $q_{exp,\ SWIG\ 1} \approx 1 \times 10^{-4}\,\mathrm{mbar\,l/s}$

Chamber 4 is the the first UHV stage, which requires a baked-out in order to reach a suitable base pressure. It connects to the previous chamber by one of the two pressure interfaces of SWIG 3. Both consist of a $30\,\mathrm{mm}$ long tube with $3.5\,\mathrm{mm}$ diameter. Knudsen numbers are in the molecular regime and the calculated conductance of both interfaces is $C_{theo,\ SWIG\ 3} \approx 0.17\,\mathrm{l/s}$. The flow from chamber 3 towards chamber 4 can be estimated to $q_{theo,\ SWIG\ 3} \approx 4.5 \times 10^{-8}\,\mathrm{mbar\,l/s}$. Combining the pumping of $S_{chamber\ 4} \approx 400\,\mathrm{l/s}$ of the attached Leybold TURBOVAC MAG W 400 iP with the partial pressure originating from the pressure interface of $p_{chamber\ 4} \approx 9 \times 10^{-11}\,\mathrm{mbar}$ lead to a flow of $q_{exp,\ SWIG\ 3} \approx 3.6 \times 10^{-8}\,\mathrm{mbar\,l/s}$. This pressure is already comparable to the typical base pressure of a UHV chamber ($1 \times 10^{-10}\,\mathrm{mbar}$) and can not be measured via the Leybold IONIVAC ITR 90 pressure gauge (minimum readout pressure: $5 \times 10^{-10}\,\mathrm{mbar}$). The conductance and flow of the pressure interface was experimentally measured by artificially increasing the pressure of chamber 3, i.e. by stopping one or both Roots pumps. In principle, the pressure interfaces of SWIG 3 could be designed both, smaller and longer (comparable in size to the one used for SWIG 1) in order to further decrease leak rates, but the larger ion guide diameter benefit from a more simple design, construction, and mechanical alignment. The low pressure in chamber 4 makes further optimization of leak rates obsolete, especially as there is another pressure interface of comparable leak rate towards the deposition chamber. Actually, chamber 4 is obsolete for the differential pumping because of the drastically decreased leak rates of the previous ion guides, but due to historical and constructive reasons it has not been eliminated, yet.

The deposition chamber employs an equal pressure gauge, pump and pressure interface as chamber 4 and reaches a calculated flow of $q_{theo,\ prep} \approx 1.5 \times 10^{-11}\,\mathrm{mbar\,l/s}$. The estimated partial pressure from the residual gas flow is in the $10^{-13}\,\mathrm{mbar}$ region. Thus, the resulting overall pressure, typically in the $10^{-10}\,\mathrm{mbar}$ regime, is almost entirely defined by the base pressure of the UHV chamber itself and essentially independent of the residual gas flow from the ESI source.

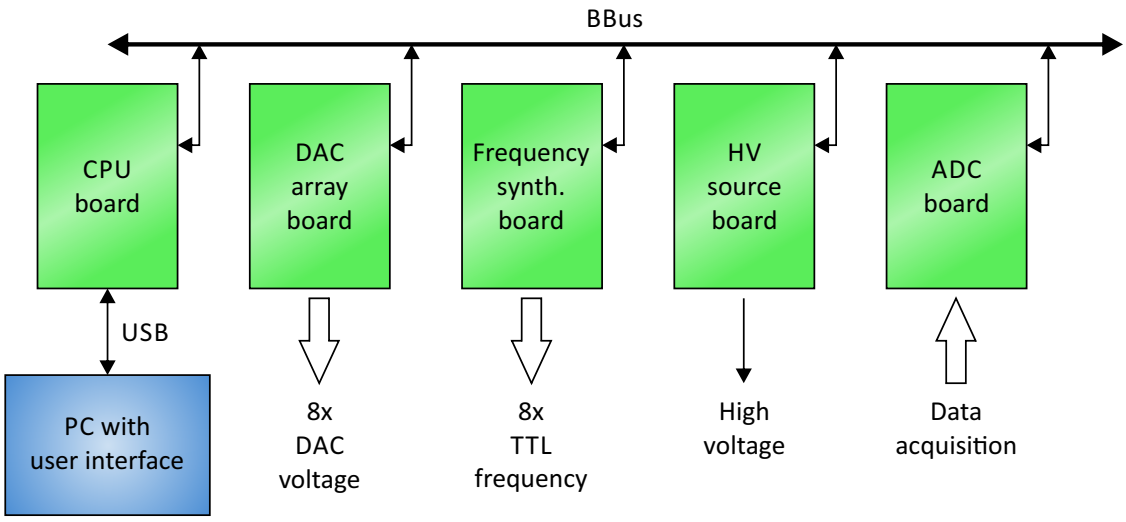

Figure 3.10.: Schematic overview of the control electronics of the ES-CIBD system. From [211] with modifications.

3.8. Supply and control electronics

The previous chapters concentrated on the physics and the performance of the ES-CIBD system and its components, but even the most subtle ion guide geometry is worthless without a sophisticated supply and control electronics with an easy to handle user interface. Unfortunately, most of the ion guides are home-build and follow new concepts of operation, which reduces the amount of appropriate and commercially available out of the box electronics for the ES-CIBD to almost zero. Thanks to previous efforts [52, 210, 211] many building blocks of currently installed home-build electronics have already been developed and implemented at the beginning of this thesis. However, an important part of the work in this thesis was the self-improvement in electrical engineering in order to follow the path of previous works and further improve the electronic control unit and develop new components. The following sections will describe the operation principles of all important components of the ES-CIBD electronics and its user interface.

3.8.1. The control electronics

A schematic of the basic operation of the ES-CIBD electronics is provided in Figure 3.10. The home-build central processing unit (CPU) board on the top left is the most central part of the whole unit (see Figure 3.11b). It has already been described in detail by [211] but due to its importance, a short recap will be provided in this thesis. The CPU board

a)

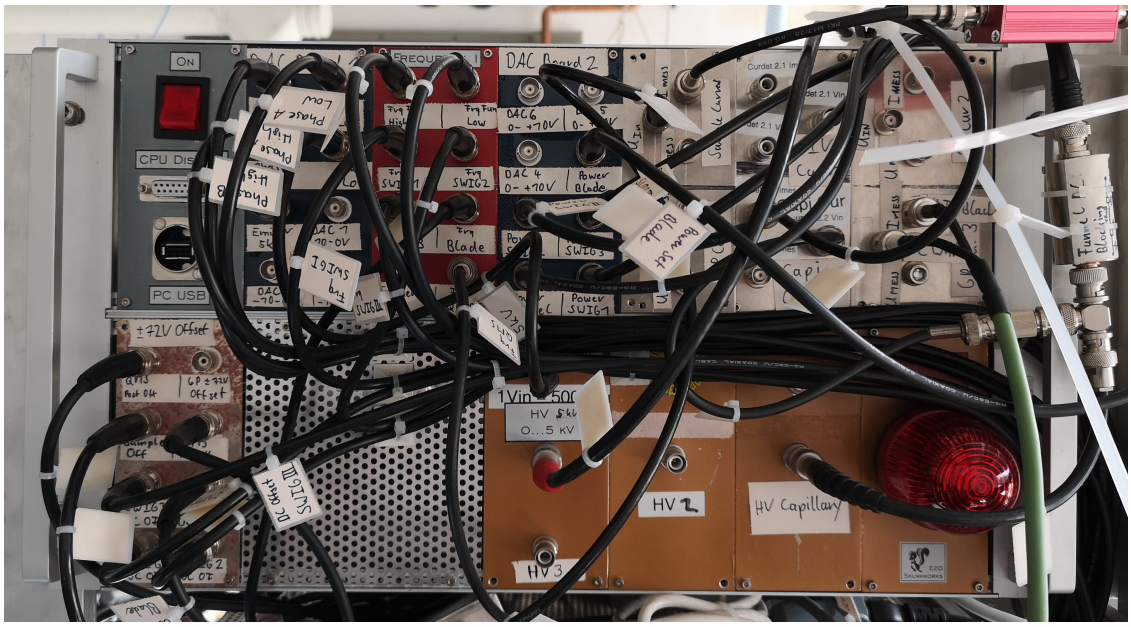

b)

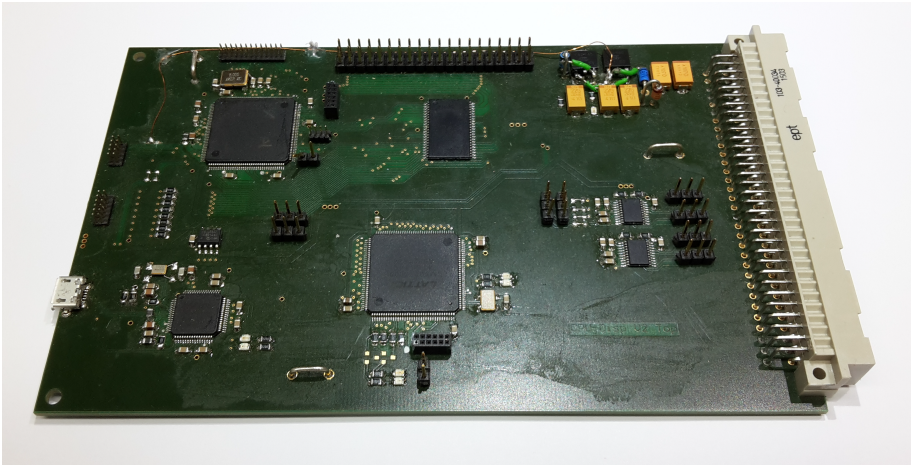

Figure 3.11.: a) Photograph of ES-CIBD control electronics. b) The CPU board. From [211]

represents the interface between all control and measurement boards of the ES-CIBD and a PC with the user interface. The communication with a lab PC allows for sending and receiving data and commands from a tailor-made control software via a universal serial bus (USB). The further handling and distribution of all kinds of signals to their recipients in the ES-CIBD is realized via a modified full-duplex serial peripheral bus, we have called it board bus (BBus). Communication as well as all timing relevant processes are handled by the CPU board via this bus system. All other boards of the electronics, that are either used for signal generation or data acquisition are connected to the BBus via a flexible ribbon cable.

For fast prototyping and simple maintenance all depicted boards are made from eurocard format printed circuit boards (PCBs), located in a 19" rack housing (see Figure 3.11a). The differently coloured front panels indicate the function of the boards. The CPU board employs a dark grey front panel, digital to analog converter (DAC) array boards are indicated in blue for $0-10\,\mathrm{V}$ outputs and in rusty red for $\pm 72\,\mathrm{V}$ outputs, frequency synthesizer boards are red, analog to digital converter (ADC) boards are metallic silver and high voltage (HV) sources are painted in gold. The ES-CIBD and all externally located electronics like all the power supplies and the RF generators are operated and controlled by these boards.

The DAC array boards:

The basic design of the DAC array board was first described in [211]. It provides 8 analog DC control voltages with adjustable output range between $-10\,\mathrm{V}$ and $10\,\mathrm{V}$ and 16 bit resolution. The DAC boards are used to drive the current and voltage control inputs of the DC power supplies of the RF generators of the ion guides and the dQMS. Along with this thesis, a second type of DAC array boards was developed and the original design was modified by adding a high voltage compatible operational amplifier "LTC6090" with $\pm 72\,\mathrm{V}$ output voltage. The board is typically used to apply the DC offsets for all SWIG and Blade ion guides, as well as the landing energy of the ion beam.

The frequency synthesizer board:

This board was developed and precisely described in [211] and provides 8 adjustable frequencies with up to $70\,\mathrm{MHz}$ and $5\,\mathrm{V}$ amplitude. In principle the board can produce both, sine and square-wave but currently only the square wave output is used. This board controls the frequencies of all RF generators and the dQMS.

The HV source board:

The HV source board was introduced in [52] and provides a high voltage in the range from $-1.1-1.1\,\mathrm{kV}$. It is used for the potentials of the counter electrode of the ESI source and

a)

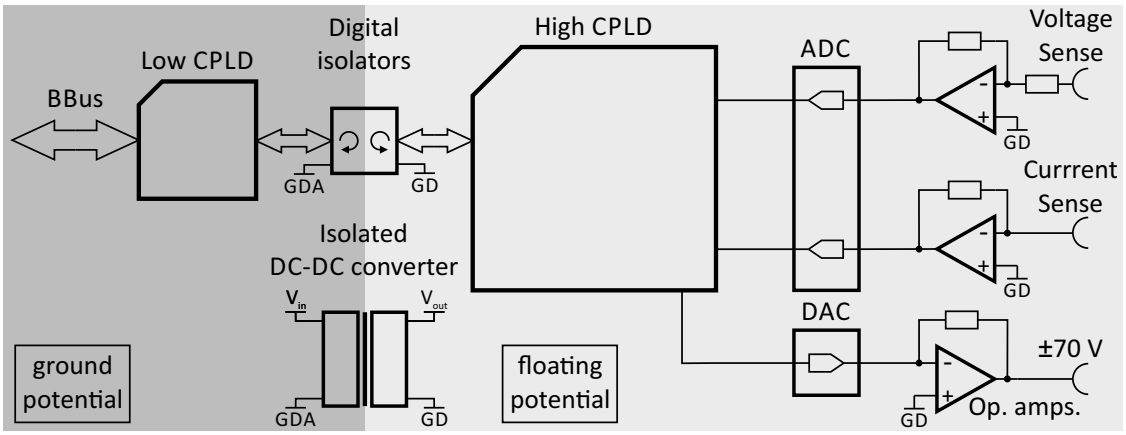

b)

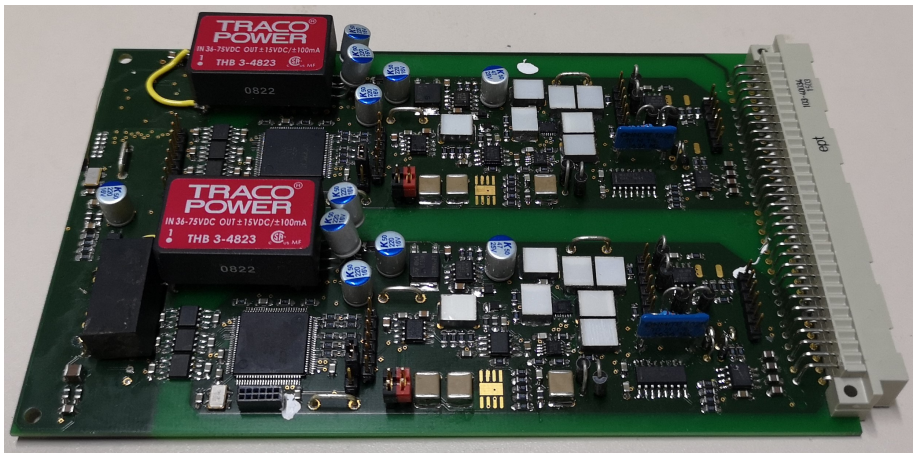

Figure 3.12.: a) Overview over the most important ADC board components. From [52] with modifications. b) Photograph of the ADC board

the supply of the DC cascade of the Twin. Along with this thesis, the capacitive load of the output relay was found to be too large which caused contact welding after a certain time of operation. This problem could by be solved by smaller capacities and a resistor in series with the relay to limit the current during switching. Furthermore, the software was adapted to avoid the switching of larger potential differences, thus also reducing the load. Besides this board, a preliminary installed adjustable $\pm 5\,\mathrm{kV}$ HV source was implemented to supply the emitter of the ESI source.

The ADC board

The ADC board was completely redesigned during the work of this thesis and some additional functionality was added. Figure 3.12a shows an overview of the components of the ADC board. The dark grey part of the diagram on the left is connected to common ground

potential and provides data connection via digital isolators and power via a isolated DC-DC converter to the floating section to the right in light grey. The communication with the CPU takes place via the BBus on the very left and is managed by a complex programmable logical device (CPLD). This additional logic device was installed to handle the distribution of signals to the two high side CPLDs. In reality, each ADC board has two data acquisition units with independent floating potentials (see 3.12b). For simplicity only one is depicted in Figure 3.12a. All data acquisition electronics locate on the floating potential side and composes from a current sense and a voltage sense input. The reference potential for the measurements is supplied via the third pin and can be shifted by further $\pm 70\,\mathrm{V}$ via an adjustable internally generated offset voltage, controlled via a DAC. The isolation quality of the floating system was tested by application of $5\,\mathrm{kV}$ for $1\,\mathrm{min}$ to the reference pin without breakdown. However, for long term operation without degradation the applied potential is recommended to not exceed $1\,\mathrm{kV}$. The two inputs of the 24 bit ADC in Figure 3.12a are connected to the operational amplifier responsible for voltage and current sensing, respectively. The mode of operation might be chosen by the user, but only one of both modes can be operated at a time. The voltage sense provides an input range of $\pm 10\,\mathrm{V}$ compared to the floating internal GD. The current detector employs an adjustable feedback resistor to allow for selectable current ranges from $0.5 - 50\,\mu\mathrm{A}$. During operation in the lowest current range, the noise level on the current data has a standard deviation of about $1\,\mathrm{pA}$ for an integration time of $80\,\mathrm{ms}$. Besides that, one of the voltage sensors was modified in order to measure the sample temperature via the voltage of an attached type K thermocouple.

3.8.2. RF generators

Previous versions of RF generators were rather large in a 19” rack housing and employed long coaxial cables with termination resistors to connect to the ion guides in order to avoid larger amounts of electronics closely to the vacuum chamber [52, 211]. For the first experiments with the TWIN, SWIG and Blade this was convenient due to decent RF amplitudes of $< 50\,\mathrm{V}$, a cable impedance and termination resistor of $93\,\Omega$ and a resulting power consumption of the order of $30\,\mathrm{W}$.
This design concept reached its limits during the layout of the dQMS supply electronics. Standard sine-shaped QMS electronics operate with LC circuits at few kV amplitude and a RF frequency in the MHz regime. The goal for the dQMS supply electronics was to reach a comparable performance with a square wave of adjustable frequency. Starting from the

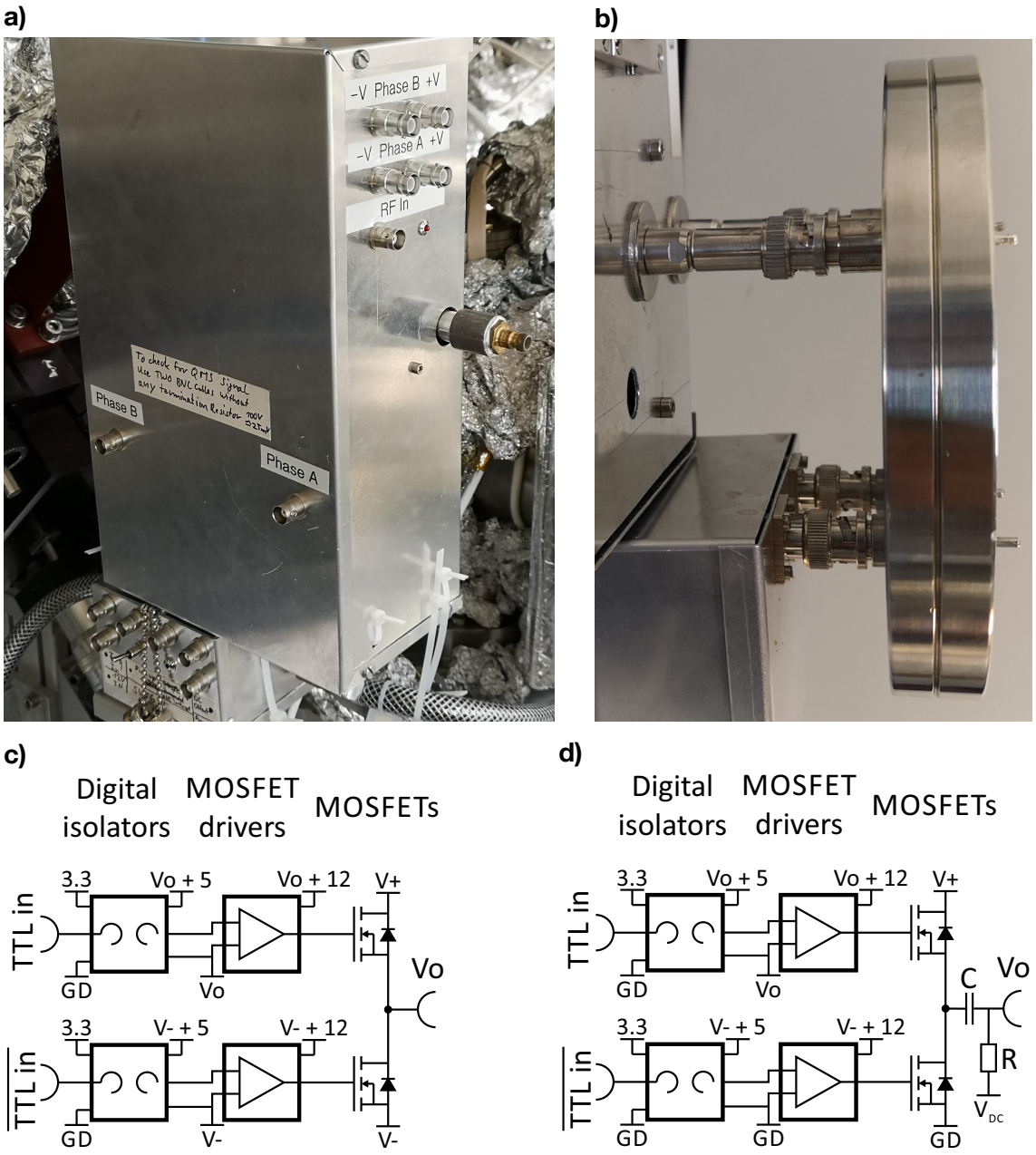

Figure 3.13.: Photographs and schematic circuitry of the RF generators of the dQMS and SWIG 3. a) housings of the dQMS RF generator in the larger Aluminium box on top and the SWIG 3 RF generator in the smaller Aluminium box below. The tubing on the bottom and the brass connector on the right are used for water-cooling. b) vacuum feed-through of both electronics. c) and d) schematic circuitry of the dQMS and SWIG RF generators, respectively.

above mentioned RF generators, the first step towards the dQMS supply electronics was the elimination of the termination resistor. Such a resistor would reach an unacceptable power consumption of the order of $10\,\mathrm{kW}$ for amplitudes in the kV region. The second problem is the power consumption of the continuous charging and discharging of the rod electrodes themselves. From the perspective of the RF generator, these electrodes are nothing more than a capacitive load of about $100\,\mathrm{pF}$. Combined with few kV RF amplitude and $1\,\mathrm{MHz}$ RF frequency a power consumption of several $100\,\mathrm{W}$ is reached.
The solution for both problems was found by the shortest possible leads (about $20\,\mathrm{cm}$) between the output transistors of the RF generator and electrodes. This design approach reduces unnecessary capacitances and minimizes the impact of non perfect impedance matching between RF generator and leads as the one way propagation delay of the signal (about $1\,\mathrm{ns}$) is small compared to the rise and fall times of the square wave signal (about $30\,\mathrm{ns}$, [212]). To realize such a system, the RF generator needs to be as small as possible and mounted directly to an electrical feed through of the vacuum chamber that is located closely to the electrodes of the dQMS. A photograph of the current dQMS RF generator (larger aluminium box on top) and SWIG 3 (smaller box on the bottom) is depicted in Figure 3.13a. Figure 3.13b shows the electric vacuum feed-through of both RF generators. Coaxial connectors, directly mounted on their housings without a coaxial cable in between ensure shortest possible leads. To handle the thermal power dissipation of both RF generators in a compact size, a water-cooling with quick coupling system is installed.
The dQMS RF generator is operated by four floating power supplies and is controlled by a square-wave signal. Figure 3.13c depicts the basic operation principle of the dQMS. The control input signal and its inverted value are transferred to the source potential of the pull-up and pull-down transistors via digital isolators and auxiliary power supplies decouple from ground with extreme low capacity in the $10\,\mathrm{pF}$ range. Thus, no relevant additional capacity is added to the rod system, hindering the switching parameters.MOSFET drivers amplify the signal to supply the gates of the high voltage transistors, which pull the output towards the upper or lower voltage level. The signal of the second phases of the dQMS is controlled by a second signal at separate base level, in the current design generated by inverting the first signal, leading to $50\,\%$ residence time on the upper and lower level respectively. In principle, the dQMS supply could produce any arbitrary rectangular wave form, just by providing a more sophisticated signal at the inputs. The supply voltages originate from four home-build $1\,\mathrm{kV}$ high voltage supplies, controlled via a $0-10\,\mathrm{V}$ analog signals from the DAC board. With such a system, it was possible to build an dQMS supply electronic with a maximum RF amplitude of about $1\,\mathrm{kV}$ and a maximum Frequency

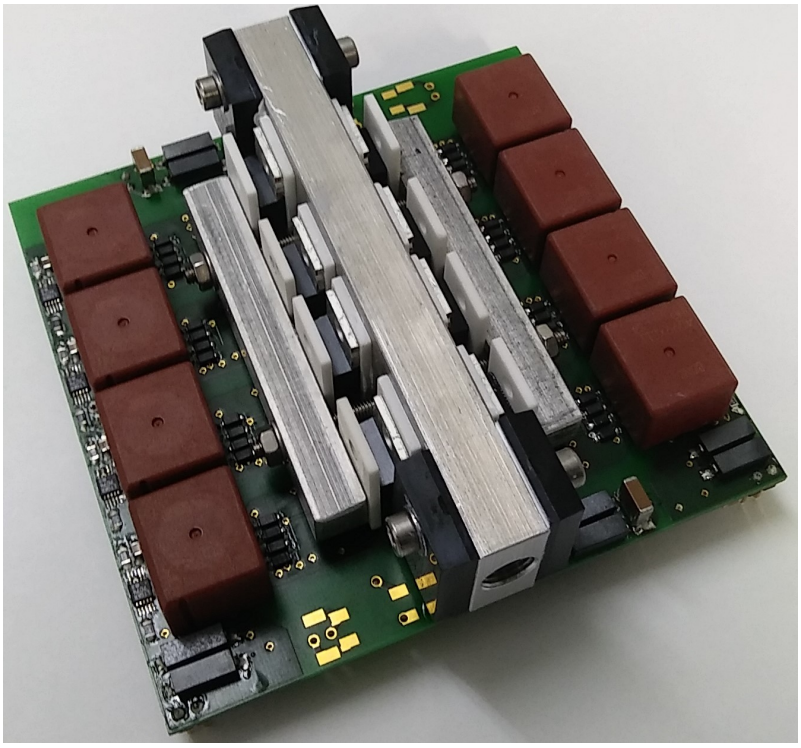

Figure 3.14.: Photograph of a high frequency RF generator used for SWIG ion guides.

of about 2 MHz. The rising and falling edges of the signal are about 30 ns long without significant overshooting. The output transistors employ water-cooling in order to dissipate the overall power of up to 1 kW in the limited space close to the vacuum flange.
After the successful operation of the dQMS, a second version with equal operation principle but higher output frequencies up to 20 MHz but lower amplitudes up to 350 V was developed in order to operate the other RF ion guides. Further improvements and miniaturization allowed to significantly shrink the size of the circuitry and a much smaller housing compared to the dQMS (see Figure 3.13a). An overview of the components of the SWIGs RF generator is depicted in Figure 3.13d. The main difference compared to the dQMS is that a single supply voltage V_+ and ground potential is used to generate the RF signal. The offset DC potential is added by an RC circuit at the output. Here, the capacity C needs to be much larger than the capacity of the ion guide to avoid significant reduction of the RF amplitude and the time constant of the system RC needs to be much longer than a period of the RF cycle in order to avoid significant discharging of the capacity via the resistor. A photograph of the PCB is shown in Figure 3.14. The output transistors are mounted to the

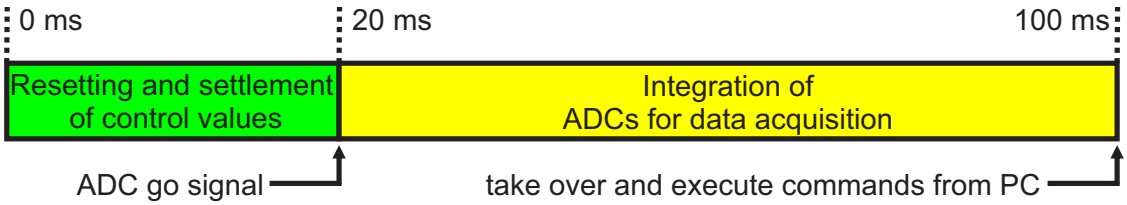

Figure 3.15.: Schematic diagram of the timing in the control electronics.

aluminium bar in the center for water-cooling via aluminium oxide sheets, thus ensuring electrical insulation of the transistors from ground but high heat conductivity towards the cooling for power dissipation.

3.8.3. Timing of the electronics

As already mentioned above, the timing of control parameters and data acquisition is very important. This was one of the reasons to install a separate CPU board. The schematic diagram in Figure 3.15 depicts the currently used timing structure. The system employs a $100\,\mathrm{ms}$ cycle of resetting all changed parameters and subsequent data acquisition. At the beginning of each cycle, the first $20\,\mathrm{ms}$ are reserved by the CPU unit to check for changed control values, like DAC outputs or frequencies and execution of the respective commands. This process typically takes only few milliseconds maximum, depending on the amount of commands to be executed. Afterwards, all data from the ADCs are collected, which takes approximately another millisecond. The mayor component of the $20\,\mathrm{ms}$ is therefore not used for digital communication in the control electronics, but was scheduled for the settling of all analog signals, e.g. voltage levels of supply electronics. This overhead seemed to be necessary for a subsequent integration over a stable signal. At the very end of this first $20\,\mathrm{ms}$ block, an ”ADC go” signal is sent from the CPU in order to start data acquisition of all ADCs simultaneously. The currently used settings employ $80\,\mathrm{ms}$ of integration of the ADCs for sufficiently low noise levels of each measurement. The communication with the lab PC is possible during the whole $100\,\mathrm{ms}$ cylce, but only commands that have been transmitted successfully during the last $100\,\mathrm{ms}$ period can be executed during the subsequent one. The software in the PC is programmed to adapt the timing structure of the CPU for sending and receiving data and commands.

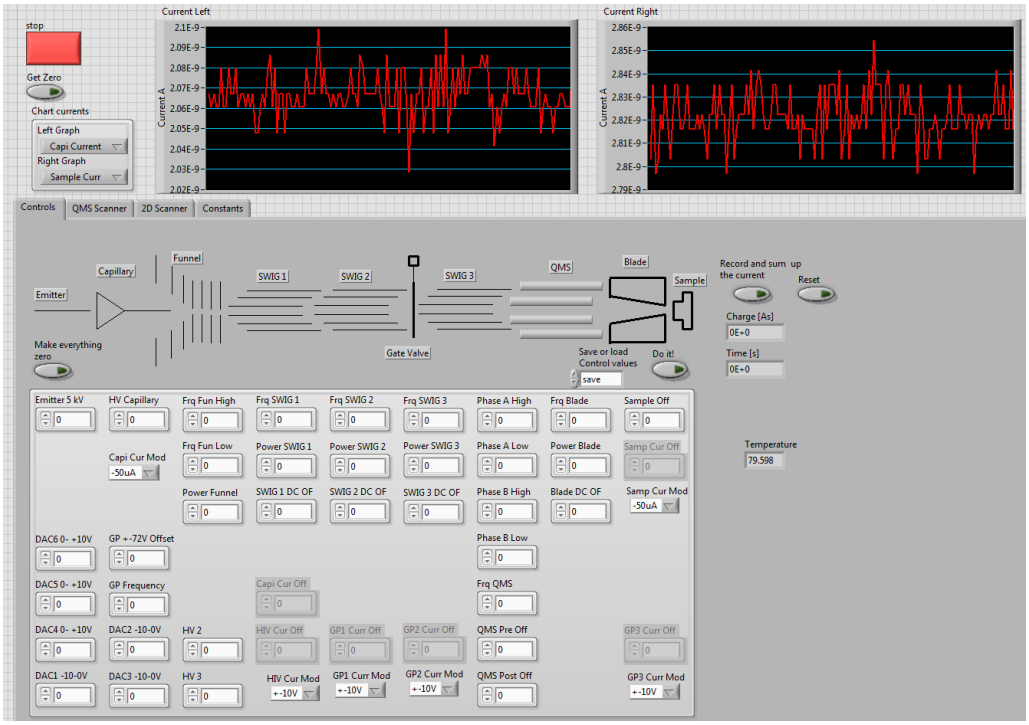

Figure 3.16.: Screenshot of the ”Controls” tab of the LabVIEW control software.

3.8.4. The LabVIEW control software

The aforementioned control software on the lab PC with user interface is programmed in LabVIEW. The advantage of this language is its popularity for all kinds of laboratory software, like pumps, pressure gauges and others. Furthermore, it is a rather high level graphical programming language including several debugging and fault analysis features, which makes it easy to learn and implement.

Figure 3.16 depicts a screenshot of the user interface of the current ES-CIBD control software on the lab PC. Starting on the top left, there is a big stop button in order to switch all supply voltages and frequencies off and disconnect the communication between the lab PC and the ES-CIBD electronics. The rest of the topmost buttons correspond to the two charts on their right. These two charts are used to display the evolution of the data of two of the ADCs. Typically the current on the metal capillary acting as a counter electrode of the ESI source is displayed on the left, the sample current on the right. The ion current on the capillary is a good indicator for the stability of the electrospray, whilst the current on the sample is important to control for successful deposition. The ”Get zero” button

bellow the stop button allows to calibrate the zero value of the ADCs. Below, there are two controls to change the displayed data of the two charts to other ADCs for flexibility. The large grey box below the charts consists of four tabs hosting control values, a QMS scanner, a 2D scanner, and some calibration constants. Figure 3.16 is a screenshot of the ”Controls” tab. On the very top, the sequence of components of the ES-CIBD are sketched for illustration. The columns of control values below the components in the light grey box list their most important control values. The separated controls on the bottom left and right are typically not connected during standard operation. Another helpful feature in this tab is the save and load function on the top right of the light grey box. It allows to save and load all current parameters to a file in order to rapidly start and stop operation and switch between different deposition modes. For controlled and synchronous running up of all control values, the green button on the left defines the point in time, when the parameters are loaded. Its counterpart on the top left of the light grey box switches all supply electronics and frequencies off synchronously.
With the two buttons and displays on the top right of the controls tab, the ion current onto the sample can be recorded while depositing. The two displays show the time since the beginning of deposition and the time integral over the current, which corresponds to the deposited charge and represents a measure for the coverage of the sample. Besides that, all data acquired from the current sensors of the capillary and the sample are saved to a file, together with all other parameters. The reset function restarts the clock and sets the charge to zero. Below these functions, the reading of the sample temperature is located.
The user interface in the ”QMS Scanner” tab is depicted in Figure 3.17. For illustrative reasons, the data of a typical m/z resolved spectrum was edited to the picture. Currently, the dQMS is operated anlogously to a sine-shaped driven QMS. Each m/z resolved scan ramps the RF amplitude and the resolving DC simultaneously in order to record a spectrum (see section 2.2.3). The RF frequency is constant and the duty cycle of the square wave is $50\,\%$. The first step towards performing a scan is choosing a start and a end m/z of the scan. In the following, the offset voltage needs to be adjusted to define the kinetic energy of the charged particles in the dQMS. The resolution of the scan also needs to be chosen in order to account for the trade-off between high transmission and high resolution. In the current program, this is realized by defining an offset towards lower resolving DC and an decrease in slope compared to the line of apizes (see section 2.2.3). High values correspond to poorly resolved spectra with high transmission and vice versa. Now, the RF frequency has to be adjusted in order to not exceed the maximum applicable voltages or power dissipation. For the user, save operation is indicated by green lamps on the bottom

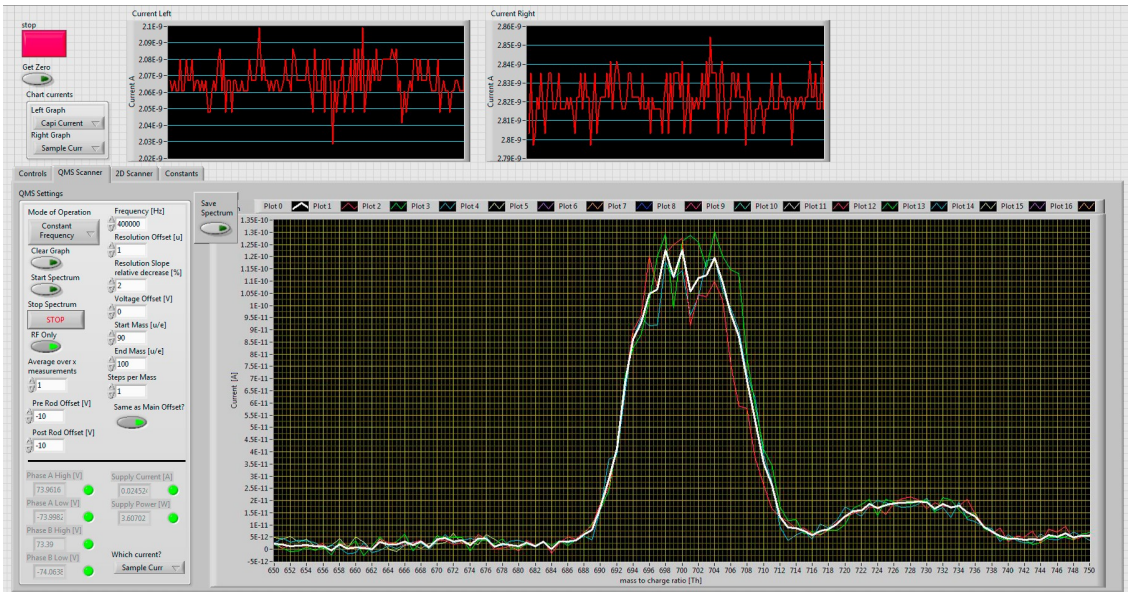

Figure 3.17.: Screenshot of the ”QMS Scanner” tab of the LabVIEW control software, edited with a typical m/z resolved spectrum.

left. Here, all important parameters, like the upper and lower potentials of both phases, the supply current, and the resulting power dissipation are indicated. Pre-defined limits avoid damage of the dQMS electronics and in case of violation an error message is displayed to the user and the violated parameter is indicated to the user by switching the corresponding green lamp to red. The step width between two adjacent points in the spectrum, as well as the integration of more than one value of the ADC can be adjusted. Furthermore, the offset potentials of the pre and post rod system may be chosen independently, or automatically adapted to the offset of the main rods.

The recorded spectra are displayed in real time in the graph and after completion of a full scan, the software automatically performs the next scan. Each scan line is depicted with a thin line of different colour. The average over all completed spectra is depicted via the thicker white line. The repetition of scans is important to distinguish between real features of the scan and artefacts, e.g. due to a fluctuating beam intensity from the ESI source. The whole data set, including all parameters and a .jpg file of a screen shot of the graph can be saved via the ”Save Spectrum” button. For safety reasons, each scan is also saved by default to a backup folder in order to avoid loss of data.

The ”2D Scanner” tab follows a similar layout, despite that two parameters might be varied independent of each other and the colour code indicates the recorded data. A screenshot

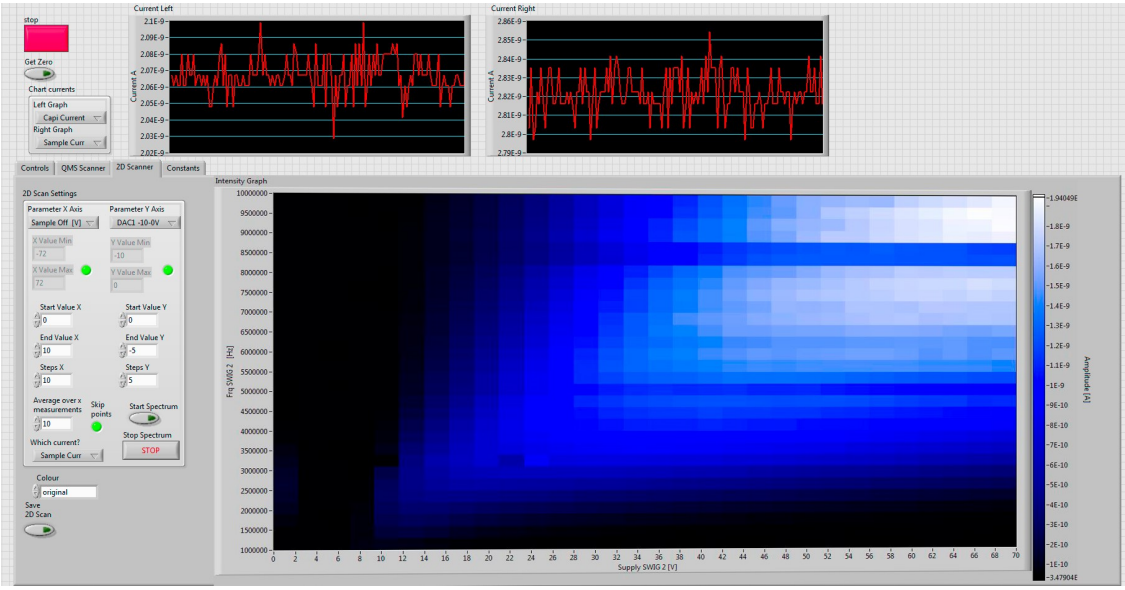

Figure 3.18.: Screenshot of the ”2D Scanner” tab of the LabVIEW control software, edited with a 2D Scan.

of the tab, edited with some typical data in the graph is depicted in Figure 3.18. On the top left, any two parameters to be investigated can be chosen for the x- and y-axis of the spectrum. Below that, the predefined upper and lower limits of said parameters are displayed including a green indicator lamp. In order to perform a scan, the user needs to chose a suitable range and step width for both parameters. The averaging over more than one data point and the ADC, from which the data originates can be adjusted as well. A save function and an intrinsic auto save stores the data, all parameters and a screen shot of the scan. An example of an application of the 2D scanner is the edited data in the graph of Figure 3.18. It displays the original scan of the transmission properties of SWIG 2, which is also depicted in Figure 4.13. The RF frequency and amplitude is varied in order to gain information about suitable operation parameters of the ion guide.

4 | Numerical ion trajectory simulations

An analytical description of ion movement in multipoles and stacked ring ion guides was already given in the previous chapter, but especially when it comes to more complex field geometries, e.g. non ideal electrodes, conical inscribed radii, fringing effects and interfaces between ion guides, influence of residual gas, or the Coulomb interaction of an ensemble of charged particles, analytical descriptions reach their limits. A very practical approach to gain further insight is the investigation of such problems by numerical ion trajectory simulations. Here, it is possible to calculate the electric or magnetic field of any arbitrary ion guide geometry filled with any distribution and type of charged particles. The trajectories of the charged particles are calculated from the forces of the fields and interparticle interactions, such as the Coulomb repulsion or scattering with residual gas atoms. Interpolation over many reasonably small time steps provides the ion trajectories of all present charged particles and information of the investigated system's behaviour.
In the framework of this thesis, ion trajectory simulations of multipole ion guides have been conducted by using the software-package SIMION 8.1. Its roots go back to the 1970's and an electrostatic optics program which was successively upgraded by Dahl and Manura since the 1990's [213–215]. Summarizing a few examples from literature, SIMION was already extensively and successfully used to calculate electron trajectories [216, 217], ion trajectories in different RF ion guides [52, 141, 218], and ion motion in elevated pressure regimes [219, 220]. The simulations in this chapter are conducted with a customized code of H. Schlichting [210]. Due to the scope of this thesis, solely simulations from RF multipoles will be shown.
The following sections provides a short introduction to concepts of SIMION and the custom-made extensions of the code. Subsequently, the results from high order multipole simulations are compared to the analytical description of section 2.2. Afterwards, results from simulations with different RF signals and electrode geometries are presented. The last section compares simulation results with experimental data.

4.1. Basic concepts of SIMION

Before performing ion trajectory simulations, like the ones presented below, the experimenter needs to consider a multitude of parameters and define circumstances of interest. Starting with the basics, it is necessary to define a set of electrodes and a simulation volume, in which SIMION may calculate the ion trajectories. Reasonably, a so-called geometry file is used to define the shape and size of the simulation volume and electrodes.

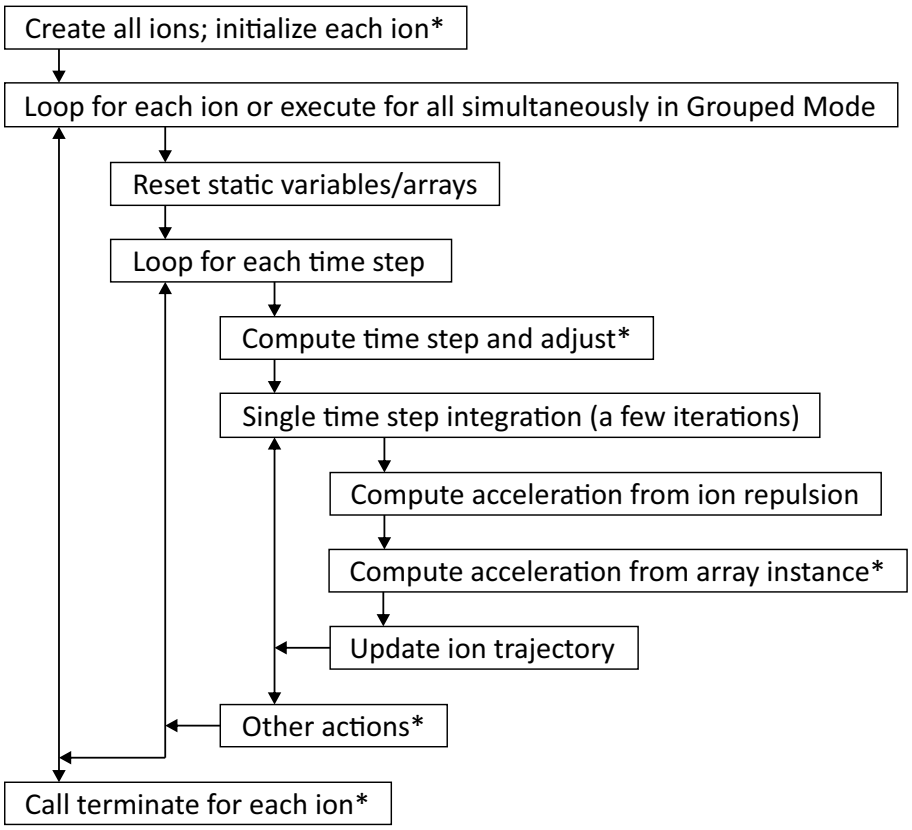

Figure 4.1.: Flow chart of an ion trajectory simulation using SIMION. Computational steps marked with an asterisk allow for tailored integration of custom-made code. From [215] with modifications.

From this file, SIMION generates a grid of voxels in order to calculate the electric field of each electrodes at each voxel [215]. The size of each grid unit needs to be carefully chosen by the user. The resulting meshes are stored in so-called potential array (PA) files which need to be loaded into the RAM during simulations for fast access. As RAM size is limited and rather expensive, there is a competition between precision of the field and PA file size. It is crucial to test new geometries for different meshes in order to find a good trade-off in voxel sizes (in all three dimensions) for high field-precision near small objects and acceptable file size.

The force acting on a charged particle for each position in the simulation volume is calculated from the linear superposition of the field evoked by any individual electrode. The spatial intensity of the electrodes field is calculated prior to simulation and multiplied by their time dependent actual potential to save computation time. The acting forces are assumed constant for the actual time step and the trajectories are calculated. Recalculation

of electric fields and forces is performed for each time step of the simulation. Additionally, the forces from ion-ion interactions or scattering events with background-gas may be included. The iteration process of a simulation is sketched in Figure 4.1. A major advantage of SIMION is the possibility to introduce customized sections of code in several different iteration steps. This allows for tailored introduction of e.g. arbitrary and time dependent potentials on each electrode, residual gas scattering with tunable temperature and cross-section, Coulomb interaction between ions, and simulation of continuous ion beams.

In the framework of this thesis, the properties of multipole ion guides are simulated. Especially the ion transmission efficiency T for realistic parameters has been a subject of interest. A continuous beam of ions is supplied to the ion guide and the ejected beam is recorded. The ions start randomly distributed on a disc of radius r_{inject} with defined kinetic energies in z-direction $E_{kin,z}$ and the xy-plane $E_{kin,xy}$. The direction of motion is always positive in z, but random in xy. After ions pass a certain distance in the ion guide, they are detected on an imaginary detector electrode. Ions are considered lost either when they impinge on an ion guide electrode, or exit the simulation volume. By definition, transmitted ions are those that reach the detector.

To make simulations more realistic, also Coulomb interaction between ions can be taken into account. The built-in factor repulsion approach of SIMION is used to simulate space charge effects by a super-particle approximation and limit computational effort at an acceptable level. In terms of Coulomb interaction, every ion is considered a point charge consisting of an elevated number of charges $k \cdot q$, where k is the so-called repulsion factor. Therefore, the interaction originating from such a super ion approximates the presence of k ions (typically few thousand). This approximation is necessary to reduce required computational power for larger many body problems. The computation of the actual field is dominant in time consumption for small numbers of ions. With increasing amounts of ions, the number of Coulomb interactions increases quadratic, whereas the effort for field calculation stays constant and the time for trajectory calculation increases linearly. Thus the user has to chose a subtle trade-off, to keep k reasonably low as a high value leads to wrong, granular positioning of space charge, whereas low numbers of ions leads to bad statistics and high numbers of ions to extensive computational time. Note, that the ion charge is exclusively magnified with the repulsion factor k when considering the Coulomb interaction between the ensemble of charged particles in order to investigate space charge effects. When calculating the forces from the electric field of the electrodes, each particle is considered a single ion.

To acquire a meaningful set of data, the user program is designed to start a continuous ion beam with a certain set of ion guide parameters until the first ions reach the aforementioned detector. Depending on the time it took the ions, a suitable log-time is calculated, in which data is recorded from the ion beam. If no ion is left in the simulation volume or no ion reaches the detector in a predefined time-frame, the transmission T of the ion guide is considered to be negligibly small and the simulation is aborted.

4.2. Workflow with SIMION

As a first example, the work-flow and results of a rather standard simulation are described. The goal of this subsection is to give the reader an impression of how the simulations work and where potential pitfalls may interfere.
Before starting any simulation, it is crucial to recap the exact geometry of the simulated ion guide. For this example, the smallest operational higher order multipole in the ES-CIBD device was modelled. It has an inscribed radius of about $r_i = 0.82\,\mathrm{mm}$ and consists of $N = 8$ electrode pairs. For simulation, we chose the electrodes to be of length $l = 160\,\mathrm{mm}$. The electrode radius to approximate a multipole field using cylindrical electrodes is given by $r_e = r_i/(N-1) \approx 0.117\,\mathrm{mm}$ [132]. The resulting wire diameter of about $0.22\,\mathrm{mm}$ is bigger than the wires used in SWIG 1 of the ES-CIBD (about $0.18\,\mathrm{mm}$, see section 3.4). Nevertheless this larger diameter was chosen for simulations to be compatible with theory. The simulation volume was limited by a box of $2\,\mathrm{mm} \times 2\,\mathrm{mm} \times 160\,\mathrm{mm}$. The resulting potential array was calculated with a resolution of $600\,\mathrm{grid\ units/mm}$ in x and y direction and $0.15\,\mathrm{grid\ units/mm}$ in z-direction, corresponding to PA files with an overall size of about $5\,\mathrm{GB}$.
For standard multipole simulations, the injection disk and the detector are placed with a distance of $150\,\mathrm{mm}$. Both were located $5\,\mathrm{mm}$ towards the center with respect to the ends of the multipole electrodes to guarantee for a homogeneous field. The effective length, in which ions needed to pass the multipole therefore is also $150\,\mathrm{mm}$. The ions started from a disk of $r_{inject} = 0.9\,r_i$ and were equipped with $E_{kin,xy} = 1\,\mathrm{eV}$ of kinetic energy in xy plane and $E_{kin,z} = 10\,\mathrm{eV}$ in positive z-direction. Space charge effects were deemed negligible low unless otherwise noted.
For illustrative purposes, a set of typical results of a simulation is plotted in Figure 4.2. The driving RF frequency $f = 5\,\mathrm{MHz}$ and amplitude $U_{RF} = 16\,\mathrm{V}$ were chosen in such a way, that an absolute transmission of about $T \approx 50\,\%$ was reached for our standard

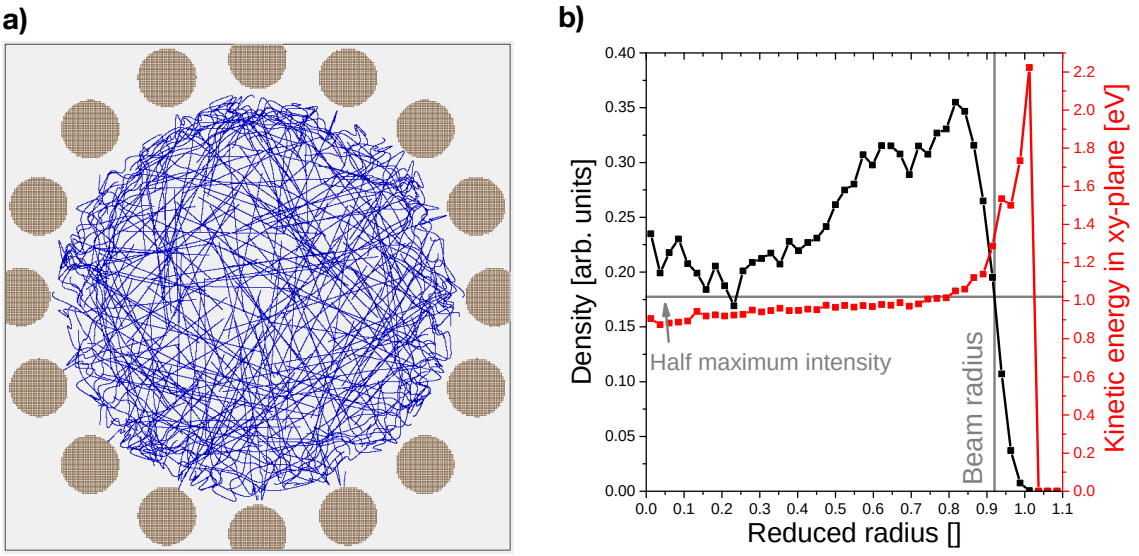

Figure 4.2.: Ion trajectory simulation results of an ion beam in a hexadecapole (16-pole). A cut-through in xy-plane of the electrodes (hatched areas) and some ion trajectories (blue lines) are depicted in a). b) shows a plot of the radial density distribution and the radial energy distribution of the beam at the exit of the 16-pole. The half maximum intensity and the corresponding ion beam radius are depicted in grey (see section 4.3.2)

test ion, Rhodamine B (m/z = 443 Th). The top left image shows a cross section of the multipole in xy-plane. The blue lines indicate trajectories of single ions in the ion guide's volume and the hatched areas indicate its electrodes. The simulation space is limited by the quadratic box. The ions show smooth and rather linear trajectories in the center of the ion guide and oscillatory motion close to the electrodes. This behaviour is a consequence of the multipole field's short penetration depth and the resulting almost field-free center (see also subsection 2.2.1). Qualitatively, all ion trajectories follow the same cycle:
An ion moving in the center region follows a rather linear trajectory due to weak fields. Once approaching an electrode, the ion's motions starts to get influenced by the oscillating electric field. In case of an ion approaching from closely to the center of the multipole towards an electrode, the ion starts to oscillate forth and back with respect to the electrode. The influence of neighbouring electrodes cancel each other and the ion is typically guided towards the center region. In case of an ion approaching in a gap, the oscillation happens between neighbouring electrodes. After a few oscillations, the ion is reflected backwards towards the center region, but the angle of the reflection is rather randomly distributed. In both cases, the oscillatory motion between the electrodes is the reason for the effective

trapping potential that confines the ions in the multipole (see section 2.2). During a simulation, an ion is considered lost due to impinging on an electrode or exiting the ion guide between two electrodes instead of being reflected. For the particular case of Figure 4.2a, impinging on electrodes is the dominant loss process.
The above described movement is true for well chosen parameters, where the mass and charge of the ion and its kinetic energy allow for trapping via the applied RF signal on the electrodes. On the one hand, much higher RF amplitudes, low RF frequencies, or low ion masses promote imping of ions on electrodes by too slow polarity changes of the RF signal. On the other hand, very low RF amplitudes, inappropriately high RF frequencies, or elevated ion masses lead to a strongly reduced oscillatory component of the ion trajectory, thus almost independent of the ion guide's field. Ions are not reflected backwards to the center of the ion guide and continue their path either towards an electrode or leave the ion guide volume in between the electrodes. For good confinement and transmission of charged particles, the RF parameters need to be carefully tuned corresponding to the ion's mass, charge, and kinetic energy.
Therefore, it is interesting to have a look at the radially resolved features of the ion beam. Figure 4.2b depicts a plot of the ion beam density distribution and the kinetic energies in xy-plane versus the ion's radial position in the beam. In this context, the ion beam density is defined as the number of ions per surface element of the starting disk or the detector. Please note that all ions contributing to the distribution of Figure 4.2b have already been reflected about 30 times by the oscillatory field prior to their detection, i.e. the majority of ions in the beam preserved their initial kinetic energy in xy-direction despite their their numerous interactions with the multipole field. The number of reflections may be approximated by $n = \sqrt{\frac{E_{kin,xy}}{E_{kin,z}}} \cdot \frac{l}{d}$ with the ion's kinetic energies in xy- and z-plane ($E_{kin,xy} = 1\,\mathrm{eV}$, $E_{kin,z} = 10\,\mathrm{eV}$), the length in z direction $l = 150\,\mathrm{mm}$ and the diameter of the multipole $d = 2r_i = 1.64\,\mathrm{mm}$.
The two grey lines in Figure 4.2b indicate the half maximum density of the radial beam distribution and the corresponding ion beam radius. in this thesis, all simulated ion beam radii originate from the half maximum width of the density distribution at the exit of the ion guide. The beam radius is discussed in more detail below and in section 4.3.2.
When performing ion trajectory simulations, it is always important to search for possible sources of artefacts. One of the main candidates of the above mentioned type of simulations is the generation of the beam. The ions are "born" randomly distributed on a disk, which is typically not the natural distribution of ions inside a multipole. Furthermore, they are placed at a certain radial position and velocity in the field of the ion guide. This

is of minor importance when being ”born” in the field free center region, but close to the electrodes, ions follow a typical oscillation in the RF field (see Figure 4.2a), meaning that their motion is in a certain phase correlation with respect to the RF signal. An ion with, e.g., an opposing direction of motion, or a too close position to a certain electrode at the moment of birth with respect to the typical oscillation will have an atypical trajectory. Poorly injected ions may gain kinetic energy in the xy-plane or may be lost in near future. Nevertheless, these artefacts seem not to be dominant effects for the investigations presented in the following.

4.3. Comparing multipole simulations with theory

To provide evidence for the simulation’s validity, a first attempt to compare their results with the theory from section 2.2.1 was performed in this thesis. As a first example, the transmission spectrum of a higher order multipole is depicted in Figure 4.3. On the left-hand side, the transmission efficiency of a 16-pole, operated at a RF frequency $f = 6\,\mathrm{MHz}$ is plotted in black against different RF amplitudes U_{RF}. Starting at the lower end of the scale, transmission efficiency steeply increases with RF amplitude until a peak is reached followed by a less steep decay. Please note that at elevated frequencies the peak widens to a plateau at transmission efficiency close to unity. The red curve in the plot represents the corresponding analytically derived effective trapping potential V^* from equation (23). Intuitively, one might expect a more step like transmission function with high efficiencies for high trapping potentials $V^* > E_{kin,xy}/q$ and no transmission otherwise. Actually, the transmission curve shows a rather smooth behaviour, especially the falling edge for higher amplitudes. However, both curves, transmission, and trapping potential qualitatively follow the same trends and share approximately the same peak amplitude.
For the following argumentation it is worth discussing the possible ion motion in a multipole first. Figure 4.3c shows a sketch of all possible types of ion trajectories. The size of the ion guide is indicated by the inscribed radius r_i and the black circle. The first type of ion motion is indicated in red and represents a circular trajectory of constant radius. Here, all kinetic energy of the ion in xy-plane is stored in an angular motion and the trapping potential of the ion guide has to compensate the centrifugal forces in order to keep ions confined. The second type of motion is indicated by the blue dotted line. The motion of the ion is exclusively in radial direction. The green line indicates a more realistic intermediate case.

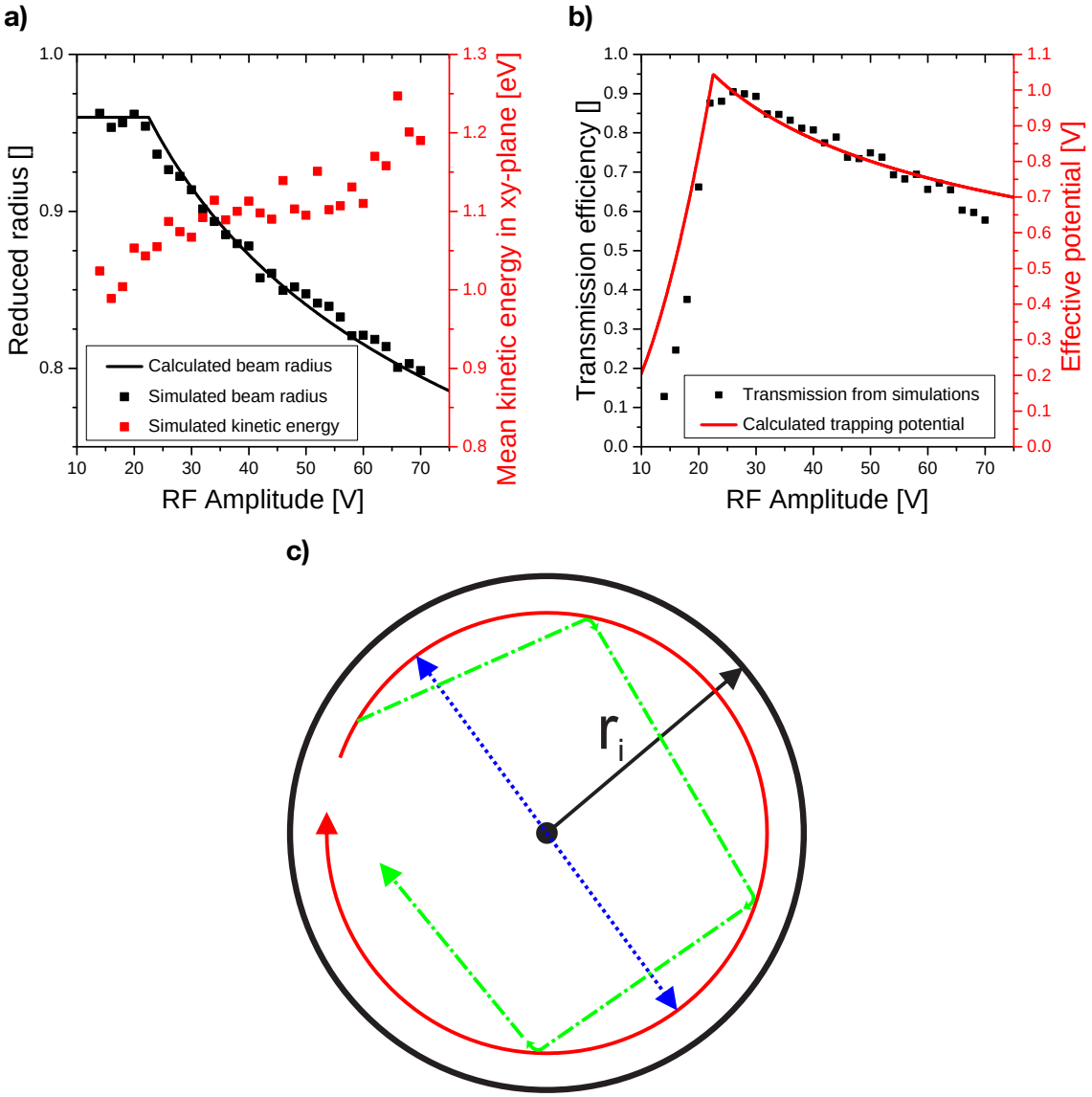

Figure 4.3.: Simulated and theoretically derived ion beam properties of a 16-pole, operated with a sine-shaped RF signal at 6 MHz. a) shows the evolution of transmission efficiency with increasing amplitude (black) and the corresponding theoretically derived trapping potential (red). Both follow the same trend of a steep increase with a peak at medium amplitude and a subsequent smooth decay. b) depicts good agreement between the simulated and theoretically derived ion beam diameters (black) and the evolution of the kinetic energy in xy-plane (red).

An important aspect is the influence of the type of motion on its capabilities to be trapped by the effective potential of a multipole. In the following a charged particle of mass m, charge q, and energy E moves in an electrostatic 2D (ignoring the z-component) pseudo potential of the form $V^*(r) = c \cdot r^n$ (simplified from equation (19)). The two limiting cases of purely radial and circular motion are discussed. For a particle starting in the center of the potential with solely radial velocity component (blue trajectory in Figure 4.3c), the energy is stored either as kinetic energy in the field free center or in potential energy at the turning point. The particle reaches a maximum radius r_m in the potential when its kinetic energy is zero

$$E/q = V^*(r_m) = c \cdot r_m^n \quad \text{and} \quad r_m = \sqrt[n]{\frac{E}{q \cdot c}} \tag{45}$$

For the second case of a charged particle with a circular motion (red trajectory in Figure 4.3c), the repelling forces of the potential $F_{pot}(r_m)$ have to compensate for the centrifugal forces $F_c(r_m)$.

$$F_c(r_m) = -F_{pot}(r_m) \tag{46}$$

$$\text{with} \quad F_{pot}(r_m) = q \cdot E(r_m) = q \cdot -\frac{dV^*}{dr}(r_m) = -q \cdot c \cdot n \cdot r_m^{n-1} \tag{47}$$

In case of purely circular motion on a radius r_m, the energy E of the particle distributes on a constant kinetic component E_{kin} due to its velocity v on the circular trajectory and a constant potential energy component E_{pot} due to its position in potential at radius r_m.

$$E = E_{kin} + E_{pot} \quad \text{with} \quad E_{kin} = 1/2\, mv^2 \quad \text{and} \quad E_{pot} = q \cdot c \cdot r_m^n \tag{48}$$

With aid of equation (48), the centrifugal force can be described by:

$$F_c(r_m) = \frac{m \cdot v^2}{r_m} = \frac{2\,(E - q \cdot c \cdot r_m^n)}{r_m} \tag{49}$$

Insertion of equation (49) and equation (47) in equation (46) relates the radius of the circular motion r_m with the energy of the charged particle E.

$$\text{circular motion: } r_m = \sqrt[n]{\frac{2}{n} \cdot \frac{E}{q \cdot c} - \frac{2 \cdot r_m^n}{n}} \tag{50}$$

The form of equation (50) was chosen for simple comparison with its counterpart from radial motion (see equation (45)).

$$\text{radial motion: } r_m = \sqrt[n]{\frac{E}{q \cdot c}} \tag{51}$$

Please note that the radius r_m is always positive and n is a positive integer value of $n = 2$ for a quadrupole, $n = 4$ for a hexapole, $n = 6$ for a octopole, and so on. Thus, the radius of circular motion is always smaller than the maximum radius of the radial motion. For $n = 2$ the first term of the circular case equals the radial case but is reduced by a positive number. For $n > 2$ the first therm is already smaller compared to the radial motion case and gets further reduced by another positive component. In conclusion, an ion with circular motion reaches lower radii in the effective trapping potential of multipole and therefore gets confined for lower potential heights.

Coming back to the transmission efficiency in Figure 4.3a, values close to unity happens when the effective trapping potential is capable to confine all possible ion motions ($V^* \cdot q > E$). The angular component of motion is one explanation for the smooth decay of the transmission curve for lower effective trapping potentials ($V^* \cdot q < E$). With decreasing potential height, more and more trajectories, especially with mainly radial motion are not confined any more and transmission efficiency decays. Apparently, the relation between effective potential depth and transmission efficiency is rather complicated.

A better parameter to compare the agreement between theory and simulations might therefore be the ion beam radius from Figure 4.3b. The black data points represent the simulations, while the solid black line is the theoretically derived value for the trapping radius r_{trap} (see section 2.2.1). The data points for the simulated radius originate from the half maximum of the radially resolved density distribution at the exit of the multipole (see Figure 4.2b). The parameters limiting the trapping radius r_{trap} are the maximum allowed ion beam radius $r_{max} = 0.96 r_i$ (horizontal section of the solid black line in Figure 4.3b) and the maximum allowed radius for adiabatic motion $r_{adiabatic}$ with the adiabaticity parameter $\eta = 0.45$ (see equation (21), decreasing section of the solid black line in Figure 4.3b).

The values of r_{max} and η originate from table 4.1. Theory and simulation show rather good agreement. A more detailed discussion of the relevance of the ion beam radius can be found below in section 4.3.2.
The red data points in Figure 4.3b show the mean kinetic energy of ions at the multipole exit. For low amplitudes, ions with rather low kinetic energies are preferably transmitted by the multipole. With increasing amplitude, the mean kinetic energy in xy plane of transmitted ions is slightly above the injection value of $1\,\mathrm{eV}$. The slight increase of kinetic energy at least partly originates from the way of ion generation (see discussion above). Therefore, no significant gain of kinetic energy from the RF field is observable for transmitted ions of the displayed set of simulations.

4.3.1. Transmission

Starting from such a simulation, the influence of all kinds of parameters on the properties of the ion guide may be investigated. Most importantly, we are interested in its transmission efficiencies and the properties of the ion beam at the exit. For this purpose, simulations with multipoles of different order $N = 4,\ 6,\ 8$ but equal inscribed diameter $r_i = 0.82\,\mathrm{mm}$ were compared. All multipoles employ cylindrical electrodes with an electrode radius of $r_e = r_i/(N-1)$ [132] to approximate an ideal multipole field geometry. Furthermore, all multipoles were supplied with ions of equal injection parameters $r_{inject} = 0.9\,r_i$, $E_{kin,xy} = 1\,\mathrm{eV}$, $E_{kin,z} = 10\,\mathrm{eV}$. Each multipole geometry was investigated for a set of suitable RF frequencies Ω and amplitudes U_{RF} in order to show the full spectrum from very low transmission up to a broad plateau of high transmission, respectively.

Figure 4.4 depicts the resulting transmission spectra. The RF amplitude range and colour of all heat-maps were chosen equally for a comparable representation. The frequency range was adapted for each multipole order to generate a comparable range of transmissions. The first thing to mention is that the maximum absolute transmission increases with the order of the multipole. This effect is most probably an artefact from the process of ion generation (see above). The field of the electrodes of lower order multipoles have a much larger penetration depth towards its center. Ions starting from the outer rim of the starting disk are ”born” into a higher potential but with the same kinetic energy. The resulting sum energy may be higher, which makes their transmission much less likely. Higher order multipoles have a larger quasi field-free center, resulting in a larger spatial acceptance (see also section 2.2.1).

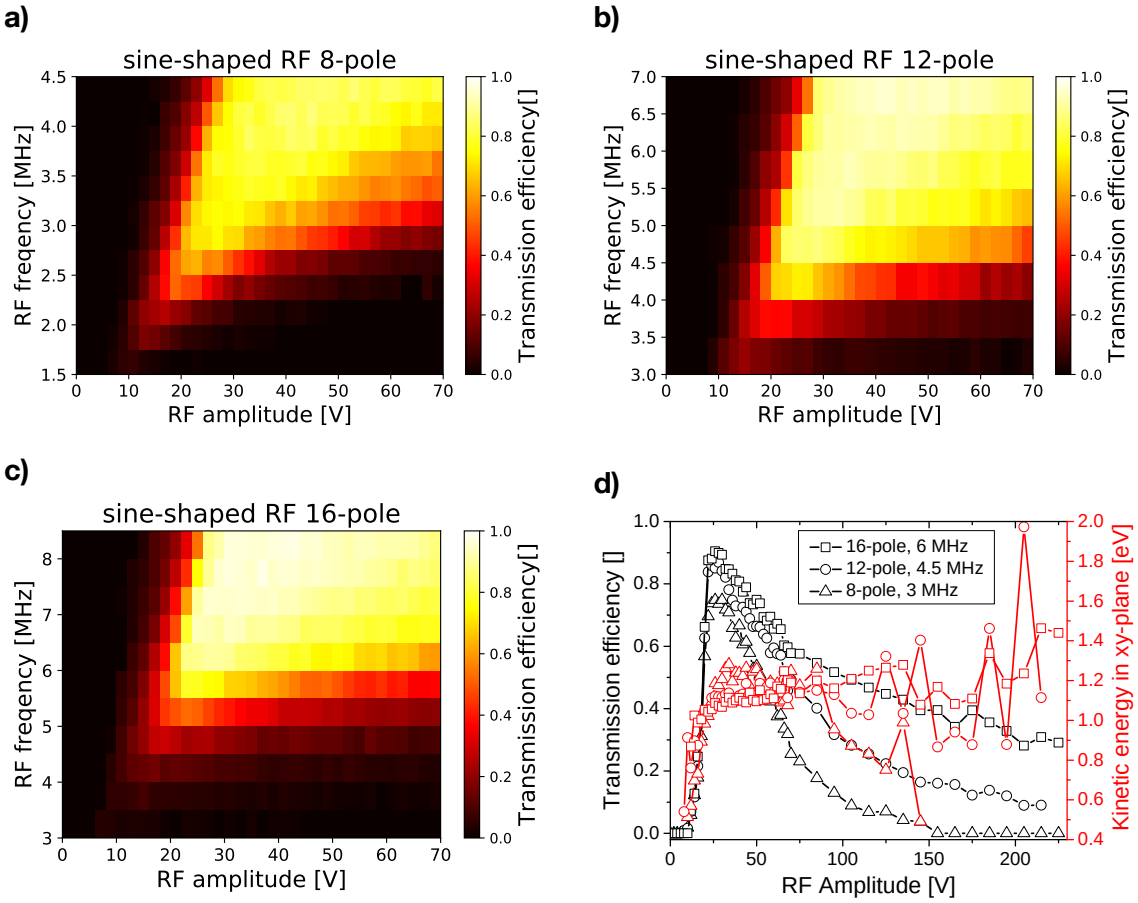

Figure 4.4.: Comparison of simulated transmission properties of a variety of multipoles operated with sine-shaped RF signal (see Figure 4.8 for square-wave signals). a)-c) transmission heat-maps of equal amplitude and colour code but adjusted frequency range for different multipole orders. The position of the rising edge of transmission is proportional to the RF frequency but its shape is independent of the multipole order whilst the following decay is faster for lower order multipoles. The higher amplitude spectra in d) confirms this result and additionally depicts the evolution of the ions mean kinetic energy in the xy-plane.

To gain further insight, it is worth discussing the shape of the transmission curves. The location of the steep increase in transmission shifts in position with a linear dependency between RF amplitude and frequency and also shares a comparable shape for all multipole orders. This effect may be supported by equation 23, when assuming for simplicity, that the transmission follows the same trends as the theoretically derived trapping potential V^*. The height of the potential depends on the fraction of U_{RF}/Ω and the shape of the piecewise-defined function is independent of the order of the multipole for $r_{max} < r_{adiabatic}$. This condition is valid for RF amplitudes in the rising edge of the transmission efficiency below its maximum. As already discussed above and in section 2.2.1, one would expect maximum transmission exactly when U_{RF} is chosen such, that $r_{max} = r_{adiabatic}$. The second part of the piecewise-defined trapping potential V^* describes the behaviour for elevated RF amplitudes (or in other words $r_{max} > r_{adiabatic}$) and scales with $U_{RF}^{-\frac{2}{N-2}}$. In simpler terms, for lower order multipoles, one would expect a faster decrease in transmission for increasing RF amplitudes beyond its peak intensity. This is in fact the case when comparing the spectra of different multipole orders for amplitudes above their peak transmission. For 16-poles, the amplitude range of high transmission widens up much faster with increasing frequency and the subsequent reduction in transmission with increasing amplitudes is much smoother when comparing it for example to the 8-pole.

The curves of Figure 4.4d compare the behaviour of different multipole orders for a larger amplitude range. The black and red curves represent the evolution of transmission efficiency and kinetic energy in xy-plane, respectively. Squared data points originate from a 16-pole, circles from a 12-pole and triangles from an 8-pole. The different frequencies were chosen just high enough to reach peak transmissions close to unity without forming a broad plateau of high transmission. The rising edges of the transmission at low amplitudes are quite similar for all mulitpole orders, but the following decay is much faster for lower order multipoles, although peak transmissions are about the same height and located at comparable amplitudes. The red curves indicating the mean kinetic energies in xy-plane show no significant increase for high amplitudes. The data at the rising edges of the transmission curves, as well as the data from the 8-pole with poor transmission in the range between $100 - 150\,\mathrm{V}$ RF amplitude shows preferred transmission of ions with lower kinetic energy in xy-plane.

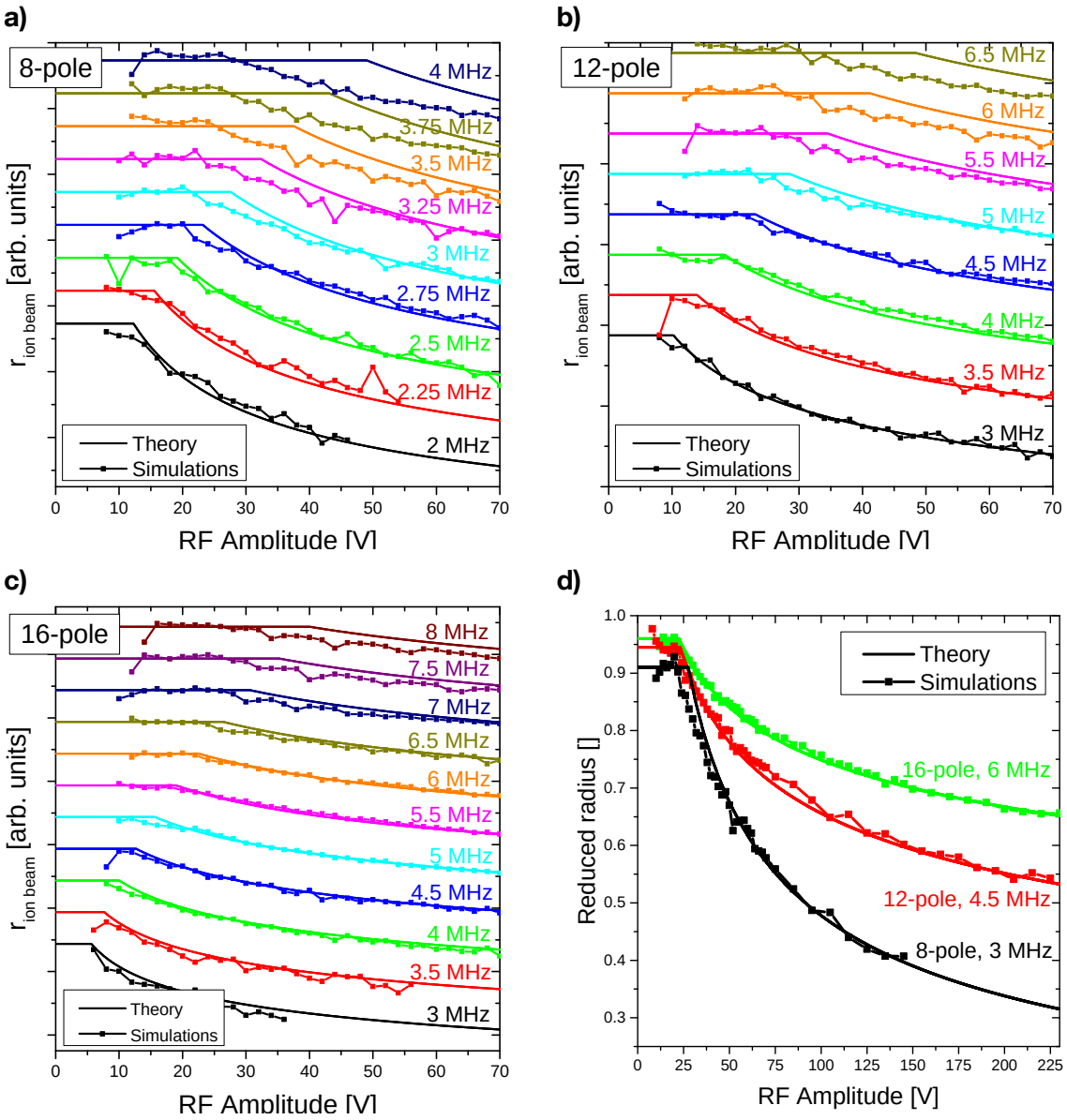

Figure 4.5.: Ion beam radii for various multipole orders, RF amplitudes, and frequencies. The data points connected with lines represent the simulated ion beam radii at the exit of a multipole. The theoretical derived trapping radius r_{trap} discussed in section 2.2.1 is depicted by the solid lines. Maximum allowed radius and adiabaticity parameters can be found in Table 4.1.

parameters of r_{trap}	$N = 4$	$N = 6$	$N = 8$
maximum allowed radius r_{max}	0.91 r_i	0.945 r_i	0.96 r_i
adiabaticity parameter η	0.5	0.45	0.45

Table 4.1.: Maximum allowed radius of ion motion and adiabaticity parameter derived from simulated data of the ion beam radii in Figure 4.5 using the analytical theory of section 2.2.1.

4.3.2. Ion beam radius

In subsection 2.2.1 the properties of linear multipole ion guides are described with an analytical theory. Most importantly, a maximum effective trapping potential V^* was derived in equation (23) that is dependent on the multipole parameters and limited by the maximum allowed trapping radius r_{trap}. The arguments behind the limitation of allowed radial positions are a maximum overall radius r_{max}, that still allows for oscillations of the ions between the electrodes, and a maximum radius $r_{adiabatic}$ for which adiabatic motion of the ion is ensured. In this framework, non-adiabatic motion means, that the ion beam successively gains kinetic energy from the ion guide's RF field and therefore shows strongly increasing kinetic energies in xy-plane after being transmitted through the ion guide. In analytical theory, the limit for adiabatic motion is described by the adiabaticity parameter η (see equation (20)).

A rather interesting comparison between theory and simulations is the test for the different regimes of said trapping radius r_{trap}. To gain some information, the properties of the beam at the exit of the ion guide was investigated and compared to the theory. The ion beam radius is derived from the density distribution of the ion beam at the exit and was defined as the half maximum beam density radius (see Figure 4.2b). For simulation parameters with intermediate transmission efficiencies $0 < T < 1$, ions from the boundaries of the distribution are successively lost by impinging on the electrodes, or exiting the ion guide between electrodes (see section 4.2). For such a medium transmission case, the resulting ion beam radius should be limited by the maximum trapping radius $r_{ionbeam} \approx r_{trap}$. We assume, that ions with trajectories close to or exceeding r_{trap} continuously contribute to the loss processes, others may be transmitted. Evidence for this might also be found in the radial kinetic energy distribution, e.g. in Figure 4.2b, where exclusively the outermost ions show strongly elevated kinetic energies in xy-plane, which might indicate their loss in the near future.

To gain some evidence supporting the aforementioned standpoints, the resulting ion beam radii $r_{ionbeam}$ from the ion trajectory simulations are plotted against the theoretically derived trapping radius r_{trap} in Figure 4.5. The solid lines indicate the theoretically derived values for r_{trap} and the data points are the corresponding values from a simulation. During horizontal sections, the trapping radius is limited by the maximum allowed radius $r_{trap} = r_{max}$. In the sloping sections, it is limited by adiabatic motion $r_{trap} = r_{adiabatic}$. Please note that the slope and boundary of $r_{adiabatic}$ depends on the multipole (see section 2.2.1). The lower end of the tested frequency range is limited by poor transmission and therefore poor statistics of the ion beam distribution, while transmission at the upper end is already close to unity for a rather wide amplitude range. The corresponding set of transmission efficiency data is depicted in Figure 4.4. The first information one could gain from the fitted data are the maximum allowed radius r_0 and the adiabaticity parameter η for each geometry (see Table 4.1). The maximum allowed radius r_{max} seems to increase with the order of the multipole, most probably due to the reduced penetration depth of the electric field, while the adiabaticity parameter η decreases.

The high amplitude data in Figure 4.5d gives an impression of the absolute ion beam radius compared to the inscribed radius of the multipole. Theory and simulation match quite well over the whole amplitude range for all investigated multipoles. Furthermore, it is worth mentioning, that the maximum allowed ion beam radius is generally larger for higher order multipoles when comparing frequencies of comparable peak transmission (see Figure 4.4d) which is one of the reasons for the better acceptance of injected ions.

For all simulations with frequencies on the lower end of the chosen range, the data fits quite well with the theoretical predictions. For high frequencies, the simulated ion beam radius is lower than the trapping radius at amplitudes close to the boundary condition, where $r_{trap} = r_{max} = r_{adiabatic}$. This specific amplitude was described as $U_{RF,max}$ in the theoretical section 2.2.1 (equation (24)) and indicates the amplitude, for which the maximum possible effective trapping potential V^*_{max} is reached. Therefore, the transmission efficiency of the multipole is expected maximal around this special amplitude and the condition of medium transmission is violated here at first.

The apparent compression of the ion beam in proximity of the kink of the fitting at elevated frequencies observed in Figure 4.5 indicates a third limit for the ion beam radius. At certain RF frequencies and amplitudes, the effective trapping potential becomes large enough to trap all charged particles and furthermore compress their trajectories to smaller radii due to the strong repulsion from the electrodes. The ion beam radius is thus additionally limited by a maximum reachable radius in the effective trapping potential r_{pot}. This limitation

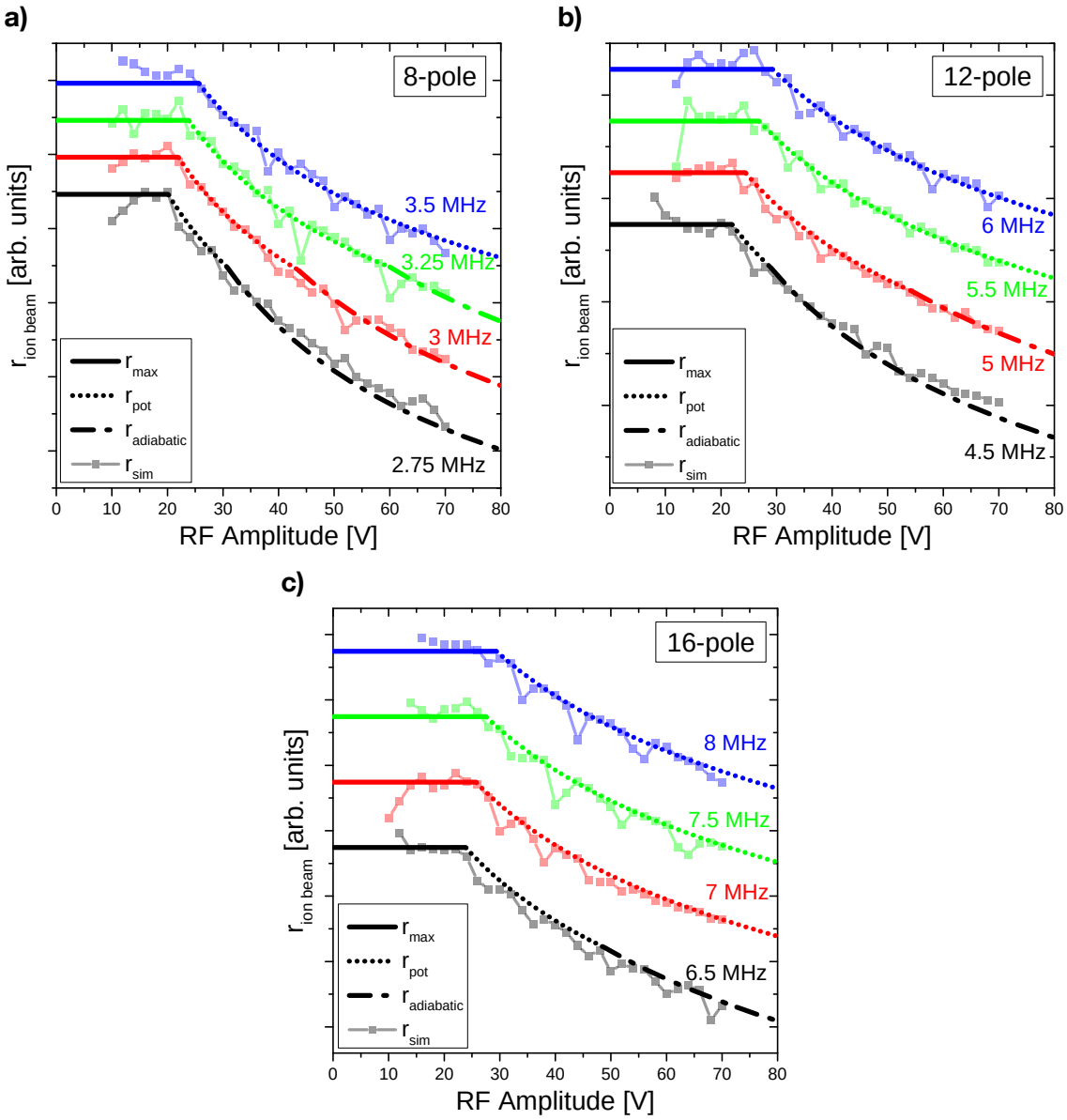

Figure 4.6.: Ion beam radii from simulations and theory for high frequencies. Compared to Figure 4.5, the ion beam radius was limited additionally by the depth of the trapping potential in the dotted section by r_{pot}.

originates from the finite kinetic energy of the ions in radial direction $E_{kin,r}$ in a large effective trapping potential. Following the previous argumentation of possible ion motions (see Figure 4.3c and the following discussion) the maximum reachable radius in this limit is reached when the maximum kinetic energy of the ion in radial direction equals the effective trapping potential times the charge of the particle $E_{kin,r} = V^*(r_{pot}) \cdot q$. Thus, the ion beam radius can be described by a minimum function $r_{ionbeam} = Min(r_{max}, r_{adiabatic}, r_{pot})$. A set of of elevated frequency data as shown in Figure 4.5 was fitted with the above mentioned additional limitations of the ion beam radius. The result is depicted in the graphs of Figure 4.6, showing a set of transmission spectra for all three multipole orders with sections of $V^*(r_{pot}) \cdot q > E_{kin,xy}$. Therefore, the ion beam radius $r_{ionbeam}$ is at least partially limited by r_{pot}. In contrast to Figure 4.5 the fitting curve now consists of three sections. The maximum allowed radius r_{max} limited section (solid line), the trapping potential r_{pot} limited section (dotted line), and the adiabatic motion $r_{adiabatic}$ limited section (dashed and dotted line). Best fitting of all curves was reached for effective kinetic energies in radial direction of about $E_{kin,r} \approx 1\,\mathrm{eV}$. This result seems to be rather meaningful, as this energy corresponds to the initial energy in xy-plane during the injection of ions and the motion is assumed to be adiabatic for such operation parameters.
With this approach, it becomes possible to almost perfectly match the simulated ion beam radius with the theoretically predicted ones over the whole range of amplitudes, frequencies, and multipole orders.

4.3.3. Discrepancies between theory and simulations

Besides all the similarities between simulations and theoretical description, there are still some effects that have not been predicted. First of all, one of the main ingredients for the theoretical treatment is the adiabaticity, which states no energy transfer between the RF field and ion motion. From the standpoint of simulations, this is not entirely true. In Figure 4.3b and 4.5d, for ion guide settings with low RF amplitude, we can observe that the mean kinetic energy in xy-plane of transmitted particles is below their injection values. For such conditions, the transmission of low energy ions is strongly preferred over those with higher energy. On the other hand, ions with strongly increased kinetic energy can also be found, especially for high RF amplitudes. However, for parameters with reasonable transmission efficiencies and moderate RF amplitudes close to the peak transmission efficiency, the mean kinetic energy seems to be more or less constant and adiabaticity for the ensemble of ions is confirmed in the framework of the current simulations.

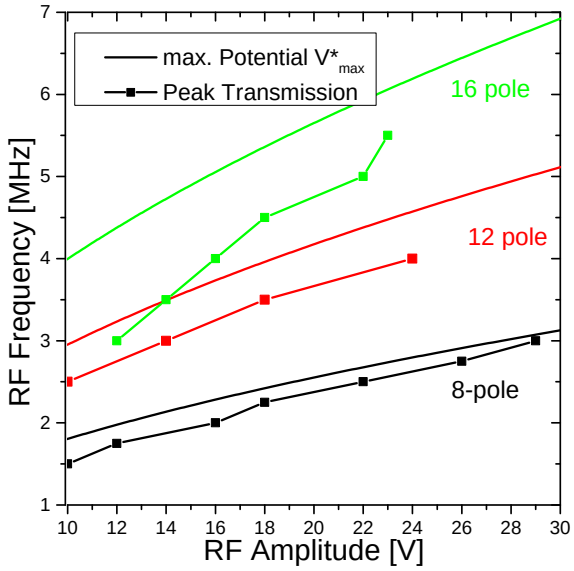

Figure 4.7.: Comparison between the peak position of the theoretically derived maximum effective trapping potential V^*_{max} from equation 25 (solid line) and the positions of peak transmission efficiency from simulations (data points). The reason for the offset between both is unknown so far.

Furthermore, one could argue about the smeared out transmission spectra. From the standpoint of theoretical description, one would expect something more like a sharp step function, where the transmission jumps from zero to unity as soon as the radial kinetic energy exceeds the product of effective trapping potential times ion charge. Most possibly, the rather undefined reflection angle of an ion from the potential walls (see also [132]) and the resulting variety of possible motions (see Figure 4.3c) allow for some margin of effective radial kinetic energy and smeared out transmission spectra, especially for finite residence times of ions in the ion guide. For future investigations of this hypotheses, it is necessary to record and evaluate the motion of ions more precisely, especially its splitting into radial and circular motion components.

Another mismatch between simulations and theory may be found in the exact position of the transmission peaks. For most of the transmission spectra of Figure 4.4, the peak transmission does not exactly match with the maximum effective trapping potential V^*_{max} from theory. Figure 4.7 depicts V^*_{max} as solid lines and the actually simulated peak transmissions as dotted lines. The simulated peak positions seem to follow the trend of V^*_{max}, but are shifted upwards by a few volts in amplitude. The reason for this is still unclear and needs to be investigated in future works, too.

4.3.4. Sine-shaped and square-wave RF signals

All aforementioned theoretical discussions and simulations consider a sine-shaped RF signal. In reality, the RF signals of such systems are mostly realized via resonantly driven LC-circuits with fixed RF frequency. Regarding the results from simulations, it appears that the operation frequency is a very important parameter for linear multipoles and it might be worth the effort making it accessible to the experimenter. This becomes even more important when considering the theory of section 2.2 for different types of ions with a broad range of mass-to-charge ratios. To gain equal maximum effective trapping potential V^*_{max} in equation 25 for variable mass m and charge q of ions, one could simply adjust the frequency Ω. From the view of electrical engineering, one of the most simple ways to generate an oscillating RF signal with variable frequency is to employ two switches, one to pull the output to an upper potential level, and one pulling it down to a lower potential value. The timing of the switching events can be easily controlled via a suitable driving circuit, making the resulting frequency of the signal tunable. The major difference in signals is a change from a sine-shaped wave in the resonant LC case to a square-wave in the digital case.

There are few publications addressing numerically calculated stability diagrams of a digitally operated QMS (see section 3.5), and especially higher order multipoles have not been discussed in literature. For this purpose, the properties of a square-wave driven multipole were investigated in this thesis using ion trajectory simulations and the results were compared with the sine-shaped case. The RF signal discussed in this section consists of a square-wave with equal residence time on the high and lower potential level, U_{high} and U_{low} respectively. Corresponding to the sine-shaped case, the difference between both potentials is given by twice the amplitude $U_{high} - U_{low} = 2U_{RF}$ and the periodicity is defined by the RF frequency Ω.

Figure 4.8 depicts the square-wave counterpart to the corresponding set of sine-shape simulations in Figure 4.4. The general form of the transmission curves, their peak values, and the kinetic energies are comparable to the sine-shaped case. The dominant difference between both wave forms is a compression of the transmission curve to lower amplitudes in the square-wave case, which is presented in more detail in Figure 4.8e. Here, the transmission curves of the higher amplitude data from Figures 4.4d and 4.8d are compared to each other. The solid lines with the solid triangles represent the square-wave case and the dotted lines with the hollow triangles represent the sine-shaped case. The peak transmissions and the general form is approximately identical, but the square-wave multipole's

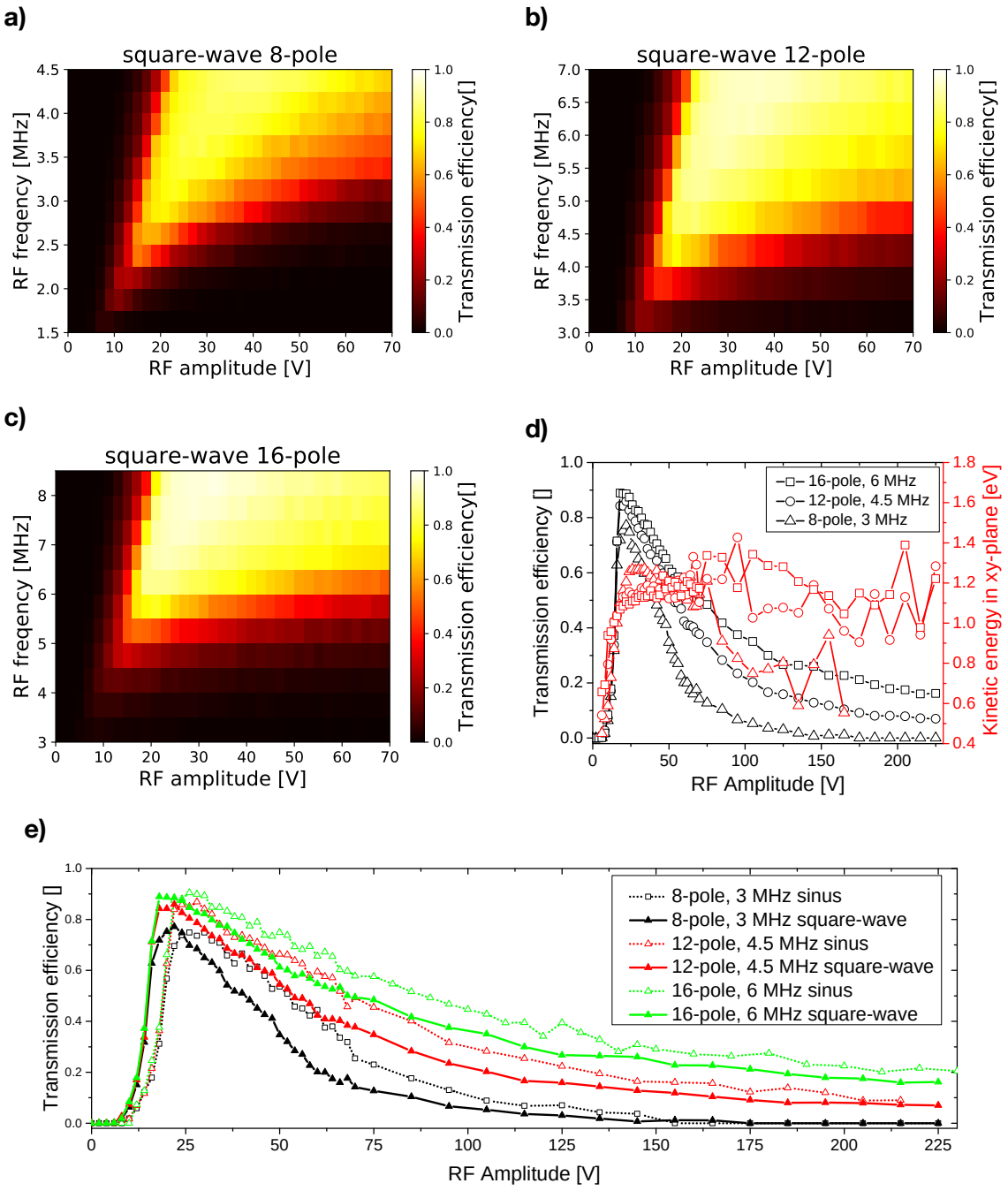

Figure 4.8.: Transmission properties of a variety of multipoles, operated with square-wave signals (see Figure 4.4 for sine-shaped equivalent). a)-c) transmission heat-maps of equal amplitude and colour code but adjusted frequency range for different multipole orders. d) transmission and kinetic energy in xy-plane for a larger amplitude range. e) shows a comparison of the square-wave high amplitude data with its sine-shaped counterpart from Figure 4.4. The most prominent difference between both is a compression to lower amplitudes in the square-wave case.

parameters of r_{trap}	$N = 4$	$N = 6$	$N = 8$
maximum allowed radius r_{max}	0.91 r_i	0.945 r_i	0.96 r_i
adiabaticity parameter η	0.4	0.37	0.35

Table 4.2.: Maximum allowed radius of ion motion and apparent adiabaticity parameter derived from simulated data of the ion beam radii of square-wave driven multipoles in Figure 4.5.

transmission curves appear to be at lower amplitude for each corresponding pair of simulations.

The strong similarities in the transmission properties lead to the assumption that application of qualitatively equal concepts for the analytical description of the square-wave and the sine-shaped case might be possible. Most importantly, it is assumed that the restrictions of the maximum allowed radius of trajectories via the overall maximum radius r_{max} and the maximum radius of adiabatic motion $r_{adiabatic}$ should be valid in both cases. In analogy to the sine-shaped case in Figure 4.5, Figure 4.9 depicts the ion beam radii for the square-wave counterpart. The data resembles one another and can be nicely described by the theory from the sine-shaped case with equal maximum allowed radius r_{max}, but about $20\,\%$ lower apparent adiabaticty parameter η in the square-wave case (see Table 4.1).

In analogy to section 4.3.2, the maximum allowed radius given by the height of the trapping potential may be introduced for the square-wave case, too. Due to a lack of an analytical description, the data will be interpreted again with the formulas derived for the sine-shaped case. The fitting of the elevated frequency data where r_{pot} becomes relevant is depicted in Figure 4.10. Good agreement was achieved with an apparent radial kinetic energy of the ions of $E_{kin,r} \approx 0.6\,\mathrm{eV}$. Besides that, the mismatch between the peak trapping potential and the calculated maximum trapping potential might also be found in the square-wave case.

Summarizing the observations so far, the transmission spectra of the square-wave multipoles in Figure 4.8e seem to be compressed to lower amplitudes compared to the sine-shaped ones, the apparent adiabaticity parameter of the digital multipoles are about $\eta_{digital} \approx 0.8\,\eta_{sine}$, and the apparent effective potential depth from the considerations with r_{pot} may be estimated to be $V^*_{digital} \approx 0.6\,V^*_{sine}$. Going one step backwards and recapitulating the formulas from the theoretical derivations of section 2.2.1 one might notice, that the adiabaticity parameter is proportional to the RF amplitude $\eta \propto U_{RF}$ (Equation 20) and the trapping potential is proportional to its square $V^* \propto U^2_{RF}$ (Equation 19). Therefore, the

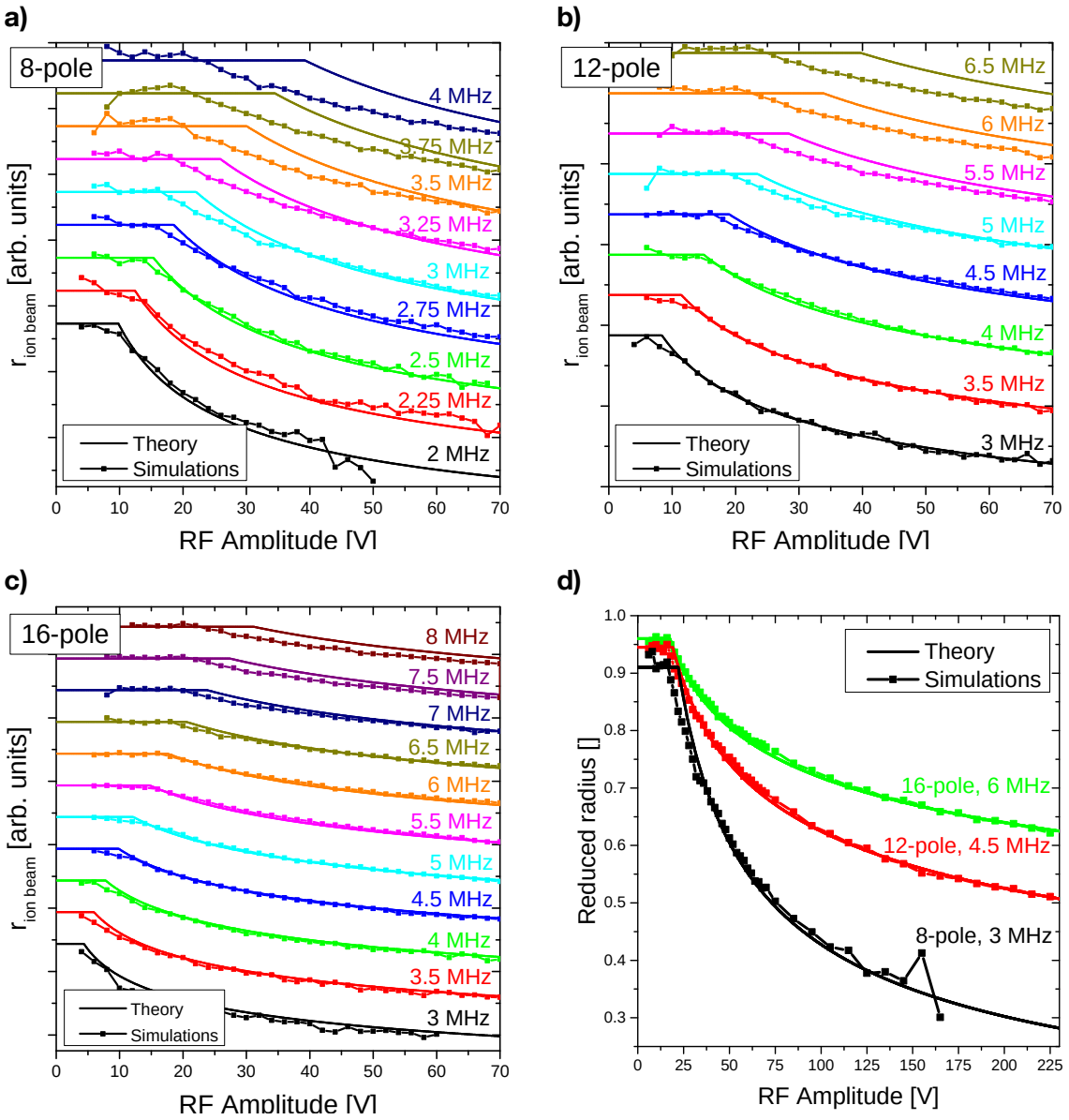

Figure 4.9.: Ion beam radii for various square-wave driven multipoles. The data point connected with lines represent the simulated ion beam radius at the exit of a multipole. The theoretical derived trapping radius r_{trap} discussed in section 2.2.1 is depicted by the solid lines. Parameters for r_{max} and η may be found in Table 4.2.

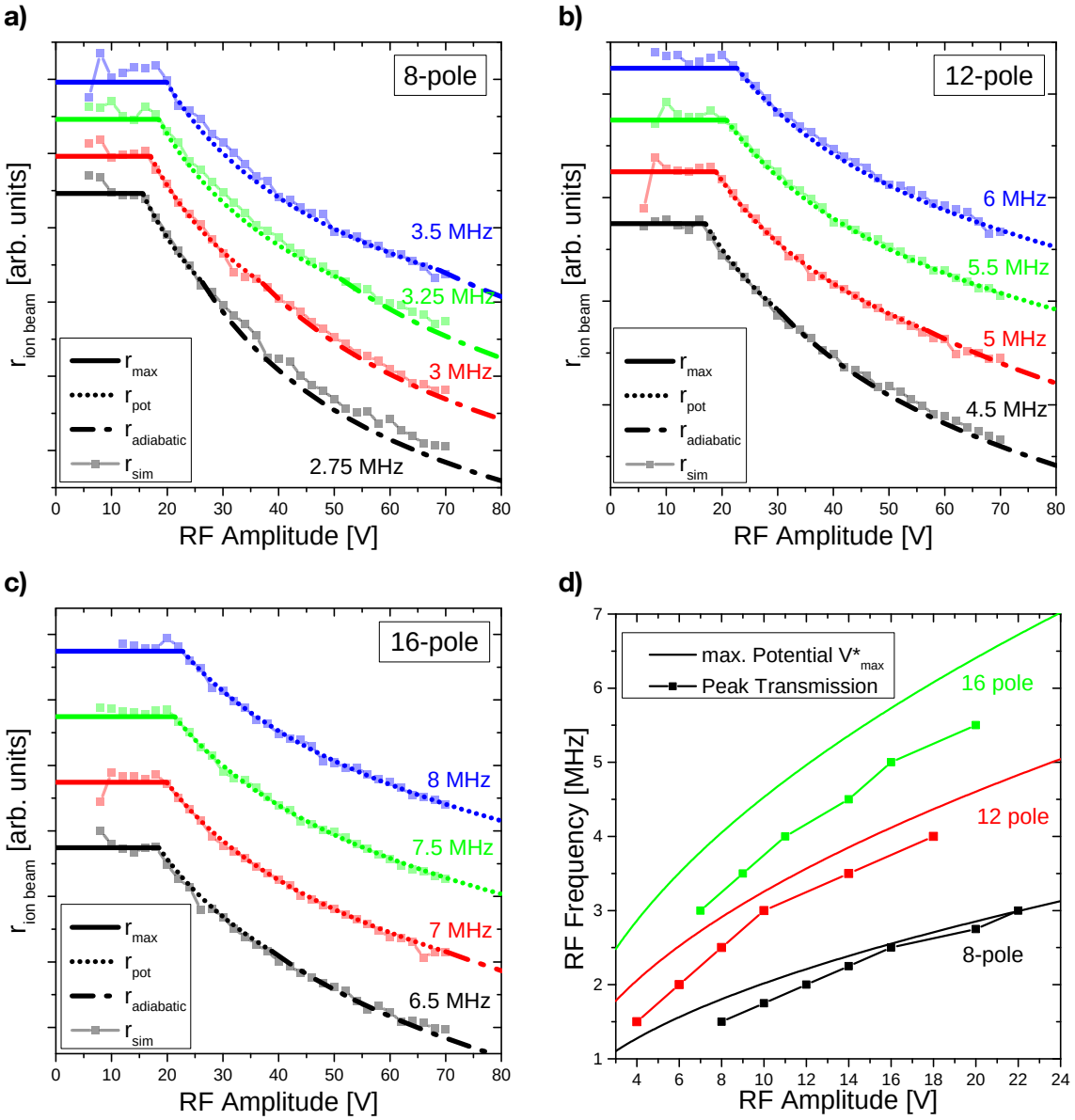

Figure 4.10.: a)-c)Ion beam radii from simulations and theoretically derived values for square-wave driven multipoles. d) depicts the mismatch between the simulated peak position and the calculated curve for the maximum trapping potential.

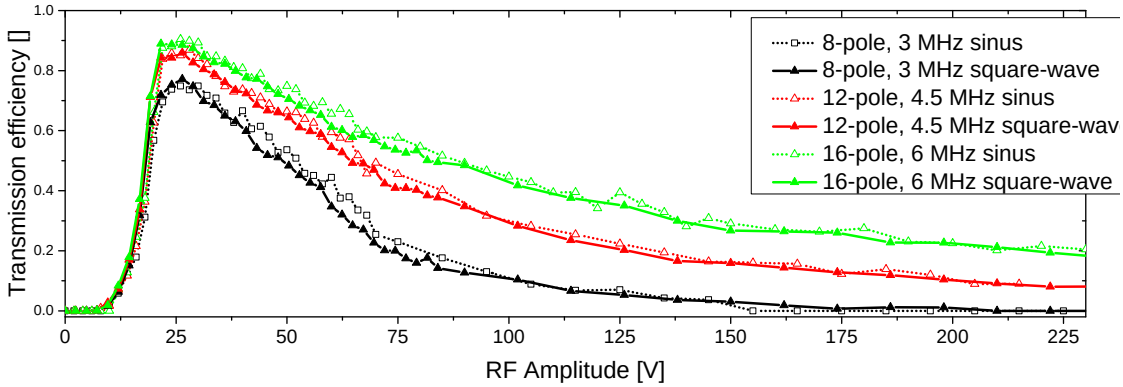

Figure 4.11.: Comparison of the higher amplitude spectra of the sine-shaped and the square-wave driven multipoles. The square-wave amplitude is rescaled by a factor of 0.8.

author suggests to describe the digital multipole with the same formalism as the sine-shaped one, but rescale the RF amplitude by an effective RF amplitude for the digital case $U_{RF,eff} \approx 0.8\, U_{RF}$. in the precision of the currently available data set, the effective RF amplitude approach would allow for explanation of all observed effects of the square-wave signal by the using the r_{max} and η parameters of the sine-shaped case. For illustration purposes, Figure 4.11 shows the comparison of the high amplitude data of sine-shaped and square-wave RF signal with rescaled effective amplitude. The agreement between transmission curves of the respective pairs of simulations strongly supports the validity of the effective amplitude approach.

Another hint may be provided by the theoretical description of the digital QMS (see section 3.5). Here, the significant points in the stability diagram, e.g. the apex of the first stability region, share about the same DC offset for sine-shaped and square-wave operation, but the RF amplitude is decreased in the square-wave case by a factor of about 0.78, which matches rather precisely our present findings.

Concluding the discussion, apart from the apparently necessary amplitude rescaling, no significant difference between sine-shaped and square-wave driven multipoles have been observed in this study. For further progress, it would be necessary to refine the data from simulations e.g. by longer integration times. Furthermore, a better understanding from an analytical point of view would most probably also be worth the effort. The main benefit of a square-wave signal is the tuneable RF frequency, which allows to operate the ion guides with moderate amplitudes for all possible m/z. Furthermore, small variations in the signal shape provide an interesting playground for further optimizations, e.g. in the case of a

digital quadrupole mass spectrometer (see section 3.5).

4.4. Electrode geometry

All so far discussed multipoles employ electrode geometries aiming to generate an ideal multipole field. Here, a few digital 16-poles of equal inscribed diameter but variable electrode radii are compared. A rather intuitive way of defining a parameter for different geometries is the electrode-gap ratio. The distance between the centres of neighbouring electrodes is calculated from twice the electrode radius r_e and the gap size x (see Figure 4.12a). For comparison, the reduced electrode-gap ratio $2\,r_e/x$ is introduced. The above discussed multipoles aim to approximate an ideal multipole field from circular rods with an electrode radius $r_e = r_i/(N-1)$ [132]. For the case of a 16-pole, this corresponds to an electrode gap ratio of about 1.78, which acts as a reference for comparison with other values. Different electrode gap ratios are investigated for a suitable range of RF amplitude, equal standard injection parameters ($r_{inject} = 0.9\,r_i$, $E_{kin,xy} = 1\,\mathrm{eV}$, and $E_{kin,z} = 10\,\mathrm{eV}$) and a RF frequency of $\Omega = 5\,\mathrm{MHz}$. The frequency was chosen such that the reference electrode gap ratio of 1.78 shows a medium peak transmission and improving or declining transmission properties for other ratios are easily observable. The resulting transmission spectra for six different electrode-gap ratios are depicted in Figure 4.12b. The black line is the reference spectrum with a ratio of about 1.78 of the ideal multipole field [132]. Smaller electrodes seem to cause significantly flatter and lower curves compared to the reference for equal RF signals, while higher values show minor impact on the shape and height of the transmission curves.

In principle, small electrodes are also capable to achieve good transmission, but at higher RF frequencies and amplitudes. For the actual design of multipoles, and especially for very small ones, good transmission properties are not the only criterion for an appropriate electrode diameter (see section 3.4). Efficient pumping of residual gas from the confined ion beam is promoted by larger gaps and mechanical alignment faults as well as bending of electrodes also prohibit very small gaps in order to avoid physical and electrical contact between neighbouring electrodes. A good compromise may be found with a electrode gap ratio around 1 or slightly above.

The electrode radius r_e with respect to the wire to inter wire ratio w can be calculated as

$$r_e = \frac{sin(\pi/2N)}{(1/w + 1 - sin(\pi/2N))}\, r_i \tag{52}$$

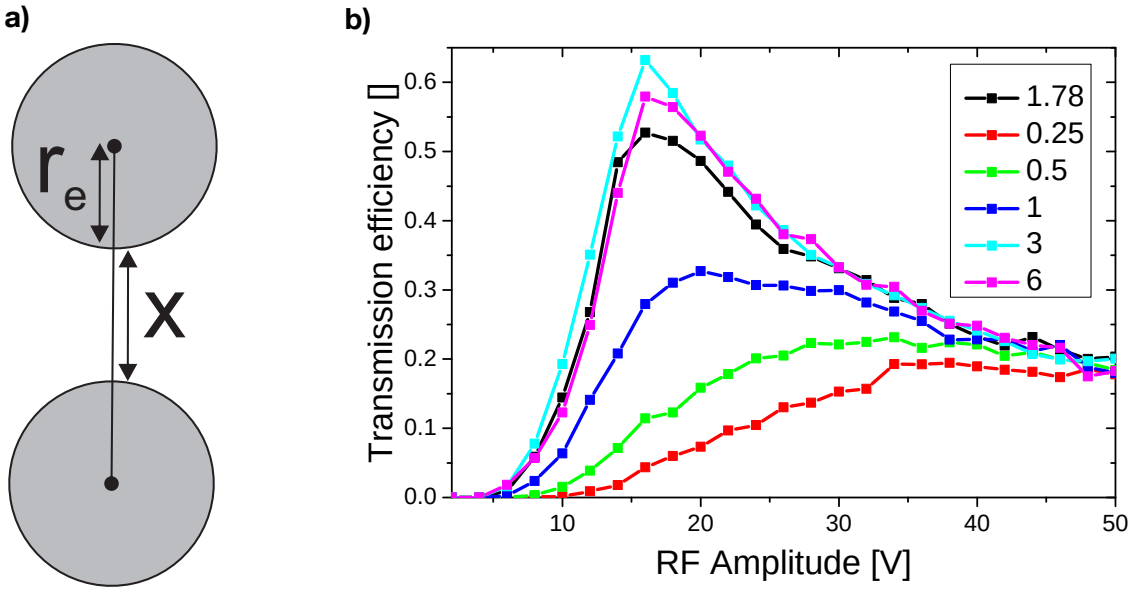

Figure 4.12.: Influence of electrode size on the transmission properties of a multipole. a) depicts the center to centre distance of two neighbouring electrodes, composing from twice the electrode radius $2\ r_e$ and the spacing x. b) shows the transmission spectra for different electrode-gap ratios $2\ r_e/x$.

with the number of pole pairs N and the inscribed radius of the multipole r_i.

4.5. Comparing simulations with experiments

The following sections compare results from the ion trajectory simulations with experiment. As the ES-CIBD is now operational, properties of the SWIG, the dQMS, and the Blade are compared with their simulated counterpart. From the experimenter point of view, it is very difficult to measure e.g. the kinetic energy distribution in xy-plane or the radial density distribution precisely in order to compare it to simulations and analytical theory. In particular, the ion beam intensity is the only property of the ion beam, that may be easily measured at different locations in the ES-CIBD.

Transmission properties of an ion guide are determined by monitoring the ion current on a detector electrode. In the ES-CIBD typically the electrodes of the subsequent ion guide or the sample itself are used. All of them are electrically insulated from their environment and therefore allow for ion current measurements with controlled potential.

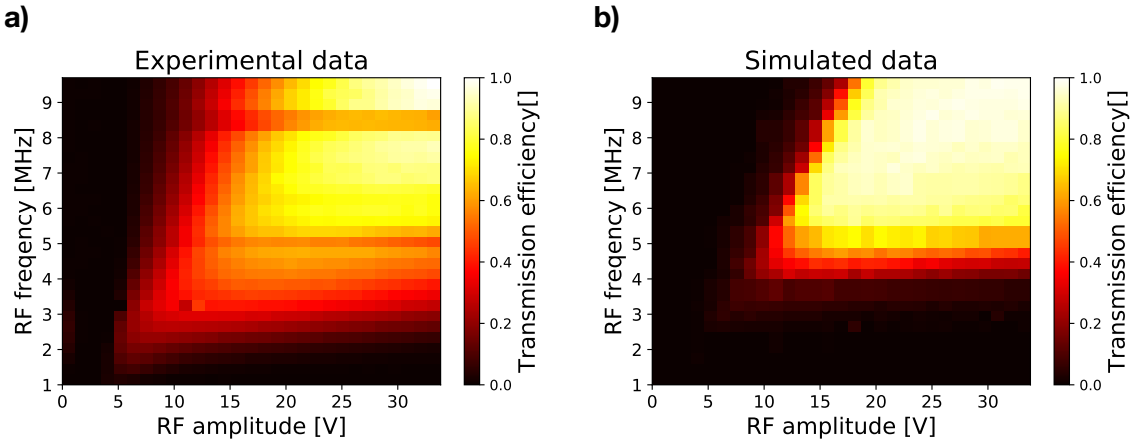

Figure 4.13.: Comparison between simulated and experimentally acquired transmission data of a 16-pole.

4.5.1. The SWIG

A comparison of simulated transmission and experimentally obtained data is depicted in Figure 4.13. The data originates from SWIG 2 and was measured for our test molecule, Rhodamine B. The electrode geometry is a 16-pole with an inscribed radius of about $0.82\,\mathrm{mm}$ and electrodes of about $0.09\,\mathrm{mm}$ radius resulting in a electrode gap ratio of about 0.73. The ion source is SWIG 1. In simulations, ions are started on a disk with a radius of $0.9\,r_i$ and a kinetic energy of $0.7\,\mathrm{eV}$ in xy-plane and $10\,\mathrm{eV}$ in z-direction. The RF amplitude and frequency ranges were chosen equally and the transmission was normalized to unity. Comparing both data sets, the region of good transmission in yellow is similar for simulations and experiment, but it is surrounded by a much larger region of medium transmission in the latter case. Besides, both spectra show the characteristic linear dependency between amplitude and frequency for the onset of transmission and the fast broadening of the plateau with good transmission for increasing frequencies.

There are several potential candidates for the reasons between simulations and experimental data. The electrode geometry used in the simulations for example does not include the fringing fields at both ends of the multipole and the ions are not injected from the exit of another SWIG. Furthermore, the real electrodes of a SWIG have several inaccuracies, e.g. their alignment and positioning due to the manufacturing process. Another reason for the smeared-out transmission in the experiments might be an ion beam that is not monodisperse. The m/z resolved spectrum of Figure 5.1a reveals that the Rhodamine B ion is the most dominant, but not the only ion species. Additionally, one would expect a certain

distribution of kinetic energy in xy-plane of the incident ion beam, rather than the precise value used for simulations.
Besides some inaccuracies, the results from the simulations provide helpful information concerning the appropriate design of the electrode geometry of the Twin, the SWIGs and the Blade, as well as for the layout of the electronic control unit and the RF supplies. Furthermore, ion trajectory simulations provide further insight into some effects that might not be obvious from analytical theory or experimentally gained data alone.

4.5.2. Combining a mass spectrometer with a ”Blade” ion guide

It is a commonly used technique to employ a quadrupole in combination with other ion guides or mass spectrometers. In many cases, it is also used as an ion guide, e.g. for transfer to another location or pressure regime. In commercially available triple quadrupole systems, the first quadrupole selects a certain m/z from an incident ion beam, in the second, the ions scatter with gas atoms, are fragmented and transported towards the third quadrupole for another m/z analysis. From such experiments, oscillating features on transmission curves have been reported for ion beams that are fed from one quadrupole to another [221–225]. The additional features originate from inefficient extraction of ions from a quadrupole by phase-space sensitive devices like other ion guides [226]. Such additional features do typically not occur for standard detectors like multipliers, as they employ large accelerating voltages to extract the ions [226].
In the case of the current ES-CIBD device the mass spectrometer (see section 3.5) is followed by a Blade, which is in principle a conical multipole (see section 3.6) and thus is in fact sensitive to the spatial extent and the kinetic energy of the incident ions. In the following, the resulting effects and problems are qualitatively discussed via a set of illustrative examples.
A comparison of simulated and experimental data for RF-only spectra of Rhodamine B ions of $m/z = 443\,\mathrm{Th}$ is shown in Figure 4.14. The quadrupole was operated with a RF frequency of $0.4\,\mathrm{MHz}$ and the Blade was operated with a RF frequency of $3\,\mathrm{MHz}$ and an amplitude of $80\,\mathrm{V}$. The black curve in 4.14a was recorded directly at the exit of the mass spectrometer, collecting the current from the the Blade electrodes. It represents a typical RF-only spectrum with the characteristic intensity drop when exceeding the critical amplitude for the m/z of Rhodamine B ions. The red curve comes from an RF-only spectrum, recorded on a detector plate behind the Blade. The fluctuating intensity indicates a

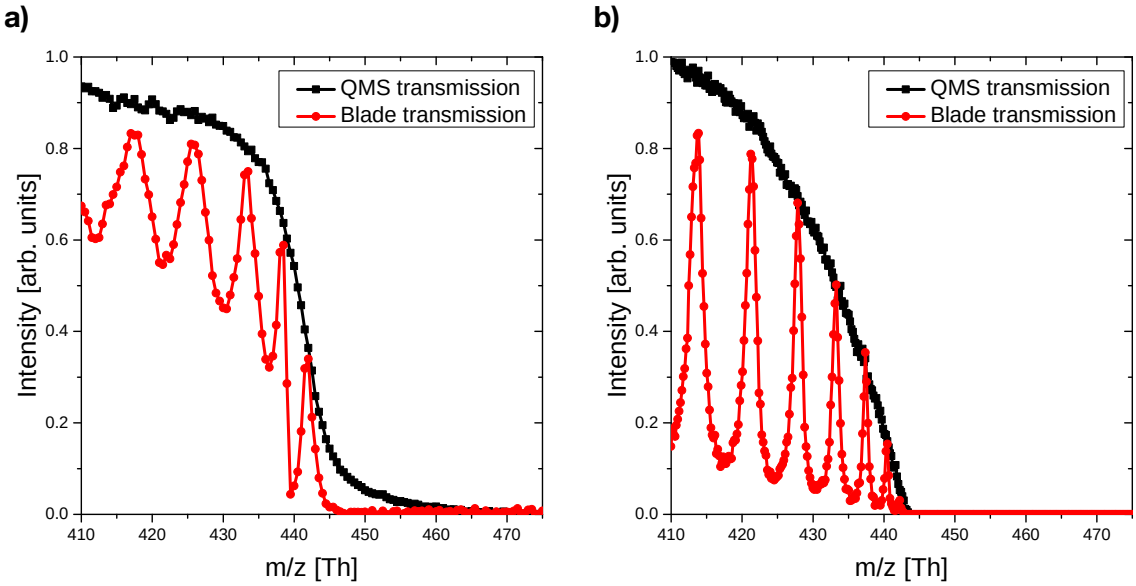

Figure 4.14.: a) experimentally measured and b) simulated RF-only spectra of Rhodamine B ions ($m/z = 443\,Th$). The black curves represent the intensity after the mass spectrometer and the red ones originate from ions that have additionally passed the subsequent Blade ion guide.

non-constant transmission efficiency of the Blade throughout the spectrum. Figure 4.14b depicts the corresponding data from ion trajectory simulations. Both, the QMS transmission and the combination with a Blade, show qualitatively similar effects.

The fluctuations are not restricted to RFonly spectra, m/z resolved scans show similar fluctuations (see Figure 4.15). Spectra of three different scan lines with increasing resolution are shown. The black curves represent the experimentally measured transmission on a detector electrode at the exit of the Blade and the red lines originate from corresponding ion trajectory simulations. For better comparability, the corresponding simulated peak from the mass spectrometer is indicated by the upwards shifted, green line. For comparison, all intensities have been normalized to unity. For all three resolutions, the combined system leads to additional features in the peak of the m/z resolved spectrum. In contrast to the RF-only spectra, the features are much more irregular in their spacing and height. When comparing the curves from all three graphs, there is no apparent systematic behaviour of the features.

To understand these effects, it is necessary to consider the nature of ion motion in the quadrupole. For this purpose, the ion trajectory simulations of the Blade-induced maximum at $m/z = 436\,\mathrm{Th}$ and the minimum at $m/z = 440\,\mathrm{Th}$ in Figure 4.15a are compared

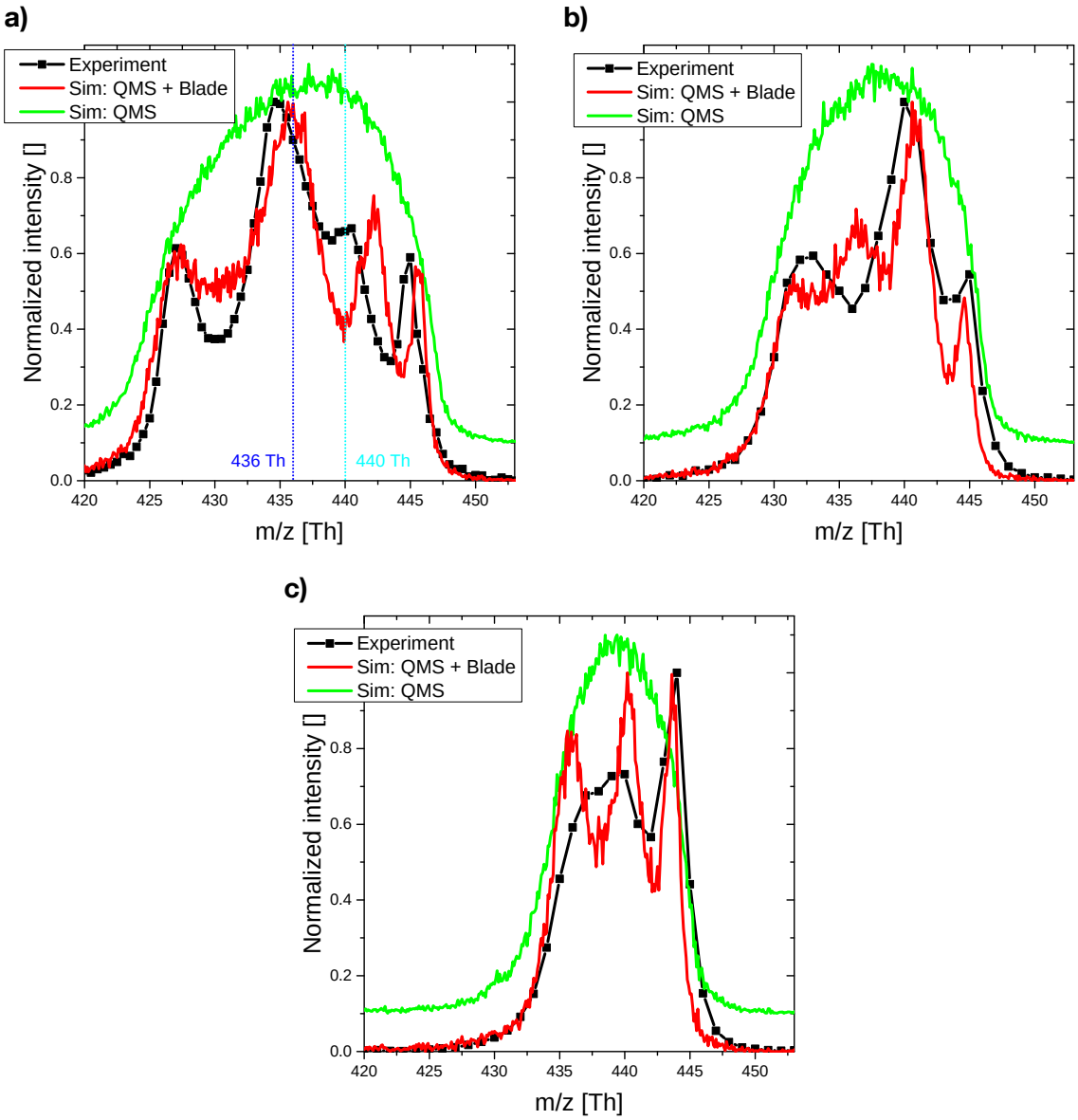

Figure 4.15.: Experimentally measured (black) and simulated transmission spectra (red) of the combined quadrupole with subsequent Blade. The offset green curve indicates the simulated intensity directly after the quadrupole. All spectra have been normalized to unity for better comparison. The three different graphs originate from scans with increasing resolving DC component of the scan line and therefore increasing resolution.

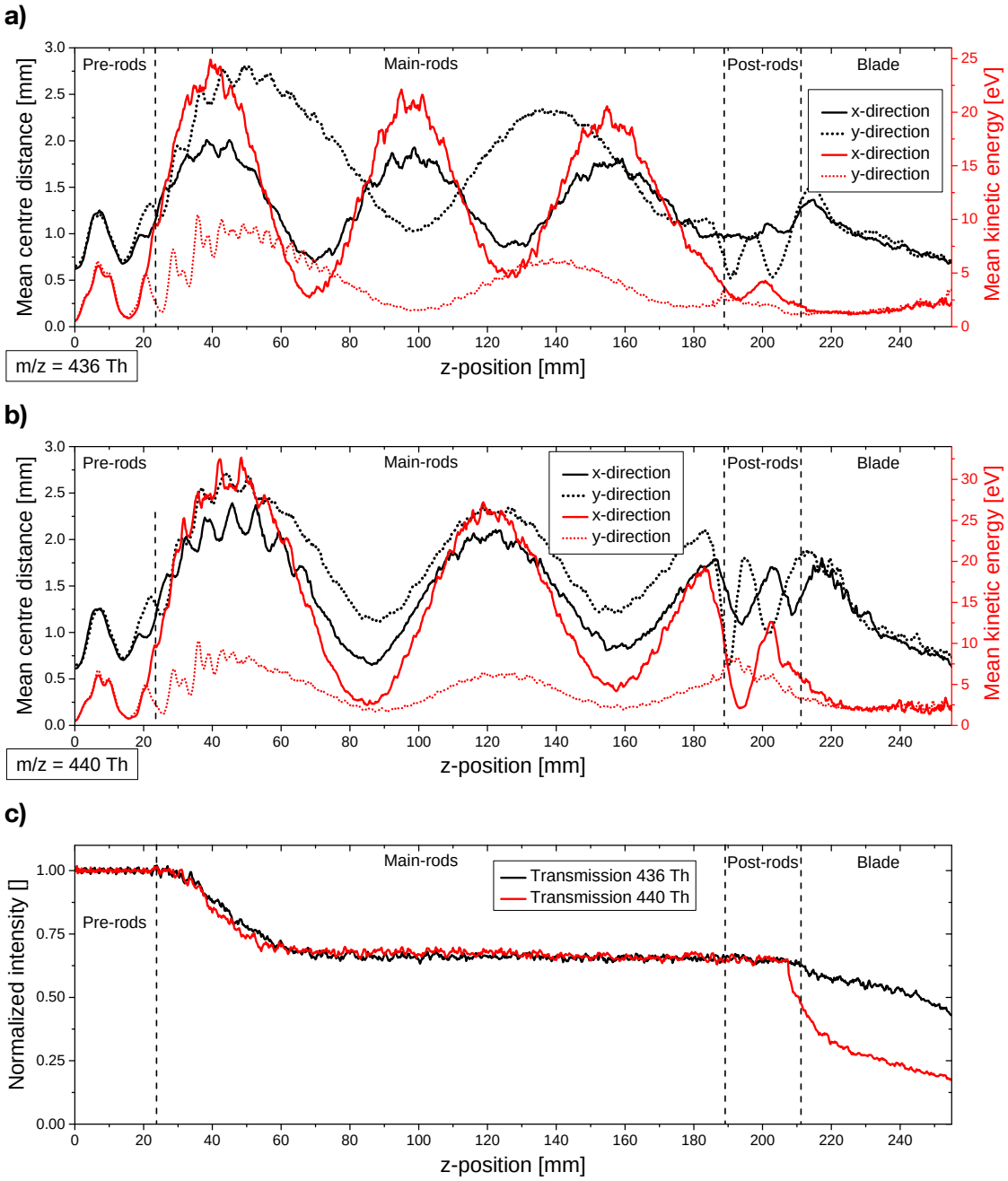

Figure 4.16.: Examples for axially resolved beam properties of the two simulations marked in Figure 4.15a at 436 Th and 440 Th. a) and b) depict the mean displacement from the center and the corresponding kinetic energy component in xy-plane. c) compares the ion beam intensity along the z-axis of both simulations.

as an example. The evolution of the three most important ion beam properties: spatial extent, kinetic energy in xy-plane, and intensity along the z-axis of the combined system are presented in Figure 4.16. For better comprehensibility the two simulations need to be described and compared, starting with the injection of ions.

For comparison with experimental data, the injection parameters approximate the exit of SWIG 3 with an inscribed diameter of about $2.5\,\mathrm{mm}$. For computational reasons, the SWIG 3 electrode geometry could not be included into the simulations. The exit of SWIG 3 is located just a few millimetres away from the entrance of the quadrupole. A starting disk of $3\,\mathrm{mm}$ in diameter at the entrance of the quadrupole was chosen in order to account for the beam-spread in the small region without trapping potential in between. The kinetic energy in xy-plane was chosen to $1\,\mathrm{eV}$ and the kinetic energy in z-direction of about $17\,\mathrm{eV}$ were adopted from the experiments. Please note that the starting disk is small compared to the inscribed diameter of the quadrupole's rod system ($r_i \approx 16\,\mathrm{mm}$).

After injection, ions pass the pre-rod system of the mass spectrometer. Here, the RF-component and no resolving DC components are applied. Therefore, an almost perfectly symmetric oscillation in mean center distance of the ion beam in x- and y-direction can be observed in the short first section of both simulations. When coming closer to the main rod system of the mass spectrometer, the symmetry of motion and kinetic energy in both directions vanishes and an oscillation of typically different amplitude and frequency in x- and y-direction starts. The mean radial displacement of the ions from the center axis follows a sine-shaped trend with different amplitudes and periodicity in x- and y-direction. This can be explained by the oscillation of a charged particle in a parabolic effective trapping potential with different heights in x- and y-direction, which is the case in a quadrupole operating with resolving DC.

The mean kinetic energy component in both directions oscillate in phase with the mean center distance. This comes from the increasing oscillations of the ions between the electrodes due to higher field strength for larger center distances. The energy attributed to the effective trapping potential is actually stored in the fast oscillation of ions between the electrodes (see section 2.2 and [132]). Therefore, the characteristic oscillations in the spatial directions can also be found in their respective kinetic energy component.

Figure 4.16c depicts the ion beam's intensity evolution along the z-axis of the system. As expected from the green transmission curve in Figure 4.15a, the transmission efficiency does not significantly differ for both settings until the quadrupole's exit is reached. The difference in absolute transmission of the combined system mainly originates from the interface between quadrupole and Blade, and is a result of the ion beam's size in phase

space. In Figure 4.16a, both spatial oscillations in x- and y-direction of the ion beam are in a minimum when coupled out of the main rod system, leading to decent spatial size and kinetic energy. 4.16b shows a case where both oscillations are close to their maximum positions at the end of the main rods. The size of the ion beam in phase space is much larger and partially exceeding the area of good acceptance of the Blade. Ions with large spatial displacement or high kinetic energy are lost from the beam and the transmission efficiency is reduced.
In the case of the RF-only spectrum of Figure 4.14, no resolving DC is present, leading to symmetric effective potentials and symmetric motion in both directions. The resulting oscillations in transmission are therefore regular. In the case of m/z spectra with resolving DC component, the additional transmission features come from the overlap of two different oscillations in x- and y-direction, leading to a much more complex appearance. Please note that the oscillations of the ion beam in the quadrupole depend on a multitude of parameter such as the ion injection (radius, kinetic energy in x-,y- and z-direction) and the heights of the trapping potential in both directions which is determined by the RF parameters (RF frequency, amplitude, and resolving DC). Regions of good transmission can be easily determined by a spectrum and a change from bad to good transmission at a specific position in the spectrum can also be accomplished by a small change of the field axis potential, thus changing the output phase of the oscillations in the quadrupole. The height of the oscillations might be influenced by the geometry of the Blade and its RF parameters.

5 Results and Performance

The following chapter demonstrates an overview of the so far performed experiments and depositions of analytes on surface in UHV and the subsequent investigation via STM. After completion of the set-up first pilot runs were conducted with a fluorescent dye, a porphyrin derivative, n-doped graphene nanoribbons, a polypeptide and various DNA specimen applying positive and negative spray modii to test the usability of the system. These molecules represent a wide range of masses from few hundreds to some mega Dalton as well chemically different types of molecules. Success of the electrospray and ion transmission to UHV was controlled by recording m/z resolved spectra and ion currents. An Ag(111) single crystal was used to soft-land the deponents for further investigation by UHV-STM.

5.1. Characterization of the ES-CIBD with model systems

Rhodamine B, a frequently used test molecule for investigations on the properties of ion guides and the dQMS (see sections 4.5.1 and 4.5.2) is available as a chloride or as base - we used the salt. The cation has a mass of $443\,\mathrm{Da}$. Rhodamine B was solved in a water, methanol, acidic acid (volume ratio (v/v): $47.5\,\%$, $47.5\,\%$, $5\,\%$) mixture at a final concentration of $1 \times 10^{-4}\,\mathrm{M}$ (see appendix A). Consequently it was sprayed in positive mode with a fused silica emitter of $75\,\mu\mathrm{m}$ inner diameter at a voltage of typically $2.5\,\mathrm{kV}$ and a flow rate of about $500\,\mathrm{nL/min}$. A sheath gas - as done at some later runs - was not applied. In Figure 5.1a a dominant peak at $443\,\mathrm{Da}$ emerges, representing the single charged ion. Figure 5.1b and 5.1c demonstrates the tradeoff between high selectivity for clean depositions and high transmission for fast depositions. The resolution of a m/z spectrum needs to be chosen sufficiently high to identify a molecule and to separate it from other species, but as low as possible to guarantee for high transmission efficiency. For the overview spectrum of Figure 5.1a, a resolution of about 110 was chosen to easily distinguish between different peaks but reach a high transmission efficiency. Some minor intensity peaks are found at slightly lower m/z, but only one very dominant charge state of the Rhodamine B cation is present. The chart of Figure 5.1b presents a series of higher resolved spectra, that reveal a second peak of the Rhodamine B cation which is attributed to an isotope, generated most probably by a single C^{13} atom in the molecule. The transmission scale is normalized arbitrarily to a spectrum with an assumed transmission efficiency of nearly $100\,\%$ and a resolution of about 55. The transmission efficiency decreases with increasing

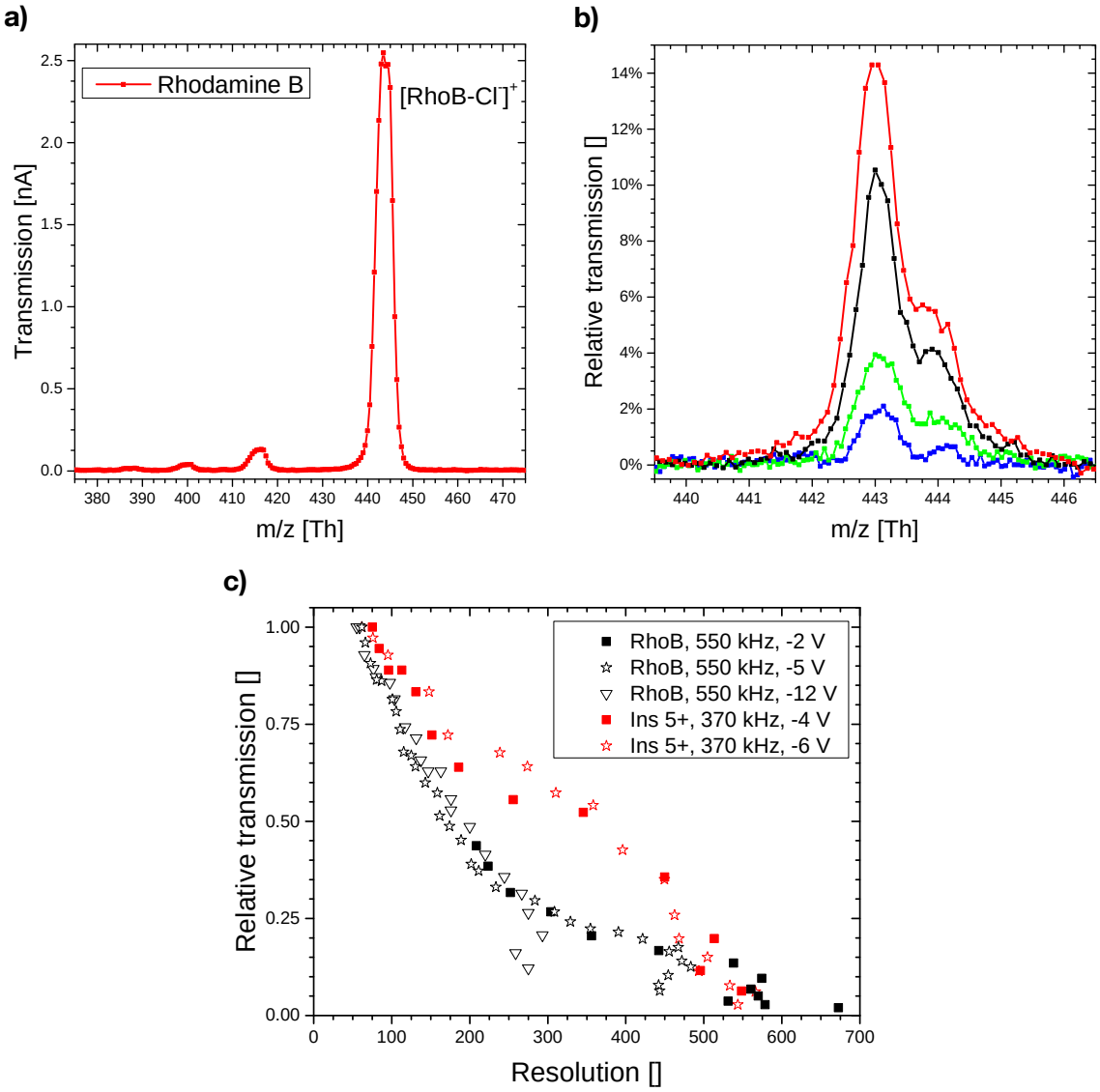

Figure 5.1.: Investigations on the properties of the dQMS. a) Overview m/z resolved spectrum of Rhodamine B with the singly charged cation as the dominant peak and few minor intense peaks with lower m/z. b) series of high resolution m/z spectra with $\frac{m/z}{\Delta\, m/z}$ (FWHM) ranging from about 530 (red) to about 670 (blue). c) resolution vs peak transmission of the dQMS. Data points are normalized with their corresponding highest transmission value. Test ions are the Rhodamine B cation and the Insulin $5+$ ion (see section 5.2). Operation frequencies of the dQMS and field axis potentials with respect to SWIG 1 are given in the graph's legend.

resolution $\frac{m/z}{\Delta\, m/z}$ (FWHM) of the dQMS as analyzed by a series of scans with increasing resolving DC portion (see Figure 5.1c). The data points are normalized to their corresponding highest transmission value. Here for both test ions the absolute transmission efficiency for resolutions ≤ 75 is supposed to be close to unity. The data was recorded for two test ions, the Rhodamine B cation with $443\,\mathrm{Th}$ and the Insulin $5+$ ion of about $1162.5\,\mathrm{Th}$ (see section 5.2). The RF frequency of the dQMS and the field axis potential with respect to SWIG 1 are indicated in the chart's legend. Ions typically do not scatter with residual gas atoms downstream of SWIG 1 and the kinetic energy in z-direction can be estimated by the difference in field axis potentials $E_{kin\ z} = q \cdot (U_{dQMS} - U_{SWIG\ 1})$ (see section 3.1). As a rough guideline, high transmission is reached for a resolution below about 150. Reasonable high precision depositions may be performed with a resolution of about 500 and a transmission in the $10 - 15\,\%$ range. Higher resolutions are in principle possible, but not very favourable because they come on the expense of low intensities and therefore large preparation times.

The advantage of Rhodamine B as a test molecule is its favourable spray behaviour due to its high solubility and its ionic nature, as well as its high stability and availability. According to the m/z resolved spectrum the ion beam almost exclusively consists of one ion species. Taking this together, Rhodamine B qualifies for an ideal model system to analyze several system parameters, in particular to optimize beam intensities and to calculate recoveries:

The recovery is defined as the probability of an analyte molecule that passes the ESI emitter to be landed on the deposition target. Low ionization efficiency and losses during the transmission process and the m/z selection are dominant loss processes.

Previous publications using m/z selected ions for soft-landing provide several reference values of recovery: $0.001 - 0.1\,\%$ for four different m/z selected proteins [227], $0.3\,\%$ for Keggin polyoxometalate [121], $0.05\,\%$ for tetrapeptide MLFA, $0.06\,\%$ for sodium dodecylbenzenesulfonate, and $0.3\,\%$ for Jacobsen's catalyst [228]. For our test molecule Rhodamine B a recovery of $0.5\,\%$ with a deposition current of $0.15\,\mathrm{nA}$ was reported by Cooks [228]. In case of the ES-CIBD a recovery with up to $2.7\,\%$ and a deposition current of $2.2\,\mathrm{nA}$ was achieved for Rhodamine B. Recoveries of other molecules are the same order of magnitude (Insulin: $0.7\,\%$, pUC19: $4.4\,\%$). Significantly lower recovery rates (NR-10: $0.04\,\%$) are often a result low ionization efficiency due to an inappropriate solution and poor spray properties such as an inappropriate position or high voltage of the emitter, poor desolvation of the molecule, low evaporation rates of the solvent and low electric conductivity (see also section 2.1). A high molecule concentration in the spray

solution also leads to poor ionization efficiencies [99].
One of the main reasons for the significantly improved recovery rates are the highly efficient vacuum ion guides. The probability of an ion emitted from the ESI source (into first vacuum stage), that is transmitted to UHV and m/z filtered with a resolution of 110 to reach a deposition target can be roughly estimated to $25\,\%$ ($5 - 10\,\%$ in case of [121]), which corresponds to a transmission efficiency of about $80\,\%$ per each of the six ion guides. The corresponding ion currents are listed in the table in Figure 3.2 and are measured from our test molecule Rhodamine B to characterize the transmission properties of the ES-CIBD.

5.2. Insulin

In the current work insulin served as object to test the performance of the ES-CIBD exemplary for the group of non-elongated biomolecules, specifically globular proteins. The used Insulin is a $5807.65\,\mathrm{Da}$ [229] peptide hormone consisting of two subunits connected via disulfide-bonds. In addition to the metabolic active monomeric form which dominates at physiological conditions in serum [230], insulin builds various non-active oligomeric stages in vitro, dependent on the conditions in the solvent: low ionic strengths, low pH, and low concentration of the protein promote monomeric and dimeric states while higher pH, higher concentration, and high ionic strengths, divalent metal ions such as Zinc or Cobalt, chloride and phenolic compounds drive assembly to tetramers, hexamers or even higher structures including insulin aggregates [231–239]. Self-aggregation of insulin in solution is considered a spontaneous process and critical for long-term storage why attempts are made to retain the monomeric form e.g., by adding special protic ionic solvents [240].
With an isoelectric point at 5.2 and 4 basic amino acids insulin can, at acidic conditions, theoretically carry up to six positive charges involving the basic residues and the N-terminus of each subunit. Up to eight charges are observed if particular supercharging agents are added to the background electrolyte in the spray process, in particular at low pH [241]. For ESI however other factors than number of basic residues play a dominant role for charging efficiency, such as protein and droplet surface area [242] and in consequence physical parameters like flow rate in combination with the diameter of the emitter [243]. Conducting Rayleigh limit calculations [69] of a sphere at standard conditions, the protein monomer should carry five charges and the dimer eight charges at maximum. Experimental data revealed six and eight charges respectively [231], if supercharging agents are used

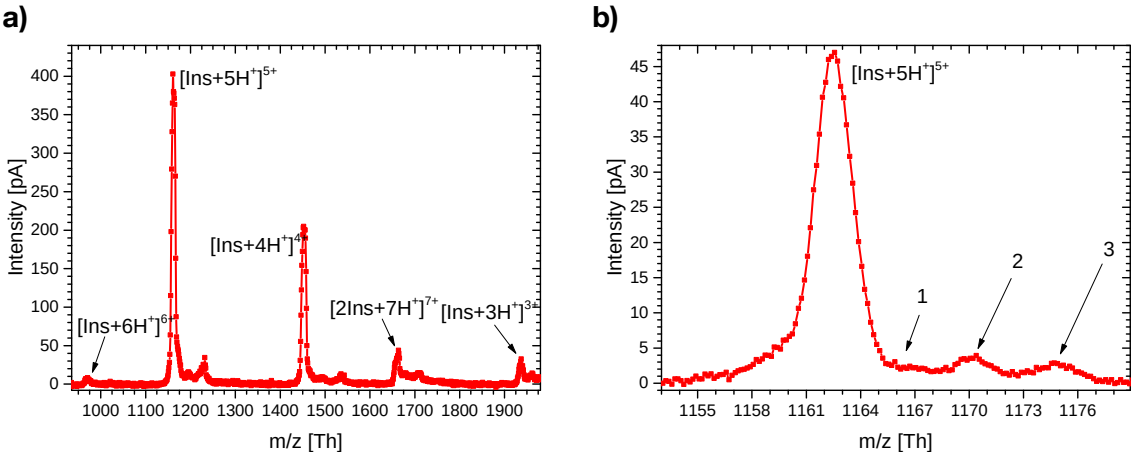

Figure 5.2.: m/z resolved spectra of insulin obtained in positive spray mode. a) Overview spectrum with a resolution of about 130. The two most prominent signals represent the $4+$ and $5+$ charged monomers with calculated masses of $1452.9\,\mathrm{Th}$ and $1162.5\,\mathrm{Th}$. Three of the lower intensity variants reflect the $6+$ ($968.9\,\mathrm{Th}$) and $3+$ ($1936.9\,\mathrm{Th}$) monomers, and an odd protonated dimer $7+$ ($1660.3\,\mathrm{Th}$). b) Close-up view of satellite peaks in proximity to the $5+$ monomer, captured at a resolution of about 490. Three additional low-abundant signals are detected which can be attributed to adducts with a single water molecule $[\mathrm{Ins} + \mathrm{H_2O} + 5\,\mathrm{H^+}]^{5+}$ ($1166.1\,\mathrm{Th}$) or a sodium ion $[\mathrm{Ins} + \mathrm{Na^+} + 4\,\mathrm{H^+}]^{5+}$ ($1166.9\,\mathrm{Th}$), an adduct with two water molecules $[\mathrm{Ins} + 2\,\mathrm{H_2O} + 5\,\mathrm{H^+}]^{5+}$ ($1169.7\,\mathrm{Th}$) or a potassium ion $[\mathrm{Ins} + \mathrm{K^+} + 4\,\mathrm{H^+}]^{5+}$ ($1170.1\,\mathrm{Th}$), as well as a proposed acetic acid adduct monomer $[\mathrm{Ins} + \mathrm{AcAc} + 5\,\mathrm{H^+}]^{5+}$ ($1174.5\,\mathrm{Th}$) or an adduct with a sodium and a potassium ion $[\mathrm{Ins} + \mathrm{Na^+} + \mathrm{K^+} + 3\,\mathrm{H^+}]^{5+}$ ($1175.5\,\mathrm{Th}$).

up to 8 charges for a monomer [241].

In our experiments conducted at room temperature $8 \times 10^{-5}\,\mathrm{M}$ insulin in an acidic aqueous solution with acetonitrile (ACN) as organic compound was injected and ionized in positive spray mode (see appendix A). The analyte signal in the overview spectrum of Figure 5.2a appeared predominantly as two main peaks representing the $4+$ and $5+$ charged monomers in addition to less prominent peaks possibly representing monomeric molecules with $3+$ and $6+$ charges according to mass calculation (see Figure 5.2a). In principle, some of these peaks may be partly overlaid or even completely replaced by the respective double-charged dimers, e.g. $[2\,\mathrm{Ins} + 6\,\mathrm{H^+}]^{6+}$ and $[2\,\mathrm{Ins} + 8\,\mathrm{H^+}]^{8+}$ coincident with the monomer's m/z values which cannot be distinguished from the corresponding dimers by the method used. Additional low abundant peaks may be attributed to either dimers or adducts.

Hints for dimers present in the gas phase are given by a peak compatible with the odd

charged oligomeric form $[2\,\mathrm{Ins} + 7\,\mathrm{H}^+]^{\,7+}$ compatible with the analysis of the Robinson group [231]. For the insulin concentration tested, the respective dimers are quite likely to coexist as those emerge at levels as low as $2\,\%$ of the concentration we used. Dimer probability strongly increases with rising concentrations [231]. Hexamers or even higher oligomeric states seem less likely if taking the electrolyte composition into consideration that trigger rather smaller entities.

Adducts with water molecules are described for hexamers elsewhere [244]. Presumably those emerge with the monomer as well as suggested by the current experiments with high resolution (see Figure 5.2b). In particular, three low-intensity signals appear in close proximity to the $5+$ charged variant. The first can be attributed to monomers carrying a single water molecule or a sodium ion. The second can be attributed to a monomer with two attached water molecules or one potassium ion. The third peak is presumed as an acetic acid or a sodium and potassium adduct of the monomer.

Monomers, dimers and hexamers are considered native states of insulin, however electrospray ionization may produce also higher oligomers which, due to their correlation with the insulin concentration, are regarded ESI 'artefacts' [245] they may be excluded via m/z selection. The occurrence of main peaks matching with the theoretical masses of commonly charged monomeric and dimeric states and the lack of higher oligomers suggests that the ESI-CIBD system preserves the native states of the molecules. We will investigate this topic in more detail in further studies depositing layers of homogeneous species by m/z selection and analysing them by STM.

Most ESI depositions of small to medium-size proteins at UHV conditions have been performed by the groups of Rauschenbach, Cooks and Laskin: Bovine serum albumin, cytochrome C, haemoglobin, ubiquitin, apomyoglobin, insulin, lysozyme, trypsin, neurotensin, bradykinin, and a protein kinase A subunit (list not complete) were processed for further investigation by scanning probe microscopy, holography, in situ infrared reflection–absorption spectroscopy [87, 88, 99, 227, 246–248] up to attempts to prepare protein microarrays [43]. While this panel is quite impressive, there where also clear signatures of rather low efficiency of the deposition process however due to low ionization efficiency and losses during the transmission process resulting in a total recovery of $0.001 - 0.1\,\%$ [227] for four different m/z selected proteins (see also section 5.1). In comparison, the ES-CIBD delivers ions of Insulin with recoveries of $0.37\,\%$ for the $5+$ charge state and $0.23\,\%$ for the $4+$ species after m/z selection with a resolution of 130. Taking the sum of all Insulin related peaks of Figure 5.2a, an overall recovery of about $0.7\,\%$ is achieved.

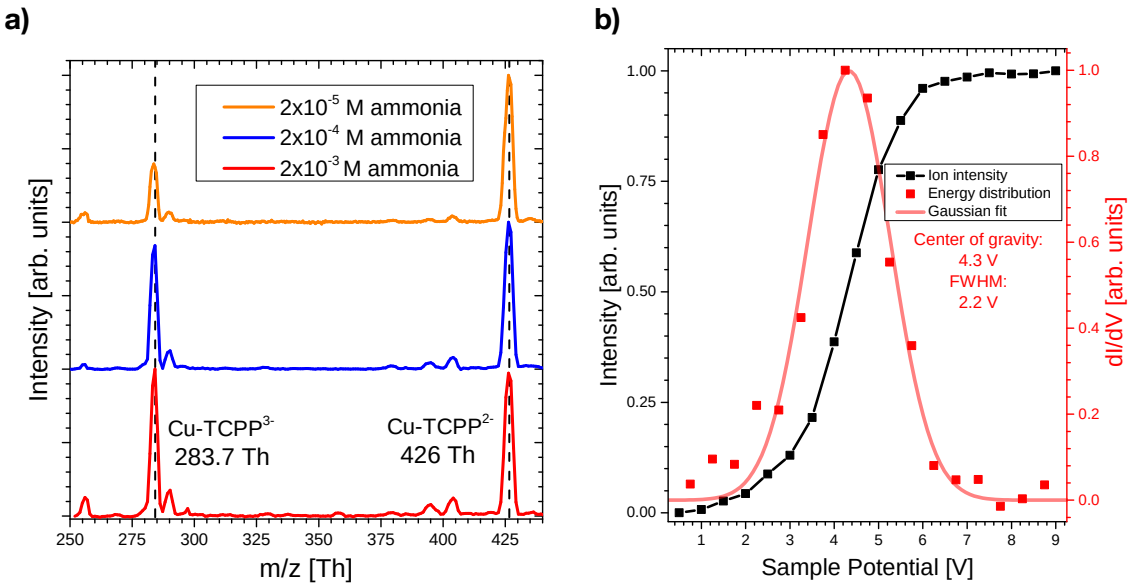

Figure 5.3.: a) m/z resolved spectra of Cu-TCPP in negative spray mode at three different ammonia concentrations. The two dominant peaks can be attributed to double and triple deprotonated Cu-TCPP. b) Beam characterization prior to the deposition of Cu-TCPP by measuring the ion flux as a function of the deposition sample potential. The numerical derivative of the flux represents the energy distribution of the ions and may be fitted with a Gaussian.

5.3. Deposition of an unsublimable porphyrin derivative

The first negative spray mode attempts were performed on a synthetic porphyrin derivative, Copper 5,10,15,20-tetrakis (4-carboxylphenyl)-porphyrin (Cu-TCPP) with $854\,\mathrm{Da}$ mass. Porphyrins are extensively used and investigated in science due to their biological relevance as reactive component in hemoglobin, chlorophyll and other biomolecules, as well as their metalorganic nature [249, 250]. Unless otherwise noted, the solution consisted of a methanol-water mixture (v/v: $80\,\%$,$20\,\%$) with $1.7 \times 10^{-4}\,\mathrm{M}$ ammonia and $8.3 \times 10^{-5}\,\mathrm{M}$ Cu-TCPP. The emitter, a fused silica tubing of $75\,\mu\mathrm{m}$ inner diameter and $360\,\mu\mathrm{m}$ outer diameter, was supplied with $500\,\mathrm{nL/min}$ of solution and a voltage of about $1.95\,\mathrm{kV}$ was applied (see appendix A).

m/z resolved spectra of Cu-TCPP with different ammonia concentrations are depicted in Figure 5.3a. In this case, the two dominant charge states originate from the double and triple charged species. In negative spray mode molecules are mostly charged by depro-

tonation [251]. But there is a striking difference between depositions in positive mode (mostly protonation) and deprotonation. In both cases a current on the sample can be monitored, either by actual discharging of the ion or by formation of a mirror charge in the conductive surface. In case of protonation the molecule carries an additional H-atom which might sufficiently agile that it can reach the substrate surface [252, 253]. Here it recombines with another H-atom and - in case of ambient temperature and far below - can desorb as a neutral. In case of a lacking H-atom (deprotonation) there is no such opportunity to rebuilt the "original" molecule. Formation of ions from solution can by influenced by adding a proton acceptor to the solvent. In the presented case, the relative intensities of the different charge states are influenced by the variations in the ammonia concentration. A high ammonia concentration promotes triple deprotonated states, whereas lower concentrations prefer formation of the double deprotonated species. Noteworthy amounts of the single charged molecule were solely found for ammonia concentrations of $2 \times 10^{-4}\,\mathrm{M}$ and $2 \times 10^{-5}\,\mathrm{M}$ with intensities of $4\,\%$ and $15\,\%$ with respect to the main peak.
Before deposition, the kinetic energy of the impinging particles has to be determined. For very low values, there is a trade-off between intensity and landing energy of the particles while impinging on the sample. In Figure 5.3b intensity versus potential of the deposition sample is shown for Cu-TCPP. The energy distribution of the ion beam is calculated from the first derivative of the intensity. By a Gaussian fit, the full width half maximum (FWHM), the energy spread, is determined to about $2.2\,\mathrm{V}$ with a center of gravity at $4.3\,\mathrm{V}$. The mean kinetic landing energy is calculated from the charge of the ion times the offset between the sample potential and center of gravity. The experimenter has to decide for a suitable deposition potential. In case of Cu-TCPP a sample potential of $5.5\,\mathrm{V}$ was found suitable to reach high intensities but low kinetic energy for soft-landing. During deposition of the double deprotonated species of Figure 5.5, an average ion current of about $0.4\,\mathrm{nA}$ was achieved. The recovery of the doubly charged species is about $0.3\,\%$.
Earlier ambient atomic force microscopy studies on TCPP, the unmetalated version of the Cu-TCPP molecule, showed - aside a wide open hexagonal structure - also a square shaped assembly of the molecules on a hexagonal boron nitride (hBN) substrate (see Figure 5.4a) [254]. The arrangement of molecules is indicated by an ball-and-stick model superimposed on the AFM image with carbon atoms marked in light grey, hydrogen in white, nitrogen in blue and oxygen in red. The 2-dimensional assembly of the single molecules was supposed to be driven by hydrogen bonds between the carboxylic groups of neighboring molecules. The molecules had been deposited on the substrate by immersion in solution and subsequent drying with a Nitrogen stream. While this procedure apparently

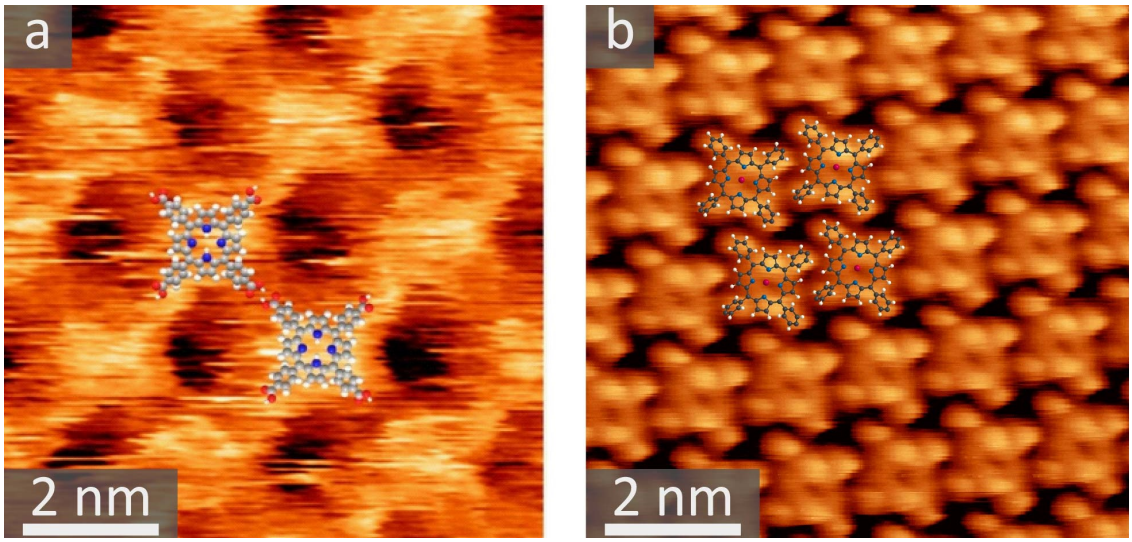

Figure 5.4.: AFM and STM images of TCPP and Cu-TPP. a) depicts an ambient AFM image of Cu-TCPP on hBN, deposited by immersion and dried by nitrogen. The intramolecular coupling is formed by hydrogen bonds between the carboxylic groups of neighboring molecules. From [254]. b) UHV STM investigation ($U = 0.1\,\mathrm{V}$, $I = 10\,\mathrm{pA}$, $T = 300\,\mathrm{K}$) of Cu-TCPP molecules on Ag(111) that decomposed to Cu-TPP during the thermal treatment by an OMBE for deposition ($\approx 680\,\mathrm{K}$). Courtesy of [255].

did not impact integrity of the molecule, wet methods like drop-casting or immersion may introduce residual solvent and impurities from the atmosphere. In contrast, if adopting classical UHV deposition techniques like OMBE on Cu-TCPP, the molecule was found impaired in its integrity (see Figure 5.4b). During the thermal treatment of the molecule with a temperature of about $680\,\mathrm{K}$, a strong increase of the carbon dioxide peak in the residual gas spectrum indicated the carboxylic groups to have split off. The resulting STM image of Figure 5.4b, which depicts the ordered layer of molecules, confirmed these findings. A ball-and-stick model of the molecules indicates their arrangement with carbon atoms in dark grey, hydrogen in white, nitrogen in blue and the central copper atom in red. Concluding from the packaging and the size of the structures, the Cu-TCPP seemed to be decomposed to copper incorporated 5,10,15,20-Tetraphenylporphyrin (Cu-TPP) lacking four COOH groups.

The STM images of Figure 5.5 show a deposition of double deprotonated Cu-TCPP on a Ag(111) surface now generated by the ES-CIBD system. From this preparation one of the striking benefits of the system becomes obvious: the Cu-TCPP molecule has still its carboxylic groups after passing the entire ESI process and landing in UHV, which was not

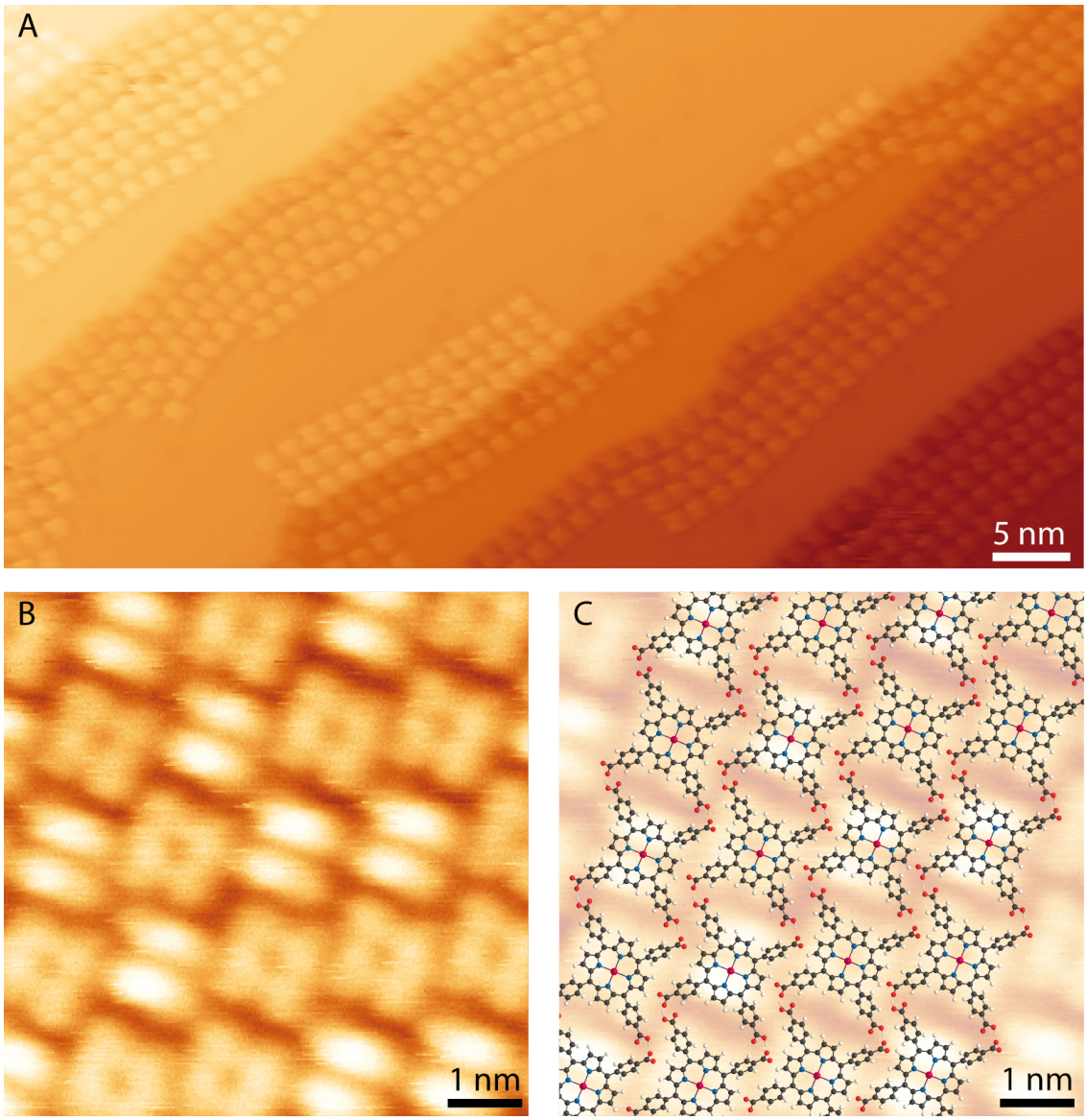

Figure 5.5.: Room temperature UHV STM measurements of self-assembled Cu-TCPP on Ag(111) ($U = 1.2\,\mathrm{V}$; $I = 20\,\mathrm{pA}$). (A) Overview STM image of the sample. The molecules tend to accumulate on the step edges for sub-monolayer coverages. (B) Detailed STM image of the self-assembly of the molecules. (C) Equal STM image as (B) overlaid with a ball-and-stick model of the molecules. Black, blue, red and white spheres represent carbon, nitrogen, oxygen and hydrogen, respectively. The central sphere represents the central copper atom. Courtesy of [255].

achievable via OMBE. UHV conditions and prior m/z selection minimize impurities and ensure for intact molecules. In contrast to the self-assembly on hBN [254] the molecules do not arrange in a quadratic fashion with the carboxylic groups pointing at each other. The zoom-in image and the respective ball-and-stick model in Figure 5.5 B and C reveal a closer packing of the molecules. The protrusions assigned to the carboxylic groups point closer to the center of the neighboring molecule, which indicates hydrogen bonding with the phenyl or the central tetra pyrrole ring. The reason might be the different environments (ambient pressure versus UHV) and substrates (hBN versus Ag(111)) as well as the absence of two protons most probably at the carboxylic groups due to the negative electrospray process. Importantly, the overview scan shows a clean silver surface between the molecular islands without detectable impurities such as fragments or residual solvent molecules. The Cu-TCPP supermolecular assemblies decorate the step edges reflecting appreciable surface mobility.

5.4. Deposition of DNA

As a representative molecule for rather elongated molecules such as nucleic acids, the double-strand (ds) circular plasmid pUC19 was processed [256]. This desoxyribonucleic acid (DNA) of bacterial-origin constitutes a B-form [257] and consists of 2686 base pairs translating into a molecular mass of approximately $1.7\,\mathrm{MDa}$. Presented data were obtained spraying an aqueous solution of pUC-DNA with $66\,\%$ ACN as organic component (see appendix A). At these conditions, dsDNA molecules carry negative charges predominantly on the phosphate backbone accessible for negative mode electrospray ionization. Completely ignoring any limitation by electrostatic repulsion, each single phosphodiester residue can potentially carry one negative charge introduced by eliminating the positive counter ion, which would result in 5372 charge states and a lower limit of about $325\,\mathrm{Th}$. In contrast to the m/z resolved spectra of other test molecules in this thesis with single or few peaks only (porphyrin, dye, protein), the experimental m/z spectrum of pUC19 shows a wide distribution between $1150\,\mathrm{Th}$ and $2000\,\mathrm{Th}$ (see Figure 5.6). The center of gravity locates at about $1500\,\mathrm{Th}$. This broad curve shape is however typical for such extended, non-globular molecules and similar to those obtained by other groups with related plasmid-type species using ESI-MS [258].
Currently, a maximum resolution of about 700 is achieved with the ES-CIBD system. In order to resolve single adjacent charge states of a pUC19 spectrum a resolution of about

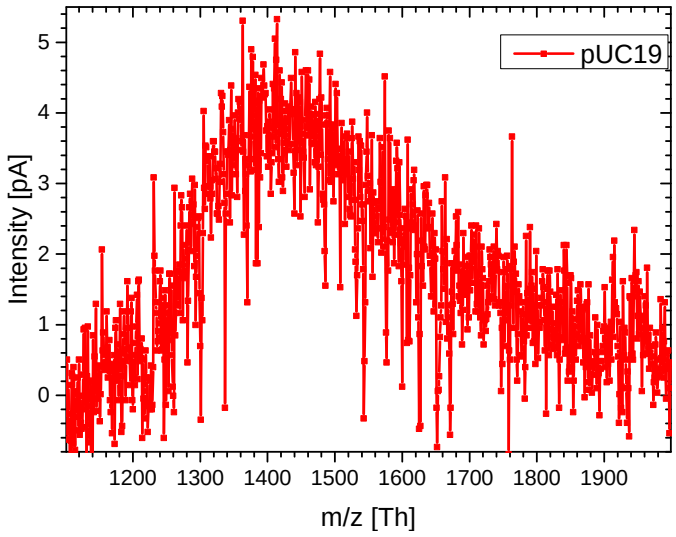

Figure 5.6.: m/z resolved spectrum of plasmid DNA pUC19. The molecular mass of about 1.7 MDa leads to a wide range of accessible charge states of low spacing. Single charge states could not be resolved but their distribution can be estimated from the spectrum.

1500 would be necessary for the center of the spectrum and 2000 for the whole spectrum. The overall current of the entire range can be estimated to about 400 pA taken from an high pass measurement in RF-only mode cutting below 1100 Th. The overall current distributes over about 600 possible charge states, leading to a maximum intensity of a single charge state of the order of 1 pA.

The center of gravity m/z of about 1500 Th translates into approximately 1100 e charges per DNA molecule. This is roughly 10-fold higher than expected for the maximal charging deduced from the Rayleigh limit [69] for a globular molecule in an aqueous solution, thus indicating a string like conformation. As a general consequence of the linear appearance, transition from charged droplets produced by the ESI source to single gas-phase ions very likely follow the chain ejection model (CEM) rather than the charge residue model (CRM) (see section 2.1.2, [71]). Assuming a cylindrical shape of the dsDNA instead of a globular one, the corresponding adapted Rayleigh limit for pUC19 can by estimated by [69]

$$q = \pi \cdot l \sqrt{6\gamma \cdot \epsilon_0 \cdot r} \approx 1100\,\mathrm{e} \tag{53}$$

with the surface tension of water $\gamma = 72.75\,\mathrm{mN/m}$ at $T = 20\,^{\circ}\mathrm{C}$ [259] and the permittivity ϵ_o. The length of a dsDNA strand in aqueous solution can be calculated from the number of bases via $l = 2686 \cdot 0.34\,\mathrm{nm} \approx 0.91\,\mu\mathrm{m}$ [260] and its radius is about $r = 1\,\mathrm{nm}$ [260,

261]. This calculated charge state is consistent with the experimental results. Elevated number of charges were also experimentally determined by other groups using charge detection mass spectrometry of various DNA molecules [262, 263].
Schultz et al. further discuss the effects of secondary winding (supercoiling) of the molecules on the charging state upon ESI spraying and in relation to the m/z spectrum profile [262]. In short, more relaxed (open circle) species potentially carry more charges than the more rigid and compact (supercoiled) forms and standard deviation of the readings from multiple experiments is higher for the latter. Here, pilot experiments were done with pUC19 plasmid DNA, which nominally is provided by the supplier in supercoiled state (see section A). As such it appears as long, compacted however still flexible fiber with a potentially lower charge capacity as its relaxed form. This however is subject of further and complementing studies covering also different structural variants.
For depositions, the dQMS was operated in an RF-only mode at $1100\,\mathrm{Th}$, i.e. cutting all masses below this threshold and transmitting all pUC19 attributed charge states. The kinetic energy distribution of the ion beam had a width of about $2\,\mathrm{V}$ (comparable to Figure 5.3b) and the sample potential for deposition was chosen about $1.5\,\mathrm{V}$ above the center of gravity for soft-landing. With an ion beam intensity of about $0.4\,\mathrm{nA}$ over $15\,\mathrm{min}$ a rather dense coverage of the Ag(111) surface was generated as detected by UHV-STM (see Figure 5.7). The recovery is about $4.4\,\%$.
Mega-Dalton sized DNA was handled in only a few ESI-settings to date, mainly in an analytical-only mode to determine molecular masses using charge detection mass spectrometry [262, 263] and ESI-FTICR [258]. Deposition of large dsDNA was achieved utilizing a rather simple ESI source without any prior m/z selection process and incomplete desolvation [265]. Other groups demonstrated in-situ deposition via pulse injection [266–268], where the inevitable deposition of solvent and other impurities is a problem, too. m/z selected UHV deposition was so far only shown for low molecular weight salmon sperm DNA [32]. Hence, to our knowledge this is the first time that high-molecular weight molecule such as plasmid DNA was deposited as m/z selected pure fraction of the target molecule, free of contaminations from fluids or residual neutral gas atoms and omitting unwanted crosstalk from molecular fragments or debris while preserving molecule's integrity.

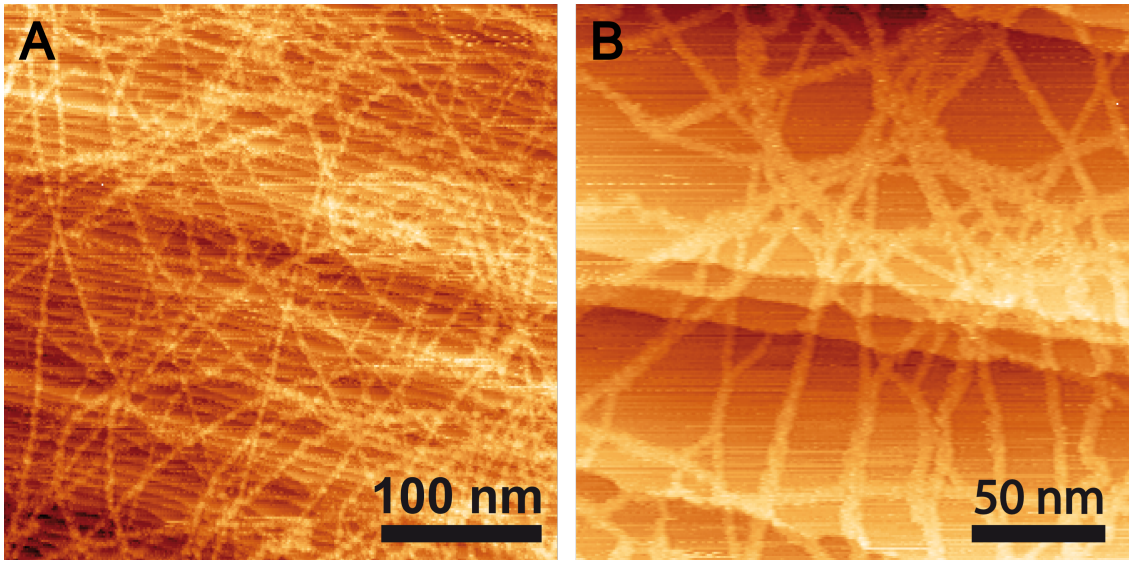

Figure 5.7.: Room temperature UHV-STM measurements of pUC19 plasmid DNA on Ag(111). a) ($U = 1.3\,\mathrm{V}$; $I = 90\,\mathrm{pA}$) High coverage of multiple strands crossing each other. b) ($U = 1.3\,\mathrm{V}$; $I = 10\,\mathrm{pA}$) Close up view with helical twisted and supercoiled strands crossing step edges of the crystal. Courtesy of [264].

5.5. Deposition of GNRs

To further demonstrate versatility of the ES-CIBD and as a representative of non biological molecules, a n-doped graphene nanoribbon (GNR) synthesized by [269] was deposited. Synthetic low-dimensional carbon nanostructures, such as graphene, nanoribbons and nanotubes gained special attention in science during the last decades due to their unique electronic, optical and mechanical properties. Especially GNRs are promising candidates for potential application in electronics [270–272], photonics [273] and energy conversion [274–276].

As properties of GNRs strongly depend on their exact geometry such as length, width and edge structure, synthesis of molecules and subsequent investigations require precise control of the molecules down to the atomistic level [269]. Electrospray deposition attempts of GNR or carbon nanotubes from liquids with subsequent AFM imaging have been reported in literature [277, 278]. The ES-CIBD with its capability of additional purification via m/z selection in UHV is a powerful tool to guarantee for intact molecules and a clean and homogeneous deposition. The molecule under investigation is the smallest linear speciesof a series of nanoribbons (NR) with 10 conjugated lineary-fused carbon rings, NR-10 from [269] with a molecular mass of about $2321.4\,\mathrm{Da}$ and a length of $2.9\,\mathrm{nm}$. The chemical

structure formula is shown in Figure 5.8a.
In contrast to other preparations NR-10 is not dissolvable in classical aqueous ESI solvents and was also not easily chargeable by standard weaker organic acids commonly used in ESI. Instead, almost neat tetrahydrofuran (THF) ($\approx 94\,\%$) as organic component was required in combination with the much stronger trichloroacetic acid (TCA). These rather challenging conditions demanded a number of technical modifications of the component's materials to comply with this "corrosive" environment.
For experiments a finale solution of $10^{-4}\,\mathrm{M}$ NR-10 dissolved in a THF water mixture ((v/v): $94\,\%/6\,\%$) and $2 \times 10^{-6}\,\mathrm{M}$ TCA was used (see A). The m/z resolved spectrum in Figure 5.8b reveals that the dominant ionic species is the doubly protonated monomer. The shoulder towards higher m/z can be attributed to multiple water adducts, in particular a monomer adduct with up to 3 water molecules seems likely from mass determination with a fit via Gaussians. The adducts are filtered from the beam during deposition. From the m/z resolved spectrum there are at present no hints, that the strong acid TCA needed for charging and electrical conductivity reasons, could have had triggered an acidic decomposition of the diacetal protection groups of NR-10 resulting in a truncated or even reactive diketone species. However, since other intensities of currently unknown origin have not been characterized yet, the final prove of this assessment is not possible at this stage. Recovery was determined up to $0.04\,\%$. This value is significant lower than the rates achieved with the other objects discussed before. This is presumably an effect of the quite different electrolyte conditions with low conductivity. This aspect will be investigated further to enhance knowledge about optimization of the solvent conditions. Soft-landing was performed with about $2\,\mathrm{eV}/z$ of kinetic energy. The deposition took place at room temperature.
STM investigations at a temperature of $T = 153\,\mathrm{K}$ reveal formation of large islands of flat lying molecules on the surface with a regular self-assembly, indicating translational and rotational degrees of freedom of the GNRs at room temperature.

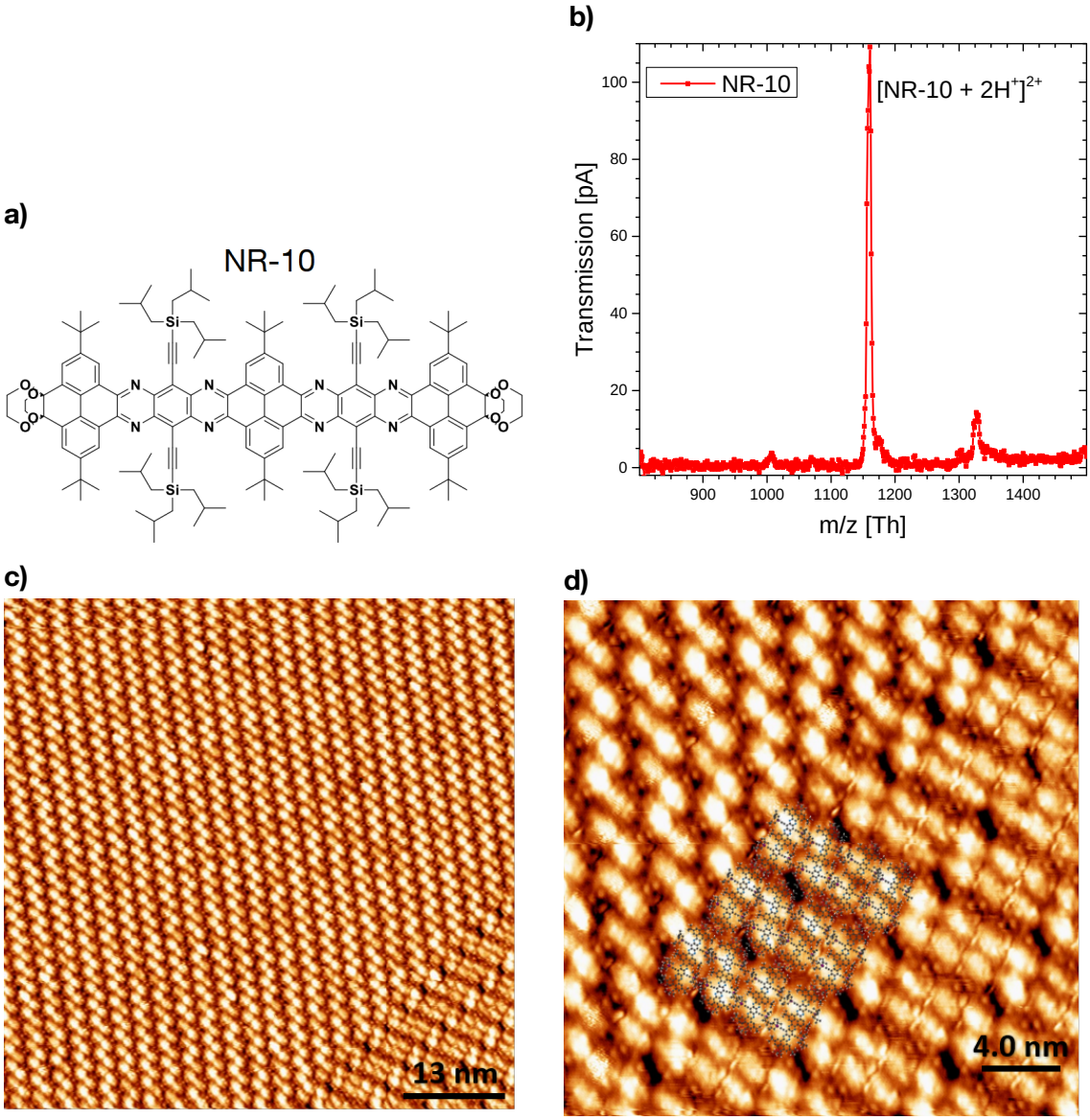

Figure 5.8.: a) structural formula of NR-10 with a molecular mass of 2321.4 Da. From [269] with modifications. b) m/z resolved sprectrum of NR-10 with the most prominent doubly protonated species. c) overview STM measurement of NR-10 molecules on Ag(111). d) zoom-in measurement with a ball-and-stick model indicating the positions of the flat lying molecules on the surface. (U = 2.1 V ; I = 13 pA ; T = 153 K). b) - d) courtesy of [279].

6 Conclusions and Outlook

The aim of this work is the design of a versatile and efficient deposition system – predominantly for complex, reactive, functional organic or bio-molecules and nanoparticles which are not deposable by another clean UHV compatible technique – and to get it operational. In the course of the development of the ES-CIBD system a lot of challenges had to be mastered in very different areas: The well-known ESI process was chosen as the first method implemented to manage the ionization process of the analyte. Here, a medium sized glass emitter ($75\ \mu\mathrm{m}$) was used as a compromise between spray efficiency and solvent throughput. A funnel shaped inlet, the state-of-the-art design adapted from Rauschenbach [99], provides best transfer efficiency of the ions into the first vacuum chamber. A heated transfer capillary manages the pressure difference from ambient to $2\,\mathrm{mbar}$ while the solvent is evaporating. Care has to be taken to complete desolvation and not freeze the droplets due to the enthalpy of vaporization. Thus, selecting suitable geometric dimensions of this capillary was the first challenge. The diameter and length according to Rauschenbach resulted in a very high ion-transmission rate, though the neutral gas load to the first pressure stage was not satisfactory compared to commercial mass spectrometers. A future optimization step will presumably reduce the pumping efforts, while preserving the transmission efficiency.

The ESI source proved to be a very valuable tool to make different species ”fly” which are non-sublimable: small or simple (bio-) organic molecules such as spermine or the tetrapyrole derivative Cu-TPP and ZnPC, nanocarbons like graphene nano-ribbons, peptides and proteins like insulin, lysozyme, BSA, carbonic anhydrase, and finally, several types of DNA (double/single strand) up to $1.7\,\mathrm{MDa}$, with no mass limit in sight. Hereby, the selection of a sprayable solvent turned out to be the dominant challenge. As the first step a solvent mixture has to be composed for a specific analyte – i) capable to dissolve this analyte sufficiently and ii) meeting key requirements on a vaporization and charging carrier. Keeping this in mind, acids or bases added to deliver the necessary electrical conductivity and analyte's charging may have negative impacts to the molecule's integrity e.g. by catalyzing its acidic or basic decomposition or by breaking the protection groups potentially producing reactive derivatives. On the other hand, the corrosivity of e.g. THF as an organic solvent damaging a number of synthetic polymers and thus critical for certain components of the system is a matter of concern. Finally, surface tension, density, viscosity, vapor pressure and electrical conductivity or permittivity, respectively, have to be fine-adjusted to fit the droplet parameters adequately and generating a sprayable droplet size from the solution. Analyzing the resulting mass-to-charge ratios (m/z), the assumptions concerning the chemical stability of the analyte can be verified now. This whole

tradeoff has to be assessed for every analyte species separately.
Having this in mind, an alternative to ESI like electrosonic spray ionization ESSI seems promising, since the spray process is assisted by ultrasound. The most important process of droplet formation might be simplified. An extra spray unit in front of the tube of the capillary would be sufficient. Additionally, controlled heating of the sheath-gas is of interest. Furthermore, small modifications could provide access to other ionization techniques like desorption electrospray ionization (DESI), or laser assisted ionization such as matrix-assisted laser desorption/ionization (MALDI), or cluster sources [280].
Focusing of the ions from the supersonic expansion at the exit of the transfer capillary into the first chamber is the next crucial step. At a pressure in the millibar regime, ion trajectories are still strongly influenced by frequent collisions with the residual gas particles. To prevent ions from being swallowed by the vacuum pump, an ion guide is used to provide a radially confining RF field around the supersonic expansion in combination with an in-axis DC gradient to drag the ions along a desired path. Focusing of ions to a small beam with high intensity and moderate kinetic energy is equally important as low residual gas flow towards the subsequent vacuum regime for efficient differential pumping. The combination of an ion funnel with an ion tunnel to form a so-called Twin ion guide (patent pending [177]) reached superior characteristics in all aspects. The funnel section provides efficient focusing down to a beam diameter of about $1.5\,\mathrm{mm}$ while removing the neutral gas atoms and the subsequent tunnel section forms an elongated pressure interface reducing the residual gas flow by a factor of about 20 compared to typically used thin apertures. Well-chosen electrode geometries, appropriate stacking and an RF supply with adjustable amplitude and frequency are key to reach an ion transmission efficiency up to $80\,\%$ in the Twin. As a further step of optimization, the Twin can be elongated to reduce the beam of neutrals transferred to the next chamber. The interplate distance in the funnel regime can be adapted to optimize the tradeoff between workload, lateral pumping of neutrals and transfer efficiency of the ions.
Downstream, recently developed high order multipole ion guides are used to transfer the ions to UHV. Commercially available multipoles typically employ 4, 6, or 8 solid metal rod electrodes with diameters of at least few mm to ensure mechanical stability. The small wire ion guides (SWIGs, patent pending [178]) used in the ES-CIBD are made from 16 thin wire electrodes with a diameter of $0.18\,\mathrm{mm}$ in case of the smallest used SWIG with an inscribed radius of $1.64\,\mathrm{mm}$. A larger number of electrodes is beneficial for efficient transmission of a wide range of m/z with moderate RF amplitudes. The short penetration depth of the confining field from the electrodes towards the center of the ion guide allow

for acceptance and transmission of an ion beam with a size almost as large as the inscribed radius. The small electrodes compared to the inscribed radius lead to an overall diameter of the ion guide, that is only slightly larger than the ion beam itself. Commercially available multipoles typically use thin apertures across the beam as pressure interfaces to transfer ions to subsequent vacuum regimes, thus interrupting the confining RF field and limiting transmission efficiency. In case of the small overall size of a SWIG the pressure interface can be realized by an elongated tube around the electrodes. The main benefits are a continuous confining RF field over several pressure regimes providing high ion transmission efficiencies and a 10 fold reduced residual gas flow compared to an aperture, though having a slightly larger diameter to provide space for the electrodes. In principle, the whole range from the medium vacuum at the exit of the Twin down to UHV could be spanned by a single highly efficient SWIG. Again, a step of optimization for the SWIGs seams possible. Their electrode dimensions and the pressure interfaces may be further improved to reduce gas-load into the subsequent chambers.

Inside the deposition chamber at UHV conditions, a digitally operated quadrupole mass spectrometer (dQMS) analyzes and purifies the ion beam. The square-wave supply provides control of the RF frequency parameter, leading to an in principle unlimited range of accessible m/z. The strongly improved transmission and resolution properties compared to other competing ion beam deposition devices allows for precise selection of the m/z of transmitted ions while maintaining high intensities for low deposition time. A resolution $\frac{m/z}{\Delta\, m/z}$ (FWHM) up to 150 provide high transmission efficiencies $> 75\,\%$. Reasonable high precise selection with a resolution of above 500 still provides $10 - 15\,\%$ transmission.

Further improvement of the dQMS may be realized via small modifications in the RF supply and implementation of pulse width modulation, auxiliary excitation voltages, or EC signals. Furthermore, the dimensions of the rod-system may be optimized, a longer QMS leads to a better resolution.

Subsequently to the dQMS, a Blade ion guide (patent pending [176]) designed as a conical multipole made of metal sheet electrodes refocuses the ion beam towards the single crystal serving as a deposition target. The landing energy of the ions can be adjusted by changing the potential of the target. For the typical energy distribution of the ions in the beam a value of about $2\,\mathrm{eV/z}$ can be reached, well below the commonly assumed limit for soft-landing of intact molecules of about $10\,\mathrm{eV/z}$.

The width of the energy distribution is probably the most difficult parameter amenable for optimization. Any energy added to the ions which is statistically distributed cannot be ”removed” without breaking the 3rd law of thermodynamics, i.e. the ions cannot be

cooled down, as they are moving in a conservative potential. The center of energetic gravity can be reduced by slowing the ions down by an electric potential, but this keeps the energy distribution constant. Thus, very careful handling of the ions in the regimes of high RF amplitudes especially around the dQMS is necessary. However, a controllable RF frequency allows for adjustable amplitudes for all m/z .

The versatility and quality of depositions originating from the ES-CIBD was proven by investigations of several different chemical species and molecular sizes. The spectrum ranges from the small test molecule Rhodamine B ($m = 443\,\mathrm{Da}$), to a small and thermolabile porphyrine derivate with reactive carboxylic side groups and a mass of $m = 854\,\mathrm{Da}$, over a n-doped graphene nanoribbon (GNR, $m = 2.3\,\mathrm{kDa}$), further to the insulin protein of $\approx 5.8\,\mathrm{kDa}$, to large pUC19 DNA strands with 2686 base pairs and a mass of $m = 1.7\,\mathrm{MDa}$. A high ion beam intensity up to $2.2\,\mathrm{nA}$ allows for fast sample production, typically within $1\,\mathrm{h}$. The time integral over the deposited current – the deposited charge – in combination with the size and charge state of the analyte gives precise information on the coverage of the sample surface. The subsequent investigations via STM show generally clean depositions without any detectable impurities, e.g. from residual gas, solvent molecules from the sprayed solution or fragmented ions.

Another important aspect for rare and expensive molecules is the probability of a molecule, emanating from the emitter of the ESI source to be successfully landed on the surface after transport to UHV and m/z selection. This so-called ”recovery” is defined as the number of deposited units divided by the number of sprayed unity. In the ES-CIBD system recovery reaches up to $4.4\,\%$, well above the values reported in literature. The high transmission efficiency of the entity of all vacuum ion guides combined (about $25\,\%$) as well as high ionization efficiency via a properly prepared spray solution and appropriate spray parameters lead to favourable recoveries.

The data confirms that ESI-CIBD is a highly controllable and efficient deposition method paving the way for sub-molecular to atomic structure analysis of selected fractions of small and large biomolecules at UHV conditions without spurious interference from compromised molecules, debris or contaminations.

Future investigations are planned to optimize the properties of the ES-CIBD and its components. Testing and expanding the range of deposable chemical species and molecule masses, as well as reactive-landing experiments promise a whole new playground in surface and nanoscale science and unique scientific investigations. An improved version of the ES-CIBD including a vacuum suitcase for access to other investigative techniques is under design.

Appendix A.

Experimental Section

Spray solutions:
The test solution consisted of 10^{-4} M Rhodamine B dissolved in $47.5\,\%$ methanol / $47.5\,\%$ water / $5\,\%$ acidic acid (v/v). The electro spray emitter was cut from a fused silica tubing of $75\,\mu$m inner diameter and $360\,\mu$m outer diameter. The flow rate of the syringe pump was approximately $500\,\mathrm{nl/min}$ and the spray voltage was about $2.5\,\mathrm{kV}$.
In case of the porphyrin 10^{-4} M of Cu-TCPP was dissolved in $100\,\%$ v/v methanol. For the electro spray, $20\,\%$ v/v of 10^{-3} M ammonia dissolved in water was added yielding a final solution of 8.3×10^{-5} M Cu-TCPP and 1.7×10^{-4} M ammonia. The electro spray emitter was cut from a fused silica tubing of $75\,\mu$m inner diameter and $360\,\mu$m outer diameter. The flow rate of the syringe pump was approximately $500\,\mathrm{nl/min}$ and the spray voltage was about $-1.95\,\mathrm{kV}$.
In case of Insulin, the stock solution consisted of $1\,\mathrm{g/l}$ dissolved in water which was previously titrated to a pH of 2 by acetic acid. For the electro spray, $47.5\,\%$ v/v of stock solution, $47.5\,\%$ v/v of acetonitrile and $5\,\%$ v/v acidic acid was used. The final concentration was about 8×10^{-5} M Insulin and $\approx 8 \times 10^{-4}$ M acetic acid. The emitter was cut from a $50\,\mu$m inner and $360\,\mu$m outer diameter fused silica tubing and the pumping speed was about $167\,\mathrm{nl/min}$. The spray voltage was about $2.6\,\mathrm{kV}$.
In case of the pUC19, a stock solution of molecules has been dissolved in water. For the electro spray, $66\,\%$ v/v of acetonitrile was added for a final concentration of about $17\,\mathrm{mg/l}$ or 10^{-8} M of pUC19. Full sequence of pUC19 might be found in the NCBI GenBank [281] accession number M77789.2. At these conditions, DNA molecules carry negative charges predominantly on the phosphate backbone accessible for negative mode electrospray ionization. The emitter again was cut from a $75\,\mu$m inner and $360\,\mu$m outer diameter fused silica tubing and the pumping speed was about $500\,\mathrm{nl/min}$. The spray voltage was about $-2.3\,\mathrm{kV}$.
In case of the NR-10, the stock solution consisted of $3.2 \times 10^{-4}\,\mathrm{g/ml}$ dissolved in tetrahydrofuran (THF). Prior to deposition $25\,\mu$l of 3×10^{-5} M TCA dissolved in water was added into $250\,\mu$l THF. Then $125\,\mu$l stock solution was added giving a final concentration of 1×10^{-4} M NR-10 and 2×10^{-6} M TCA. The spray voltage was $3.5\,\mathrm{kV}$ an the flow rate had to be adjusted between $1 - 1.5\,\mu\mathrm{l/min}$ due to instabilities in the spray. An average current of about $55\,\mathrm{pA}$ was reached. The deposition time was about $90\,\mathrm{min}$.

Reagents:
Methanol: Sigma Aldrich, CHROMASOLV $\geq 99.9\,\%$, for HPLC;
Water: Carl Roth, ROTISOLV Ultra LC-MS;

Appendix A. Experimental Section

Acetonitrile: Sigma Aldrich, puriss., absolute
Ammonia: Carl Roth, Ammonia solution 25 %, ROTIPURAN;
Acetic Acid: Fluka Analytical,≥ 99.8 % puriss.
Rhodamine B: Sigma Aldrich, ≥ 95 % (HPLC)
Insulin: Sigma Aldrich, Human Recombinant, dry powder, for research or further manufacturing use
Plasmid DNA pUC19: Carl Roth
Trichloroacetic acid : Carl Roth□≥ 99 %, p.a.
THF: Carl Roth, ≥ 99.5 %
NR10: synthesized by [269]

Bibliography

[1] C. B. Duke. “The birth and evolution of surface science: Child of the union of science and technology”. *Proceedings of the National Academy of Sciences* **100** (2003), 3858–3864. DOI: 10.1073/pnas.0730358100.

[2] G. Binnig, H. Rohrer, C. Gerber and E. Weibel. “Tunneling through a controllable vacuum gap”. *Applied Physics Letters* **40** (1982), 178–180. DOI: 10.1063/1.92999.

[3] G. Binnig, C. F. Quate and C. Gerber. “Atomic Force Microscope”. *Physical Review Letters* **56** (1986), 930–933. DOI: 10.1103/physrevlett.56.930.

[4] G. E. Moore. “Cramming more components onto integrated circuits, Reprinted from Electronics, volume 38, number 8, April 19, 1965, pp.114 ff.” *IEEE Solid-State Circuits Society Newsletter* **11** (2006), 33–35. DOI: 10.1109/N-SSC.2006.4785860.

[5] J. V. Barth, G. Costantini and K. Kern. “Engineering atomic and molecular nanostructures at surfaces”. *Nature* **437** (2005), 671–679. DOI: 10.1038/nature04166.

[6] R. K. Cavin, P. Lugli and V. V. Zhirnov. “Science and Engineering Beyond Moore’s Law”. *Proceedings of the IEEE* **100** (2012), 1720–1749. DOI: 10.1109/jproc.2012.2190155.

[7] J. H. Burroughes, D. D. C. Bradley, A. R. Brown, R. N. Marks, K. Mackay, R. H. Friend, P. L. Burns and A. B. Holmes. “Light-emitting diodes based on conjugated polymers”. *Nature* **347** (1990), 539–541. DOI: 10.1038/347539a0.

[8] S. Günes, H. Neugebauer and N. S. Sariciftci. “Conjugated Polymer-Based Organic Solar Cells”. *Chemical Reviews* **107** (2007), 1324–1338. DOI: 10.1021/cr050149z.

[9] M. R. Wasielewski. “Photoinduced electron transfer in supramolecular systems for artificial photosynthesis”. *Chemical Reviews* **92** (1992), 435–461. DOI: 10.1021/cr00011a005.

[10] D. Gerster, J. Reichert, H. Bi, J. V. Barth, S. M. Kaniber, A. W. Holleitner, I. Visoly-Fisher, S. Sergani and I. Carmeli. "Photocurrent of a single photosynthetic protein". *Nature Nanotechnology* **7** (2012), 673–676. DOI: 10.1038/nnano.2012.165.

[11] S. Mathew, A. Yella, P. Gao, R. Humphry-Baker, B. F. E. Curchod, N. Ashari-Astani, I. Tavernelli, U. Rothlisberger, M. K. Nazeeruddin and M. Grätzel. "Dye-sensitized solar cells with 13% efficiency achieved through the molecular engineering of porphyrin sensitizers". *Nature Chemistry* **6** (2014), 242–247. DOI: 10.1038/nchem.1861.

[12] A. Endo, M. Ogasawara, A. Takahashi, D. Yokoyama, Y. Kato and C. Adachi. "Thermally Activated Delayed Fluorescence from Sn(4+)-Porphyrin Complexes and Their Application to Organic Light Emitting Diodes - A Novel Mechanism for Electroluminescence". *Advanced Materials* **21** (2009), 4802–4806. DOI: 10.1002/adma.200900983.

[13] X. W. Sun, J. Z. Huang, J. X. Wang and Z. Xu. "A ZnO Nanorod Inorganic/Organic Heterostructure Light-Emitting Diode Emitting at 342 nm". *Nano Letters* **8** (2008), 1219–1223. DOI: 10.1021/nl080340z.

[14] Y. Shirai, A. J. Osgood, Y. Zhao, K. F. Kelly and J. M. Tour. "Directional Control in Thermally Driven Single-Molecule Nanocars". *Nano Letters* **5** (2005), 2330–2334. DOI: 10.1021/nl051915k.

[15] T. Kudernac, N. Ruangsupapichat, M. Parschau, B. Maciá, N. Katsonis, S. R. Harutyunyan, K.-H. Ernst and B. L. Feringa. "Electrically driven directional motion of a four-wheeled molecule on a metal surface". *Nature* **479** (2011), 208–211. DOI: 10.1038/nature10587.

[16] G. A. Somorjai and Y. Li. "Impact of surface chemistry". *Proceedings of the National Academy of Sciences* **108** (2010), 917–924. DOI: 10.1073/pnas.1006669107.

[17] K. Zhou and Y. Li. "Catalysis Based on Nanocrystals with Well-Defined Facets". *Angewandte Chemie International Edition* **51** (2011), 602–613. DOI: 10.1002/anie.201102619.

[18] K. Qadir, S. H. Joo, B. S. Mun, D. R. Butcher, J. R. Renzas, F. Aksoy, Z. Liu, G. A. Somorjai and J. Y. Park. "Intrinsic Relation between Catalytic Activity of CO Oxidation on Ru Nanoparticles and Ru Oxides Uncovered with Ambient Pressure XPS". *Nano Letters* **12** (2012), 5761–5768. DOI: 10.1021/nl303072d.

[19] J. Liu, F. R. Lucci, M. Yang, S. Lee, M. D. Marcinkowski, A. J. Therrien, C. T. Williams, E. C. H. Sykes and M. Flytzani-Stephanopoulos. “Tackling CO Poisoning with Single-Atom Alloy Catalysts”. *Journal of the American Chemical Society* **138** (2016), 6396–6399. DOI: 10.1021/jacs.6b03339.

[20] H.-J. Freund. “The Surface Science of Catalysis and More, Using Ultrathin Oxide Films as Templates: A Perspective”. *Journal of the American Chemical Society* **138** (2016), 8985–8996. DOI: 10.1021/jacs.6b05565.

[21] M. D. Marcinkowski, M. T. Darby, J. Liu, J. M. Wimble, F. R. Lucci, S. Lee, A. Michaelides, M. Flytzani-Stephanopoulos, M. Stamatakis and E. C. H. Sykes. “Pt/Cu single-atom alloys as coke-resistant catalysts for efficient C–H activation”. *Nature Chemistry* **10** (2018), 325–332. DOI: 10.1038/nchem.2915.

[22] R. Purrello, S. Gurrieri and R. Lauceri. “Porphyrin assemblies as chemical sensors”. *Coordination Chemistry Reviews* **190-192** (1999), 683–706. DOI: 10.1016/S0010-8545(99)00106-X.

[23] J. Homola, S. S. Yee and G. Gauglitz. “Surface plasmon resonance sensors: review”. *Sensors and Actuators B: Chemical* **54** (1999), 3–15. DOI: 10.1016/s0925-4005(98)00321-9.

[24] H. Song, M. A. Reed and T. Lee. “Single Molecule Electronic Devices”. *Advanced Materials* **23** (2011), 1583–1608. DOI: 10.1002/adma.201004291.

[25] M. L. Perrin, E. Burzurí and H. S. J. van der Zant. “Single-molecule transistors”. *Chemical Society Reviews* **44** (2015), 902–919. DOI: 10.1039/C4CS00231H.

[26] X. Li. “An All-Optical Quantum Gate in a Semiconductor Quantum Dot”. *Science* **301** (2003), 809–811. DOI: 10.1126/science.1083800.

[27] B. M. Maune, M. G. Borselli, B. Huang, T. D. Ladd, P. W. Deelman, K. S. Holabird, A. A. Kiselev, I. Alvarado-Rodriguez, R. S. Ross, A. E. Schmitz, M. Sokolich, C. A. Watson, M. F. Gyure and A. T. Hunter. “Coherent singlet-triplet oscillations in a silicon-based double quantum dot”. *Nature* **481** (2012), 344–347. DOI: 10.1038/nature10707.

[28] S. A. Wolf. “Spintronics: A Spin-Based Electronics Vision for the Future”. *Science* **294** (2001), 1488–1495. DOI: 10.1126/science.1065389.

[29] D. D. Awschalom and M. E. Flatté. “Challenges for semiconductor spintronics”. *Nature Physics* **3** (2007), 153–159. DOI: 10.1038/nphys551.

[30] L. Bogani and W. Wernsdorfer. “Molecular spintronics using single-molecule magnets”. *Nature Materials* **7** (2008), 179–186. DOI: 10.1038/nmat2133.

[31] T. Zambelli, Y. Boutayeb, F. Gayral, J. Lagoute, N. K. Girdhar, A. Gourdon, S. Gauthier, M.-J. Blanco, J.-C. Chambron, V. Heitz and J.-P. Sauvage. “Deposition of large organic molecules in ultra-high vacuum: A comparison between thermal sublimation and pulse-injection”. *International Journal of Nanoscience* **03** (2004), 331–341. DOI: 10.1142/s0219581x04002115.

[32] C. Hamann, R. Woltmann, I.-P. Hong, N. Hauptmann, S. Karan and R. Berndt. “Ultrahigh Vacuum Deposition of Organic Molecules by Electrospray Ionization”. *Rev. Sci. Instrum.* **82** (2011), 033903. DOI: 10.1063/1.3553010.

[33] S. Banerjee and S. Mazumdar. “Electrospray Ionization Mass Spectrometry: A Technique to Access the Information beyond the Molecular Weight of the Analyte”. *International Journal of Analytical Chemistry* **2012** (2012), 1–40. DOI: 10.1155/2012/282574.

[34] J. H. Gross. *Mass Spectrometry*. Ed. by J. H. Gross. Springer International Publishing, 2017. DOI: 10.1007/978-3-319-54398-7.

[35] M. Wilm. “Principles of Electrospray Ionization”. *Molecular & Cellular Proteomics* **10** (2011). DOI: 10.1074/mcp.M111.009407.

[36] J. Fenn, M. Mann, C. Meng, S. Wong and C. Whitehouse. “Electrospray ionization for mass spectrometry of large biomolecules”. *Science* **246** (1989), 64–71. DOI: 10.1126/science.2675315.

[37] J. B. Fenn. “Electrospray Wings for Molecular Elephants (Nobel Lecture)”. *Angew. Chem., Int. Ed.* **42** (2003). Nobelpreis, 3871.

[38] G. Verbeck, W. Hoffmann and B. Walton. “Soft-landing preparative mass spectrometry”. *The Analyst* **137** (2012), 4393. DOI: 10.1039/C2AN35550G.

[39] S. Rauschenbach, M. Ternes, L. Harnau and K. Kern. “Mass Spectrometry as a Preparative Tool for the Surface Science of Large Molecules”. *Annual Review of Analytical Chemistry* **9** (2016), 473–498. DOI: 10.1146/annurev-anchem-071015-041633.

[40] V. Franchetti, B. Solka, W. Baitinger, J. Amy and R. Cooks. “Soft landing of ions as a means of surface modification”. *International Journal of Mass Spectrometry and Ion Physics* **23** (1977), 29–35. DOI: 10.1016/0020-7381(77)80004-1.

[41] V. Grill, J. Shen, C. Evans and R. G. Cooks. “Collisions of ions with surfaces at chemically relevant energies: Instrumentation and phenomena”. *Review of Scientific Instruments* **72** (2001), 3149–3179. DOI: 10.1063/1.1382641.

[42] S. Abb, N. Tarrat, J. Cortés, B. Andriyevsky, L. Harnau, J. C. Sch□n, S. Rauschenbach and K. Kern. “Carbohydrate Self-Assembly at Surfaces: STM Imaging of Sucrose Conformation and Ordering on Cu(100)”. *Angewandte Chemie International Edition* **58** (2019), 8336–8340. DOI: 10.1002/anie.201901340.

[43] Z. Ouyang. “Preparing Protein Microarrays by Soft-Landing of Mass-Selected Ions”. *Science* **301** (2003), 1351–1354. DOI: 10.1126/science.1088776.

[44] S. Rauschenbach, F. L. Stadler, E. Lunedei, N. Malinowski, S. Koltsov, G. Costantini and K. Kern. “Electrospray Ion Beam Deposition of Clusters and Biomolecules”. *Small* **2** (2006), 540–547. DOI: 10.1002/smll.200500479.

[45] N. Vats, Y. Wang, S. Sen, S. Szilagyi, H. Ochner, S. Abb, M. Burghard, W. Sigle, K. Kern, P. A. van Aken and S. Rauschenbach. “Substrate-Selective Morphology of Cesium Iodide Clusters on Graphene”. *ACS Nano* **14** (2020), 4626–4635. DOI: 10.1021/acsnano.9b10053.

[46] M. Scigelova, M. Hornshaw, A. Giannakopulos and A. Makarov. “Fourier Transform Mass Spectrometry”. *Molecular & Cellular Proteomics* **10** (2011). DOI: 10.1074/mcp.M111.009431.

[47] D. Grinfeld, H. Stewart, M. Skoblin, E. Denisov, M. Monastyrsky and A. Makarov. “Space-charge dynamics in Orbitrap mass spectrometers”. *International Journal of Modern Physics A* **34** (2019), 1942007. DOI: 10.1142/S0217751X19420077.

[48] C. N. McEwen and B. S. Larsen. “Fifty years of desorption ionization of nonvolatile compounds”. *International Journal of Mass Spectrometry* **377** (2015), 515–531. DOI: 10.1016/j.ijms.2014.07.018.

[49] M. L. Vestal. “Methods of Ion Generation”. *Chemical Reviews* **101** (2001), 361–376. DOI: 10.1021/cr990104w.

[50] M. E. Monge, G. A. Harris, P. Dwivedi and F. M. Fernández. “Mass Spectrometry: Recent Advances in Direct Open Air Surface Sampling/Ionization”. *Chemical Reviews* **113** (2013), 2269–2308. DOI: 10.1021/cr300309q.

[51] G. Siuzdak, B. Bothner, M. Yeager, C. Brugidou, C. M. Fauquet, K. Hoey and C.-M. Change. “Mass spectrometry and viral analysis”. *Chemistry & Biology* **3** (1996), 45–48. DOI: 10.1016/S1074-5521(96)90083-6.

[52] T. Kaposi. “A Compact and Versatile Electrospray Ion Beam Deposition Setup Advanced Sample Preparation for Experiments in Surface Science”. TUM, 2016.

[53] G. Taylor. “Disintegration of Water Drops in an Electric Field”. *Proc. Roy. Soc. London* **280** (1964), 383. DOI: 10.1098/rspa.1964.0151.

[54] J. Rosell-Llompart, J. Grifoll and I. G. Loscertales. “Electrosprays in the cone-jet mode: From Taylor cone formation to spray development”. *Journal of Aerosol Science* **125** (2018), 2–31. DOI: 10.1016/j.jaerosci.2018.04.008.

[55] M. Cloupeau and B. Prunet-Foch. “Electrostatic spraying of liquids: Main functioning modes”. *Journal of Electrostatics* **25** (1990), 165–184. DOI: 10.1016/0304-3886(90)90025-Q.

[56] J. Grace and J. Marijnissen. “A review of liquid atomization by electrical means”. *Journal of Aerosol Science* **25** (1994), 1005–1019. DOI: 10.1016/0021-8502(94)90198-8.

[57] A. Jaworek and A. Krupa. “Classification of the modes of EHD spraying”. *Journal of Aerosol Science* **30** (1999), 873–893. DOI: 10.1016/S0021-8502(98)00787-3.

[58] I. Marginean, P. Nemes and A. Vertes. “Astable regime in electrosprays”. *Physical Review E* **76** (2007), 026320. DOI: 10.1103/PhysRevE.76.026320.

[59] S. Verdoold, L. Agostinho, C. Yurteri and J. Marijnissen. “A generic electrospray classification”. *Journal of Aerosol Science* **67** (2014), 87–103. DOI: 10.1016/j.jaerosci.2013.09.008.

[60] J. Zeleny. “Instability of Electrified Liquid Surfaces”. *Physical Review* **10** (1917), 1–6. DOI: 10.1103/PhysRev.10.1.

[61] M. Cloupeau and B. Prunet-Foch. “Electrostatic spraying of liquids in cone-jet mode”. *Journal of Electrostatics* **22** (1989), 135–159. DOI: 10.1016/0304-3886(89)90081-8.

[62] R. Juraschek and F. Roellgen. “Pulsation phenomena during electrospray ionization”. *International Journal of Mass Spectrometry* **177** (1998), 1–15. DOI: 10.1016/s1387-3806(98)14025-3.

[63] J. F. D. L. Mora. “The effect of charge emission from electrified liquid cones”. *Journal of Fluid Mechanics* **243** (1992), 561. DOI: 10.1017/s0022112092002829.

[64] K. Tang and A. Gomez. “On the structure of an electrostatic spray of monodisperse droplets”. *Physics of Fluids* **6** (1994), 2317–2332. DOI: 10.1063/1.868182.

[65] J. Rosell-Llompart and J. F. de la Mora. “Generation of monodisperse droplets 0.3 to 4 μm in diameter from electrified cone-jets of highly conducting and viscous liquids”. *Journal of Aerosol Science* **25** (1994), 1093–1119. DOI: 10.1016/0021-8502(94)90204-6.

[66] K. Tang and A. Gomez. “Monodisperse Electrosprays of Low Electric Conductivity Liquids in the Cone-Jet Mode”. *Journal of Colloid and Interface Science* **184** (1996), 500–511. DOI: 10.1006/jcis.1996.0645.

[67] I. Marginean, R. T. Kelly, J. S. Page, K. Tang and R. D. Smith. “Electrospray Characteristic Curves: In Pursuit of Improved Performance in the Nanoflow Regime”. *Anal. Chem.* **79** (2007), 8030. DOI: 10.1021/ac0707986.

[68] I. Marginean, J. S. Page, R. T. Kelly, K. Tang and R. D. Smith. “Effect of pressure on electrospray characteristics”. *Appl. Phys. Lett.* **95** (2009), 184103. DOI: 10.1063/1.3258494.

[69] L. Rayleigh. “On the equilibrium of liquid conducting masses charged with electricity”. *The London, Edinburgh, and Dublin Philosophical Magazine and Journal of Science* **14** (1882), 184–186. DOI: 10.1080/14786448208628425.

[70] D. Duft, T. Achtzehn, R. Mueller, B. A. Huber and T. Leisner. “Rayleigh jets from levitated microdroplets”. *Nature* **421** (2003), 128–128. DOI: 10.1038/421128a.

[71] L. Konermann, E. Ahadi, A. D. Rodriguez and S. Vahidi. “Unraveling the Mechanism of Electrospray Ionization”. *Analytical Chemistry* **85** (2012), 2–9. DOI: 10.1021/ac302789c.

[72] R. G. McAllister, H. Metwally, Y. Sun and L. Konermann. “Release of Native-like Gaseous Proteins from Electrospray Droplets via the Charged Residue Mechanism: Insights from Molecular Dynamics Simulations”. *Journal of the American Chemical Society* **137** (2015), 12667–12676. DOI: 10.1021/jacs.5b07913.

[73] E. Ahadi and L. Konermann. “Ejection of Solvated Ions from Electrosprayed Methanol/Water Nanodroplets Studied by Molecular Dynamics Simulations”. *Journal of the American Chemical Society* **133** (2011), 9354–9363. DOI: 10.1021/ja111492s.

[74] J. V. Iribarne and B. A. Thomson. “On the evaporation of small ions from charged droplets”. *The Journal of Chemical Physics* **64** (1976), 2287–2294. DOI: 10.1063/1.432536.

[75] A. Gomez and K. Tang. “Charge and fission of droplets in electrostatic sprays”. *Physics of Fluids* **6** (1994), 404–414. DOI: 10.1063/1.868037.

[76] E. Ahadi and L. Konermann. “Surface Charge of Electrosprayed Water Nanodroplets: A Molecular Dynamics Study”. *Journal of the American Chemical Society* **132** (2010), 11270–11277. DOI: 10.1021/ja1041989.

[77] M. Dole, L. L. Mack, R. L. Hines, R. C. Mobley, L. D. Ferguson and M. B. Alice. “Molecular Beams of Macroions”. *The Journal of Chemical Physics* **49** (1968), 2240–2249. DOI: 10.1063/1.1670391.

[78] A. T. Iavarone and E. R. Williams. “Mechanism of Charging and Supercharging Molecules in Electrospray Ionization”. *Journal of the American Chemical Society* **125** (2003), 2319–2327. DOI: 10.1021/ja021202t.

[79] P. Kebarle and U. H. Verkerk. “Electrospray: From ions in solution to ions in the gas phase, what we know now”. *Mass Spectrometry Reviews* **28** (2009), 898–917. DOI: 10.1002/mas.20247.

[80] C. J. Hogan, J. A. Carroll, H. W. Rohrs, P. Biswas and M. L. Gross. “Combined Charged Residue-Field Emission Model of Macromolecular Electrospray Ionization”. *Analytical Chemistry* **81** (2009), 369–377. DOI: 10.1021/ac8016532.

[81] A. J. R. Heck and R. H. H. van den Heuvel. “Investigation of intact protein complexes by mass spectrometry”. *Mass Spectrometry Reviews* **23** (2004), 368–389. DOI: 10.1002/mas.10081.

[82] J. F. de la Mora. “Electrospray ionization of large multiply charged species proceeds via Dole’s charged residue mechanism”. *Analytica Chimica Acta* **406** (2000), 93–104. DOI: 10.1016/S0003-2670(99)00601-7.

[83] I. A. Kaltashov and A. Mohimen. “Estimates of Protein Surface Areas in Solution by Electrospray Ionization Mass Spectrometry”. *Anal. Chem.* **77** (2005), 5370–5379. DOI: 10.1021/ac050511+.

[84] E. Ahadi and L. Konermann. “Modeling the Behavior of Coarse-Grained Polymer Chains in Charged Water Droplets: Implications for the Mechanism of Electrospray Ionization”. *The Journal of Physical Chemistry B* **116** (2011), 104–112. DOI: 10.1021/jp209344z.

[85] A. Fersht. “Structure and mechanism in protein science. A guide to enzyme catalysis and protein folding”. *Protein Science* **9** (2008), 207–207. DOI: 10.1110/ps.9.1.207.

[86] L. Konermann, A. D. Rodriguez and J. Liu. “On the Formation of Highly Charged Gaseous Ions from Unfolded Proteins by Electrospray Ionization”. *Analytical Chemistry* **84** (2012), 6798–6804. DOI: 10.1021/ac301298g.

[87] Z. Deng, N. Thontasen, N. Malinowski, G. Rinke, L. Harnau, S. Rauschenbach and K. Kern. “A Close Look at Proteins: Submolecular Resolution of Two- and Three-Dimensionally Folded Cytochrome c at Surfaces”. *Nano Letters* **12** (2012), 2452–2458. DOI: 10.1021/nl3005385.

[88] G. Rinke, S. Rauschenbach, L. Harnau, A. Albarghash, M. Pauly and K. Kern. “Active Conformation Control of Unfolded Proteins by Hyperthermal Collision with a Metal Surface”. *Nano Letters* **14** (2014), 5609–5615. DOI: 10.1021/nl502122j.

[89] I. Peters, H. Metwally and L. Konermann. “Mechanism of Electrospray Supercharging for Unfolded Proteins: Solvent-Mediated Stabilization of Protonated Sites During Chain Ejection”. *Analytical Chemistry* **91** (2019). PMID: 31045347, 6943–6952. DOI: 10.1021/acs.analchem.9b01470.

[90] A. Jaworek. “Micro- and nanoparticle production by electrospraying”. *Powder Technology* **176** (2007), 18–35. DOI: 10.1016/j.powtec.2007.01.035.

[91] D. Simons, B. Colby and C. Evans. “Electrohydrodynamic ionization mass spectrometry - the ionization of liquid glycerol and non-volatile organic solutes”. *Int. J. Mass Spectrom. Ion Phys.* **15** (1974), 291–302. DOI: 10.1016/0020-7381(74)85006-0.

[92] F. Foret, H. Zhou, E. Gangl and B. L. Karger. “Subatmospheric electrospray interface for coupling of microcolumn separations with mass spectrometry”. *Electrophoresis* **21** (2000), 1363–1371. DOI: 10.1002/(SICI)1522-2683(20000401)21:7<1363::AID-ELPS1363>3.0.CO;2-U.

[93] J. S. Page, K. Tang, R. T. Kelly and R. D. Smith. “Subambient Pressure Ionization with Nanoelectrospray Source and Interface for Improved Sensitivity in Mass Spectrometry”. *Analytical Chemistry* **80** (2008), 1800–1805. DOI: 10.1021/ac702354b.

[94] L. C. Chen, M. K. Mandal and K. Hiraoka. “High Pressure (>1 atm) Electrospray Ionization Mass Spectrometry”. *J. Am. Soc. Mass. Spectrom.* **22** (2011), 0539. DOI: 10.1007/s13361-010-0058-8.

[95] L. C. Chen, S. Ninomiya and K. Hiraoka. “Super-atmospheric Pressure Ionization Mass Spectrometry and Its Application to Ultrafast Online Protein Digestion Analysis”. *J. Mass Spectrom.* **51** (2016), 396–411. DOI: 10.1002/jms.3779.

[96] H. Stahnke, S. Kittlaus, G. Kempe, C. Hemmerling and L. Alder. “The influence of electrospray ion source design on matrix effects”. *Journal of Mass Spectrometry* **47** (2012), 875–884. DOI: 10.1002/jms.3047.

[97] C. M. Whitehouse, R. N. Dreyer, M. Yamashita and J. B. Fenn. “Electrospray interface for liquid chromatographs and mass spectrometers”. *Analytical Chemistry* **57** (1985), 675–679. DOI: 10.1021/ac00280a023.

[98] S. K. Chowdhury, V. Katta and B. T. Chait. “An electrospray-ionization mass spectrometer with new features”. *Rapid Communications in Mass Spectrometry* **4** (1990), 81–87. DOI: 10.1002/rcm.1290040305.

[99] M. Pauly, M. Sroka, J. Reiss, G. Rinke, A. Albarghash, R. Vogelgesang, H. Hahne, B. Kuster, J. Sesterhenn, K. Kern and S. Rauschenbach. “A hydrodynamically optimized nano-electrospray ionization source and vacuum interface”. *The Analyst* **139** (2014), 1856. DOI: 10.1039/c3an01836a.

[100] A. P.Bruins. “Electrospray and MALDI Mass Spectrometry Fundamentals, Instrumentation, Practicalities, and Biological Applications”. *Electrospray and MALDI Mass Spectrometry Fundamentals, Instrumentation, Practicalities, and Biological Applications*. Ed. by R. B. Cole. 2.0. Vol. 4. Wiley, 2010. Chap. 4. ESI Source Design, 123.

[101] T. Kenderdine, Z. Xia, E. R. Williams and D. Fabris. “Submicrometer Nanospray Emitters Provide New Insights into the Mechanism of Cation Adduction to Anionic Oligonucleotides”. *Analytical Chemistry* **90** (2018), 13541–13548. DOI: 10.1021/acs.analchem.8b03632.

[102] M. S. Wilm and M. Mann. “Electrospray and Taylor-Cone theory, Dole’s beam of macromolecules at last?” *International Journal of Mass Spectrometry and Ion Processes* **136** (1994), 167–180. DOI: 10.1016/0168-1176(94)04024-9.

[103] G. A. Valaskovic, N. L. Kelleher, D. P. Little, D. J. Aaserud and F. W. McLafferty. “Attomole-Sensitivity Electrospray Source for Large-Molecule Mass Spectrometry”. *Analytical Chemistry* **67** (1995), 3802–3805. DOI: 10.1021/ac00116a030.

[104] J. H. Wahl, D. C. Gale and R. D. Smith. “Sheathless capillary electrophoresis-electrospray ionization mass spectrometry using 10 μm I.D. capillaries: Analyses of tryptic digests of cytochrome c”. *Journal of Chromatography A* **659** (1994), 217–222. DOI: 10.1016/0021-9673(94)85026-7.

[105] R. T. Kelly, J. S. Page, Q. Luo, R. J. Moore, D. J. Orton, K. Tang and R. D. Smith. “Chemically Etched Open Tubular and Monolithic Emitters for Nanoelectrospray Ionization Mass Spectrometry”. *Analytical Chemistry* **78** (2006), 7796–7801. DOI: 10.1021/ac061133r.

[106] M. S. Kriger, K. D. Cook and R. S. Ramsey. “Durable Gold-Coated Fused Silica Capillaries for Use in Electrospray Mass Spectrometry”. *Analytical Chemistry* **67** (1995), 385–389. DOI: 10.1021/ac00098a025.

[107] D. R. Barnidge, S. Nilsson and K. E. Markides. “A Design for Low-Flow Sheathless Electrospray Emitters”. *Analytical Chemistry* **71** (1999), 4115–4118. DOI: 10.1021/ac990252m.

[108] B. B. Schneider, H. Javaheri and T. R. Covey. “Ion sampling effects under conditions of total solvent consumption”. *Rapid Communications in Mass Spectrometry* **20** (2006), 1538–1544. DOI: 10.1002/rcm.2511.

[109] J. S. Page, I. Marginean, E. S. Baker, R. T. Kelly, K. Tang and R. D. Smith. “Biases in ion transmission through an electrospray ionization-mass spectrometry capillary inlet”. *Journal of the American Society for Mass Spectrometry* **20** (2009), 2265–2272. DOI: 10.1016/j.jasms.2009.08.018.

[110] J. T. Cox, I. Marginean, R. D. Smith and K. Tang. "On the Ionization and Ion Transmission Efficiencies of Different ESI-MS Interfaces". *Journal of The American Society for Mass Spectrometry* **26** (2014), 55–62. DOI: 10.1007/s13361-014-0998-5.

[111] S. Arscott and D. Troadec. "Electrospraying from nanofluidic capillary slot". *Applied Physics Letters* **87** (2005), 134101. DOI: 10.1063/1.2058223.

[112] G. A. Schultz, T. N. Corso, S. J. Prosser and S. Zhang. "A Fully Integrated Monolithic Microchip Electrospray Device for Mass Spectrometry". *Analytical Chemistry* **72** (2000), 4058–4063. DOI: 10.1021/ac000325y.

[113] W. Deng, J. F. Klemic, X. Li, M. A. Reed and A. Gomez. "Increase of electrospray throughput using multiplexed microfabricated sources for the scalable generation of monodisperse droplets". *Journal of Aerosol Science* **37** (2006), 696–714. DOI: 10.1016/j.jaerosci.2005.05.011.

[114] C. Yu, F. Tang, X. Qian, Y. Chen, Q. Yu, K. Ni and X. Wang. "Multi-channel microfluidic chip coupling with mass spectrometry for simultaneous electro-sprays and extraction". *Scientific Reports* **7** (2017), 17389. DOI: 10.1038/s41598-017-17764-6.

[115] W. Shui, Y. Yu, X. Xu, Z. Huang, G. Xu and P. Yang. "Micro-electrospray with stainless steel emitters". *Rapid Communications in Mass Spectrometry* **17** (2003), 1541–1547. DOI: 10.1002/rcm.1083.

[116] M.-H. Duby, W. Deng, K. Kim, T. Gomez and A. Gomez. "Stabilization of monodisperse electrosprays in the multi-jet mode via electric field enhancement". *Journal of Aerosol Science* **37** (2006), 306–322. DOI: 10.1016/j.jaerosci.2005.05.013.

[117] R. T. Kelly, J. S. Page, K. Tang and R. D. Smith. "Array of Chemically Etched Fused-Silica Emitters for Improving the Sensitivity and Quantitation of Electrospray Ionization Mass Spectrometry". *Analytical Chemistry* **79** (2007), 4192–4198. DOI: 10.1021/ac062417e.

[118] J. T. Cox, I. Marginean, R. T. Kelly, R. D. Smith and K. Tang. "Improving the Sensitivity of Mass Spectrometry by Using a New Sheath Flow Electrospray Emitter Array at Subambient Pressures". *Journal of The American Society for Mass Spectrometry* **25** (2014), 2028–2037. DOI: 10.1007/s13361-014-0856-5.

[119] I. G. Loscertales, A. Barrero, I. Guerrero, R. Cortijo, M. Marquez and A. M. Gañán-Calvo. “Micro/Nano Encapsulation via Electrified Coaxial Liquid Jets”. *Science* **295** (2002), 1695–1698. DOI: 10.1126/science.1067595.

[120] B. Lin and J. Sunner. “Ion transport by viscous gas flow through capillaries”. *Journal of the American Society for Mass Spectrometry* **5** (1994), 873–885. DOI: 10.1016/1044-0305(94)87012-8.

[121] K. D. D. Gunaratne, V. Prabhakaran, Y. M. Ibrahim, R. V. Norheim, G. E. Johnson and J. Laskin. “Design and performance of a high-flux electrospray ionization source for ion soft landing”. *The Analyst* **140** (2015), 2957–2963. DOI: 10.1039/C5AN00220F.

[122] H. Busch. “Berechnung der Bahn von Kathodenstrahlen im axialsymmetrischen elektromagnetischen Felde”. *Annalen der Physik* **386** (1926), 974–993. DOI: 10.1002/andp.19263862507.

[123] F. Gray. “Electrostatic Electron-Optics”. *Bell System Technical Journal* **18** (1939), 1–31. DOI: 10.1002/j.1538-7305.1939.tb00805.x.

[124] W. Paul and H. Steinwedel. “Ein neues Massenspektrometer ohne Magnetfeld”. *Zeitschrift für Naturforschung A* **8** (1953). DOI: 10.1515/zna-1953-0710.

[125] W. Paul, H. P. Reinhard and U. von Zahn. “Das elektrische Massenfilter als Massenspektrometer und Isotopentrenner”. *Zeitschrift für Physik* **152** (1958), 143–182. DOI: 10.1007/bf01327353.

[126] P. H. Dawson. *Quadrupole Mass Spectrometry and Its Applications.* Ed. by P. H. Dawson. Elsevier, 1976. DOI: 10.1016/c2013-0-04436-2.

[127] P. H. Dawson. “Quadrupole mass analyzers: Performance, design and some recent applications”. *Mass Spectrometry Reviews* **5** (1986), 1–37. DOI: 10.1002/mas.1280050102.

[128] S. M. Osovets. “Use of high-frequency electromagnetic fields for plasma containment and stabilization”. *Journal of Nuclear Energy. Part C, Plasma Physics, Accelerators, Thermonuclear Research* **6** (1964), 421–435. DOI: 10.1088/0368-3281/6/4/308.

[129] M. Reiser. *Theory and Design of Charged Particle Beams*. Wiley Series in Beam Physics and Accelerator Technology. Wiley, 2008.

[130] D. Heddle. *Electrostatic Lens Systems, 2nd edition*. CRC Press, 2000.

[131] J. Orloff. *Handbook of Charged Particle Optics Second Edition*. Ed. by J. Orloff. CRC Press, 2009. DOI: 10.1002/0471443395.img005.

[132] D. Gerlich. "Inhomogeneous RF Fields: A Versatile Tool for the Study of Processes with Slow Ions". *Book* (1992), 1–176. DOI: 10.1002/9780470141397.ch1.

[133] L. Landau and E. Lifshitz. *Mechanics*. Course of theoretical physics. Pergamon, 1960.

[134] D. R. Nicholson. "Introduction to plasma theory". *Journal of Plasma Physics* **28** (1982), b1–b10. DOI: 10.1017/s0022377800000350.

[135] A. Walz. "Design and Optimization of Transmission Performance in an ESIBD System" (2015).

[136] A. V. Tolmachev, H. R. Udseth and R. D. Smith. "Charge Capacity Limitations of Radio Frequency Ion Guides in Their Use for Improved Ion Accumulation and Trapping in Mass Spectrometry". *Analytical Chemistry* **72** (2000), 970–978. DOI: 10.1021/ac990729u.

[137] M. H. Friedman, A. L. Yergey and J. E. Campana. "Fundamentals of ion motion in electric radio-frequency multipole fields". *Journal of Physics E: Scientific Instruments* **15** (1982), 53–56. DOI: 10.1088/0022-3735/15/1/010.

[138] I. Szabo. "New ion-optical devices utilizing oscillatory electric fields. I. Principle of operation and analytical theory of multipole devices with two-dimensional electric fields". *International Journal of Mass Spectrometry and Ion Processes* **73** (1986), 197–235. DOI: 10.1016/0168-1176(86)80001-5.

[139] D. Gerlich. "Low energy reactions measured with guided beams". *Elsevier Science Publisher B.V.* (1986), 541.

[140] R. T. Kelly, A. V. Tolmachev, J. S. Page, K. Tang and R. D. Smith. "The ion funnel: Theory, implementations, and applications". *Mass Spectrometry Reviews* (2009), 294–312. DOI: 10.1002/mas.20232.

[141] A. V. Tolmachev, T. Kim, H. R. Udseth, R. D. Smith, T. H. Bailey and J. H. Futrell. "Simulation-based optimization of the electrodynamic ion funnel for high sensitivity electrospray ionization mass spectrometry". *International Journal of Mass Spectrometry* **203** (2000), 31–47. DOI: 10.1016/s1387-3806(00)00265-7.

[142] N. R. Sernicola. “Aufbau und Simulation einer Ionenoptik im Feinvakuum”. Technische Uni München, 2014.

[143] W. Paul and M. Raether. “Das elektrische Massenfilter”. *Zeitschrift für Physik* **140** (1955), 262–273. DOI: 10.1007/bf01328923.

[144] W. Paul. “Electromagnetic Traps for Charged and Neutral Particles (Nobel Lecture)”. *Angewandte Chemie International Edition in English* **29** (1990), 739–748. DOI: 10.1002/anie.199007391.

[145] D. J. Douglas and N. V. Konenkov. “Mass resolution of linear quadrupole ion traps with round rods”. *Rapid Communications in Mass Spectrometry* **28** (2014), 2252–2258. DOI: 10.1002/rcm.7018.

[146] I.E.Dayton, F.C.Shoemaker and R.F.Mozley. “Measurement of 2-dimensional fields. Part II: Study of a Quadrupole Magnet”. *Rev. Sci. Instrum.* **25** (1954), 0485. DOI: 10.1063/1.1771107.

[147] P. Dawson and Y. Bingqi. “The second stability region of the quadrupole mass filter. I. Ion optical properties”. *Int. J. Mass Spectrom. Ion Processes* **56** (1984), 25–39. DOI: 10.1016/0168-1176(84)85076-4.

[148] P. Dawson and Y. Bingqi. “The second stability region of the quadrupole mass filter. II. Experimental results”. *Int. J. Mass Spectrom. Ion Processes* **56** (1984), 41–50. DOI: 10.1016/0168-1176(84)85077-6.

[149] N. Konenkov and V. Kratenko. “Characteristics of a quadrupole mass filter in the separation mode of a few stability regions”. *Int. J. Mass Spectrom. Ion Processes* **108** (1991), 115–136. DOI: 10.1016/0168-1176(91)85029-L.

[150] W. Chen, B. A. Collings and D. J. Douglas. “High-Resolution Mass Spectrometry with a Quadrupole Operated in the Fourth Stability Region”. *Anal. Chem.* **72** (2000), 540–545. DOI: 10.1021/ac990815u.

[151] Z. Du, D. Douglas, T. Glebova and N. Konenkov. “Peak structure with a quadrupole mass filter operated in the third stability region”. *Int. J. Mass Spectrom.* **197** (2000), 113–121. DOI: 10.1016/S1387-3806(99)00222-5.

[152] G. E. Johnson, D. Gunaratne and J. Laskin. “Soft- and reactive landing of ions onto surfaces: Concepts and applications”. *Mass Spectrometry Reviews* **35** (2015), 439–479. DOI: 10.1002/mas.21451.

[153] J. Shen, Y. H. Yim, B. Feng, V. Grill, C. Evans and R. Cooks. “Soft landing of ions onto self-assembled hydrocarbon and fluorocarbon monolayer surfaces”. *International Journal of Mass Spectrometry* **182-183** (1999), 423–435. DOI: 10.1016/s1387-3806(98)14251-3.

[154] B. Gologan, Z. Takáts, J. Alvarez, J. M. Wiseman, N. Talaty, Z. Ouyang and R. G. Cooks. “Ion soft-landing into liquids: Protein identification, separation, and purification with retention of biological activity”. *Journal of the American Society for Mass Spectrometry* **15** (2004), 1874–1884. DOI: 10.1016/j.jasms.2004.09.005.

[155] J. Alvarez, J. H. Futrell and J. Laskin. “Soft-Landing of Peptides onto Self-Assembled Monolayer Surfaces”. *J. Phys. Chem. A* **110** (2006), 1678. DOI: 10.1021/jp0555044.

[156] S. A. Miller. “Soft-Landing of Polyatomic Ions at Fluorinated Self-Assembled Monolayer Surfaces”. *Science* **275** (1997), 1447–1450. DOI: 10.1126/science.275.5305.1447.

[157] O. Hadjar, J. H. Futrell and J. Laskin. “First Observation of Charge Reduction and Desorption Kinetics of Multiply Protonated Peptides Soft Landed onto Self-Assembled Monolayer Surfaces”. *The Journal of Physical Chemistry C* **111** (2007), 18220–18225. DOI: 10.1021/jp075293y.

[158] J. Laskin, P. Wang and O. Hadjar. “Soft-Landing of Co III (salen) + and Mn III (salen)+ on Self-Assembled Monolayer Surfaces”. *J. Phys. Chem. C* **114** (2010), 5305. DOI: 10.1021/jp904384q.

[159] G. E. Johnson, T. Priest and J. Laskin. “Charge Retention by Gold Clusters on Surfaces Prepared Using Soft Landing of Mass Selected Ions”. *ACS Nano* **6** (2011), 573–582. DOI: 10.1021/nn2039565.

[160] G. E. Johnson, T. Priest and J. Laskin. “Coverage-Dependent Charge Reduction of Cationic Gold Clusters on Surfaces Prepared Using Soft Landing of Mass-Selected Ions”. *The Journal of Physical Chemistry C* **116** (2012), 24977–24986. DOI: 10.1021/jp308795r.

[161] G. Rinke, S. Rauschenbach, S. Schrettl, T. N. Hoheisel, J. Blohm, R. Gutzler, F. Rosei, H. Frauenrath and K. Kern. “Soft-landing electrospray ion beam deposition of sensitive oligoynes on surfaces in vacuum”. *International Journal of Mass Spectrometry* **377** (2015), 228–234. DOI: 10.1016/j.ijms.2014.06.026.

[162] S. Abb, L. Harnau, R. Gutzler, S. Rauschenbach and K. Kern. “Two-dimensional honeycomb network through sequence-controlled self-assembly of oligopeptides”. *Nature Communications* **7** (2016). DOI: 10.1038/ncomms10335.

[163] S. Rauschenbach, R. Vogelgesang, N. Malinowski, J. W. Gerlach, M. Benyoucef, G. Costantini, Z. Deng, N. Thontasen and K. Kern. “Electrospray Ion Beam Deposition: Soft-Landing and Fragmentation of Functional Molecules at Solid Surfaces”. *ACS Nano* **3** (2009), 2901–2910. DOI: 10.1021/nn900022p.

[164] N. Thontasen, G. Levita, N. Malinowski, Z. Deng, S. Rauschenbach and K. Kern. “Grafting Crown Ether Alkali Host-Guest Complexes at Surfaces by Electrospray Ion Beam Deposition”. *The Journal of Physical Chemistry C* **114** (2010), 17768–17772. DOI: 10.1021/jp106123q.

[165] G. Dubey, R. Urcuyo, S. Abb, G. Rinke, M. Burghard, S. Rauschenbach and K. Kern. “Chemical Modification of Graphene via Hyperthermal Molecular Reaction”. *Journal of the American Chemical Society* **136** (2014), 13482–13485. DOI: 10.1021/ja5046499.

[166] P. Wang, O. Hadjar, P. L. Gassman and J. Laskin. “Reactive landing of peptide ions on self-assembled monolayer surfaces: an alternative approach for covalent immobilization of peptides on surfaces”. *Physical Chemistry Chemical Physics* **10** (2008), 1512. DOI: 10.1039/b717617a.

[167] P. Wang and J. Laskin. “Helical Peptide Arrays on Self-Assembled Monolayer Surfaces through Soft and Reactive Landing of Mass-Selected Ions”. *Angew. Chem., Int. Ed.* **47** (2008), 6678. DOI: 10.1002/anie.200801366.

[168] J. Laskin, P. Wang and O. Hadjar. “Soft-landing of Peptide Ions onto Self-assembled Monolayer Surfaces:an Overview”. *Phys. Chem. Chem. Phys.* **10** (2008), 1079. DOI: 10.1039/b712710c.

[169] G. E. Johnson and J. Laskin. “Preparation of Surface Organometallic Catalysts by Gas-Phase Ligand Stripping and Reactive Landing of Mass-Selected Ions”. *Chem. Eur. J.* **16** (2010), 14433. DOI: 10.1002/chem.201002292.

[170] W.-P. Peng, G. E. Johnson, I. C. Fortmeyer, P. Wang, O. Hadjar, R. G. Cooks and J. Laskin. “Redox Chemistry in Thin Layers of Organometallic Complexes Prepared Using Ion Soft Landing”. *Phys. Chem. Chem. Phys.* **13** (2011), 267. DOI: 10.1039/c0cp01457e.

[171] J. O’Hanlon. *A User’s Guide to Vacuum Technology*. John Wiley & Sons, 2003.

[172] K. Jousten. *Handbook of Vacuum Technology*. John Wiley & Sons, 2008. DOI: 10.1002/9783527688265.

[173] G. Binnig and H. Rohrer. "Scanning tunneling microscopy—from birth to adolescence". *Reviews of Modern Physics* **59** (1987), 615–625. DOI: 10.1103/revmodphys.59.615.

[174] C. J. Chen. "Introduction to Scanning Tunneling Microscopy" (2007). DOI: 10.1093/acprof:oso/9780199211500.001.0001.

[175] G. Gamow. "Zur Quantentheorie des Atomkernes". *Zeitschrift für Physik* **51** (1928), 204–212. DOI: 10.1007/BF01343196.

[176] H. Schlichting, J. Barth and A. Walz. "Ion guide comprising electrode plates and ion beam deposition system". European patent application 18165950.9. International patent application PCT/EP2019/058723. (05.04.2018).

[177] T. Kaposi, H. Schlichting, J. Barth and A. Walz. "Partly sealed ion guide and ion beam deposition system". European patent application 18165948.3. International patent application PCT/EP2019/058678. (05.04.2018).

[178] T. Kaposi, H. Schlichting, J. Barth and A. Walz. "Ion guide comprising electrode wires and ion beam deposition system". European patent application 18165949.1. International patent application PCT/EP2019/058679. (05.04.2018).

[179] S. Fischer. "Combined STM and X-ray spectroscopy study of surface-confined biologically relevant molecules". PhD thesis. Technische Universität München, 2013.

[180] S. C. Oh. "Single layer films of functional molecules on noble metal surfaces visited by scanning tunneling microscopy and X-ray spectroscopy". PhD thesis. Technische Universität München, 2014.

[181] L. Bernier, H. Pinfold, M. Pauly, S. Rauschenbach and J. Reiss. "Gas Flow and Ion Transfer in Heated ESI Capillary Interfaces". *Journal of The American Society for Mass Spectrometry* **29** (2018), 761–773. DOI: 10.1007/s13361-018-1895-0.

[182] L. Bernier, M. Taesch, S. Rauschenbach and J. Reiss. "Transfer conditions and transmission bias in capillaries of vacuum interfaces". *International Journal of Mass Spectrometry* **447** (2020), 116239. DOI: 10.1016/j.ijms.2019.116239.

[183] T. Buberl. "Charakterisierung neuartiger Ionenleiter für ionenstrahlgestützte Deposition: Experiment und Simulation". Technische Uni München, 2013.

[184] D. Reinisch. “Entwurf und Aufbau einer ESI-Quelle”. Technische Uni München, 2013.

[185] D. Gerlich. “Experimental Investigations of Ion-Molecule Reactions Relevant to Interstellar Chemistry”. *J. Chem. Soc., Faraday Trans.* **89** (1993), 2199. DOI: 10.1039/FT9938902199.

[186] D. Gerlich. “lon-Neutral Collisions in a 22-Pole Trap at Very Low Energies”. *Phys. Scr.* **T59** (1995), 256. DOI: 10.1088/0031-8949/1995/T59/035.

[187] A. Dzhonson, D. Gerlich, E. J. Bieske and J. P. Maier. “Apparatus for the study of electronic spectra of collisionally cooled cations:para-dichlorobenzene”. *J. Mol. Struct.* **795** (2006), 93. DOI: 10.1016/j.molstruc.2005.11.044.

[188] R. Otto, P. Hlavenka, S. Trippel, J. Mikosch, K. Singer, M. Weidemüller and R. Wester. “How can a 22-pole ion trap exhibit ten local minima in the effective potential?” *Journal of Physics B: Atomic, Molecular and Optical Physics* **42** (2009), 154007. DOI: 10.1088/0953-4075/42/15/154007.

[189] J. A. Richards, R. M. Huey and J. Hlller. “A New Operating Mode for the Quadrupole Mass Filter”. *Int. J. Mass Spectrom. Ion Phys.* **012** (1973), 317. DOI: 10.1016/0020-7381(73)80102-0.

[190] D. L. Shinholt, S. N. Anthony, A. W. Alexander, B. E. Draper and M. F. Jarrold. “A frequency and amplitude scanned quadrupole mass filter for the analysis of high m/z ions”. *Rev. Sci. Instrum.* **85** (2014), 113109. DOI: 10.1063/1.4900627.

[191] G. F. Brabeck and P. T. Reilly. “Mapping ion stability in digitally driven ion traps and guides”. *Int. J. Mass Spectrom.* **364** (2014), 1–8. DOI: 10.1016/j.ijms.2014.03.008.

[192] N. Konenkov, L. Cousins, V. Baranov and M. Sudakov. “Quadrupole Mass Filter Operation with Auxiliary Quadrupolar Excitation: Theory and Experiment”. *Int. J. Mass Spectrom.* **208** (2001), 017. DOI: 10.1016/S1387-3806(01)00375-X.

[193] N. V. Konenkov, M. Sudakov and D. J. Douglas. “Matrix methods for the calculation of stability diagrams in quadrupole mass spectrometry”. *J Am Soc Mass Spectrom* **13** (2002), 597–613. DOI: 10.1016/S1044-0305(02)00365-3.

[194] D. Douglas. “Linear quadrupoles in mass spectrometry”. *Mass Spectrometry Reviews* **28** (2009), 937–960. DOI: 10.1002/mas.20249.

[195] D. J. Douglas and N. V. Konenkov. “Quadrupole mass filter operation with dipole direct current and quadrupole radiofrequency excitation”. *Rapid Commun. Mass Spectrom.* **32** (2018), 1971–1977. DOI: 10.1002/rcm.8266.

[196] E. P. Sheretov. “Opportunities for Optimization of the RF Signal Applied to Electrodes of Quadrupole Mass Spectrometers. Part I. General Theory”. *Int. J. Mass Spectrom.* **198** (2000), 083. DOI: 10.1016/S1387-3806(00)00165-2.

[197] E. P. Sheretov, B. I. Kolotilin, N. V. Veselkin, A. V. Brykov and E. V. Fedosov. “Opportunities for Optimization of the RF Signal Applied to Electrodes of Quadrupole Mass Spectrometers. Part II. EC Signals”. *Int. J. Mass Spectrom.* **198** (2000), 097. DOI: 10.1016/S1387-3806(00)00164-0.

[198] C. Ding, N. V. Konenkov and D. J. Douglas. “Quadrupole mass filters with octopole fields”. *Rapid Commun. Mass Spectrom.* **17** (2003), 2495. DOI: 10.1002/rcm.1235.

[199] A. Moradian and D. J. Douglas. “Experimental investigation of mass analysis using an island of stability with a quadrupole with 2.0% added octopole field”. *Rapid Communications in Mass Spectrometry* **21** (2007), 3306–3310. DOI: 10.1002/rcm.3224.

[200] A. Moradian and D. J. Douglas. “Mass selective axial ion ejection from linear quadrupoles with added octopole fields”. *Journal of the American Society for Mass Spectrometry* **19** (2008), 270–280. DOI: 10.1016/j.jasms.2007.10.025.

[201] Z. Xiao, X. Zhao and D. J. Douglas. “Quadrupole mass filters with added hexapole fields”. *Rapid Communications in Mass Spectrometry* **24** (2010), 1985–1992. DOI: 10.1002/rcm.4596.

[202] S. Rauschenbach. “Electrospray Ion Beam Deposition and Mass Spectrometry of Nonvolatile Molecules and Nanomaterials”. Ecole Polytechnique Federal de Lausanne, 2007.

[203] O. Hadjar, P. Wang, J. H. Futrell, Y. Dessiaterik, Z. Zhu, J. P. Cowin, M. J. Iedema and J. Laskin. “Design and Performance of an Instrument for Soft Landing of Biomolecular Ions on Surfaces”. *Anal. Chem.* **79** (2007), 6566. DOI: 10.1021/ac070600h.

[204] P. Su, H. Hu, J. Warneke, M. E. Belov, G. A. Anderson and J. Laskin. “Design and Performance of a Dual-Polarity Instrument for Ion Soft Landing”. *Anal. Chem.* **91** (2019), 5904–5912. DOI: 10.1021/acs.analchem.9b00309.

[205] P. Dawson. “Ion Optical Properties of Quadrupole Mass Filters”. *Advances in Electronics and Electron Physics* **53** (1980), 153–208. DOI: 10.1016/S0065-2539(08)60260-7.

[206] M. A. Röttgen, K. Judai, J.-M. Antonietti, U. Heiz, S. Rauschenbach and K. Kern. “Conical Octopole Ion Guide: Design, Focusing, and Its Application to the Deposition of Low Energetic Clusters”. *Rev. Sci. Instrum.* **77** (2006), 013302. DOI: 10.1063/1.2162439.

[207] Q. Shao and J. Zhao. “Ion trajectory simulations of a conical octopole ion guide and its comparison with a parallel one in chemical ionization mass spectrometric applications”. *Rapid Communications in Mass Spectrometry* **32** (2018), 965–972. DOI: 10.1002/rcm.8129.

[208] Agilent. “The Innovations that power the Ultivo Triple Quadrupole LC/MS – Cyclone Ion Guide”. *Retrieved from URL: https://www.agilent.com/en/products/mass-spectrometry/lc-ms-instruments/triple-quadrupole-lc-ms/ultivo-triple-quadrupole-lc-ms/cyclone-ion (accessed on 13.07.2020)* ().

[209] R. Steinacher. “Development of Soft Landing Instrumentation for SPM Investigation Design and Implementation of an Ion Guide, ESI Source, and the System Peripherals”. Technische Uni München, 2012.

[210] H. Schlichting. private communication. 2020.

[211] M. Walz. “Design of an electronic control unit for an ESIBD System”. TUM, 2016.

[212] AnalogDevices. “Tutorial MT-097: Dealing with High-Speed Logic, Rev.0, 01/09, WK”. *Retrieved from URL: https://www.analog.com/media/en/training-seminars/tutorials/MT-097.pdf (accessed on 31.07.2020)* (2009).

[213] D. A. Dahl, J. E. Delmore and A. D. Appelhans. “SIMION PC/PS2 electrostatic lens design program”. *Review of Scientific Instruments* **61** (1990), 607–609. DOI: 10.1063/1.1141932.

[214] D. A. Dahl. “S for the personal computer in reflection”. *International Journal of Mass Spectrometry* **200** (2000), 3–25. DOI: 10.1016/s1387-3806(00)00305-5.

[215] D. J. Manura. *Simion 8.0*. Scientific Instrument Services, Inc. 2008.

[216] V. Lollobrigida, G. Greco, D. Simeone, F. Offi, A. Verna and G. Stefani. “Electron trajectory simulations of time-of-flight spectrometers for core level high-energy photoelectron spectroscopy at pulsed X-ray sources”. *Journal of Electron Spectroscopy and Related Phenomena* **205** (2015), 98–105. DOI: 10.1016/j.elspec.2015.09.005.

[217] G. Schiwietz, M. Beye, D. Kühn and G. Xiao. “The retarding Bessel–Box—An electron-spectrometer designed for pump/probe experiments”. *Journal of Electron Spectroscopy and Related Phenomena* **203** (2015), 51–59. DOI: 10.1016/j.elspec.2015.06.011.

[218] J. C. Schwartz, M. W. Senko and J. E. P. Syka. “A two-dimensional quadrupole ion trap mass spectrometer”. *Journal of the American Society for Mass Spectrometry* **13** (2002), 659–669. DOI: 10.1016/s1044-0305(02)00384-7.

[219] A. D. Appelhans and D. A. Dahl. *SIMION 8.0 SDS User Program Documentation*. 2004.

[220] A. D. Appelhans and D. A. Dahl. “SIMION ion optics simulations at atmospheric pressure”. *International Journal of Mass Spectrometry* **244** (2005), 1–14. DOI: 10.1016/j.ijms.2005.03.010.

[221] P. E. Miller. “Investigations of the RF-only Quadrupole Mass Analyzer”. University Arizona, Retrieved from URL: https://repository.arizona.edu/handle/10150/188109 (accessed on 31.07.2020), 1985.

[222] P. E. Miller and M. Denton. “The transmission properties of an RF-only quadrupole mass filter”. *International Journal of Mass Spectrometry and Ion Processes* **72** (1986), 223–238. DOI: 10.1016/0168-1176(86)80021-0.

[223] P. E. Miller and M. B. Denton. “A notch rejection quadrupole mass filter”. *International Journal of Mass Spectrometry and Ion Processes* **96** (1990), 17–26. DOI: 10.1016/0168-1176(90)80039-6.

[224] A. J. Alexander, E. W. Dyer and R. K. Boyd. “Transmission characteristics of a radio-frequency-only quadrupole gas-collision cell at high axial energies in a hybrid tandem mass spectrometer”. *Rapid Communications in Mass Spectrometry* **3** (1989), 364–372. DOI: 10.1002/rcm.1290031013.

[225] J. Wei. *Extrel Application Note GT-715D: Transmission Characteristics of RF-Only Devices: Quadrupoles and Octupoles as Ion Pipes, Retrieved from URL: https://www.extrel.com/Module/Catalog/CatalogDocFileFile/mobile/Clusters___Biomolecules___Nanoparticles/Mass_Selection_and_Deposition/GT-715_Transmission_of_Ion_Guides/GT-715D_Transmission_of_Ion_Guides.pdf?id=46 (accessed on 31.07.2020)*. (1998).

[226] F. Muntean. "Transmission study for r.f.-only quadrupoles by computer simulation". *International Journal of Mass Spectrometry and Ion Processes* **151** (1995), 197–206. DOI: 10.1016/0168-1176(95)04319-5.

[227] T. A. Blake, Z. Ouyang, J. M. Wiseman, Z. Takats, A. J. Guymon, S. Kothari and R. G. Cooks. "Preparative Linear Ion Trap Mass Spectrometer for Separation and Collection of Purified Proteins and Peptides in Arrays Using Ion Soft Landing". *Anal. Chem.* **76** (2004), 6293. DOI: 10.1021/ac048981b.

[228] Z. Nie, G. Li, M. P. Goodwin, L. Gao, J. Cyriac and R. G. Cooks. "In situ SIMS analysis and reactions of surfaces prepared by soft landing of mass-selected cations and anions using an ion trap mass spectrometer". *Journal of the American Society for Mass Spectrometry* **20** (2009), 949–956. DOI: 10.1016/j.jasms.2009.02.019.

[229] Sigmaaldrich. *Safety data sheet, Insulin, Recombinant Human, Product Number : 91077C, Version 6.3, Revision Date 03.02.2020*. Sigma-Aldrich Chemie GmbH.

[230] A. H. Pekar and B. H. Frank. "Conformation of proinsulin. Comparison of insulin and proinsulin self-association at neutral pH". *Biochemistry* **11** (1972), 4013–4016. DOI: 10.1021/bi00772a001.

[231] E. J. Nettleton, P. Tito, M. Sunde, M. Bouchard, C. M. Dobson and C. V. Robinson. "Characterization of the Oligomeric States of Insulin in Self-Assembly and Amyloid Fibril Formation by Mass Spectrometry". *Biophysical Journal* **79** (2000), 1053–1065. DOI: 10.1016/S0006-3495(00)76359-4.

[232] A. K. Attri, C. Fernandez and A. P. Minton. "pH-dependent self-association of zinc-free insulin characterized by concentration-gradient static light scattering". *Biophysical Chemistry* **148** (2010), 28–33. DOI: 10.1016/j.bpc.2010.02.002.

[233] M. Lin and C. K. Larive. "Detection of insulin aggregates with pulsed-field gradient nuclear magnetic resonance spectroscopy." *Anal Biochem* **229** (1995), 214–220.

[234] W. Kadima, M. Roy, R. W.-K. Lee, N. C. Kaarsholmj and M. F. Dunn. “Studies of the Association and Conformational Properties of Metal-free Insulin in Alkaline Sodium Chloride Solutions by One- and Two-dimensional ‘H NMR*”. *The Journal of biological chemistry* **267** (1992), 8963–8970.

[235] M. F. Dunn. “Zinc-Ligand Interactions Modulate Assembly and Stability of the Insulin Hexamer - A Review”. *BioMetals* **18** (2005), 295–303. DOI: 10.1007/s10534-005-3685-y.

[236] A. K. Attri, C. Fernandez and A. P. Minton. “Self-association of Zn-insulin at neutral pH: Investigation by concentration gradient-static and dynamic light scattering”. *Biophysical Chemistry* **148** (2010), 23–27. DOI: 10.1016/j.bpc.2010.02.001.

[237] W. Kadima, L. Øgendal, R. Bauer, N. Kaarsholm, K. Brodersen, J. F. Hansen and P. Porting. “The influence of ionic strength and pH on the aggregation properties of zinc-free insulin studied by static and dynamic laser light scattering”. *Biopolymers* **33** (1993), 1643–1657. DOI: 10.1002/bip.360331103.

[238] S. Rahuel-Clermont, C. A. French, N. C. Kaarsholm and M. F. Dunn. “Mechanisms of Stabilization of the Insulin Hexamer through Allosteric Ligand Interactions†”. *Biochemistry* **36** (1997), 5837–5845. DOI: 10.1021/bi963038q.

[239] U. Derewenda, Z. Derewenda, G. G. Dodson, R. E. Hubbard and F. Korber. “Molecular Structure of insulin: The insulin monomer and its assembly”. *British Medical Bulletin* **45** (1989), 4–18. DOI: 10.1093/oxfordjournals.bmb.a072320.

[240] A. Kumar and P. Venkatesu. “Prevention of insulin self-aggregation by a protic ionic liquid”. *RSC Advances* **3** (2013), 362–367. DOI: 10.1039/c2ra22277a.

[241] G. Bonvin, S. Rudaz and J. Schappler. “In-spray supercharging of intact proteins by capillaryelectrophoresis–electrospray ionization–mass spectrometry usingsheath liquid interface”. *Analytica Chimica Acta* **813** (2014), 97–105. DOI: 10.1016/j.aca.2013.12.043.

[242] I. A. Kaltashov and A. Mohimen. “Estimates of Protein Surface Areas in Solution by Electrospray Ionization Mass Spectrometry”. *Analytical Chemistry* **77** (2005), 5370. DOI: 10.1021/ac050511+.

[243] A. Schmidt, M. Karas and T. Dülcks. “Effect of different solution flow rates on analyte ion signals in nano-ESI MS, or: when does ESI turn into nano-ESI?” *Journal of the American Society for Mass Spectrometry* **14** (2003), 492–500. DOI: 10.1016/S1044-0305(03)00128-4.

[244] D. Fabris and C. Fenselau. “Characterization of Allosteric Insulin Hexamers by Electrospray Ionization Mass Spectrometry”. *Analytical Chemistry* **71** (1999), 384–387. DOI: 10.1021/ac980753s.

[245] U. K. B. Raja, S. Injeti, T. Culver, J. W. McCabe and L. A. Angel. “Probing the Stability of Insulin Oligomers Using Electrospray Ionization Ion Mobility Mass Spectrometry”. *European Journal of Mass Spectrometry* **21** (2015), 759–774. DOI: 10.1255/ejms.1396.

[246] J.-N. Longchamp, S. Rauschenbach, S. Abb, C. Escher, T. Latychevskaia, K. Kern and H.-W. Fink. “Imaging proteins at the single-molecule level”. *PNAS* **114** (2017), 1474–1479. DOI: 10.1073/pnas.1614519114.

[247] Q. Hu and J. Laskin. “Secondary Structures of Ubiquitin Ions Soft-Landed onto Self-Assembled Monolayer Surfaces”. *J. Phys. Chem. B* **120** (2016), 4927–4936. DOI: 10.1021/acs.jpcb.6b02448.

[248] B. Gologan, J. R. Green, J. Alvarez, J. Laskin and R. G. Cooks. “Ion / Surface Reactions and Ion Soft-landing”. *Phys. Chem. Chem. Phys.* **07** (2005), 1490. DOI: 10.1039/b418056a.

[249] J. Otsuki. “STM studies on porphyrins”. *Coordination Chemistry Reviews* **254** (2010), 2311–2341. DOI: 10.1016/j.ccr.2009.12.038.

[250] W. Auwärter, D. Ecija, F. Klappenberger and J. V. Barth. “Porphyrins at interfaces”. *Nat. Chem.* **7** (2015), 105–120. DOI: 10.1038/nchem.2159.

[251] D. Touboul and R. Zenobi. “A simple model for exploring conformation of highly-charged electrosprayed single-stranded oligonucleotides”. *Chem. Commun.* (2009), 298–300. DOI: A10.1039/b816801f.

[252] M. Röckert, M. Franke, Q. Tariq, D. Lungerich, N. Jux, M. Stark, A. Kaftan, S. Ditze, H. Marbach, M. Laurin, J. Libuda, H.-P. Steinrück and O. Lytken. “Insights in Reaction Mechanistics: Isotopic Exchange during the Metalation of Deuterated Tetraphenyl-21,23D-porphyrin on Cu(111)”. *The Journal of Physical Chemistry C* **118** (2014), 26729–26736. DOI: 10.1021/jp507303h.

[253] H. Marbach. “Surface-Mediated in Situ Metalation of Porphyrins at the Solid–Vacuum Interface”. *Accounts of Chemical Research* **48** (2015), 2649–2658. DOI: 10.1021/acs.accounts.5b00243.

[254] V. V. Korolkov, S. A. Svatek, A. Summerfield, J. Kerfoot, L. Yang, T. Taniguchi, K. Watanabe, N. R. Champness, N. A. Besley and P. H. Beton. “van der Waals-Induced Chromatic Shifts in Hydrogen-Bonded Two-Dimensional Porphyrin Arrays on Boron Nitride”. *ACS Nano* **9** (2015), 10347–10355. DOI: 10.1021/acsnano.5b04443.

[255] P. Knecht. private communication, data is soon to be published in a paper or doctoral thesis. 2020.

[256] C. Yanisch-Perron, J. Vieira and J. Messing. “Improved M13 phage cloning vectors and host strains: nucleotide sequences of the M13mpl8 and pUC19 vectors”. *Gene* **33** (1985), 103–119. DOI: 10.1016/0378-1119(85)90120-9.

[257] A. Nordheim and R. Knippers. *Molekulare Genetik*. Thieme Verlag KG, 2018. DOI: ISBN978-3-13-242637-5.

[258] X. Cheng, C. Il, Wu, Bakhtiar, Springer, Morris, Bruce, Anderson, Edmonts and Smith. “Molecular weight determination of plasmid DNA using electrospray ionization mass spectrometry”. *Nucleic Acids Research* **24** (1996), 2183–2189. DOI: 10.1093/nar/24.11.2183.

[259] D. R. Lide. “CRC Handbook of Chemistry and Physics: A Ready-Reference of Chemical and Physical Data, 85th ed”. *Journal of the American Chemical Society* **127** (2005), 4542–4542. DOI: 10.1021/ja041017a.

[260] H. Lederer, R. P. May, J. K. Kjems, G. Baer and H. Heumann. “Solution structure of a short DNA fragment studied by neutron scattering”. *European Journal of Biochemistry* **161** (1986), 191–196. DOI: 10.1111/j.1432-1033.1986.tb10141.x.

[261] M. Adrian, B. ten Heggeler-Bordier, W. Wahli, A. Z. Stasiak, A. Stasiak and J. Dubochet. “Direct visualization of supercoiled DNA molecules in solution.” *The EMBO Journal* **9** (1990), 4551–4554. DOI: 10.1002/j.1460-2075.1990.tb07907.x.

[262] J. C. Schultz, C. A. Hack and W. H. Benner. “Mass determination of megadalton-DNA electrospray ions using charge detection mass spectrometry”. *J. Am. Soc. Mass. Spectrom.* **9** (1998), 305–313. DOI: 10.1016/S1044-0305(97)00290-0.

[263] S. D. Fuerstenau and W. H. Benner. “Molecular weight determination of megadalton DNA electrospray ions using charge detection time-of-flight mass spectrometry”. *Rapid Commun. Mass Spectrom.* **9** (1995), 1528–1538. DOI: 10.1002/rcm.1290091513.

[264] K. Stoiber. private communication, data is soon to be published in a paper or doctoral thesis. 2020.

[265] K. Terasaki and T. Yokoyama. “Structural Modification of DNA Studied by Scanning Tunneling Microscopy”. *J. Phys. Chem. B* **123** (2019), 1780–1783. DOI: 10.1021/acs.jpcb.8b12100.

[266] H. Tanaka. “Scanning tunneling microscopy imaging and manipulation of DNA oligomer adsorbed on Cu(111) surfaces by a pulse injection method”. *Journal of Vacuum Science & Technology B: Microelectronics and Nanometer Structures* **15** (1997), 602. DOI: 10.1116/1.589299.

[267] H. Tanaka and T. Kawai. “Visualization of detailed structures within DNA”. *Surface Science* **539** (2003), L531–L536. DOI: 10.1016/S0039-6028(03)00794-5.

[268] Y. Yoshida, Y. Nojima, H. Tanaka and T. Kawai. “Scanning tunneling spectroscopy of single-strand deoxyribonucleic acid for sequencing”. *Journal of Vacuum Science & Technology B: Microelectronics and Nanometer Structures* **25** (2007), 242. DOI: 10.1116/1.2431180.

[269] D. Cortizo-Lacalle, J. P. Mora-Fuentes, K. Strutyński, A. Saeki, M. Melle-Franco and A. Mateo-Alonso. “Monodisperse N-Doped Graphene Nanoribbons Reaching 7.7 Nanometers in Length”. *Angewandte Chemie International Edition* **57** (2018), 703–708. DOI: 10.1002/anie.201710467.

[270] L. Jiao, X. Wang, G. Diankov, H. Wang and H. Dai. “Facile synthesis of high-quality graphene nanoribbons”. *Nature Nanotechnology* **5** (2010), 321–325. DOI: 10.1038/nnano.2010.54.

[271] D. Wei, L. Xie, K. K. Lee, Z. Hu, S. Tan, W. Chen, C. H. Sow, K. Chen, Y. Liu and A. T. S. Wee. “Controllable unzipping for intramolecular junctions of graphene nanoribbons and single-walled carbon nanotubes”. *Nature Communications* **4** (2013). DOI: 10.1038/ncomms2366.

[272] Y. Zhong, B. Kumar, S. Oh, M. T. Trinh, Y. Wu, K. Elbert, P. Li, X. Zhu, S. Xiao, F. Ng, M. L. Steigerwald and C. Nuckolls. "Helical Ribbons for Molecular Electronics". *Journal of the American Chemical Society* **136** (2014), 8122–8130. DOI: 10.1021/ja503533y.

[273] Z. Fei, M. D. Goldflam, J.-S. Wu, S. Dai, M. Wagner, A. S. McLeod, M. K. Liu, K. W. Post, S. Zhu, G. C. A. M. Janssen, M. M. Fogler and D. N. Basov. "Edge and Surface Plasmons in Graphene Nanoribbons". *Nano Letters* **15** (2015), 8271–8276. DOI: 10.1021/acs.nanolett.5b03834.

[274] X. Meng, C. Yu, X. Song, Y. Liu, S. Liang, Z. Liu, C. Hao and J. Qiu. "Nitrogen-Doped Graphene Nanoribbons with Surface Enriched Active Sites and Enhanced Performance for Dye-Sensitized Solar Cells". *Advanced Energy Materials* **5** (2015), 1500180. DOI: 10.1002/aenm.201500180.

[275] Y. Zhong, M. T. Trinh, R. Chen, G. E. Purdum, P. P. Khlyabich, M. Sezen, S. Oh, H. Zhu, B. Fowler, B. Zhang, W. Wang, C.-Y. Nam, M. Y. Sfeir, C. T. Black, M. L. Steigerwald, Y.-L. Loo, F. Ng, X.-Y. Zhu and C. Nuckolls. "Molecular helices as electron acceptors in high-performance bulk heterojunction solar cells". *Nature Communications* **6** (2015). DOI: 10.1038/ncomms9242.

[276] T. J. Sisto, Y. Zhong, B. Zhang, M. T. Trinh, K. Miyata, X. Zhong, X.-Y. Zhu, M. L. Steigerwald, F. Ng and C. Nuckolls. "Long, Atomically Precise Donor–Acceptor Cove-Edge Nanoribbons as Electron Acceptors". *Journal of the American Chemical Society* **139** (2017), 5648–5651. DOI: 10.1021/jacs.6b13093.

[277] P. Fantuzzi, L. Martini, A. Candini, V. Corradini, U. del Pennino, Y. Hu, X. Feng, K. Müllen, A. Narita and M. Affronte. "Fabrication of three terminal devices by ElectroSpray deposition of graphene nanoribbons". *Carbon* **104** (2016), 112–118. DOI: 10.1016/j.carbon.2016.03.052.

[278] J. N. O'Shea, J. B. Taylor, J. C. Swarbrick, G. Magnano, L. C. Mayor and K. Schulte. "Electrospray deposition of carbon nanotubes in vacuum". *Nanotechnology* **18** (2007), 035707. DOI: 10.1088/0957-4484/18/3/035707.

[279] R. Wei. private communication, data is soon to be published in a paper or doctoral thesis. 2020.

[280] U. Heiz, F. Vanolli, L. Trento and W.-D. Schneider. "Chemical Reactivity of Size-selected Supported Clusters: An Experimental Setup". *Rev. Sci. Instrum.* **68** (1997), 1986. DOI: 10.1063/1.1148113.

[281] D. A. Benson, M. Cavanaugh, K. Clark, I. Karsch-Mizrachi, D. J. Lipman, J. Ostell and E. W. Sayers. “GenBank”. *Nucleic Acids Res.* **41** (2012), D36–D42. DOI: 10.1093/nar/gks1195.

Acknowledgements

The finalization of the ES-CIBD was made possible by a lot of different people. First I would like to thank Prof. Johannes V. Barth, for giving me the opportunity to work as a PhD candidate at his chair. Secondly, I would like to thank Dr. Hartmut Schlichting for his supervision, support and fruitful discussions. Next I want to thank all predecessors on the project: Christian John, Richard Steinacher, Sabrina Sterzl, Theresa Buberl, Sibylle Fischer, David Reinisch, Wolfgang Witt, Nicolo Roberto Sernicola, Lukas Sigl, Seung Cheol Oh, and especially Tobias Kaposi and Michael Walz.

For the realization of this thesis special thanks goes to Peter Knecht for his STM investigations with the Cu-TCPP and Karolina Stoiber for the collaboration durring the experiments with Insulin and the pUC19 DNA. Further credit goes to Annette Hüttig for very helpful discussions about organic molecules and Prof. Dr. Peter Feulner for his widespread support in all kinds of technical and scientific topics. Last but not least, thanks to the supervisors of the STM Joachim Reichert and Anthoula Papageorgiou for their support and the measurement time.

When setting up a prototype one should also mention all the technical staff. Thanks to Reinhold Schneider for soldering and assembling all the PCBs of the electronics. Thanks to our technician Karl Eberle for his experience with construction and vacuum pumps. Thanks to all the workshops for their supply with components.

I want to thank all the E20 staff for the scientific communication and support as well as for all the social activities we did in the group.

Finally, I want to thank my whole family and especially my wife and daughter for their support during all the time of my academic pathway.